View metadata, citation and similar papers at core.ac.uk

brought to you by CORE

provided by D-Scholarship@Pitt

SEASONAL ANALYSIS OF THE RESPONSE OF JOINTED PLAIN CONCRETE PAVEMENTS TO FWD AND TRUCK LOADS

by

Jennifer K. McCracken

B.S. in Civil Engineering, University of Pittsburgh, 2006

Submitted to the Graduate Faculty of the

Swanson School of Engineering in partial fulfillment

of the requirements for the degree of

Master of Science in Civil Engineering

University of Pittsburgh

2008

UNIVERSITY OF PITTSBURGH

SWANSON SCHOOL OF ENGINEERING

This thesis was presented

by

Jennifer K. McCracken

It was defended on

April 1, 2008

and approved by

Amir Koubaa, Ph.D., Assistant Professor and Academic Coordinator,
Department of Civil and Environmental Engineering

Jeen-Shang Lin, Ph.D., Associate Professor,
Department of Civil and Environmental

Julie M. Vandenbossche, Ph.D., Assistant Professor,
Department of Civil and Environmental Engineering
Thesis Advisor

SEASONAL ANALYSIS OF THE RESPONSE OF JOINTED PLAIN CONCRETE PAVEMENTS TO FWD AND TRUCK LOADS

Jennifer K. McCracken, M.S.

University of Pittsburgh, 2008

A new pavement design procedure, known as the *Mechanistic-Empirical Design Guide* (MEPDG), is in development and incorporates new mechanistic-based models and performance prediction models. Structural response models are used to compute critical stresses, strains, and displacements in pavement systems due to traffic loads and climatic factors. These responses of the pavement structure are determined using finite element. Therefore, the MEPDG developed neural networks to reduce the necessary computational time. It is essential that the finite element models accurately depict the response of the slab to insure that calculated stress is representative of actual pavement stresses. Therefore, the focus of this study will be to develop finite element models that will be validated/calibrated from actual field strain measurements.

The following study analyzes the response of a joint plain concrete pavement (JPCP) to an applied load. The response of the pavement is characterized by performing seasonal load testing on an instrumented JPCP. The load testing consists of traversing trucks with known axle loads and configurations across the pavement and performing falling weight deflectometer (FWD) testing. The effects of varying restraint conditions, temperature and moisture gradients, and load magnitudes on the measured deflections and strains are characterized. These measured deflections and strains are also used in the development and validation/calibration of finite element models.

It was determined that temperature gradients at the time of FWD testing have an impact on load transfer efficiency, measured deflections, and the magnitude of the Void parameter, as well as the measured strain. An analysis of measured strains indicated the interface between the base and the slab is unbonded for the unrestrained slabs and bonded for the restrained slabs, indicating that the life of the bond might be a function of the restraint conditions. The primary factor affecting the measured deflections and strains was the slab restraint conditions.

TABLE OF CONTENTS

ACKNOWLEDGEMENTS XXI

1.0 INTRODUCTION 1

1.1 BACKGROUND 1

1.2 RESEARCH OBJECTIVE 2

1.3 RESEARCH APPROACH 3

1.4 STRUCTURE OF THE THESIS 3

2.0 LITERATURE REVIEW 4

2.1 SOURCES OF STRESS IN RIGID PAVEMENTS 4

2.2 FACTORS AFFECTING PAVEMENT RESPONSE TO APPLIED LOADS 5

2.2.1 Curling and Warping 5

2.2.1.1 CDOT Study 7

2.2.1.2 MnDOT's 2003 Study 8

2.2.2 Pavement Structure 9

2.2.2.1 MnDOT Study 10

2.2.3 Slab-Base Interaction 11

2.2.3.1 FAA DEN Study 12

2.2.3.2 University of Illinois DEN Study 14

2.3 COMPARISON OF FIELD MEASUREMENTS TO PREDICTED PAVEMENT RESPONSE 15

2.3.1 Guo and Dong Study 15
2.3.2 Guo and Pecht Study 16
3.0 FIELD STUDY 18
3.1 PROJECT LOCATION 18
3.2 DESIGN DETAILS 19
3.2.1 Geometric Details 20
3.2.2 Pavement Structure 20
3.2.3 Joint Details 21
3.3 TRAFFIC DETAILS 22
3.4 INSTRUMENTATION OF THE TEST SECTION 23
3.4.1 Environmental Sensors 24
3.4.1.1 Temperature Sensors 24
3.4.1.2 Concrete Moisture Sensors 27
3.4.1.3 Moisture Sensors in the Granular Layers 28
3.4.2 Dynamic Sensors 31
3.4.2.1 Dynamic Strain Sensors 31
4.0 PAVEMENT RESPONSE TO FWD LOADS 49
4.1 BACKGROUND 50
4.1.1 Joint Efficiency 51
4.1.2 Void Detection 53
4.1.3 Backcalculation of Moduli 54
4.2 CONCRETE TEMPERATURE AND MOISTURE DISTRIBUTIONS DURING FWD TESTING 56
4.2.1 Concrete Temperature Distribution 57
4.2.2 Concrete Moisture Distribution 66

4.3 JOINT PERFORMANCE 69

4.3.1 Effect of Temperature Gradients on Load Transfer Efficiency 73

4.3.2 Relationship between Strain and Load Transfer Efficiency 78

4.4 VOID DETECTION 85

4.5 SUPPORT CONDITIONS 92

4.6 DEFLECTIONS AT EACH LOCATION 99

5.0 PAVEMENT RESPONSE TO TRUCK LOADING 105

5.1 TRUCK LOAD TESTING 106

5.2 CONCRETE TEMPERATURE AND MOISTURE DISTRIBUTIONS DURING TRUCK TESTING 108

5.2.1 Concrete Temperature Distribution 109

5.2.2 Concrete Moisture Distribution 125

5.3 COMPARISON OF STRAINS MEASURED AT DIFFERENT LOCATIONS WITHIN THE SLAB 127

5.3.1 Strain in the Restrained Slabs 128

5.3.2 Strain in the Unrestrained Slabs 131

5.4 EFFECT OF AXLE CONFIGURATION ON MEASURED STRAIN 133

5.5 EFFECT OF AXLE LOAD MAGNITUDE ON MEASURED STRAIN 138

5.6 DYANMIC STRAINS MEASURED AT THE TOP AND BOTTOM OF THE SLAB 141

5.6.1 Strain at the Top and Bottom of the Restrained Slabs 142

5.6.2 Strain at the Top and Bottom of the Unrestrained Slabs 144

5.7 EFFECT OF SLAB TEMPERATURE AND GRADIENTS ON DYNAMIC STRAIN 145

6.0 DEVELOPMENT AND VALIDATION OF FINITE ELEMENT MODELS 150

6.1 MODEL INPUTS 150

6.1.1 Mesh-Slab Model Inputs 151
6.1.2 Inputs for Modeling Slab Joints 155
6.1.3 Modeling of the Loads Applied to the Pavement Structure 156
6.2 FINITE ELEMENT MODEL CALIBRATION 158
6.2.1 Calibration Using Group 1 Sensors (Adjacent to the Transverse Joint) 159
6.2.1.1 Calibration of the Restrained Slabs Using the Group 1 Sensors 160
6.2.1.2 Calibration of the Unrestrained Slabs Using the Group 1 Sensors 163
6.2.2 Calibration Using Group 2 Sensors (Along the Lane/Shoulder Joint) 165
6.2.2.1 Calibration of the Restrained Slabs Using Group 2 Sensors 166
6.2.2.2 Calibration of the Unrestrained Slabs Using the Group 2 Sensors 168
6.2.3 Calibration Using Group 3 Sensors (Midpanel) 170
6.2.3.1 Calibration of the Restrained Slabs Using the Group 3 Sensors 170
6.2.3.2 Calibration of the Unrestrained Slabs Using the Group 3 Sensors 172
7.0 CONCLUSIONS AND RECOMMENDATIONS 175
7.1 CONCLUSIONS 175
7.2 RECOMMENDATIONS 177
APPENDIX A 178
APPENDIX B 196
BIBLIOGRAPHY 202

LIST OF TABLES

Table 3.1. Summary of sensors installed in the test section. 23

Table 4.1. Seasonal temperature variation during FWD testing. 58

Table 4.2. Seasonal equivalent linear temperature gradients present during FWD testing. 87

Table 5.1. Target axle loads for each truck. 108

Table 5.2. Temperature variation during truck testing. 110

Table 5.3. Variation in the depth of the dynamic sensors of the restrained cell. 130

Table 5.4. Variation in the depth of the dynamic sensors in the unrestrained cell. 132

Table 6.1. Number of element used for generating the finite element models. 152

Table 6.2. PCC model inputs for each slab type based on measured values. 152

Table 6.3. ATPB model inputs based on measured values. 153

Table 6.4. Average seasonal elastic moduli of the ATPB for the restrained and unrestrained slabs 154

Table 6.5. Average seasonal backcalculated static k-values for the restrained and unrestrained slabs 154

Table 6.6. The measured load transfer efficiency along the transverse joint of the restrained and unrestrained slabs. 155

Table 6.7. The measured load transfer efficiency along the longitudinal joint for the unrestrained slabs 156

LIST OF FIGURES

Figure 2.1. Locations of critical stresses due to slab curling and warping. 6

Figure 2.2. Critical loading conditions due to the combined effect of environmental and vehicular loads. 7

Figure 3.1. Map of the Pittsburgh area including project location (www.mapquest.com, June 2007). 19

Figure 3.2. Test section in the westbound lanes (Wells et al 2005)..... 20

Figure 3.3. Cross-section of pavement structure (Wells et al 2005)..... 21

Figure 3.4. Dowel and tie bar configuration (Wells et al. 2005). 22

Figure 3.5. Thermocouples used to measure temperature throughout the pavement (Wells et al. 2005). 25

Figure 3.6. Location of thermocouples in Cell 4 (Wells et al. 2005). 25

Figure 3.7. Depth of thermocouples sensors located in Cell 4 (Asbahan et al. 2006)..... 26

Figure 3.8. Relative humidity sensors located throughout the PCC slab (Well et al. 2005). 27

Figure 3.9. Location of concrete moisture sensors located in Cell 4 (Asbahan et al. 2006). 27

Figure 3.10. Depths of the concrete moisture sensors located in Cell 4 (Asbahan et al. 2006). .. 28

Figure 3.11. Installation of CS605L TDR probe in the subgrade (Wells et al. 2005). 28

Figure 3.12. Locations of the TDR probes located in Cell 4 (Asbahan et al. 2006)..... 29

Figure 3.13. Depths of the TDR probes within the pavement structure in Cell 4 (Asbahan et al. 2006). 30

Figure 3.14. Tokyo Sokki PML-60-2Ld dynamic strain gauges (Wells et al. 2005). 32

Figure 3.15. Sensor layout for Cell 1 and Cell 2 (Asbahan et al. 2006) 48

Figure 4.1. Deflection measurement locations for measuring load transfer efficiency. 51

Figure 4.2. Estimating the presence of a void using FWD data. 54

Figure 4.3. Midpanel temperature conditions during FWD testing performed in the fall of 2004. 59

Figure 4.4. Midpanel temperature conditions during FWD testing performed in the fall of 2006. 59

Figure 4.5. Midpanel temperature conditions during FWD testing performed in the fall of 2007. 60

Figure 4.6. Midpanel temperature conditions during FWD testing performed in the winter of 2005..... 61

Figure 4.7. Midpanel temperature conditions during FWD testing performed in the winter of 2006..... 61

Figure 4.8. Midpanel temperature conditions during FWD testing performed in the winter of 2007..... 62

Figure 4.9. Midpanel temperature conditions during FWD testing performed in the spring of 2005..... 63

Figure 4.10. Midpanel temperature conditions during FWD testing performed in the spring of 2006..... 63

Figure 4.11. Midpanel temperature conditions during FWD testing performed in the spring of 2007..... 64

Figure 4.12. Midpanel temperature conditions during FWD testing performed in the summer of 2005..... 65

Figure 4.13. Midpanel temperature conditions during FWD testing performed in the summer of 2006..... 65

Figure 4.14. Midpanel temperature conditions during FWD testing performed in the summer of 2007..... 66

Figure 4.15. Midpanel moisture distribution throughout the PCC slab during FWD testing..... 67

Figure 4.16. Edge moisture distribution throughout the PCC slab during FWD testing. 67

Figure 4.17. Load transfer efficiencies measured for each cell. 70

Figure 4.18. Relationship between load transfer efficiency and equivalent linear temperature gradient of the unrestrained Cell 3. 74

Figure 4.19. Relationship between load transfer efficiency and age of the pavement for the unrestrained Cell 3. 76

Figure 4.20. Relationship between load transfer efficiency and equivalent linear temperature gradient of the unrestrained Cell 2. 77

Figure 4.21. Relationship between load transfer efficiency and equivalent linear temperature gradient of the unrestrained Cell 1. 78

Figure 4.22. Relationship between load transfer efficiency and strain measured in the wheelpath on the bottom of the restrained slabs. 79

Figure 4.23. Relationship between load transfer efficiency and strain measured in the wheelpath 1 in from the surface of the restrained slabs. 80

Figure 4.24. Microstrain verse load transfer efficiency for the restrained Cell 1 bottom sensors at the corner location. 80

Figure 4.25. Microstrain verse load transfer efficiency for the restrained Cell 1 top sensors at the corner location. 81

Figure 4.26. Microstrain verse load transfer efficiency for the unrestrained Cell 2 bottom sensors at the wheelpath location. 83

Figure 4.27. Microstrain verse load transfer efficiency for the unrestrained Cell 2 top at the wheelpath location. 83

Figure 4.28. Microstrain verse load transfer efficiency for the unrestrained Cell 2 bottom sensors at the corner location. 84

Figure 4.29. Microstrain verse load transfer efficiency for the unrestrained Cell 2 top sensors at the corner location. 84

Figure 4.30. Void parameters calculated along the Smart Pavement for each cell. 85

Figure 4.31. Relationship between the Void parameter and the equivalent linear temperature gradient present for unrestrained Slab A in Cell 2. 88

Figure 4.32. Relationship between the Void parameter and the equivalent linear temperature gradient present for unrestrained Slab B in Cell 3. 89

Figure 4.33. Relationship between the Void parameter and the equivalent linear temperature gradient for restrained Slab B in Cell 1. 91

Figure 4.34. The calculated k-value across the Smart Pavement. 93

Figure 4.35. Average annual seasonal support conditions across the Smart Pavement. 94

Figure 4.36. The cumulative monthly precipitation measured since construction of the Smart Pavement. 95

Figure 4.37. Comparison of the support conditions beneath the slab and the average temperature of the asphalt treated permeable base throughout testing. 96

Figure 4.38. Comparison of the support conditions beneath the slab and the equivalent linear temperature gradient of the slab during testing for unrestrained Slab A in Cell 3. 98

Figure 4.39. Comparison of support conditions beneath the slab and the equivalent linear temperature gradient of the slab during testing for restrained Slab A in Cell 1. 98

Figure 4.40. Deflections measured in the corner of each slab. 100

Figure 4.41. Deflections measured along the lane/shoulder joint. 101

Figure 4.42. Deflections measured at midpanel. 102

Figure 4.43. Deflections measured in the wheelpath, adjacent to the transverse joint. 103

Figure 5.1. Axle configurations for truck testing. 107

Figure 5.2. Verification of axle loads. 108

Figure 5.3. Midpanel temperature conditions during Class 10 truck testing performed in the fall of 2004. 111

Figure 5.4. Midpanel temperature conditions during Class 6 and 7 truck testing performed in the fall of 2004. 112

Figure 5.5. Midpanel temperature conditions during Class 10 truck testing performed in the fall of 2005. 112

Figure 5.6. Midpanel temperature conditions during Class 6 truck testing performed in the fall of 2005 113

Figure 5.7. Midpanel temperature conditions during Class 10 truck testing performed in the fall of 2006. 113

Figure 5.8. Midpanel temperature conditions during Class 6 and 7 truck testing performed in the fall of 2006. 114

Figure 5.9. Midpanel temperature conditions during Class 6, 7, and 10 truck testing performed in the fall of 2007. 114

Figure 5.10. Midpanel temperature conditions during Class 10 truck testing performed in the winter of 2005. 115

Figure 5.11. Midpanel temperature conditions during Class 6 and 7 truck testing performed in the winter of 2005. 116

Figure 5.12. Midpanel temperature conditions during Class 10 truck testing performed in the winter of 2006. 116

Figure 5.13. Midpanel temperature conditions during Class 6 and 7 truck testing performed in the winter of 2006. 117

Figure 5.14. Midpanel temperature conditions during Class 10 truck testing performed in the winter of 2007. 117

Figure 5.15. Midpanel temperature conditions during Class 6 and 7 truck testing performed in the winter of 2007. 118

Figure 5.16. Midpanel temperature conditions during Class 10 truck testing performed in the spring of 2005. 119

Figure 5.17. Midpanel temperature conditions during Class 6 and 7 truck testing performed in the spring of 2005. 119

Figure 5.18. Midpanel temperature conditions during Class 10 truck testing performed in the spring of 2006. 120

Figure 5.19. Midpanel temperature conditions during Class 6 and 7 truck testing performed in the spring of 2006. 120

Figure 5.20. Midpanel temperature conditions during Class 10 truck testing performed in the spring of 2007. 121

Figure 5.21. Midpanel temperature conditions during Class 6 and 7 truck testing performed in the spring of 2007. 121

Figure 5.22. Midpanel temperature conditions during Class 10 truck testing performed in the summer of 2005. 122

Figure 5.23. Midpanel temperature conditions during Class 6 and 7 truck testing performed in the summer of 2005. 123

Figure 5.24. Midpanel temperature conditions during Class 10 truck testing performed in the summer of 2006. 123

Figure 5.25. Midpanel temperature conditions during Class 6 and 7 truck testing performed in the summer of 2006. 124

Figure 5.26. Midpanel temperature conditions during Class 6, 7, and 10 truck testing performed in the summer of 2007. 124

Figure 5.27. Midpanel moisture distribution throughout the PCC slab during truck testing..... 125

Figure 5.28. Edge moisture distribution throughout the PCC slab during Class 10 truck testing. 126

Figure 5.29. Average strains measured at various locations at the top of the restrained slabs during the first three years after construction. 129

Figure 5.30. Average strains measured at various locations at the bottom of the slabs during the first three years after construction..... 129

Figure 5.31. Average strains measured at various locations at the bottom of the slabs during the first three years after construction..... 133

Figure 5.32. Average normalized strains measured along the edge of the restrained and unrestrained slabs for the Class 6 truck with 25,000 lb axle loads. 134

Figure 5.33. Average normalized strains measured along the edge of the restrained and unrestrained slabs for the Class 7 truck with 25,000 lb axle loads. 135

Figure 5.34. Average normalized strains measured along the edge of the restrained and unrestrained slabs for the Class 10 truck with 25,000 lb axle loads. 136

Figure 5.35. Average normalized strains measured along the edge of the restrained and unrestrained slabs for the tandem axle of the Class 6 and 10 trucks. 137

Figure 5.36. Average normalized strains measured along the edge of the restrained and unrestrained slabs for the tridem axle of the Class 7 and 10 trucks..... 138

Figure 5.37. Strains measured along the edge for the critical axle of the Class 6 truck for various load levels. 139

Figure 5.38. Strains measured along the edge for the critical axle of the Class 7 for various load levels. 140

Figure 5.39. Strains measured along the edge in the unrestrained slabs for the critical axle of the Class 10 for various load levels. 140

Figure 5.40. Strains measured along the edge of the slabs for the critical axle of all the truck classes and load levels. 141

Figure 5.41. Strain measured at the top and bottom along the edge of the restrained slabs for the 1st axle of a Class 6 truck. 143

Figure 5.42. Strain measured at the top and bottom of the slab along the edge of the restrained cell..... 145

Figure 5.43. Relationship between strains measured in the wheelpath at the bottom of the restrained slabs and slab temperature. 146

Figure 5.44. Relationship between strains measured in the corner at the bottom of the restrained slabs and slab temperature. 147

Figure 5.45. Relationship between strains measured in the wheelpath at the bottom of the unrestrained slabs and slab temperature. 147

Figure 5.46. Relationship between strains measured in the wheelpath at the top of the restrained slabs and the temperature gradient in the slab. 149

Figure 5.47. Relationship between strains measured in the wheelpath at the top of the unrestrained slabs and the temperature gradient in the slab. 149

Figure 6.1. Axle configuration and tire spacing of the Class 6 truck. 157

Figure 6.2. Axle configuration and tire spacing of the Class 7 truck. 157

Figure 6.3. Axle configuration and tire spacing of the Class 10 truck. 158

Figure 6.4. Dynamic strain sensor layout. 159

Figure 6.5. Calibration results for the sensors located adjacent to the transverse joint in the restrained slabs for the Class 6 truck. 161

Figure 6.6. Calibration results for the sensors located adjacent to the transverse joint in the restrained slabs for the Class 7 truck. 162

Figure 6.7. Calibration results for the sensors located adjacent to the transverse joint in the restrained slabs for the Class 10 truck. 162

Figure 6.8. Calibration results for the sensors located adjacent to the transverse joint in the unrestrained slabs for the Class 6 truck. 164

Figure 6.9. Calibration results for the sensors located adjacent to the transverse joint in the unrestrained slabs for the Class 7 truck. 164

Figure 6.10. Calibration results for the sensors located adjacent to the transverse joint in the unrestrained slabs for the Class 10 truck 165

Figure 6.11. Calibration results for the sensors located adjacent to lane/shoulder joint in the restrained slabs for the Class 6 truck. 166

Figure 6.12. Calibration results for the sensors located adjacent to lane/shoulder joint in the restrained slabs for the Class 7 truck. 167

Figure 6.13. Calibration results forthe sensors located adjacent to lane/shoulder joint in the restrained slabs for the Class 10 truck. 167

Figure 6.14. Calibration results for the sensors located adjacent to lane/shoulder joint in the unrestrained slabs for the Class 6 truck. 168

Figure 6.15. Calibration results for the sensors located adjacent to lane/shoulder joint in the unrestrained slabs for the Class 7 truck. 169

Figure 6.16. Calibration results for the sensors located adjacent to lane/shoulder joint in the unrestrained slabs for the Class 10 truck. 169

Figure 6.17. Calibration results for the sensors at midpanel in the restrained slabs for the Class 6 truck. 171

Figure 6.18. Calibration results for the sensors at midpanel in the restrained slabs for the Class 7 truck. 171

Figure 6.19. Calibration results for the sensors at midpanel in the restrained slabs for the Class 10 truck. 172

Figure 6.20. Calibration results for the sensors at midpanel in the unrestrained slabs for the Class 6 truck. 173

Figure 6.21. Calibration results for the sensors at midpanel in the unrestrained slabs for the Class 7 truck. 173

Figure 6.22. Calibration results for the sensors at midpanel in the unrestrained slabs for the Class 10 truck. 174

Figure A1. Relationship between load transfer efficiency and age of the pavement for the unrestrained Cell 2. 178

Figure A2. Relationship between load transfer efficiency and age of the pavement for the unrestrained Cell 2. 179

Figure A3. Relationship between load transfer efficiency and age of the pavement for the unrestrained Cell 2. 179

Figure A4. Relationship between load transfer efficiency and age of the pavement for the unrestrained Cell 3. 180

Figure A5. Relationship between load transfer efficiency and age of the pavement for the unrestrained Cell 3. 180

Figure A6. Relationship between load transfer efficiency and equivalent linear temperature gradient for the unrestrained Cell 2. 181

Figure A7. Relationship between load transfer efficiency and equivalent linear temperature gradient for the unrestrained Cell 2. 181

Figure A8. Relationship between load transfer efficiency and equivalent linear temperature gradient for the unrestrained Cell 3. 182

Figure A9. Relationship between load transfer efficiency and equivalent linear temperature gradient for the unrestrained Cell 3. 182

Figure A10. Relationship between load transfer efficiency and equivalent linear temperature gradient for the unrestrained Cell 3. 183

Figure A11. Relationship between load transfer efficiency and equivalent linear temperature gradient for the restrained Cell 1. 183

Figure A12. Relationship between load transfer efficiency and equivalent linear temperature gradient for the restrained Cell 1. 184

Figure A13. Relationship between load transfer efficiency and equivalent linear temperature gradient for the restrained Cell 1. 184

Figure A14. Relationship between load transfer efficiency and equivalent linear temperature gradient for the restrained Cell 4. 185

Figure A15. Relationship between load transfer efficiency and equivalent linear temperature gradient for the restrained Cell 4. 185

Figure A16. Relationship between load transfer efficiency and equivalent linear temperature gradient for the restrained Cell 4. 186

Figure A17. Relationship between load transfer efficiency and equivalent linear temperature gradient for the restrained Cell 4. 186

Figure A18. Relationship between the Void parameter and the equivalent linear temperature gradient present during testing for the restrained Slab A in Cell 1..... 187

Figure A19. Relationship between the Void parameter and the equivalent linear temperature gradient present during testing for the unrestrained Slab B in Cell 2..... 187

Figure A20. Relationship between the Void parameter and the equivalent linear temperature gradient present during testing for the unrestrained Slab A in Cell 3..... 188

Figure A21. Relationship between the Void parameter and the equivalent linear temperature gradient present during testing for the unrestrained Slab B in Cell 3..... 188

Figure A22. Relationship between the Void parameter and the equivalent linear temperature gradient present during testing for the unrestrained Slab C in Cell 3..... 189

Figure A23. Relationship between the Void parameter and the equivalent linear temperature gradient present during testing for the restrained Slab A in Cell 4..... 189

Figure A24. Relationship between the Void parameter and the equivalent linear temperature gradient present during testing for the restrained Slab B in Cell 4..... 190

Figure A25. Relationship between the Void parameter and the equivalent linear temperature gradient present during testing for the restrained Slab C in Cell 4..... 190

Figure A26. Comparison of the support conditions beneath the slab and the equivalent linear temperature gradient of the slab during testing for restrained Slab B in Cell 1..... 191

Figure A27. Comparison of the support conditions beneath the slab and the equivalent linear temperature gradient of the slab during testing for unrestrained Slab B in Cell 2..... 191

Figure A28. Comparison of the support conditions beneath the slab and the equivalent linear temperature gradient of the slab during testing for unrestrained Slab A in Cell 3. 192

Figure A29. Comparison of the support conditions beneath the slab and the equivalent linear temperature gradient of the slab during testing for unrestrained Slab B in Cell 3..... 192

Figure A30. Comparison of the support conditions beneath the slab and the equivalent linear temperature gradient of the slab during testing for unrestrained Slab C in Cell 3..... 193

Figure A31. Comparison of the support conditions beneath the slab and the equivalent linear temperature gradient of the slab during testing for restrained Slab A in Cell 4. 193

Figure A32. Comparison of the support conditions beneath the slab and the equivalent linear temperature gradient of the slab during testing for restrained Slab B in Cell 4..... 194

Figure A33. Comparison of the support conditions beneath the slab and the equivalent linear temperature gradient of the slab during testing for restrained Slab C in Cell 4..... 194

Figure A34. Comparison of the support conditions beneath the slab and the equivalent linear temperature gradient of the slab during testing for restrained Slab D in Cell 4. 195

Figure A35. Comparison of the support conditions beneath the slab and the equivalent linear temperature gradient of the slab during testing for restrained Slab E in Cell 4..... 195

Figure B1. Relationship between strain measured in the wheelpath at the bottom of the restrained slabs and slab temperature. 196

Figure B2. Relationship between strain measured in the wheelpath at the top of the unrestrained slabs and slab temperature. 197

Figure B3. Relationship between strain measured in the corner at the bottom of the restrained slabs and slab temperature. 197

Figure B4. Relationship between strain measured in the corner at the top of the unrestrained slabs and slasb temperature..... 198

Figure B5. Relationship between strain measured in the corner at the bottom of the unrestrained slabs and slab temperature. 198

Figure B6. Relationship between strain measured in the wheelpath at the bottom of the restrained slabs and the temperature gradient in the slab. 199

Figure B7. Relationship between strain measured in the wheelpath at the bottom of the unrestrained slabs and the temperature gradient in the slab. 199

Figure B8. Relationship between strain measured in the corner at the top of the restrained slabs and the temperature gradient in the slab. 200

Figure B9. Relationship between strain measured in the corner at the bottom of the restrained slabs and the temperature gradient in the slab. 200

Figure B10. Relationship between strain measured in the corner at the top of the unrestrained slabs and the temperature gradient in the slab. 201

Figure B11. Relationship between strain measured in the corner at the bottom of the unrestrained slabs and the temperature gradient in the slab. 201

ACKNOWLEDGEMENTS

I would first like to thank the Pennsylvania Department of Transportation and the Federal Highway Administration for their financial support and assistance in the data collection for this project.

I would like to thank my advisor, Dr. Julie Vandenbossche, for her support, encouragement, understanding, and expert guidance the past few years. Her dedication and commitment to this research and my education has been inspirational. I aspire to someday be as good of a researcher and person as she is. I honestly could never have done any of this if she hadn't believed in me from the beginning.

I would also like to express my sincerest gratitude to all the graduate and undergraduate students who offered their assistance with the project. Without their dedication, hard-work, and in some cases patience this work would not be completed. I would especially like to thank Ms. Rania Asbahan, for her support, friendship, guidance, and most of all understanding.

Finally, I would like to thank my family: Mom and Dad, Timmy, Jessie, and most of all my husband, Bob. It is with their love, support, and encouragement that I pursued my masters' degree and it is why I push myself to be all I can. I also want to thank them all for listening to me worry and complain during this work, as they continued to push me in the right direction.

1.0 INTRODUCTION

1.1 BACKGROUND

The current procedure for the design and rehabilitation of pavement structures is the AASHTO *Guide for Design of Pavement Structures.* This procedure has served well for several decades; however, there are many limitations that exist in this current empirical based design procedure. The development of the current design procedure was based on the American Association of State Highway Officials (AASHO) road test, which was conducted in the 1950's in Ottawa, Illinois. Therefore, the design was developed based on traffic conditions, paving materials and construction practices that are not representative of what is currently in use. Because of the numerous limitations, a new design guide is currently in development.

The new design procedure, known as the *Mechanistic-Empirical Design Guide* (MEPDG), incorporates mechanistic-based models and performance prediction models that reflect current paving materials and traffic conditions. Proper structural modeling of a rigid pavement is the core of a mechanistic-based design procedure. Structural response models are used to compute critical stresses, strains, and displacements in flexible and rigid pavement systems due to both traffic loads and climatic factors (temperature and moisture). This approach accounts for the incremental damage associated with each load applied to the pavement throughout the design life of the structure. The analysis increments are strategically selected to

account for changes in subgrade support, joint openings, traffic conditions, and concrete material properties with time.

The incremental design procedure incorporated in the MEPDG requires the calculation of hundreds of thousands of stress and deflection measurements to compute damage over the design life. Although finite element programs are capable of making these computations, the analysis would take days to complete. Therefore, the MEPDG developed neural networks to reduce the necessary computational time. These neural networks were trained using a database populated with critical stresses and deflections determined using the finite element software ISLAB2000. It is essential that the finite element model accurately depicts the response of the slab because a key component to the ability to predict distress is to insure that the calculated stress is representative of actual pavement stresses. Therefore, the focus of this study will be to develop finite element models that will be calibrated from actual field strain measurements. These models can then be used in future studies to validate the stress prediction models in the MEPDG.

1.2 RESEARCH OBJECTIVE

The first objective of this research is to evaluate the response of a JPCP to an applied load. The second objective is to use measured pavement response in the development of finite element models.

1.3 RESEARCH APPROACH

The first objective is met by performing seasonal load testing on an instrumented JPCP. The load testing consists of traversing trucks with known axle loads and configurations across the pavement and performing falling weight deflectometer (FWD) testing. The load testing is performed four times a year to measure and characterize seasonal deflections and strains in a JPCP. These deflections and strains are used in the development and validation/calibration of finite element models to address the second objective. These models can be used in future work to evaluate the calculation of stress and deflection in the MEPDG. .

1.4 STRUCTURE OF THE THESIS

The structure of this thesis is as follows: Chapter 2 is a literature review that includes a discussion of sources of stresses in rigid pavements, factors affecting load induced stresses and previous studies that compared strain measurements to finite element models. Chapter 3 provides a description of the instrumented pavement section used in this study. Chapter 4 presents the characterization of pavement response to falling weight deflectometer testing collected over a three-year period. Chapter 5 is an analysis of the pavement response to dynamic strains measured from trucks of known axle loads and axle configurations. Chapter 6 uses the inputs backcalculated from the FWD deflection data and strains measured in the field to develop finite element models. Finally, the models are used in a small study looking at the effects of slab restraint, season, climatic conditions and load levels. Chapter 7 presents the conclusions surmised as a result of this study and recommendations for future research.

2.0 LITERATURE REVIEW

This chapter presents a review of information available on the development of stress in concrete pavements. It begins with an overview of sources of stress in rigid pavements and is followed by a discussion of factors affecting load induced stress. The focus of this study is to characterize the response of a jointed plain concrete to an applied load, which is typically done by analyzing stress. Unfortunately, stress in a pavement can not be measured in the field therefore; strain is used to characterize response in the field and can be related to stress through empirical relationships. Following the discussion of load induced stress, a detailed discussion of past work pertaining to the use of strain measurements produced as a result of vehicle loads is then provided. Finally a discussion is provided on how these measured responses can be used to estimate the resulting accumulated damage, which can then be related to pavement performance.

2.1 SOURCES OF STRESS IN RIGID PAVEMENTS

There are a variety of sources of stress in rigid pavements. A few of these include wheel loads, changes in temperature, changes in moisture, and changes in the support conditions of the structure. Therefore, due to the numerous sources of stress in rigid pavements, a classification of broader stress-inducing factors is appropriate. These classifications are as follows:

1. restrained temperature and moisture deformations

2. externally applied loads

3. continuity of the subgrade support as affected by permanent deformations of the subgrade or loss of support through pumping. (Yoder and Witzcak, 1995).

The focus of this research effort will be on stress/strain generated by applied loads. Stress/strain due to temperature and moisture deformations, and changes in the support conditions affect the magnitude of the stress imposed by an externally applied load. Therefore, it is imperative to understand the factors affecting the magnitude of load induced stress/strain.

2.2 FACTORS AFFECTING PAVEMENT RESPONSE TO APPLIED LOADS

There are several factors affecting load pavement response. These factors include: gradients due to curling and warping, the location and configuration of the load, the pavement stiffness, and slab-base interaction. A discussion of each of these factors follows.

2.2.1 Curling and Warping

Temperature and moisture differences between the top and bottom of PCC slab cause curvature in the slab known as curling and warping. Curling, which is caused by temperature differentials in the PCC (Portland cement concrete) slab, can be either upward or downward. Upward curling is a result of a negative gradient (the slab surface is cooler than the bottom of the slab). This typically occurs between late in the evening and the early morning hours. Downward curvature occurs when a positive gradient is present (the slab surface is warmer than the bottom of the slab). Positive gradient develop in the slab during in the afternoon. Moisture differences in the

PCC slab also cause slab curvature known as warping. Upward warping is the result of the slab surface being drier than the bottom. (Jeong and Zollinger, 2005; Yu et al., 1998).

Critical tensile stresses occur at different locations as the result of upward and downward slab curvature of the PCC slab, as shown in Figure 2.1. The slab on the left side is the result of a negative gradient. This causes loss of support near the ends of the slab, and the weight of the slab exerts tensile stresses near the top of the PCC. Similarly, the slab on the right side of the figure represents a positive gradient. In this case, support is lost near the slab center and the weight of the slab exerts tensile stresses near the bottom of the slab (Jeong and Zollinger, 2005; Yu et al., 1998).

Figure 2.1. Locations of critical stresses due to slab curling and warping.

Curling and warping has a significant affect on load induced stress depending on the curvature of the slab and location of the load. As Figure 2.2 shows, the critical location of a wheel load varies as the shape of the slab changes. During a positive gradient, the slab curves downward and midslab loading constitutes the critical loading condition. Likewise, in the presence of a negative gradient, the slab curves upward and the critical loading condition is at the edge of the slab.

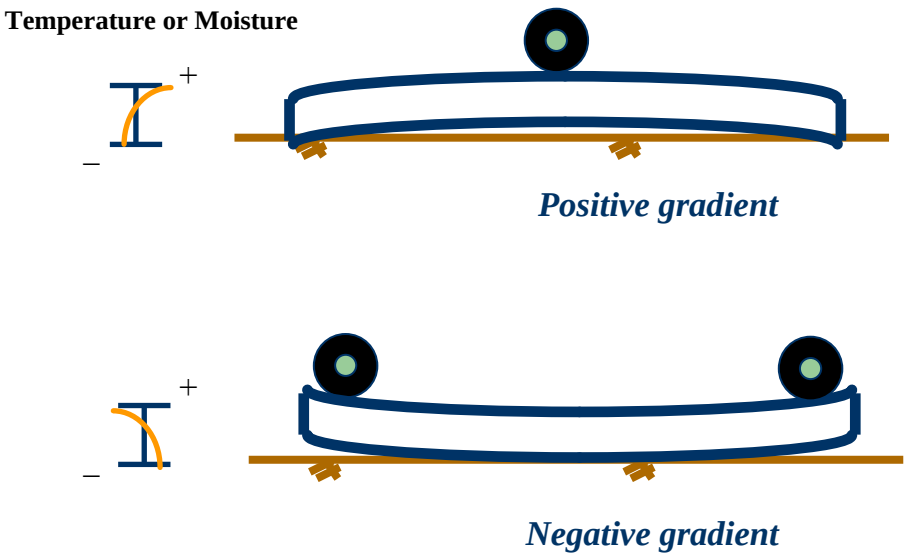

Figure 2.2. Critical loading conditions due to the combined effect of environmental and vehicular loads.

Several studies have been performed to investigate the effect of curling and warping on load induced strain. The following presents an overview of two studies in which the effect of temperature and moisture conditions on measured load-induced strain was investigated.

2.2.1.1 CDOT Study

In the summer of 1994, the Colorado Department of Transportation evaluated the response of PCC pavement slabs under temperature and wheel loadings, using data obtained from instrumented slabs (Yu et al. 1998). This instrumentation consisted of surface-mounted strain gauges, dial gauges, and thermocouples placed in the slabs. Several significant findings were determined from this study.

First, the magnitude of the built-in temperature gradient greatly affects measured critical stresses in the slab. The temperature gradient present at the time the concrete sets is referred to as the built-in temperature gradient. The magnitude of the built-in temperature gradient is influenced by the time of the day the concrete is placed and by daily fluctuations in ambient

temperature at that time. If a negative built-in temperature gradient exists, corner load stress can become critical and can cause fatigue cracking to initiate from the slab surface. Also, because negative temperature gradients occur more frequently then positive gradients, corner load stress does not have to be greater than edge stress for top-down cracking to become critical.

A second major finding is that load-induced strains are not significantly affected by temperature gradients. The temperature gradient present during loading is affecting the support conditions of the slab, through slab movement from curling and warping which in turn affects the measured strains. Also, field evaluations showed that the actual physical bond between the base and slab is not necessary to have bonded behavior in the pavement system. The friction between base and slab is usually sufficient enough to produce a bonded behavior. Although load strains are not significantly affected by temperature gradients, a trend of increased strain with increasing negative temperature gradients was discovered (Yu and al. 1998).

2.2.1.2 MnDOT's 2003 Study

In 2003, Tom Burnham, of the Minnesota Department of Transportation investigated the seasonal load response of a thin PCC pavement, at the Minnesota Road Research Project. A 7-in thick jointed plain concrete pavement was instrumented with strain gauges, thermocouples, moisture sensors, and under-slab pressure plates to measure dynamic and environmental loads. The data analyzed in this study was collected in the early and late spring, summer, and late fall of 2001. The measured peak strain values were extrapolated to the surface using plane strain theory because the strain gauges were embedded in the slab (Burnham 2003).

Several trends were experienced that help characterize pavement response to environmental and applied loadings. For instance, strain measured in the pavement was dependent on the shape of the slab during testing. During periods where positive gradients were

present, tensile strains at midpanel increased. Also, the effect of changes in speed (5 and 30 mph) on measured dynamic strain was found to be less significant then tire offset and truck dynamics. (Burnham 2003).

The seasonal response of the slab was also investigated with several notable trends. During periods when large positive temperature gradients were present, strain measured at the top of the slab increased by 60 percent from early spring to late spring, indicating that late spring is more critical to dynamic load response. The changes in strain between late spring, summer, and late fall were not as pronounced when temperature gradients were not present. However, early spring strain was again lower indicating the effect the frozen base and subgrade layers have on strain in the slab (Burnham 2003).

2.2.2 Pavement Structure

Pavement stiffness influences the response of the slab to applied loads. The stiffness of the slab is primarily a function of the slab thickness and the elastic modulus of the concrete. Slab thickness is one of the most critical design features from the standpoint of both performance and cost. In general, as the slab thickness increases, critical bending stresses and deflections decrease, reducing cracking and faulting. Additionally, the PCC elastic modulus (E_{PCC}) influences stress generation in a pavement. For the same level of strain, the slab with the higher elastic modulus will experience higher levels of stress.

The underlying layers of a pavement structure also affect stress due to applied loads. The stiffness of the subgrade and subbase is characterized by the modulus of subgrade reaction, k or k-value. Additionally, the stiffness of the base is characterized by the elastic modulus. The k-value and elastic modulus represent the stiffness of all layers beneath the slab. Typically, the k-

value and elastic modulus will be the highest during the winter season when the granular layers are frozen. During the spring, the k-value would be lower than the other seasons since moisture content in the granular layers would be higher. As the stiffness of the supporting layers changes, so does the load induced stress. (Asbahan et al 2006).

Various studies have investigated the effect the pavement structure has on load induced stresses. The following presents an overview of one study in which the effect of the stiffness of the pavement structure on load-induced strain was investigated.

2.2.2.1 MnDOT Study

In October 1982 and February 1983, a study was conducted by the Minnesota Department of Transportation to measure and analyze load-induced strains and deflections during fall and winter periods. Concrete strains were measured using electrical resistance strain gauges that were cemented to the pavement surface. This study was used to establish the effects of frozen subgrade support on concrete pavement performance (Tayabji et al. 1984).

Several results were determined about pavement performance from this study. Most importantly, it was concluded that during the winter when the subgrade is frozen pavement deflections and strains are reduced greatly. It was determined that loads applied during the winter are approximately one-seventh as damaging as loads applied during the fall (Tayabji et al.1984).

2.2.3 Slab-Base Interaction

Slab-base interaction is another factor that affects stresses in concrete pavements. There are three contact conditions as defined by Huang and Wang. These include: full contact, partial contact without initial gaps, and partial contact with initial gaps.

Typically slabs are modeled using a liquid or Winkler foundation, which consists of a series of springs. The stiffness of these springs is defined by the k-value. Once a slab is placed on a foundation, the weight of the slab will cause an initial precompression of these springs. As previously discussed, temperature gradients develop daily in the concrete slab. For example, during the evening when the temperature on top of the slab is colder than that at the bottom, the slab curves upward. Although the slab is deflecting upward, the base and slab remain in contact as long as the curvature does not exceed precompression (Huang 2004). Therefore, the two layers act as one monolithic section and the neutral axis is shifted downward and the strain/stress at the top of the slab will be higher than that at the bottom of the slab. This is beneficial to the service life of the slab since tensile stresses at the bottom of the slab are reduced.

The major difference between full and partial contact is that the weight of the slab must be considered with partial contact. Partial contact exists when temperature gradients exceed that of precompression. Partial contact without initial gaps applies to new pavements that are not subjected to significant amounts of traffic and partial contact with gaps applies to pavements that have been subjected to high intensity traffic. When the slab is not bonded or in partial contact to the base, stress/strain at the top of the slab will be equal in magnitude and opposite in sign to strain at the bottom of the slab (Huang 2004).

Several studies have investigated the effect of slab-base interaction on load induced stresses. The following presents an overview of two studies in which the effect of slab-base interaction on measured load-induced strain was investigated.

2.2.3.1 FAA DEN Study

The Federal Aviation Administration (FAA) has been developing a three-dimensional finite element model to predict the response of rigid pavement structures in recent years. In July of 2000, David Brill analyzed and compared strains measured at the Denver International Airport (DEN) test section to predicted finite-element strains and found good agreement (Brill 2000).

In 1992, the FAA introduced a major research effort to study the response and performance of PCC pavements (Lee et al. 1997). This study installed a total of 460 sensors in runway 34R/16L at the Denver International Airport to measure the response of the pavement under operational traffic (Dong et al. 1997). The sensors installed include H-bar strain gauges, linear variable differential transformers (LVDTs), position strain gauges, and temperature and moisture gauges (Brill 2000). The 3D finite element model developed by the FAA provides a unique solution to the problem of pavement loading for a particular combination of wheel loads and pavement properties. In order to verify this model, actual load conditions that closely approximate model assumption are compared to finite element readings for a certain event. Unfortunately, single observations do not accurately reflect the typical response of a pavement to a load due to variability in the sensor data. Therefore, a statistical approach that incorporates the variability of the data was used based on the mean of many measurements from similar events. Peak strains and deflections were treated as random variables. Peak strain was measured from January 1996 to August 1997 for five aircraft types including: the B-727, B-737, B-757, DC-10,

and B-777. The strain readings were then adjusted to a uniform loading weight using the following correction factor:

$$f = \frac{w_{FEA}}{w_g} \quad \textbf{(2-1)}$$

where, f is the adjustment factor, w_{FEA} is the aircraft weight assumed in the finite element analysis for the aircraft type, and w_g is the aircraft weight from the database for a particular event. After the strain readings were adjusted, the 95 percent confidence limits were computed for the means. Upon calculation of these values a thorough analysis of computed strains for interior and edge loadings were compared to peak strain values recorded from the H-bar strain gauges (Brill 2000).

The analysis showed that strains in the interior of the slab at the top predicted from the finite element model yield better agreement with measured values when complete bonding between the slab and base are assumed. The opposite was observed for strains at the bottom of the slab. Unlike the interior strains, strains measured at the edge of the slab depend on joint performance. Several variables affected the load transfer at the edge of the slab including: the type of joint, the amount of deterioration at the joint, the arrangement and orientation of wheels in the loading gear, and the degree of aggregate interlock at the joint. When measured, the edge peak strain at the top of the slab was compared to the 3D finite element model, utilizing a fully unbonded interface. A good correlation was found. However, the effect of the interface model had a small effect on strain at the top. For strain measured at the bottom of the slab the full bond interface predicted values closest to those measured. Therefore, it can be concluded that tensile strains in the concrete slab are significantly dependent on the type of bond assumed for the interface of the slab and base layer (Brill 2000).

2.2.3.2 University of Illinois DEN Study

Rufino and Roesler, also investigated slab-base interaction on strain measurements based on the instrumented test section at the Denver International Airport. They used paired strain and multidepth deflectometer gauges to characterize the interface condition of the slab and base. Measured slab responses from actual aircraft passes were then compared to theoretical results obtained using ILLI-SLAB for two conditions; bonded and unbonded. Several findings were discovered that give insight into the response of the slab for different interface conditions (Rufino and Roesler 2006).

Strain at the top and bottom of the concrete slab are the same absolute value but with a different sign for conditions when the slab-base interface behaves as unbonded. Consequently, the opposite is true when the interface is bonded and top and bottom strains are different. Therefore, comparisons between the top and bottom strains can be used to estimate the level of bond or friction between the slab and base. For interior loadings, the bottom of the slab and the top of the base were always in tension, indicating that the loaded slab always came in contact with the base. At the joints, the slab strains indicated that the interface condition was somewhere between fully bonded and unbonded. Also, positive temperature differences experienced in the slab caused greater slab-base contact friction then negative temperature differences (Rufino and Roesler 2006).

2.3 COMPARISON OF FIELD MEASUREMENTS TO PREDICTED PAVEMENT RESPONSE

The development of a new mechanistic based design guide has created the need for re-evaluating the ability to accurately characterize the stress conditions in the pavement with current models. To do this, slabs are instrumented so that the response of the slab can be measured and then compared to the predicted response. The following is a summary of two studies that provided insight on comparing the calculated with the measured response of the slab.

2.3.1 Guo and Dong Study

In 2003, Guo and Dong, investigated the compatibility of deflections and strains predicted by the 2-D finite element program, JSLAB2002, to those measured at an instrumented pavement at Ohio University. The researchers modeled a three-slab pavement system. Deflections and strains were predicted as the vehicle traversed from one end of the pavement to the other in steps of 30.5 cm (Guo and Dong 2003).

The predicted deflections matched the measured ones well. However, due to the dense-liquid model used by JSLAB2002, the non-recoverable deflections measured in the field could not be replicated by the model. The predicted strains also matched the measured in both magnitude and shape.

From this study, several other findings were determined about load induced and total stress predicted by a finite element model. First, the maximum load induced stress at the surface of an upward curled pavement was approximately 67 percent larger than for a flat slab. Secondly, the model can accurately calculate total stress when specific assumptions are used,

such as, defining the shape of the slab by utilizing the equivalent linear temperature gradient. Thirdly, it is important to evaluate total stress, not just load-induced stress, when looking at slab cracking. (Guo and Dong 2003).

2.3.2 Guo and Pecht Study

In 2006, Guo and Pecht investigated position and gear configurations of various aircrafts on the response of a rigid airport pavement. Recently, the FAA has adopted a new failure model in its design specification based on bottom-up cracking. The new model is divided into four stages including: (1) new construction to the first crack initiated (2) from crack initiation to full depth propagation, (3) from the first full depth crack to 50% of slabs cracked and (4) continued deterioration until the slab fails. In this study, Guo and Pecht specifically studied the pavement response of non-cracked slabs, which falls into the first stage of the failure model (Guo and Pecht 2006).

By analyzing the response of pavement to wheel loads, the researchers were able to qualitatively understand the pavement's failure mechanism. For example, it was observed that strain response measured in the slab interior showed the least uncertainty due to distance from the joint. Also, at the center of the slab, strains measured at the top were larger than those measured at the bottom. This is due to the friction between the bottom of the slab and top of the subbase (Guo and Pecht 2006).

Strains measured at the bottom of the slab, in the middle of the longitudinal joint, were used to analyze the effects of different gear configurations on pavement response. A gear with two, four, and six wheels was driven over the longitudinal joint. It was found that the two-wheel gear recorded the highest strains and the six-wheel gear recorded the lowest. Therefore, it was

concluded that increasing the number of wheels does not increase the potential for bottom-up cracking along the longitudinal joint. An analysis was also preformed for the same configurations and location but at the top of the slab. It was shown that gear configuration and location do affect the potential for top-down cracking. Although, the magnitude of the two-wheel gear was still the largest, it is the least critical among the various configurations for top-down cracking. Guo and Pecht concluded that tire load dictates the potential for bottom-up cracking while gear load dictates the potential for top-down cracking at the longitudinal joint. Strain gages applied to the surface of the slab were used to study the pavement response at the transverse joint. The results showed that six-wheel gears are more critical then four-wheel gears, and that the two-wheel gears were the least damaging. Therefore, the critical gear configurations at the transverse joint differ from those at the longitudinal joint (Guo and Pecht 2006).

3.0 FIELD STUDY

The scope of this research includes field measurements and finite element analysis to characterize the response of the pavement to applied loads and to predict pavement performance. Pavement temperature, moisture, FWD deflection data, and dynamic strain measurements were collected at an instrumented pavement section in Murrysville, Pennsylvania. This data was then used to predict pavement stresses using three-dimensional finite element analysis. Upon determination of stresses in the pavement, the new mechanistic-base design guide was used to predict pavement performance and distress.

The field data in this study was collected seasonally. Field collection began in August 2004 and concluded in October of 2007. Field data was collected a total of 12 times to characterize the seasonal and long-term pavement response. The following chapter presents an overview of the instrumented pavement section. This includes a description of the project location, design, construction, and joint details and instrumentation of the jointed concrete pavement located in Murrysville, Pennsylvania.

3.1 PROJECT LOCATION

The site location for the instrumented test section was selected based on a number of criteria including construction schedule, roadway grade, subgrade support characteristics, and traffic

patterns. The chosen location was a 3.4 mile section of U.S. Route 22, along construction Section B01. The majority of this section runs through the municipality of Murrysville in Westmoreland County. Murrysville is located approximately 20 miles east of the city, as shown in Figure 3.1. The test section consists of 14 Portland cement concrete (PCC) slabs.

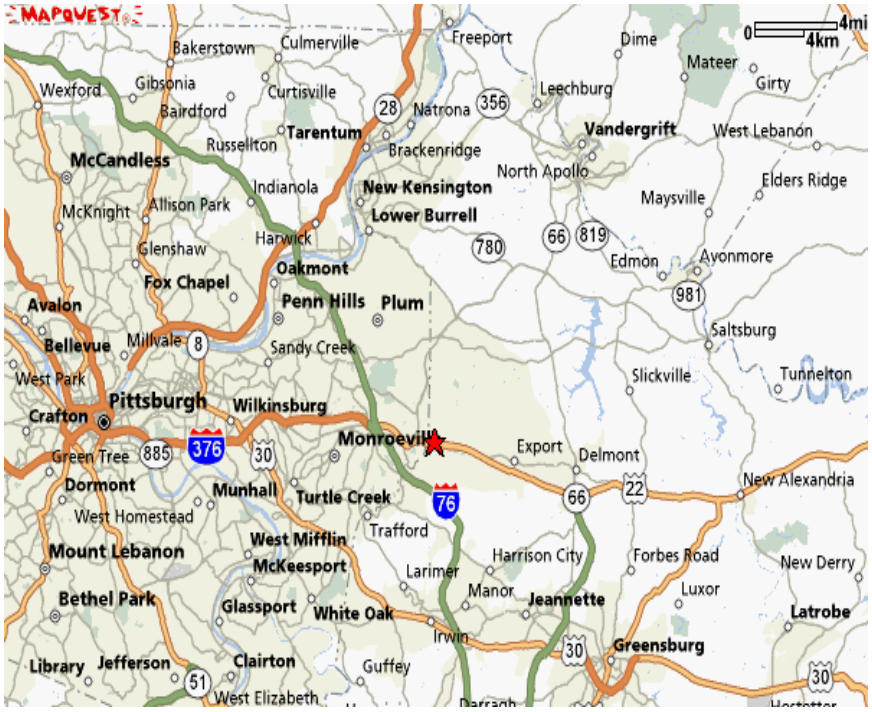

Figure 3.1. Map of the Pittsburgh area including project location (www.mapquest.com, June 2007).

3.2 DESIGN DETAILS

The design details are presented in this section. Additional information can be found in the initial construction report (Wells et al 2005).

3.2.1 Geometric Details

The pavement structure is a jointed plain concrete pavement (JPCP) with 15-ft transverse joints and 12-ft lanes. The concrete median varies in width from 14.4 ft to 2.0 ft with concrete mountable curbs. The roadway is crowned with a 2.0 percent transverse slope and 2.4 percent longitudinal slope. The roadway contains a 2.6-ft concrete curb-and-gutter shoulder which has an 8 percent transverse slope. The pavement section is shown below in Figure 3.2 (Wells et al 2005).

Figure 3.2. Test section in the westbound lanes (Wells et al 2005).

3.2.2 Pavement Structure

The pavement structure is composed of a 12-inch thick PCC layer placed over a 4-inch thick asphalt treated permeable base. The subbase material consists of slag material and is 5-inches thick. Originally, the pavement was to be constructed directly on the subgrade but poor soil conditions required the removal of 24 inches of the subgrade material. The 24 inches was

replaced with a gap-graded soil and aggregate mixture (Wells et al. 2005). The cross section of the pavement structure is shown in Figure 3.3.

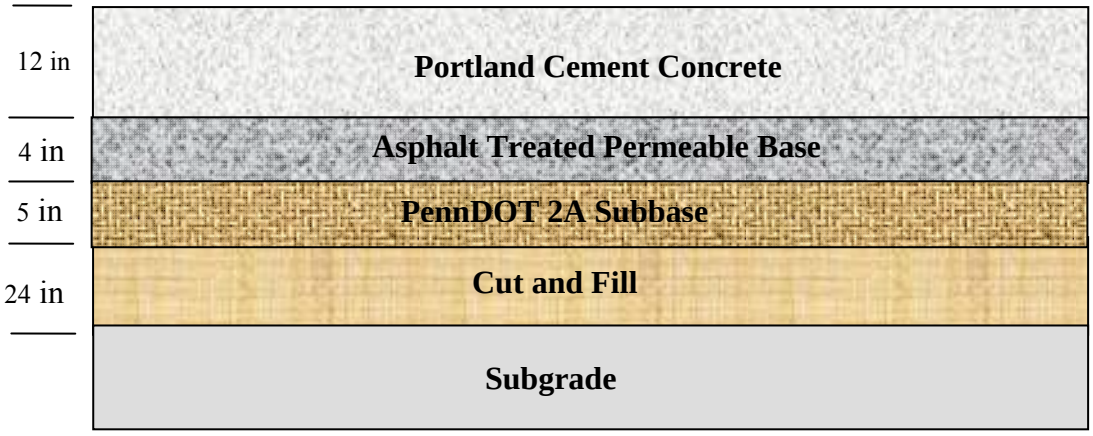

Figure 3.3. Cross-section of pavement structure (Wells et al 2005).

3.2.3 Joint Details

The test section consists of both restrained and unrestrained slabs. The restrained slabs contain No. 5 epoxy-coated tie bars placed 2.5 ft apart along the lane/shoulder and centerline joints. Also, epoxy coated 1.5-in dowel bars were spaced every 12 inches along transverse joints. The dowel and tie bar layout is shown below in Figure 3.4.

Figure 3.4. Dowel and tie bar configuration (Wells et al. 2005).

3.3 TRAFFIC DETAILS

U.S. Route 22 (SR 22) is a four-lane urban major arterial divided by a concrete median. In June 2002, which was the time of design, the two-way average daily traffic (ADT) volume was 26,950 vehicles with 5% credited to truck traffic. At the end of the design life in 2022, the projected ADT is 36,780 vehicles. The design hourly volume in June 2002 was 3,678 vehicles with a directional split of 60% in the primary direction of travel. There are several traffic signals and business entrances along the roadway; therefore the posted speed limit is 35 miles per hour (Wells et al 2005).

3.4 INSTRUMENTATION OF THE TEST SECTION

This section presents the layout of the test section and the general locations of the dynamic and environmental sensors. Nearly 400 sensors were installed at various depths throughout the pavement structure. The sensors were installed in groups of slabs known as "cells". There are a total of four cells consisting of three slabs each. The cells are labeled 1 through 4, with numbers increasing in the westward direction. Cells 1 and 2 contain sensors for measuring dynamic strains and pressures and Cells 3 and 4 measure both static strains and environmental conditions. The dynamic strain sensors in Cell 1 are a replicate of the dynamic strain sensor layout in cell 2. The same is true for Cells 3 and 4 with the exception that Cell 4 also contains environmental sensors.

Although the sensor arrangements in these two sets of cells are repetitive, there is one unique factor that separates them. Cells 2 and 3 are unrestrained by dowel and tie bars while Cells 1 and 4 contain dowels and tie bars. A summary of the types and quantities of the dynamic sensors installed in Cells 1 and 2 and environmental sensors installed in Cell 4 is presented in Table 1.1.

Table 3.1. Summary of sensors installed in the test section.

Sensor Type	Sensor Name	Qty.	Measurement	Cell
Dynamic Load	Dynamic Strain Gage	112	Dynamic Strain	1,2
Dynamic Load	Dynamic Pressure Cell	8	Dynamic Pressure	1,2
Environmental	Thermocouple	60	Temperature	4
Environmental	Moisture Sensor	24	Relative Humidity	4
Environmental	Time Domain Reflectometer	16	Moisture Content	4

Each cell has its own datalogging equipment that collects data from the sensors in the cell. The datalogger is located within a cabinet that was constructed directly adjacent to the instrumented cell and approximately twelve feet away from the edge of the curb. Electricity is provided to the cabinet and a phone service is provided for Cell 4. Data from the environmental and static sensors in Cell 3 and 4 are collected automatically. The sensors are wired to multiplexors, which are wired to the datalogger. The datalogger in Cells 3 and 4 automatically retrieves data every 15 minutes. Once per day, the data collected on the datalogger is sent via telephone modems to a database located on a computer housed at the University of Pittsburgh (Wells et al. 2005).

3.4.1 Environmental Sensors

To determine the response of the slab to applied loads, the response of the slab, as well as the climatic conditions within the structure during loading must be monitored. Therefore, environmental sensors were installed to document the temperature and moisture gradients that develop throughout the depth of the slab. A weather station was also installed in Cell 4 to monitor the ambient conditions. The weather station records air temperature, relative humidity and wind speed every fifteen minutes. A description of the environmental sensors found in the instrumented pavement structure is provided below.

3.4.1.1 Temperature Sensors

Thermocouples, shown in Figure 3.5, are used to measure temperature throughout the pavement structure. Locations of the thermocouples are shown in Figure 3.6. A total of 60 thermocouples were installed at four locations in Cell 4, as follows:

– Two locations in the corners, and

– Two locations at midpanel.

Figure 3.5. Thermocouples used to measure temperature throughout the pavement (Wells et al. 2005).

At each location, 15 sensors were placed; seven in the Portland cement concrete slab, two in the asphalt treated permeable base, two in the 2A-subbase, three in the fill material, and one in the subgrade. The approximate depths at which they were placed are indicated in Figure 3.7 (Asbahan et al. 2006).

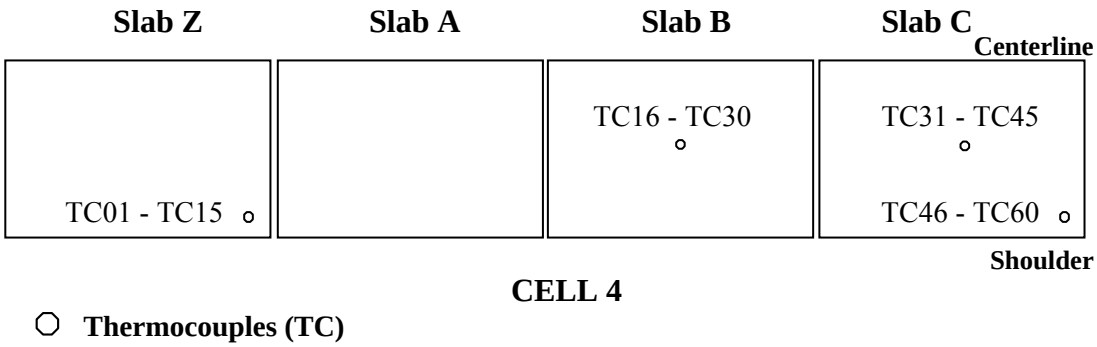

Figure 3.6. Location of thermocouples in Cell 4 (Wells et al. 2005).

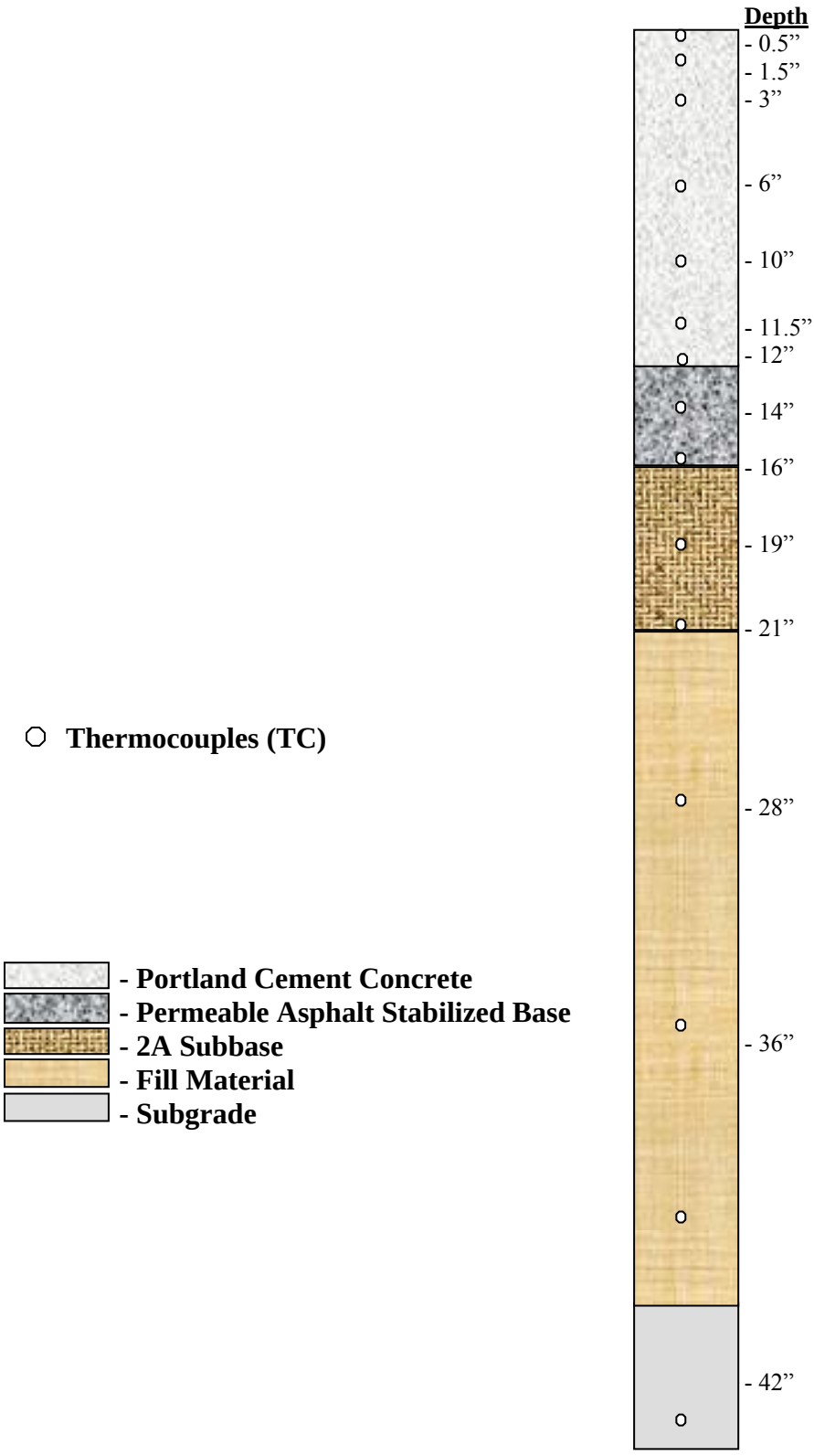

Figure 3.7. Depth of thermocouples sensors located in Cell 4 (Asbahan et al. 2006).

3.4.1.2 Concrete Moisture Sensors

In order to characterize moisture conditions in the PCC slab, Sensirion SHT75 relative humidity and temperature sensors, shown in Figure 3.8, were installed at various depths in the PCC layer, as shown in Figure 3.10. A total of twenty four sensors were installed at four locations within Cell 4. These locations consisted of at the slab corner and at midslab for two separate slabs. This is shown below in Figure 3.9 (Asbahan et al. 2006).

Figure 3.8. **Relative humidity sensors located throughout the PCC slab (Well et al. 2005)**.

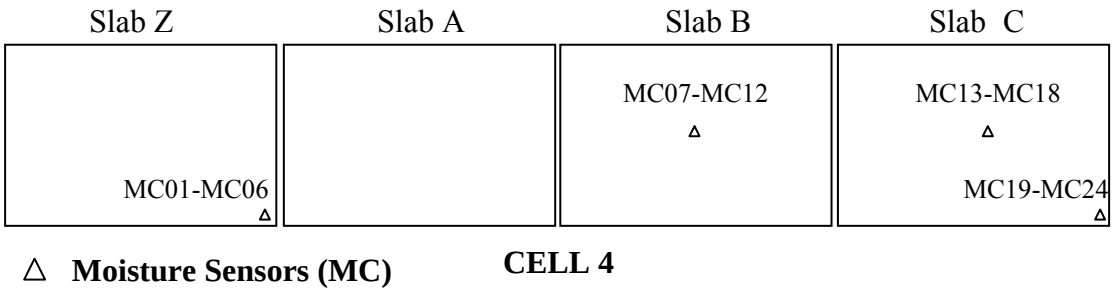

Figure 3.9. **Location of concrete moisture sensors located in Cell 4 (Asbahan et al. 2006).**

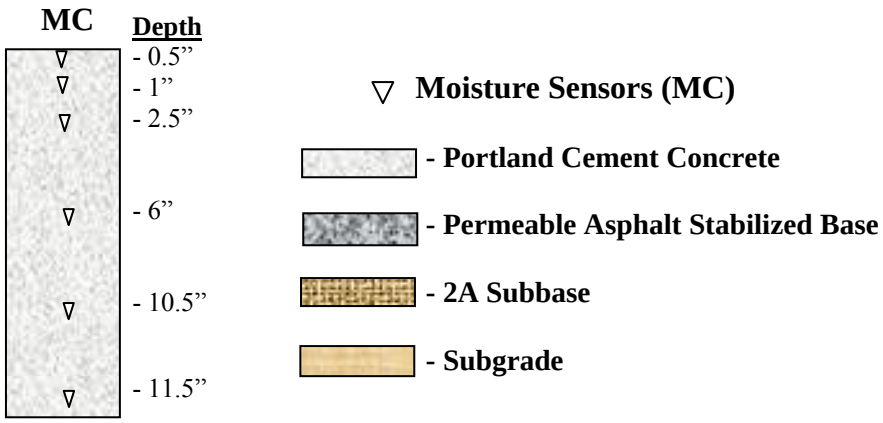

Figure 3.10. Depths of the concrete moisture sensors located in Cell 4 (Asbahan et al. 2006).

3.4.1.3 Moisture Sensors in the Granular Layers

In order to measure the moisture content and frost depth within the subgrade and subbase, a time domain reflectometry (TDR) system from Campbell Scientific was used. Sixteen CS605L wave guide probes, shown in Figure 3.11, were placed at various depths in the wheelpath and along the longitudinal edge of the slabs in Cell 4. Figure 3.12 and Figure 3.13 show the locations and depths of the TDR probes.

Figure 3.11. Installation of CS605L TDR probe in the subgrade (Wells et al. 2005).

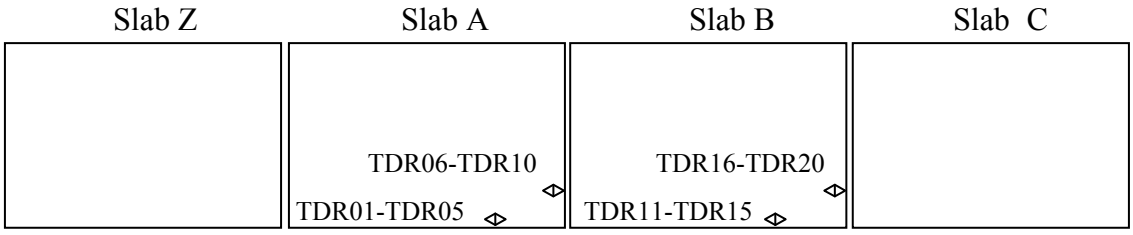

Figure 3.12. Locations of the TDR probes located in Cell 4 (Asbahan et al. 2006).

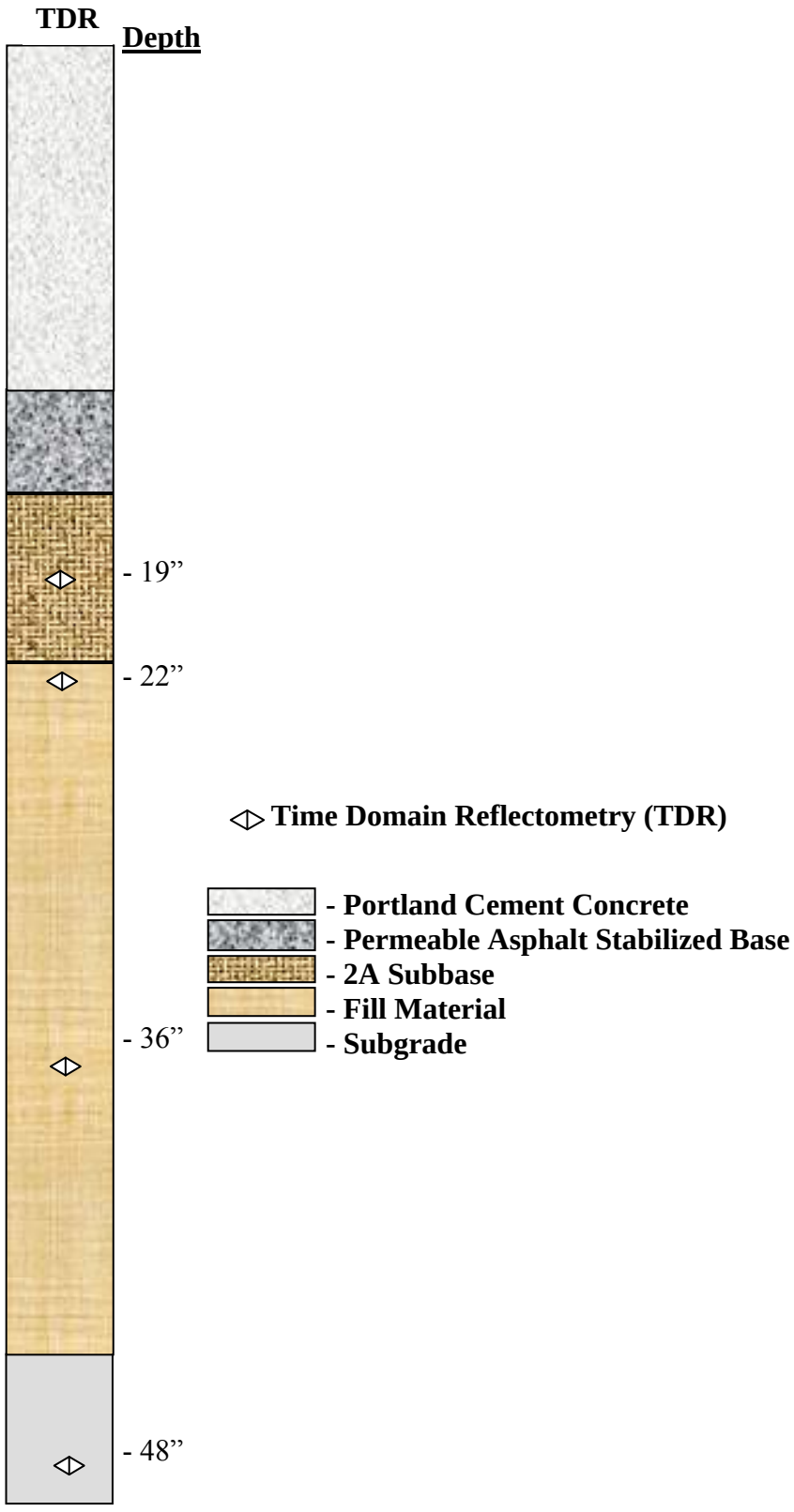

Figure 3.13. Depths of the TDR probes within the pavement structure in Cell 4 (Asbahan et al. 2006).

3.4.2 Dynamic Sensors

Dynamic sensors are used to measure the slab response to loads applied by trucks with known axle weight and configuration and the falling weight deflectometer (FWD). A description of the dynamic sensors installed in the pavement structure is provided below.

3.4.2.1 Dynamic Strain Sensors

The instrumented test section employs Tokyo Sokki PML-60-2L dynamic strain gages to measure the response of the slab to applied loads. These gages consist of a copper/nickel alloy resistance foil gage attached to two lead wires. This foil is attached to electrically insulated backing and to one of two thin acrylic plates. The plates utilized by the strain gage are sealed together to provide protection when placed in the concrete. The plates are then coated with a granular material to improve the bonding with the concrete.

The backing of the strain gage expands and contracts with the concrete. This movement causes the resistance in the gage to change, and therefore strain is determined from resistance. From resistance, strain can be found using the following relationship:

$$\varepsilon = \frac{\Delta L}{L} = \frac{\Delta R/R}{K} \qquad \textbf{(3-1)}$$

where:

ε = Strain

R = Gage resistance

ΔR = Resistance change due to strain

K = Gage factor

A photo of a dynamic strain gage installation is provided in Figure 3.14. The top sensor is half an inch below the surface of the slab and the bottom sensor is located 11.5 inches below the slab surface. Data from these sensors is collected manually at the time of dynamic loading using Optim Megadac dataloggers (Asbahan et al. 2006).

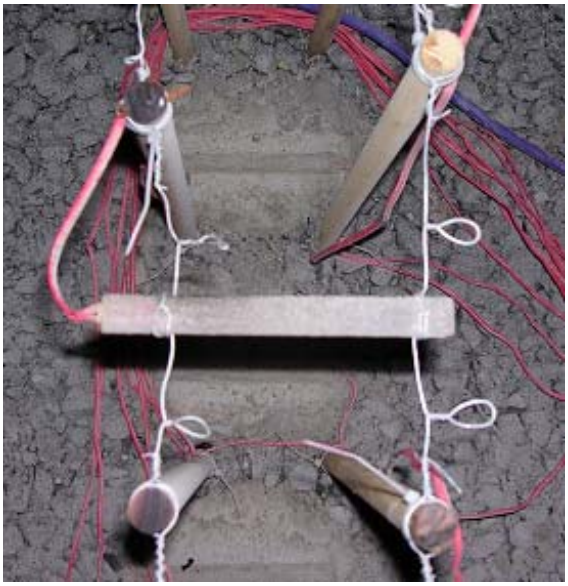

Figure 3.14. Tokyo Sokki PML-60-2Ld dynamic strain gauges (Wells et al. 2005).

Figure 3.15 outlines the locations of the dynamic strain gages located in Cells 1 and 2. Longitudinally oriented gages are located in the wheelpath at the center of the slab and in the slab corner along the edge. The transversely oriented dynamic strain gages measure strains in the wheelpath near the transverse joints. As shown in Figure 3.15 the sensor layout for the unrestrained cell (Cell 2) is almost identical to that of the restrained cell (Cell 1) (Asbahan et al. 2006).

Instrumented Restrained Panels (Dowel and Tie Bars)

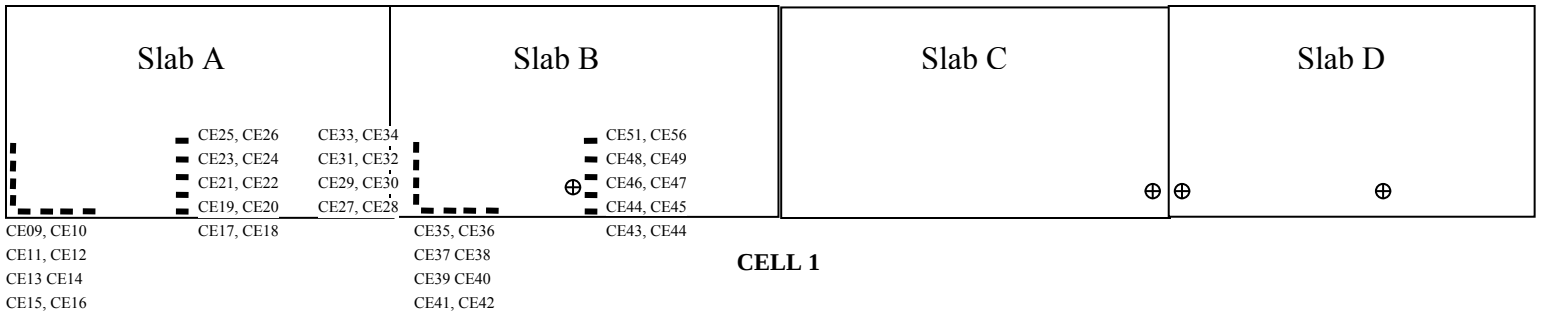

Instrumented Unrestrained Panels (No Dowel and Tie Bars)

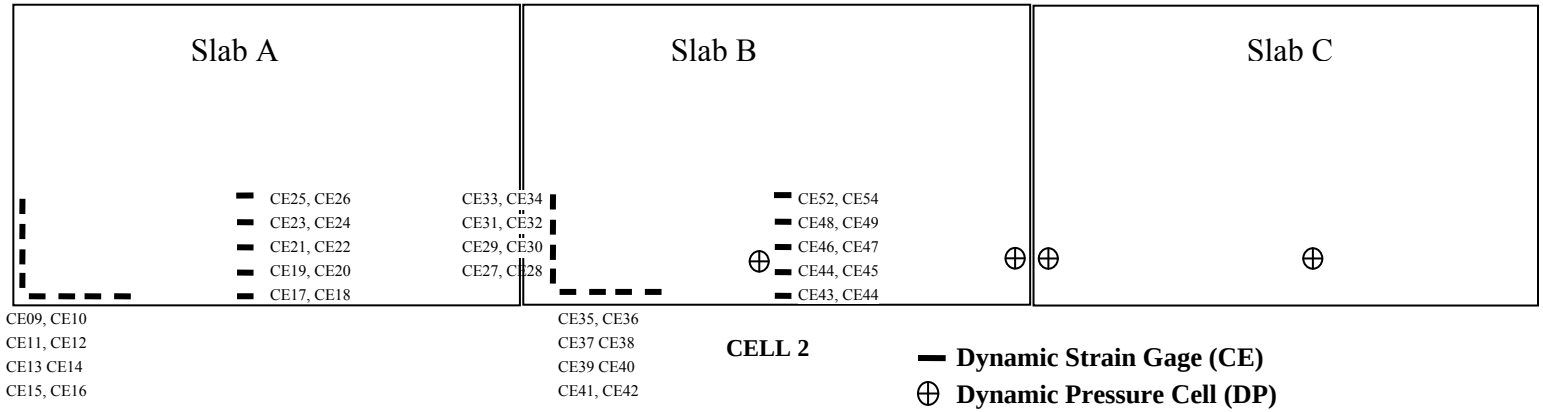

Figure 3.15. Sensor layout for Cell 1 and Cell 2 (Asbahan et al. 2006)

4.0 PAVEMENT RESPONSE TO FWD LOADS

This chapter presents the characterization of the pavement response to falling weight deflectometer testing. Static strain and deflection measurements were used to define the pavement response. Load testing with the falling weight deflectometer was performed four times a year so seasonal effects could be characterized. A summary of the results for the first three years of testing after pavement construction is provided.

This chapter begins with a background on falling weight deflectometer testing and calculation of load transfer efficiency, VOID detection, and backcalculation of the composite stiffness (k-value) of the supporting layers. Following this, is the characterization of the temperature and moisture distribution throughout the PCC slab during FWD testing, which is critical in analyzing pavement response. This chapter will then discuss the performance of the joints in both the unrestrained and restrained slabs throughout the three year period. This will include an analysis of both seasonal and long-term trends in joint performance and a comparison between measured strain and load transfer efficiency. An analysis of FWD testing conducted at the slab corners will be presented in evaluating voids beneath the slab. The third section of this chapter presents the composite stiffness of all layers beneath the slab which was backcalculated seasonally throughout the first three years after construction. Next, the seasonal and long-term deflection trends measured at each test location (midpanel, corner, adjacent to lane/shoulder joint

and adjacent to the transverse joint) in both the restrained and unrestrained slabs will be discussed.

4.1 BACKGROUND

Falling weight deflectometer testing is a nondestructive test procedure that is used in determining the structural adequacy of pavement structures. FWD testing produces a dynamic impulse load that more accurately simulates a moving wheel load than other nondestructive test methods. This improved method, of simulating a moving wheel load, allows for a more mechanistic analysis of FWD data. Typically, FWD testing is preformed at four locations throughout the slab. These locations include: the center of the slab, at midpanel adjacent to the lane/shoulder joint, the corner adjacent to the lane/shoulder joint, and the wheelpath adjacent to the transverse joint. Each location is used to complete a separate analysis of the structural adequacy of the pavement. Deflection data from the center of the slab is used for backcalculation of material properties, and midpanel deflections are used in determining remaining structural life. Deflections measured at the corner of the slab use used for detecting voids beneath the slab, and deflections collected at the approach and leave side of the joint along the wheelpath are used in determining joint performance.

This following will present background information on the analysis methods used in evaluating FWD data. It will begin with a background of the methods used in determining joint efficiency and is followed by a discussion of detecting voids beneath the slab. This background will conclude with a discussion of the AREA method, which is used in the backcalculation of material properties.

4.1.1 Joint Efficiency

As previously discussed, FWD deflections from both sides of the transverse joint, at the wheelpath, are used in estimating the load transfer effieciency of the joint, as shown in Figure 4.1. As a load is applied near the joint of a PCC pavement, both the loaded and unloaded slab deflect. A portion of the load applied to the loaded slab is transferred to the unloaded slab through aggegate interlock and the dowel bars (when present). As a result, deflections and stresses in the loaded slab decrease.

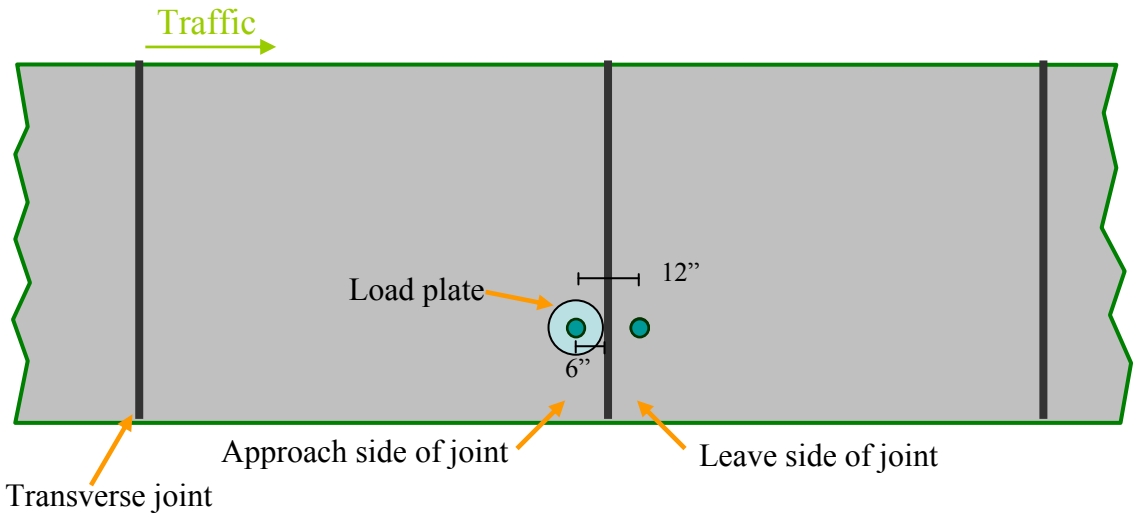

Figure 4.1. Deflection measurement locations for measuring load transfer efficiency.

Joint performance is determined by determining the load transfer efficieny (LTE). The ratio of the maximum deflection at the joint of the loaded slab to the deflection of the unloaded slab adjacent to the loaded point. The equation used in determining this relationship is found below.

$$LTE = \frac{\delta_{ul}}{\delta_l} \times 100\% \quad \textbf{(4-1)}$$

where:

LTE = Load transfer efficiency, percent

δ_{ul} = Deflection measured on the unloaded side of the joint

δ_l = Deflection measured on the loaded side of the joint

The proceding equation is based on measured deflections. However, a load transfer efficiency based on can also defined as follows:

$$LTE = \frac{\sigma_{ul}}{\sigma_l} \times 100\% \quad \textbf{(4-2)}$$

where:

LTE σ = Load transfer efficiency in stress

σ_u = Stress at the joint of the unloaded slab

σ_l = Maximum stress at the joint of the loaded slab

Since it is not possible to measure stress, the deflection-base LTE is commonly used in evaluating the joint preformance of concrete pavements in the field. Typically, when load transfer efficiency of less than 70 percent it is considered unacceptable, but the Federal Highway Administration has employed the following criteria for evaluating load transfer resoration (FHWA 1997).

- Deflection load transfer of 70 percent or less
- Differential deflections larger than 0.01 in (0.25 mm)
- Faulting across cracks or joints of 0.10 in (2.5 mm) or more
- Total faulting level of joints and cracks over 32 in/mile (500 mm/km)

Load transfer efficiency is dependent on many factors including temperature, base/subgrade support, and the aggregate interlock or the joint stiffness (Khazonovich and Gotif 2003).

4.1.2 Void Detection

FWD testing conducted at the slab corners is used to evaluate the potential for voids beneath the slab. Typically, deflections are highest when loads are applied at the corner of the slab. These high deflections can lead to permanent deformation of the underlying layers, which causes the development of voids under the slab. Applied loads in jointed concrete pavements can also cause pumping of the base from under the pavement. Pumping will occur if there is moisture directly beneath the slab, differential deflections between the approach and leave slab and unstabalized fines.

Voids beneath the slab can be detected by analyzing deflection data preformed through FWD testing in the slab corner adjacent to the lane/shoulder joint and transverse joint. Although the 1993 Design Guide suggests three methods for detecting voids this research utilizes one of these methods. This method is commonly referred to as the variable corner deflection analysis and was developed by Darter and Crovetti (1985).

In the variable corner deflection analysis, deflections are recorded at three different load levels. A linear regression is performed to define the relationship between load and deflection. The Void parameter is defined by the x-intercept. The Void parameter concept is illustrated in Figure 4.2. A fully supported condition will have a Void parameter of less than 2 mils. An x-intercept greater than 2 mils indicates the presence of a void. The magnitude of the Void parameter also provides an indication of the void size, with the void size increasing with an increase in the magnitude of the Void parameter (Darter and Crovetti 1985).

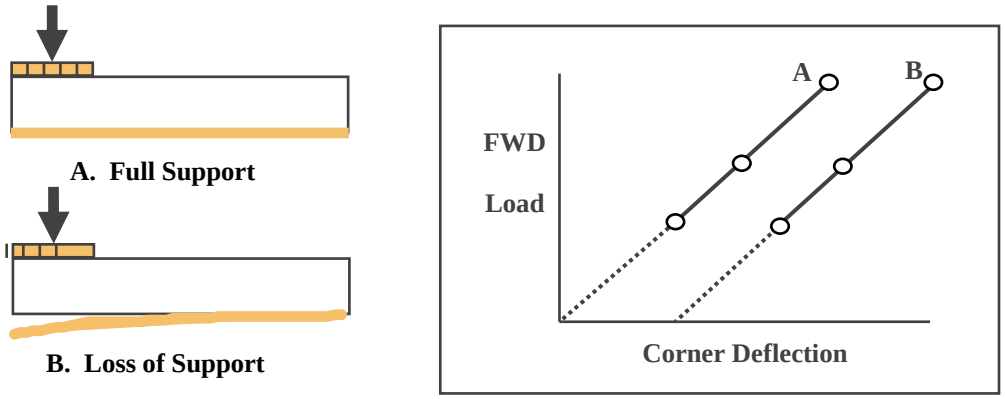

Figure 4.2. Estimating the presence of a void using FWD data.

4.1.3 Backcalculation of Moduli

One of the most important applications of FWD testing is to backcalculate the moduli of the pavement structure. The basic procedure is to measure the deflection basin and vary the set of moduli until a best match between computed and measured deflections is obtained. A variety of methods have been developed to backcalculate layer moduli and this research uses the AREA method developed by Hall et al.

This method is based on FWD deflections measured at the center of the slab, typically for a 9,000 lb load. When using this method, deflections are needed at 0, 12, 24, 36, 48, and 60 inch offsets. Upon determination of the deflections, the following equation may be used to define $AREA_{60}$ (AASHTO 1993), which is an estimate of the area of have of the deflection basin.

$$A_{60} = 4+ 6(d_8/d_0) + 5(d_{12}/d_0) + 6(d_{18}/d_0) + 9(d_{24}/d_0) + 18(d_{48}/d_0) + 12(d_{60}/d_0) \quad \textbf{(4-3)}$$

where:

A_{60} = AREA beneath the first 60 inches of the deflection basin

d_i = deflection measured at 0, 8, 12, 18, 24, 48, and 60 inches from the center of the load plate

After determining the $AREA_{60}$ parameter, this parameter is used to determine the radius of relative stiffness, Equation 4.4, shows this relationship.

$$\ell = \left[\frac{\ln\left(\frac{k_1 - AREA_{60}}{k_2} \right)}{-k_3} \right]^{\frac{1}{k_4}} \quad \textbf{(4-4)}$$

where:

l = radius of relative stiffness, in

$AREA_{60}$ = AREA beneath the first 60 inches of the deflection basin

k_1 = regression coefficient, 60

k_2 = regression coefficient, 289.708

k_3 = regression coefficient, 0.698

$1/k_4$ = regression coefficient, 2.566

The next step in the process of calculating the layer moduli of a PCC pavement is to calculate the nondimensional deflection coefficient, d* and k-value for each deflection sensor location. This is accomplished utilizing Equation 4.5 and Equation 4.6.

$$d_r^* = a * e^{-b*e^{-c*\ell}} \quad \textbf{(4-5)}$$

where:

d_r^* = nondimensional deflection coefficient for deflection at distance r from load

a, b, c = regression coefficients

l = radius of relative stiffness, in

$$k = \frac{P * d_r^*}{d_r * \ell^2} \quad \textbf{(4-6)}$$

where:

k = modulus of subgrade reaction, pci

P = applied load, lbs

d_r^* = nondimensional deflection coefficient for deflection at distance r from load

d_r = deflection at radial distance r from load

l = radius of relative stiffness, in

Upon determination of the k-value, the PCC modulus of elasticity can be estimated utilizing the following relationship:

$$E_{PCC} = \frac{12 * \ell^4 * (1 - \mu^2) * k}{h^3} \quad \textbf{(4-7)}$$

where:

E_{PCC} = PCC elastic modulus, psi

l = radius of relative stiffness, in

μ = Poisson's ratio of PCC

k = modulus of subgrade reaction, pci

h = thickness of the PCC, in

4.2 CONCRETE TEMPERATURE AND MOISTURE DISTRIBUTIONS DURING FWD TESTING

The characterization of the temperature and moisture distributions throughout the PCC slab during FWD testing is critical in analyzing pavement response. The weighted average temperature, equivalent linear temperature gradient, and temperature of the ATPB affect the shape and critical stress and deflection locations in the slab. Therefore, characterization of joint

performance, support conditions under the corner of the slab, deflection basins at known locations, and to backcalculate layer moduli can not be performed without defining the climatic conditions during testing.

The equivalent linear temperature gradient is commonly used by researchers to analyze daily and seasonal variations in temperature gradients in PCC slabs. This method, developed by Janssen and Snyder (2000), accounts for nonlinear temperature gradients in concrete slabs, by estimating the moment about the bottom of the slab. The temperature moment can be converted into an equivalent linear gradient by determining the linear gradient that produces the same magnitude of temperature moment as the measured surface profile (Janssen and Snyder 2000).

A variation in moisture throughout the depth of the slab also affects the shape of the slab and therefore the location of the critical stress and peak deflections. Therefore, characterization of this difference in moisture content throughout the depth of the slab is also beneficial in the analysis of the pavement to FWD loadings.

4.2.1 Concrete Temperature Distribution

Table 4.1, shown below, presents the variation of the weighted average temperature of the slab at midpanel during FWD testing. The largest variation in temperature was experienced during the spring of 2006 and 2007 with a range of 16 degrees Fahrenheit. The smallest variation in temperature was experienced during the first three test outings in the fall of 2004, and winter and spring of 2005. All results are typical of seasonal temperature variation.

Table 4.1. Seasonal temperature variation during FWD testing.

		Weighted Average Temperature, °F		
Season	**Testing Time**	**Maximum**	**Minimum**	**Average**
Fall 2004	9:45 am - 12:30 pm	58	53	55
Winter 2005	8:00 am - 11:45 am	34	29	31
Spring 2005	7:30 am - 10:30 am	55	52	53
Summer 2005	12:30 pm - 3:15 pm	77	72	75
Winter 2006	12:30 pm - 4:00 pm	45	39	42
Spring 2006	8:30 am - 1:00 pm	75	59	65
Summer 2006	10:00 am - 2:00 pm	96	83	89
Fall 2006	11:00 am - 2:00 pm	52	43	47
Winter 2007	11:00 am - 2:00 pm	37	28	32
Spring 2007	11:00 am - 2:00 pm	75	59	66
Summer 2007	11:30 am - 2:00 pm	84	73	78
Fall 2007	10:30 am – 2:00 pm	58	46	53

Figure 4.3 through Figure 4.14 show the variation in weighted average temperature and equivalent linear temperature gradient of the slab, and the mid-depth temperature of the ATPB during testing periods. Summary statistics of all test seasons are discussed below. Each season for all three years was combined to determine the overall range and average values of each factor.

During the fall testing periods the weighted average temperature in the PCC slab ranged between 43 and 58 degrees Fahrenheit with an average of 52 degrees Fahrenheit. The equivalent linear temperature gradient of the PCC slab varied between -0.86 and 1.17 °F/in during fall testing, with an average of 0.31 °F/in. The temperature at middepth of the ATPB ranged between 46 and 58 degrees Fahrenheit with an average of 52 degrees Fahrenheit. See Figures 4.3 through 4.5. As shown in the proceeding figures, the weighted average temperature of the concrete varied minimally during the three test outings. The fall testing encountered the least variation in weighted average temperature with an average range of 15 °F.

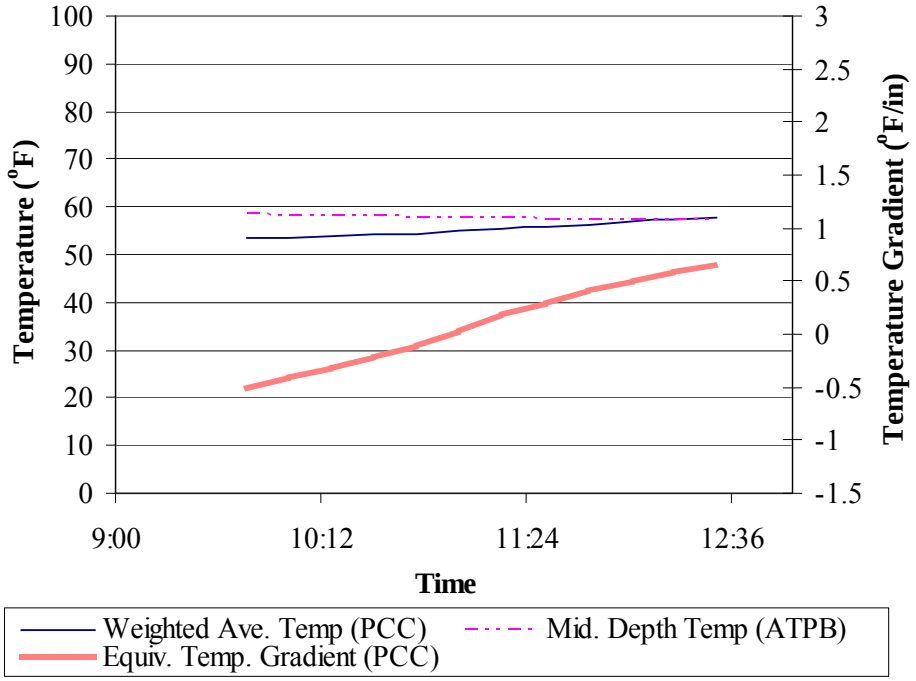

Figure 4.3. Midpanel temperature conditions during FWD testing performed in the fall of 2004.

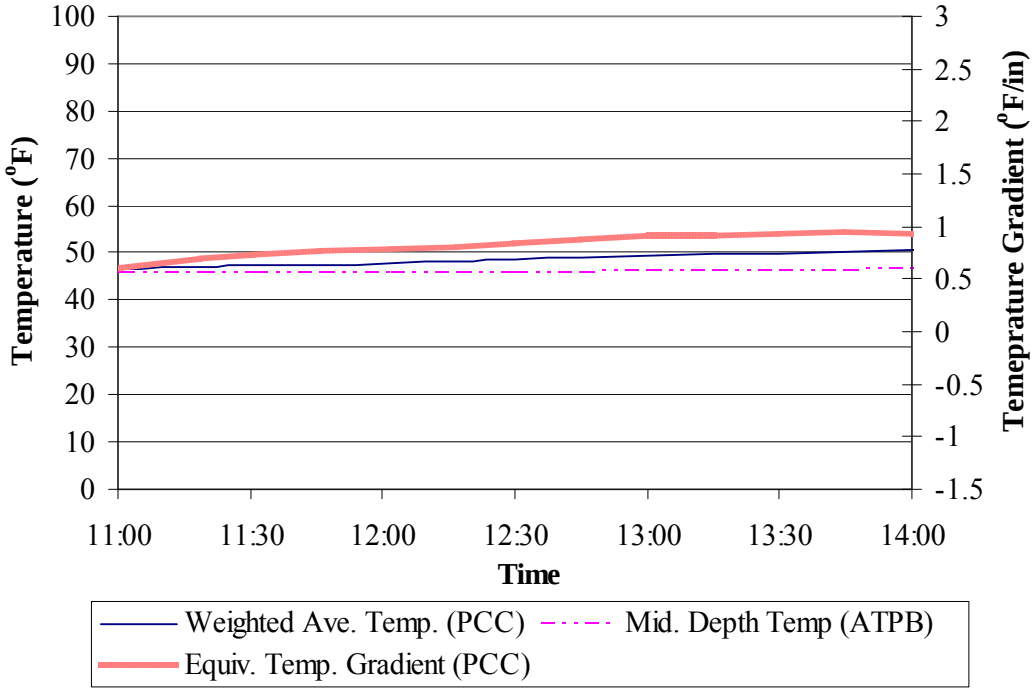

Figure 4.4. Midpanel temperature conditions during FWD testing performed in the fall of 2006.

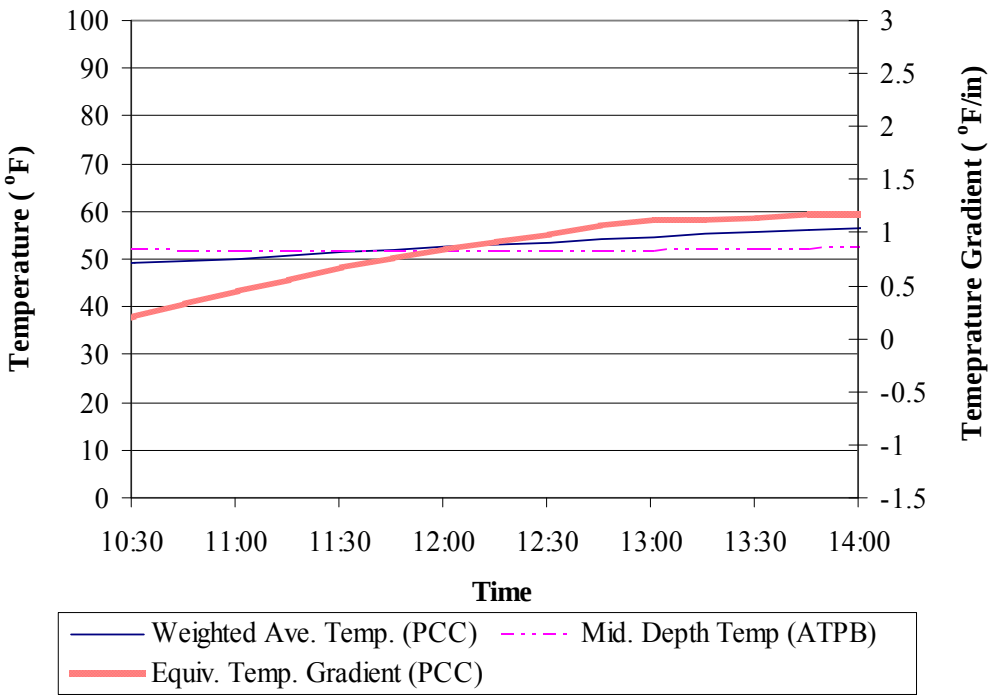

Figure 4.5. Midpanel temperature conditions during FWD testing performed in the fall of 2007.

Figure 4.6 through Figure 4.8 present the temperature of the concrete and ATPB and gradient of the slab during winter testing. The weighted average temperature for the winter testing periods ranged between 28 and 45 degrees Fahrenheit with an average of 35 degrees Fahrenheit. The equivalent linear temperature gradient varied between -0.61 and 1.34 °F/in with an average of 0.30 °F/in. The mid-depth temperature of the ATPB, measured during the FWD winter periods, fluctuated between 29 and 41 degrees Fahrenheit with an average of 35 degrees Fahrenheit. Additionally, the smallest variations in temperature gradients were experienced during winter testing, with an average range of 1.95 °F/in.

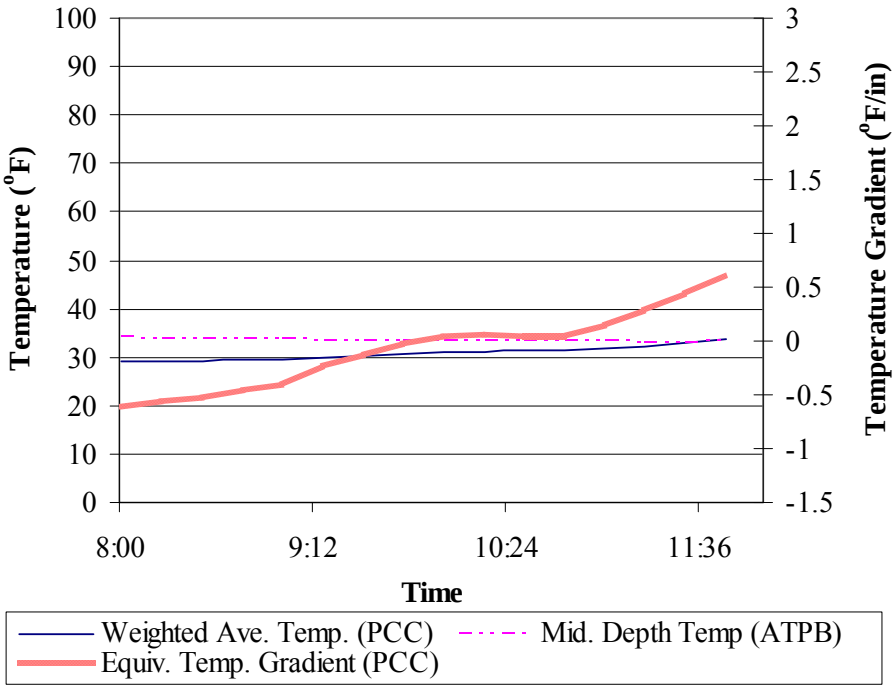

Figure 4.6. Midpanel temperature conditions during FWD testing performed in the winter of 2005.

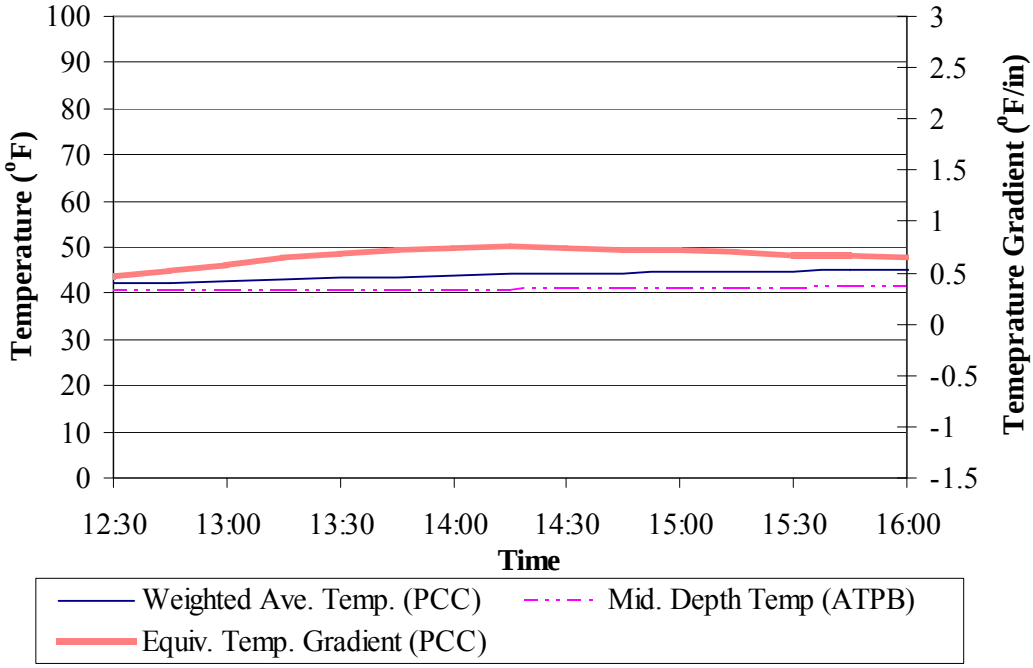

Figure 4.7. Midpanel temperature conditions during FWD testing performed in the winter of 2006.

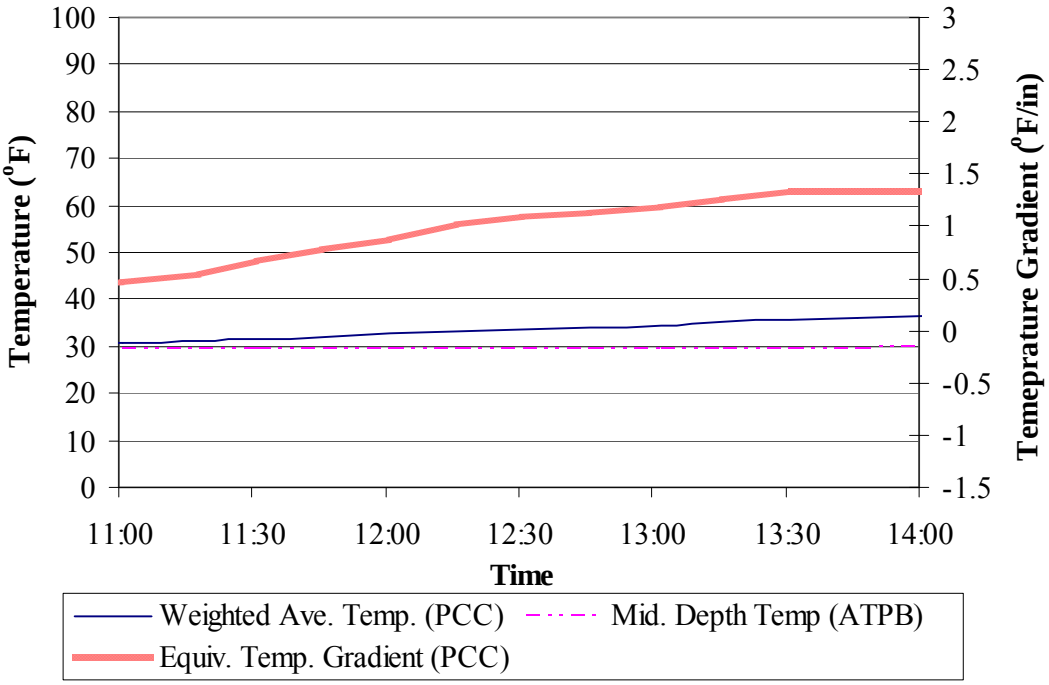

Figure 4.8. Midpanel temperature conditions during FWD testing performed in the winter of 2007.

During the spring test periods, the weighted average temperature in the PCC slab ranged between 52 and 75 degrees Fahrenheit with an average of 61 degrees Fahrenheit. The equivalent linear temperature gradient of the PCC slab varied between -0.85 and 2.28 °F/in during spring testing, with an average of 0.71 °F/in. The temperature at middepth of the ATPB ranged between 53 and 64 degrees Fahrenheit with an average of 58 degrees Fahrenheit. As shown in Figure 4.9 through Figure 4.11, the equivalent linear temperature gradient of the concrete varied significantly during spring testing. The largest average variation in temperature gradients was experienced with an average range of 3.14 °F/in. Although the temperature of the concrete varied significantly, throughout the depth of the slab during the spring, the ATPB remained relatively constant and showed the lowest variation with an average range of 11°F.

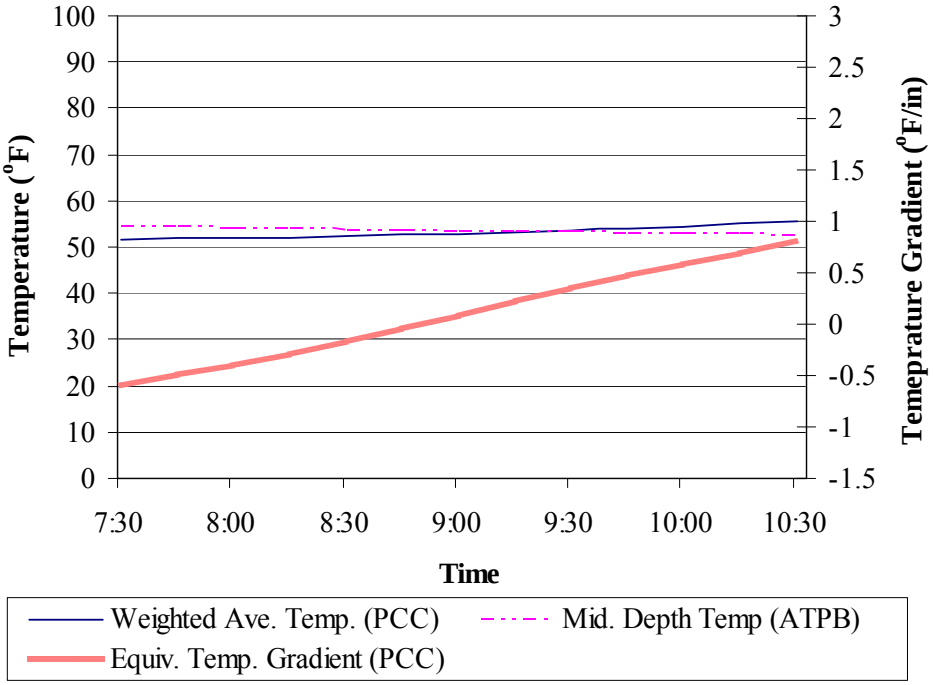

Figure 4.9. Midpanel temperature conditions during FWD testing performed in the spring of 2005.

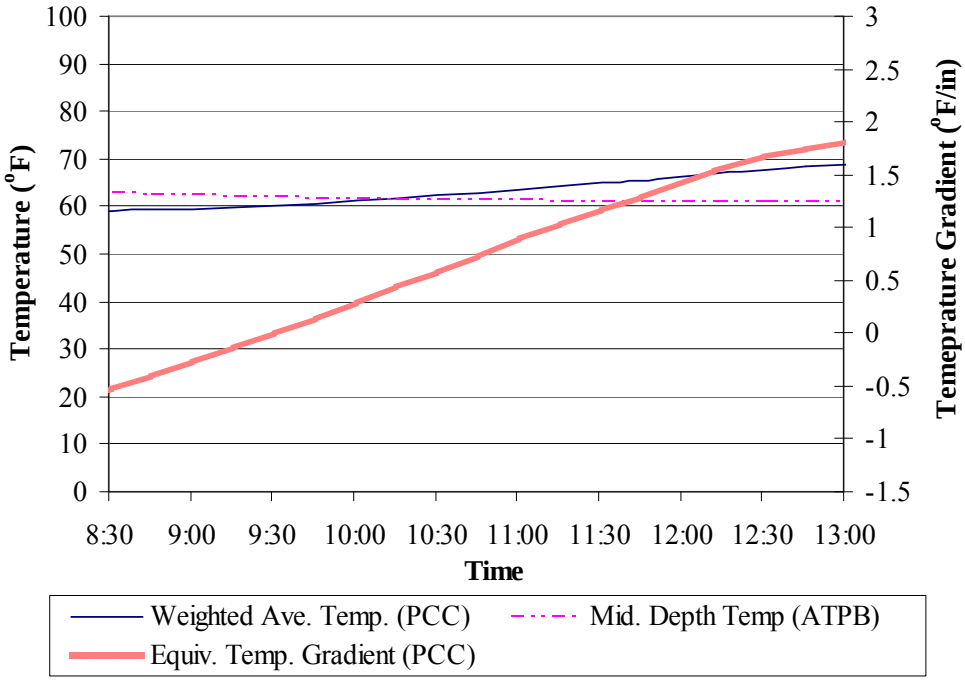

Figure 4.10. Midpanel temperature conditions during FWD testing performed in the spring of 2006.

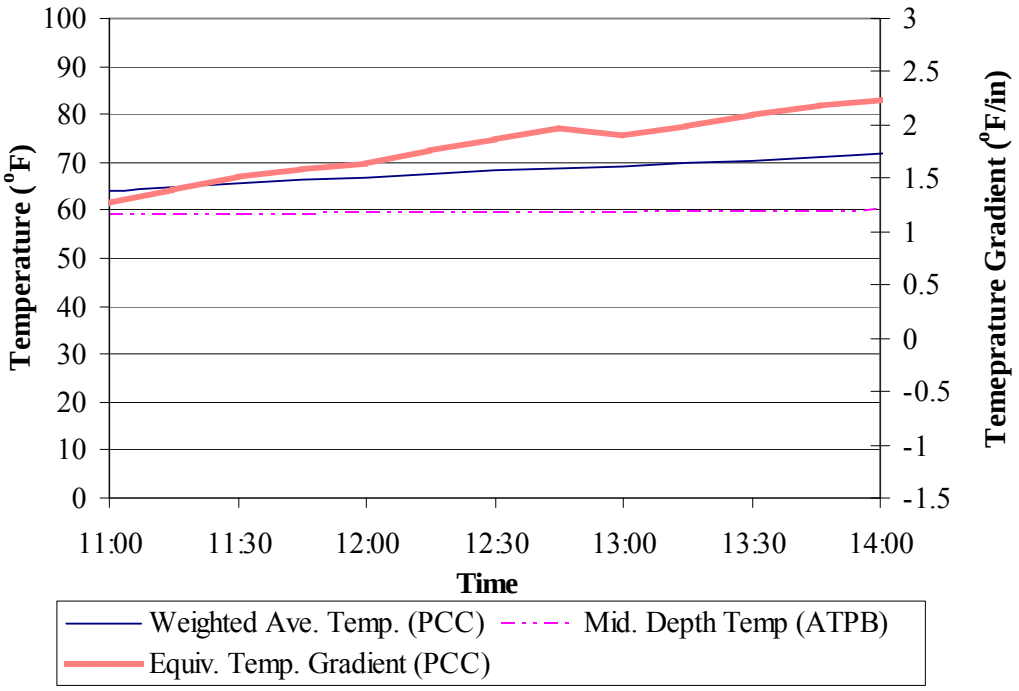

Figure 4.11. Midpanel temperature conditions during FWD testing performed in the spring of 2007.

The weighted average temperature for the summer testing periods ranged between 72 and 96 degrees Fahrenheit with an average of 80 degrees Fahrenheit. The equivalent linear temperature gradient varied between -0.73 and 2.07 °F/in with an average of 1.03 °F/in. The mid-depth temperature of the ATPB, measured during the FWD summer periods, fluctuated between 69 and 86 degrees Fahrenheit with an average of 76 degrees Fahrenheit. As shown in Figure 4.12 through Figure 4.14 the weighted average temperature t of the concrete varied considerably during summer testing. The largest average variation in weighted average temperature of the concrete was experienced with an average range of 24 °F. Additionally, the ATPB also experienced the largest variation during summer testing with an average range of 18°F.

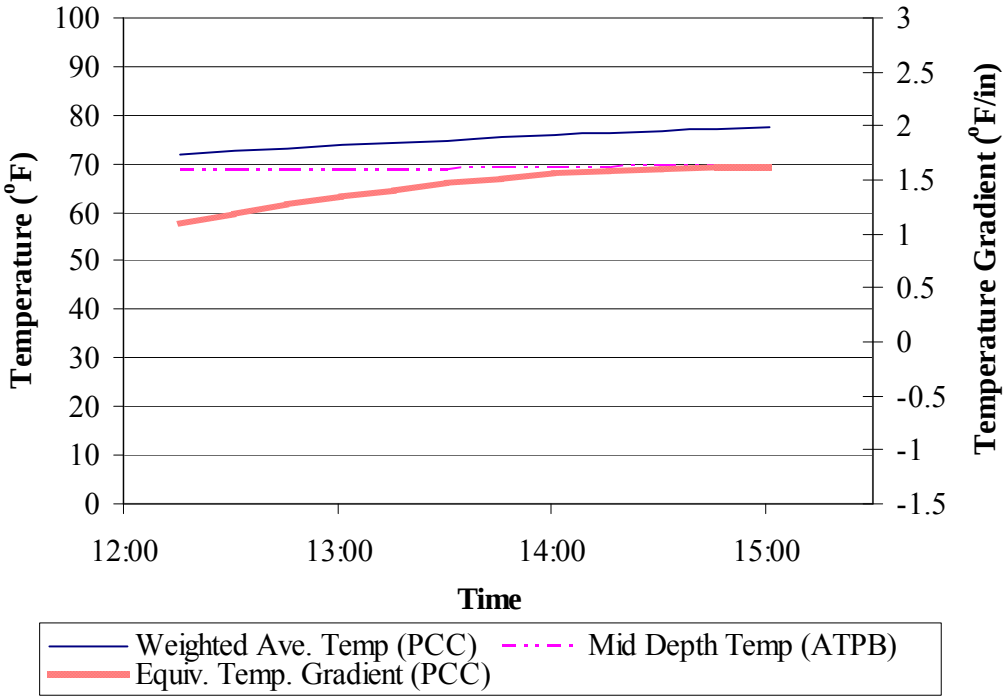

Figure 4.12. Midpanel temperature conditions during FWD testing performed in the summer of 2005.

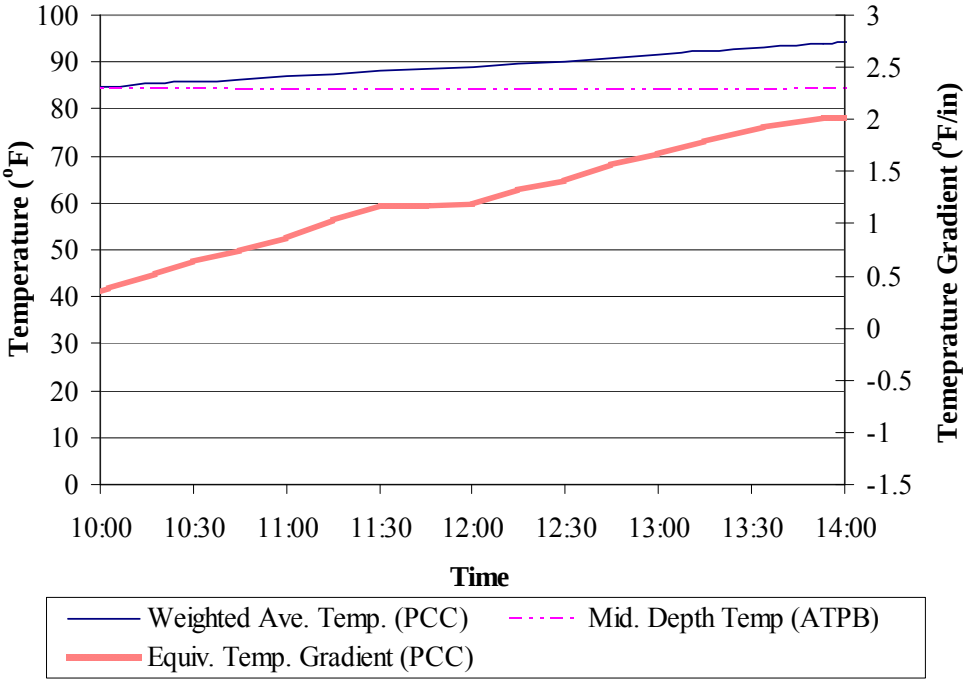

Figure 4.13. Midpanel temperature conditions during FWD testing performed in the summer of 2006.

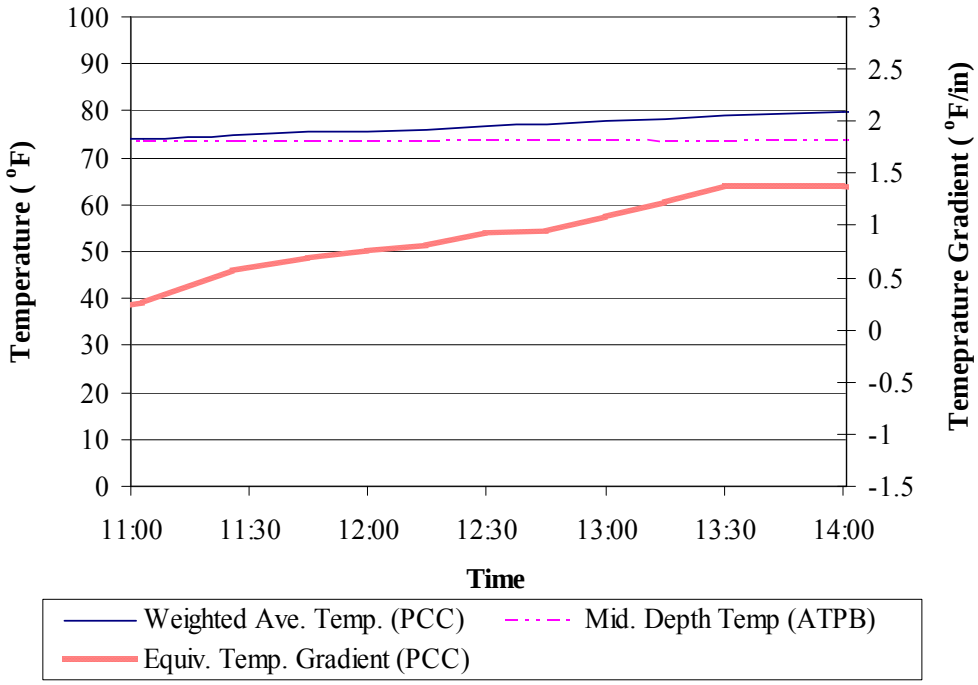

Figure 4.14. Midpanel temperature conditions during FWD testing performed in the summer of 2007.

4.2.2 Concrete Moisture Distribution

Figure 4.15 and Figure 4.16, shown below, present the variation in relative humidity throughout the PCC slab at the midpanel and edge during FWD testing. As previously discussed, the two factors affecting the response of the slab to an applied load are the change in moisture content throughout the depth of the slab (slab shape) and the change in the average relative humidity across the slab profile (crack width).

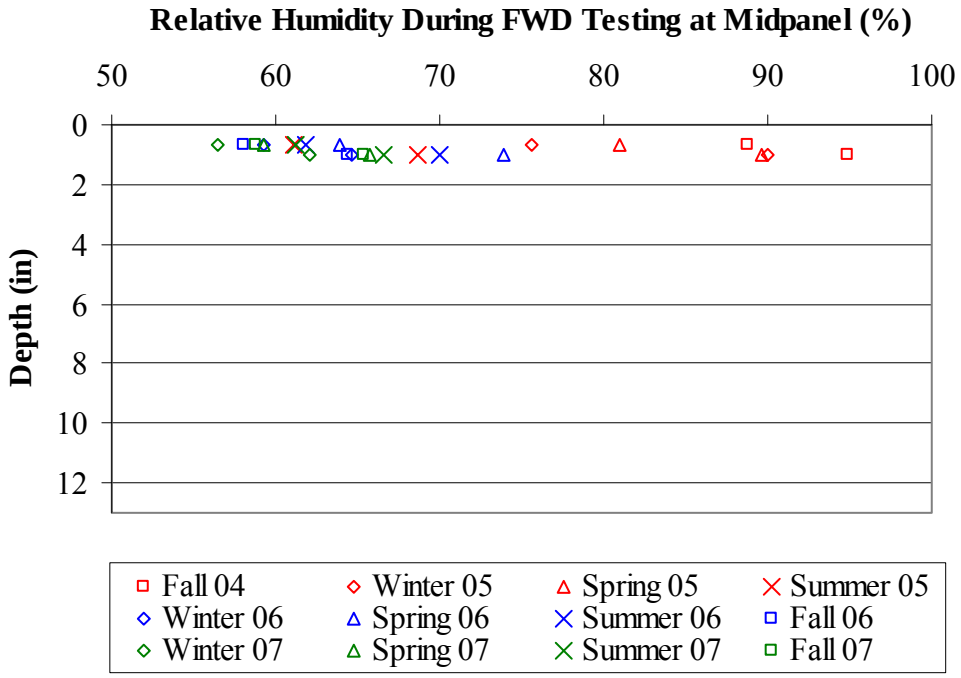

Figure 4.15. Midpanel moisture distribution throughout the PCC slab during FWD testing.

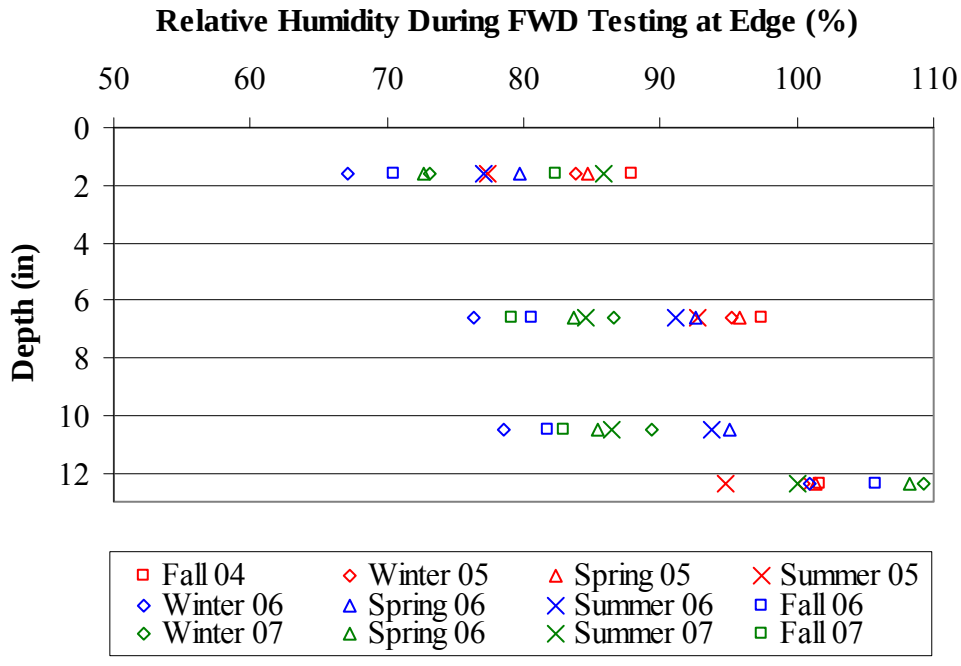

Figure 4.16. Edge moisture distribution throughout the PCC slab during FWD testing.

First the uniform change in the moisture throughout the depth of the slab will be discussed since it will affect the width of the crack at the joint. The uniform moisture content throughout the depth of the slab has continually declined since the construction of the pavement. Starting out at 100 percent relative humidity immediately after construction the relative humidity throughout the slab dropped to approximately 95 percent the first year after construction, 93 percent the second year and 83 percent the third year. The crack width at the joint will continue to increase with time until the relativity humidity within the slab stabilizes.

Next, the change in moisture content throughout the depth of the slab will be discussed. The relative humidity near the slab surface fluctuates more over time compared to other depths within the slab since it is exposed to the ambient climatic conditions. The lowest measured relative humidity, within these two inches, was found during the winter with an average of 75 percent. The largest was measured during the summer and fall with an average of 80 percent. The spring relative humidity was between the winter and summer and had an average of 79 percent. Beyond the top two inches, the relative humidity was found to be approximately 76 percent and above during all test periods. At mid-depth of the slab, the relative humidity varied between 80 and 100 percent and the bottom of the slab remained saturated. Although moisture levels above 100 percent were measured, this unrealistic and most likely indicates condensation on the sensor. This trend of variation in the top two inches of the slab and the rest of the slab remaining at 80 percent saturation or higher correspond to trends determined by Janssen through at study of concrete moisture in Illinois (Janssen 1987). The largest change in relative humidity throughout the depth of the slab was experienced during the winter of 2007 with a difference of 32 percent between the top and bottom of the slab. The smallest variation in relative humidity was experienced during the first test outing in the fall of 2004, with a 12 percent difference.

4.3 JOINT PERFORMANCE

Figure 4.17 presents the load transfer efficiencies and the stations at which they were measured throughout the first three years after paving.

At higher slab temperatures, the concrete expands and the joints lock-up. This allows the aggregate interlock provided by the surface texture at the crack face to engage and thereby better facilitate transferring loads from one side of the joint to the other. Likewise, when the slab temperatures are low and the slab contracts, the joints open and aggregate interlock will not effectively transfer load from one side of the joint to the other. Therefore, knowing the average slab temperature at the time of testing is imperative for the analysis of load transfer efficiency. The ranges of slab temperatures present during testing are summarized in Table 4.1. Figure 4.3 through Figure 4.14 show the weighted average slab temperature, the temperature in the middle of the ATPB and the temperature gradients that were present throughout each test period.

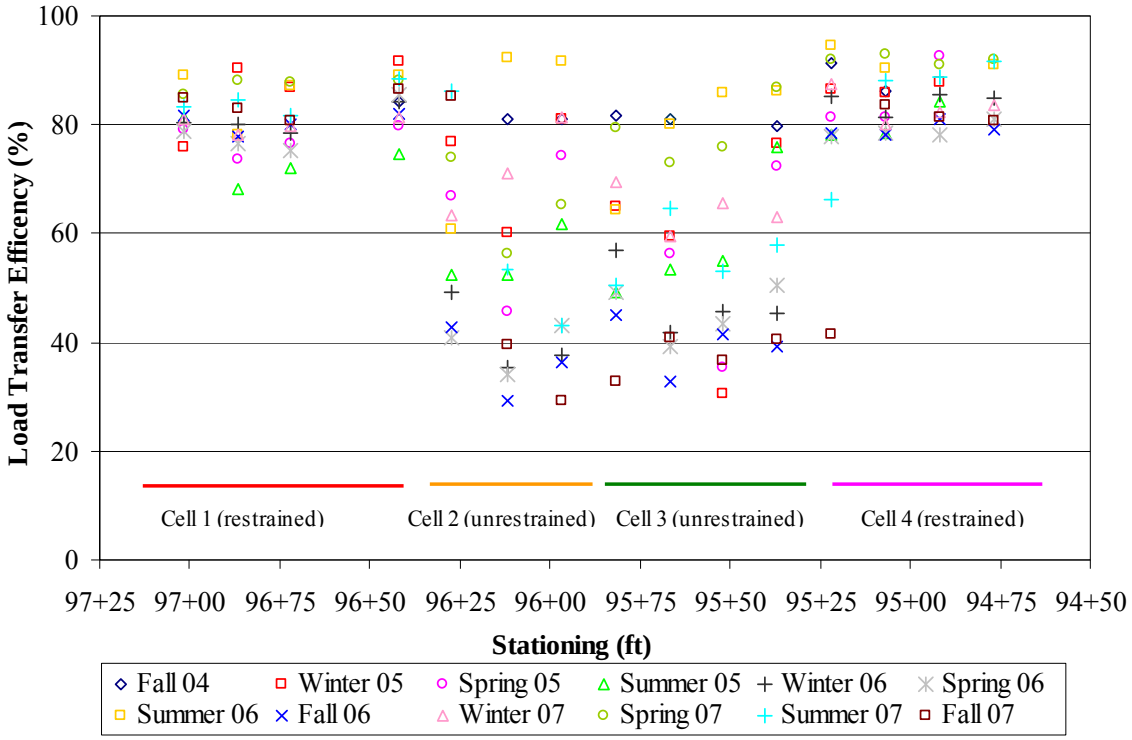

Figure 4.17. Load transfer efficiencies measured for each cell.

The initial load transfer efficiencies were measured on October 11, 2004, between 9:45 AM and 12:30 PM just shortly after the section was constructed. The load transfer efficiencies ranged between 80 and 95 percent for both the doweled and undoweled joints. The final load transfer efficiency was measured on October 30, 2007, between 10:30 am and 2:00 pm. The load transfer at this time ranged between 29 and 87 percent for both joint types. Therefore, in the three years since project construction the load transfer efficiency has decreased approximately 30 percent. This indicates significantly decreased performance in the joints of the Smart Pavement during the three years period.

During the first year, the fall testing produced the highest load transfer efficiency for both the doweled and undoweled joints. This was expected since this was the first test period after

construction. The lowest values were measured during the summer for both joints types. This was unexpected; typically LTE is highest in the summer due to small joint openings from increased temperatures. All of the undoweled joints and six of the seven doweled joints tested fell below 80 percent in the first year. This was anticipated for the undoweled joints but the load transfer efficiencies for the doweled joints should be higher this short of a time after construction. The load transfer efficiencies ranged between 68 and 92 percent throughout the year for the doweled joints and between 38 and 89 percent for the undoweled joints.

The load transfer efficiencies ranged between 75 and 94 percent for the doweled joints and between 28 and 92 percent for the undoweled joints throughout the second year of testing. The load transfer efficiencies measured for the doweled joints during the spring were the lowest with an average of 80 percent and the highest were measured during the summer with an average of 87 percent. This is only an 8 percent difference which indicates an insignificant difference between the seasonal averages. The undoweled joints had the lowest load transfer efficiencies during the fall and the highest during the summer.

The undoweled joints, which rely on aggregate interlock to provide load transfer, experienced joint openings of approximately 0.046 inches during fall testing. Typically, load transfer efficiency decreases significantly once joint openings exceed 0.03 inches, therefore the increased joint openings during fall testing attributes to the lower measured load transfer efficiencies.

At the end of the second year, the load transfer efficiency for all of the undoweled joints fell below 70 percent, with five of the seven falling below 40 percent at times. This is significant because the Federal Highway Administration (FHWA) suggests restoring joints that have less than 70 percent load transfer to prevent further damage to the pavement (FHWA 1997).

This emphasizes the need for load transfer devices for long-term performance. Figure 4.17 indicates that some of the joints would exhibit an acceptable level of load transfer efficiency if the perfect conditions were present, such as, high pavement temperatures, small crack width, and good support conditions. As previously discussed, when slab temperatures are high the joints lock-up and load transfer efficiency increases. As shown by Asbahan et al. in the interim report, the undoweled joints start locking up at 96 °F based on vibrating wire strain gage measurements (Asbahan et al. 2006). During one FWD testing outing, slab temperatures were high enough for the joints to lock-up, however, for the majority of test outings slab temperatures were much lower than 96 °F with an average slab temperature during FWD testing of 57 °F. Therefore, it can be concluded that undoweled pavements in a climate similar to that found in Pennsylvania will have low load transfer capabilities for a large portion of each day and for several months in the year. This is regardless of the aggregate interlock surface texture available at the slab face for load transfer. The reason some of the slabs were undoweled in this pavement is so the effects of restraint conditions could be characterized in this study.

The load transfer efficiencies measured during the third year ranged between 41 and 93 percent for the doweled joints and between 29 and 87 for the undoweled joints. The load transfer efficiencies measured during the fall for the doweled and undoweled joints was the lowest and was highest during the spring. These results are not typical of the Pennsylvania region. During the spring and fall seasons, increased moisture levels cause loss of support in the supporting layers of the pavement structure. The spring testing was performed on April 30, 2007. Typically the period of increased moisture and decreased support occurs at the beginning of the spring season when the pavement structure thaws. This period would have occurred prior to the end of April and the increased support conditions could be contributing to the increased

load transfer experienced during the spring 2007 testing, along with the higher pavement temperatures.

As previously mentioned, the FHWA suggests restoring joints that have less than 70 percent load transfer efficiency. The majority (larger than 50 percent) of the undoweled joints experienced LTEs below 70 percent in three of the four data collection outings in 2007. During the spring, only two of the seven joints fell below 70 percent. During the fall, which was the final test period; four of seven undoweled joints fell below 40 percent with some joints experiencing approximately 20 percent load transfer efficiency. The results of the analysis of load transfer during the third year further validates the statement that undoweled joints in climates like Pennsylvania will experience low load transfer efficiencies the majority of the year.

4.3.1 Effect of Temperature Gradients on Load Transfer Efficiency

The calculated load transfer efficiency was plotted against equivalent linear temperature gradient for both doweled and undoweled joints to see if any trends existed. Figure 4.18 shows this relationship for one of the slabs of the unrestrained cell. The weighted average temperature of the slab at the time of testing is provided next to each data point.

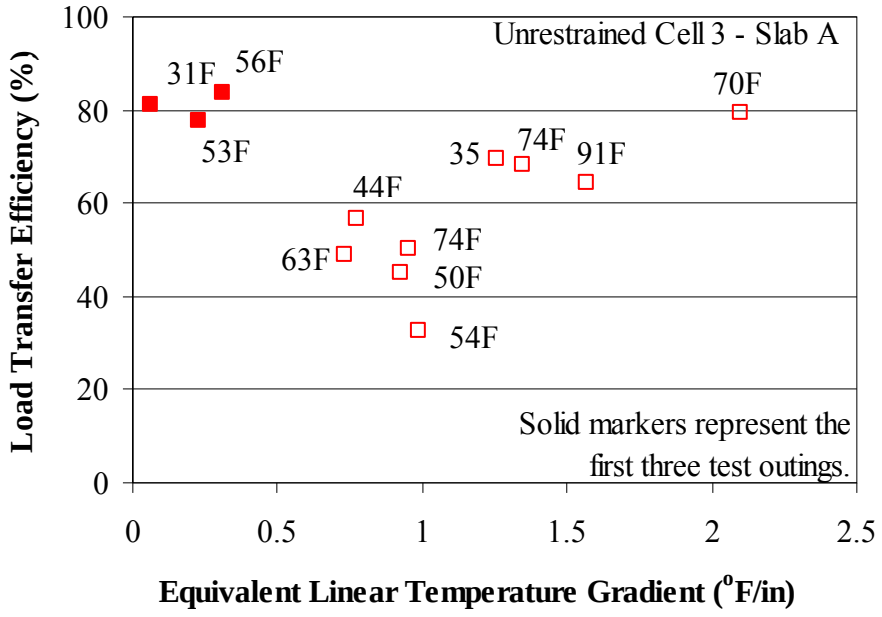

Figure 4.18. Relationship between load transfer efficiency and equivalent linear temperature gradient of the unrestrained Cell 3.

The load transfer measured for the unrestrained slabs is very dependent on the temperature gradient present at the time of testing for all but the first three data collection outings, as will be discussed in a subsequnent section. The LTE increases as the gradient increases (downward slab curvature) and decreases when negative gradients (upward slab curvature) are present.

Positive gradients develop in the afternoon when the temperature of the slab is higher. These higher temperatures tend to increase the load transfer efficiency because the cracks at the joints close as the slab expands. However, Figure 4.18 shows that when testing is performed on a slab at times when the average temperature of the slab is the same but the gradients are different, then the load transfer efficiency will be different. For example, in Figure 4.18 two separate tests were performed when the average slab temperature ranged between 70°F and 74°F

yet the load transfer efficiency for these tests ranged between 68 and 80 percent. The largest positive gradient corresponds with the largest load transfer efficiency and the largest negative gradient corresponds with the lowest load transfer efficiency. The relationship between LTE versus gradient was not observed in the first three points in Figure 4.18. These first three points (shown by solid squares) were measured during the first three FWD testing periods; therefore time could be a factor. An analysis of the load transfer efficiency and age of the pavement was carried out to determine if age was the contributing factor. The first three testing periods, preformed within the first 10 months after construction, experienced only a 6 percent variation in load transfer efficiency. The joint exhibited high load transfer efficiency during the first winter and spring even though the pavement temperatures were lower.

The transverse joints cracked the first night after paving. Repeated loading was required to "break" the slab loose. As Figure 4.19 indicates, the slab did not "break" into more discrete, finite segments until after the first spring testing. This trend was observed in all of the unrestrained slabs but varied in the amount of time it took for the slabs to break loose. This most likely can be attributed to the large difference in initial crack widths observed the first 24 hours after paving. The comparisons of load transfer efficiency to pavement age for all the unrestrained slabs can be found in appendix A.

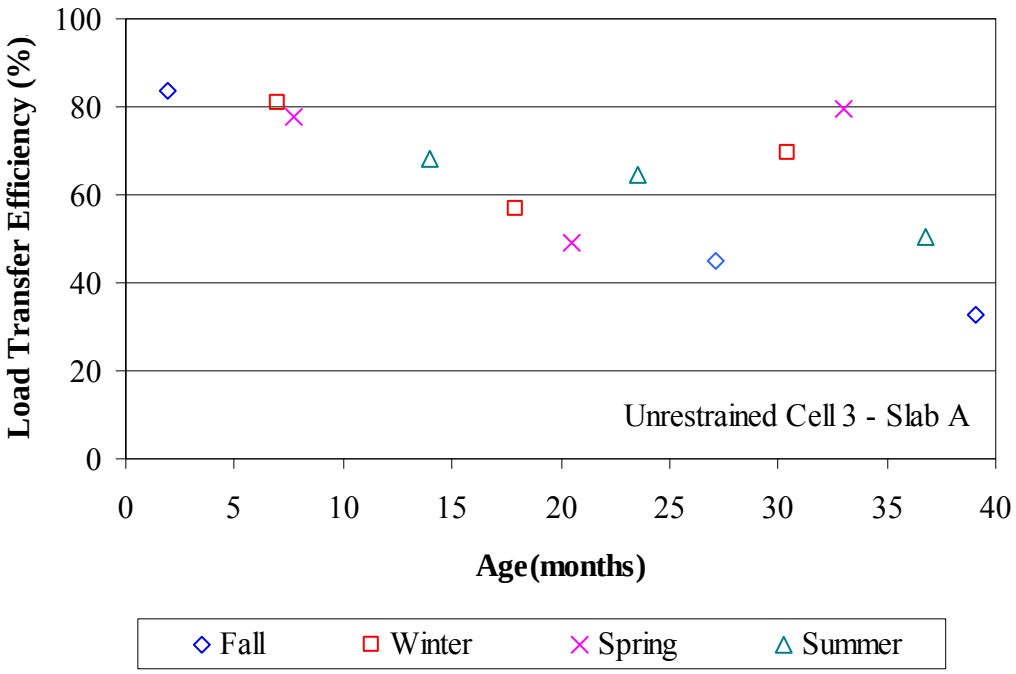

Figure 4.19. Relationship between load transfer efficiency and age of the pavement for the unrestrained Cell 3.

It was observed in Figure 4.20, that when the average slab temperature is 62°F, with a small positive gradient present, the load transfer efficiency is lower by approximately 45 percent compared to when the slab temperature is 69°F and a large positive gradient is present. Load transfer efficiency was reduced by an average of 38 percent for all of the unrestrained cells when the gradient changed from 0.5 °F/in to 2.0 °F/in at similar temperatures.

The trend of increased load transfer with increasing positive temperature gradient was seen for all of the slabs in both of the unrestrained cells. Graphs of all of the slabs can be found in appendix A This trend, of increasing load transfer with increasing positive gradients, was also experienced in a study performed at the Mn/ROAD test facility. Vandenbossche determined that load transfer efficiencies, measured for undoweled slabs, were greatly influenced by the presence of a gradient (Vandenbossche 2007).

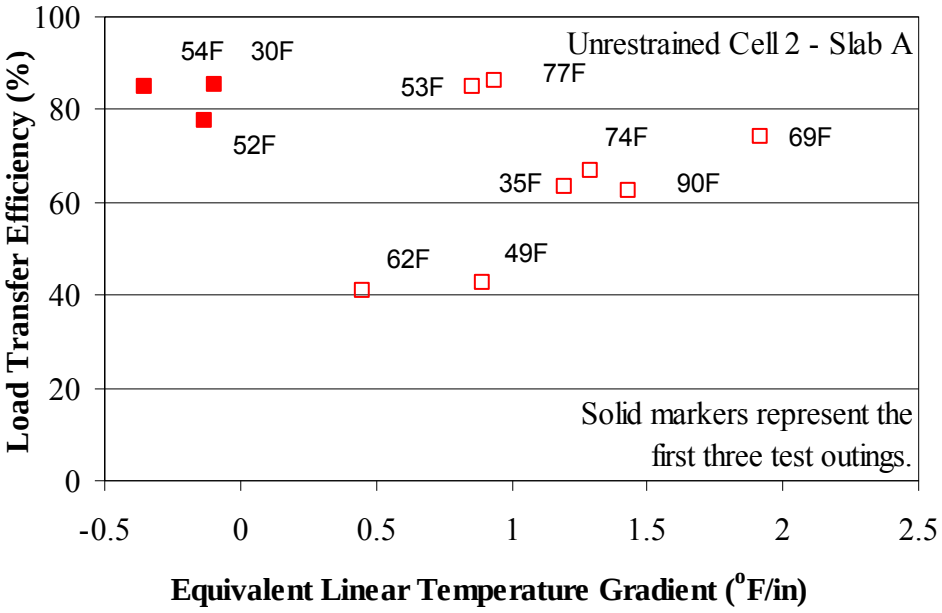

Figure 4.20. Relationship between load transfer efficiency and equivalent linear temperature gradient of the unrestrained Cell 2.

The load transfer measured for the doweled slabs was found to not be affected by temperature gradients or slab temperature, as shown in Figure 4.21. The load transfer efficiency varies between 69 and 91 percent, a 22 percent difference, while the range of gradients was large at 2.5 °F/in. This variation of 22 percent occurred over a temperature range of 61 degrees Fahrenheit. This trend, which was found in all of restrained slabs, can be seen in the figures of appendix A. This trend was also experienced in the Mn/ROAD study performed by Vandenbossche, in which doweled slabs were found to not be affected by slab temperature or temperature gradients (Vandenbossche 2007). Additionally, Khazonovich and Gotif found that LTE was affected by temperature differences and the resulting joint movement and slab curling in both unrestrained and restrained slabs. This supports the findings of this study and the study

by Vandenbossche for the restrained slabs but not the unrestrained slabs which were not affected by slab shape (Khazonovich and Gotif 2003).

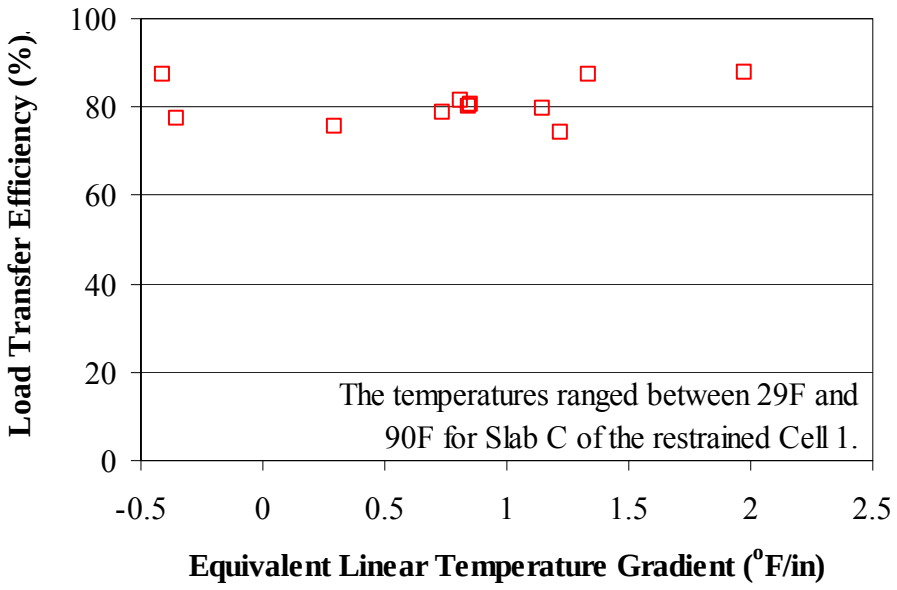

Figure 4.21. Relationship between load transfer efficiency and equivalent linear temperature gradient of the unrestrained Cell 1.

4.3.2 Relationship between Strain and Load Transfer Efficiency

Dynamic strain gages installed in both restrained and unrestrained slabs (Cells 1 and 2, respectively) were used to measure strains in conjunction with the FWD testing. As previously discussed, FWD testing was performed seasonally (winter, spring, summer, and fall) throughout the first three years following construction. Figure 4.22 through Figure 4.25 show the relationship between load transfer efficiency and measured strain at the top and bottom for the restrained slabs. Negative values indicate a compressive strain and positive values indicate tensile strains. These strains were linearly normalized to a 9,000 lb load. Each data point is

defined in the legend according to the slab for which the data point was measured (Slab A or B). Although data was collected seasonally over the three years, excessive electronic noise and erroneous measurements during field testing prohibited the use of some data collected and therefore, each graph does not have the same number of data points.

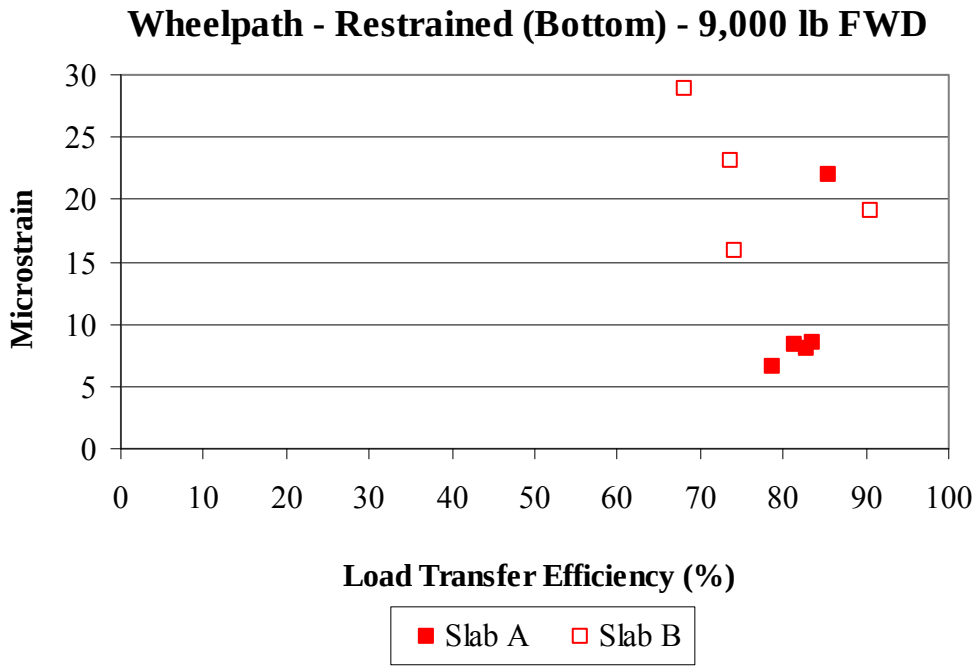

Figure 4.22. Relationship between load transfer efficiency and strain measured in the wheelpath on the bottom of the restrained slabs.

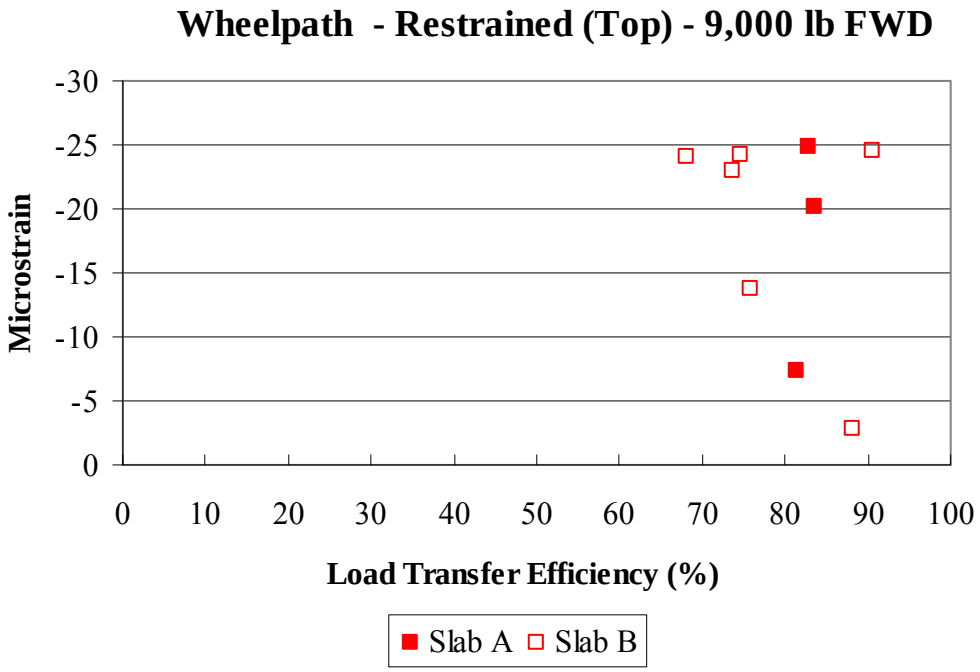

Figure 4.23. Relationship between load transfer efficiency and strain measured in the wheelpath 1 in from the surface of the restrained slabs.

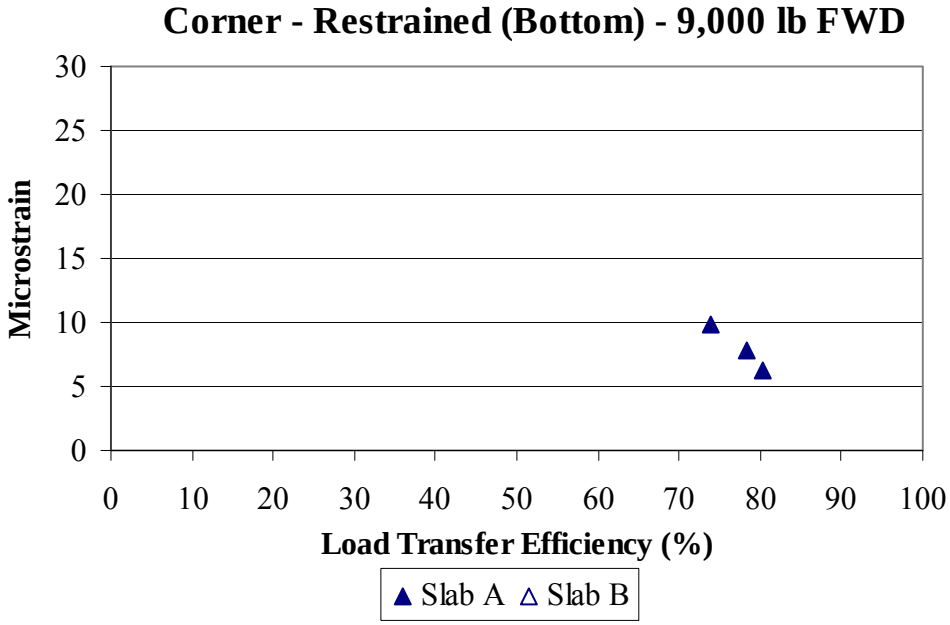

Figure 4.24. Microstrain verse load transfer efficiency for the restrained Cell 1 bottom sensors at the corner location.

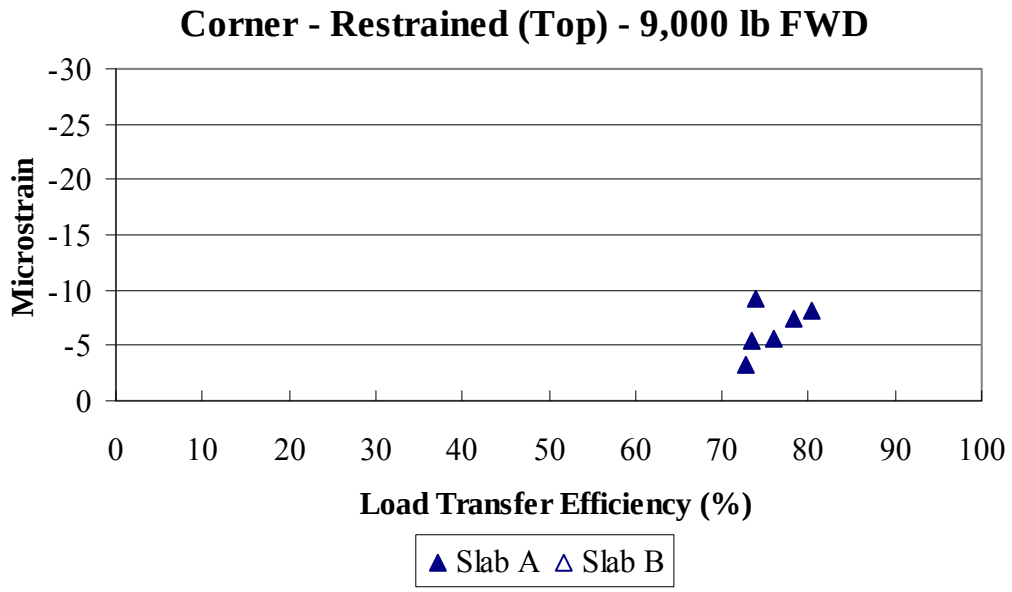

Figure 4.25. Microstrain verse load transfer efficiency for the restrained Cell 1 top sensors at the corner location.

Figure 4.22 through Figure 4.25 show that strain measured along the transverse joint of the restrained slabs has no correlation to load transfer efficiency. It would be anticipated that the strains would increase with decreasing load transfer efficiency since the loaded slab is forced to carry a larger portion of the load.

Along the transverse joint, the strain varies between 7 and 21 microstrain at the bottom of Slab A and between 6 and 29 at the bottom of Slab B. Although the strain varies drastically, there is minor variation in the load transfer efficiency with a 7 percent change in Slab A and a 22 percent variation in Slab B. Although a distinguishable relationship between LTE and strain was not experienced, there is a trend of larger variation in strain when a larger variation in load transfer efficiency is experienced. There is also less variation in the measured strains at the corner of the slab when compared to those measured in the wheelpath. This is due to the larger displacements experienced at the corner of the slabs due to temperature and moisture variation.

The relationship between microstrain and load transfer efficiency is shown in Figure 4.26 through Figure 4.29 for the unrestrained slabs. A similar trend is found for the unrestrained slabs that load transfer efficiency does not affect the magnitude of the measured strain.

Strains measured along the transverse joint of the unrestrained slab, vary between 2 and 28 microstrain at the bottom of Slab A and between 6 and 19 in Slab B. There is a drastic variation in the measured strain and because the joints are undoweled, load transfer efficiency also varies significantly. The LTE varied approximately 44 percent in Slab A and 62 percent in Slab B. Therefore, variation in LTE was less in Slab A then Slab B. This is most likely related to the fact that the magnitude of load transfer efficiency was less for Slab B compared to Slab A. This is similar to the variation in strain observed for the restrained slabs, which varied more when there were large fluctuations in load transfer efficiency. The unrestrained slabs also exhibited a similar trend to the restrained slabs when comparing the magnitude of the strains measured in the wheelpath and corner locations. Strains measured in the corner are again less then strains measured in the wheelpath.

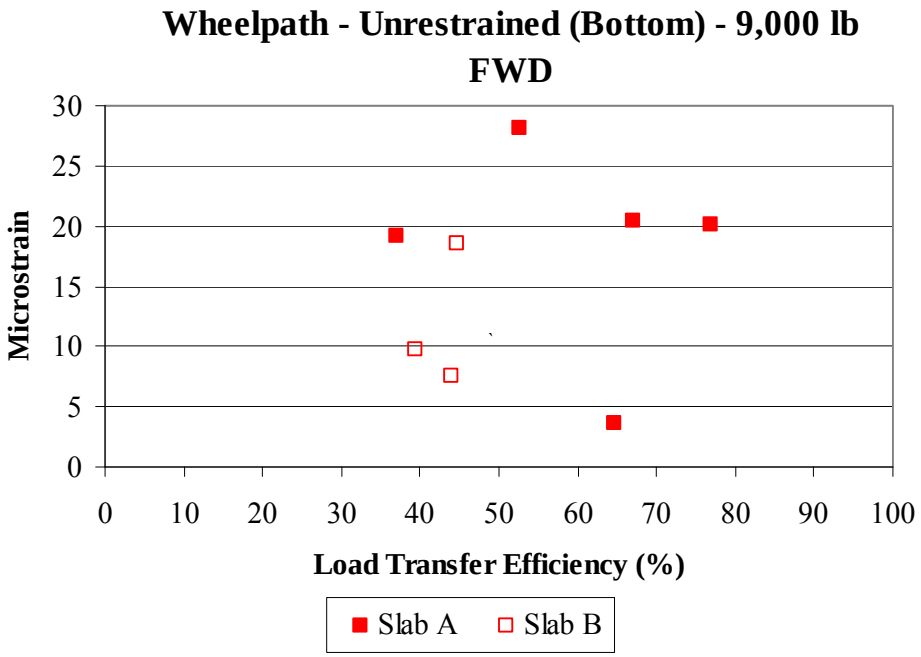

Figure 4.26. Microstrain verse load transfer efficiency for the unrestrained Cell 2 bottom sensors at the wheelpath location.

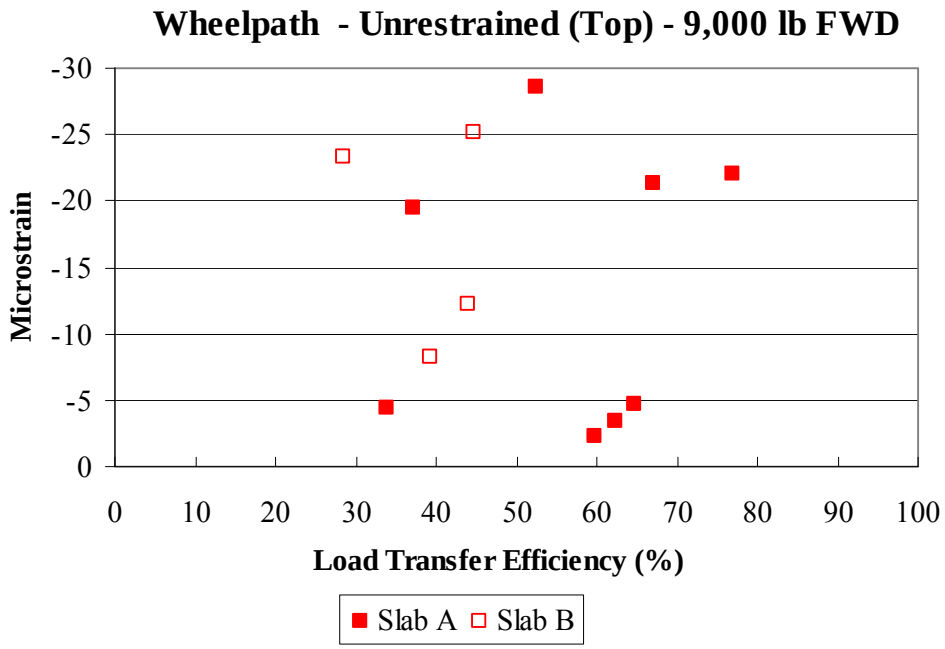

Figure 4.27. Microstrain verse load transfer efficiency for the unrestrained Cell 2 top at the wheelpath location.

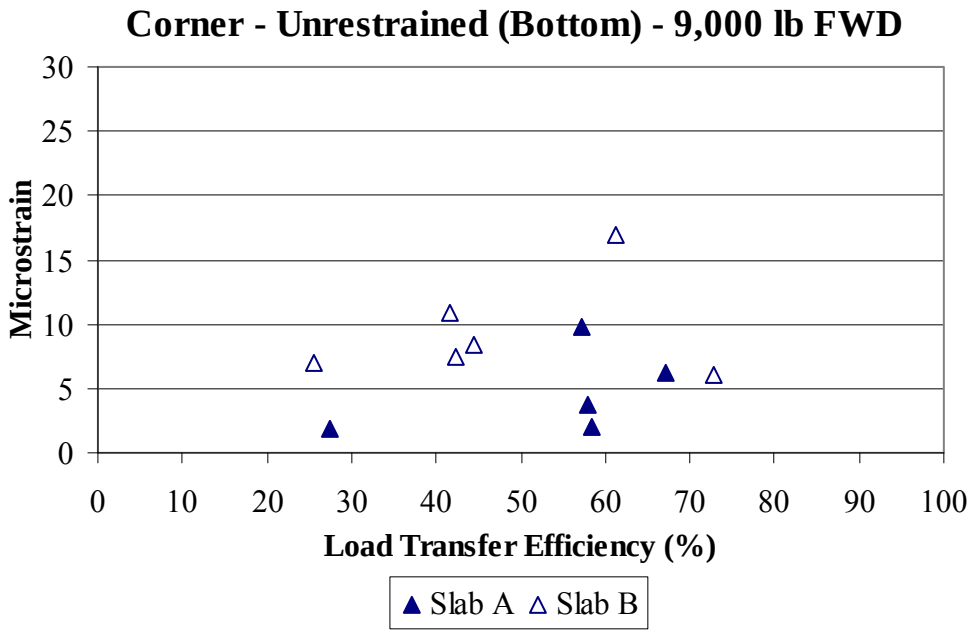

Figure 4.28. Microstrain verse load transfer efficiency for the unrestrained Cell 2 bottom sensors at the corner location.

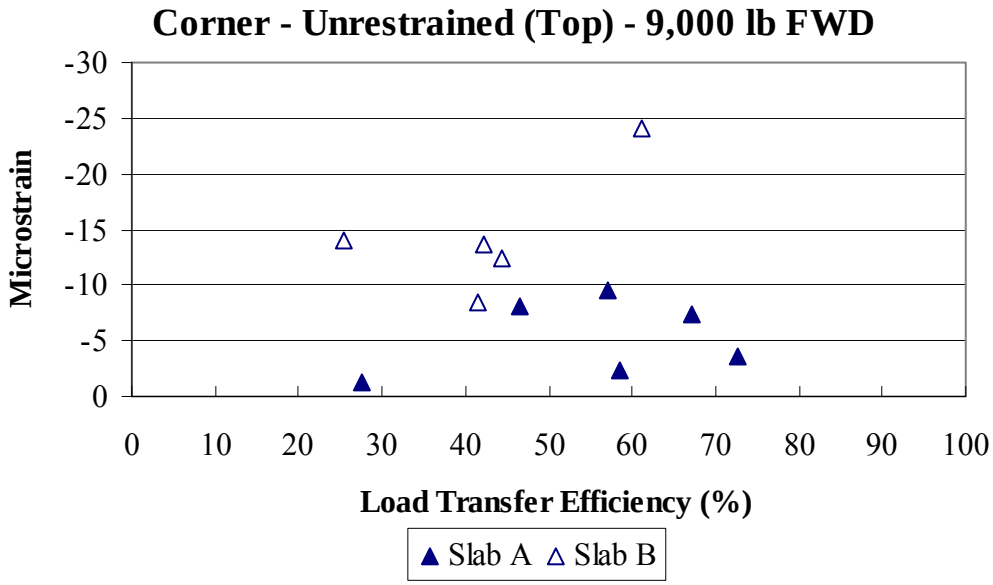

Figure 4.29. Microstrain verse load transfer efficiency for the unrestrained Cell 2 top sensors at the corner location.

4.4 VOID DETECTION

Figure 4.30 presents the calculated Void parameters along the section of roadway. All Void parameters are less than 2 mils except at one joint for an unrestrained slab in Cell 2, indicating the presence of only one void at this location. This would be anticipated since the pavement is constructed on a stabilized base. There is no distinguishable difference between the Void parameters calculated in the restrained and unrestrained slabs. However, there is seasonal variability between the Void parameters. This can be attributed to curling/warping of the slab, which influences the support at the corner. Upward curvature (due to a negative gradient) can produce a false positive while downward curvature (due to a positive gradient) can produce a false negative.

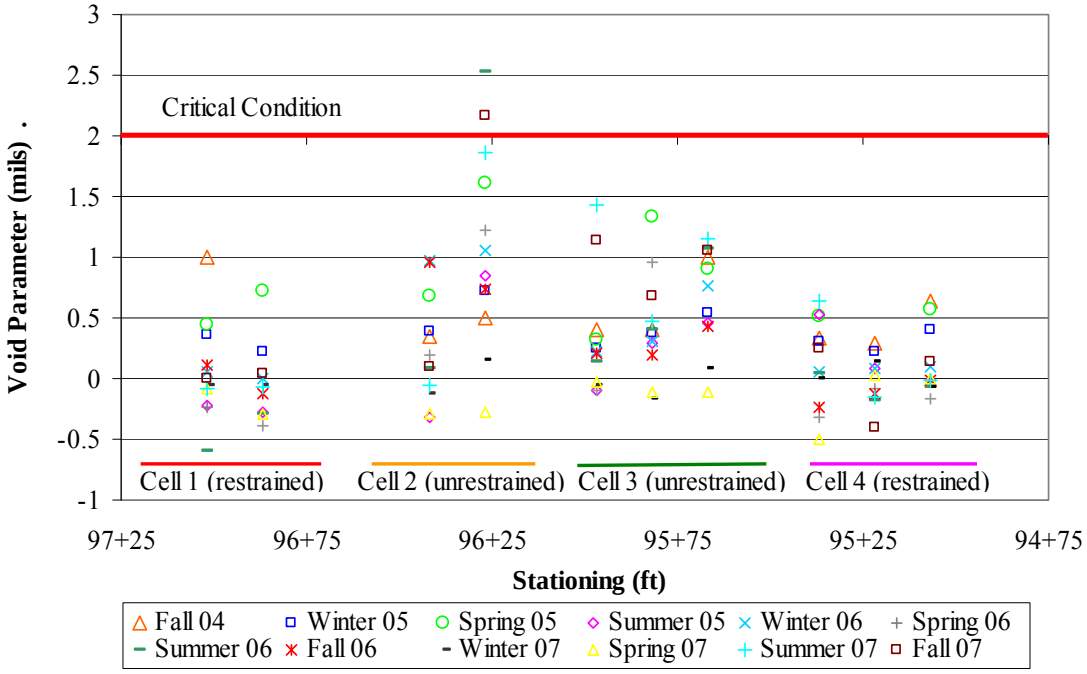

Figure 4.30. Void parameters calculated along the Smart Pavement for each cell.

Seasonally, the spring testing produced the largest variation in Void parameters and the winter testing produced the smallest variation in Void parameters for the restrained and unrestrained cells. This can be attributed to the variation in equivalent linear temperature gradients during testing. Table 4.2 shows the maximum, minimum, and average equivalent linear temperature gradients during FWD testing and Figure 4.3 through Figure 4.14 show this variation separately for each test outing. The spring testing varied on average 2.38 °F/in compared to the winter testing, which varied approximately 1.22 °F/in.

Warping of the slab, caused by moisture variations throughout the slab, also affects the Void parameters. Figure 4.15 and Figure 4.16, found in section 4.2.2, show the moisture distributions throughout the slab at the midpanel and edge during FWD testing. The edge location is of interest when analyzing the affect of moisture on the corner of the slab. The largest average variation in moisture occurred during winter testing with an average difference in relative humidity of 25 percent from the top of the slab to the bottom. The smallest variation in relative humidity occurred during spring testing with an average difference of 21 percent. Although moisture in the slab varied significantly throughout winter testing, the Void parameters did not. The Void parameters measured during the winter had the smallest variation due to the smaller variation in temperature gradients. Therefore, temperature has a larger affect on the Void parameter then moisture.

Table 4.2. Seasonal equivalent linear temperature gradients present during FWD testing.

Test Time Season	Testing Time
Fall 2004	9:45 am - 12:30 pm
Winter 2005	8:00 am - 11:45 am
Spring 2005	7:30 am - 10:30 am
Summer 2005	12:30 pm - 3:15 pm
Winter 2006	12:30 pm - 4:00 pm
Spring 2006	8:30 am - 1:00 pm
Summer 2006	10:00 am - 2:00 pm
Fall 20006	11:00 am - 2:00 pm
Winter 2007	11:00 am - 2:00 pm
Spring 2007	11:00 am - 2:00 pm
Summer 2007	11:00 am - 2:00 pm
Fall 2007	10:30 am - 2:00 pm

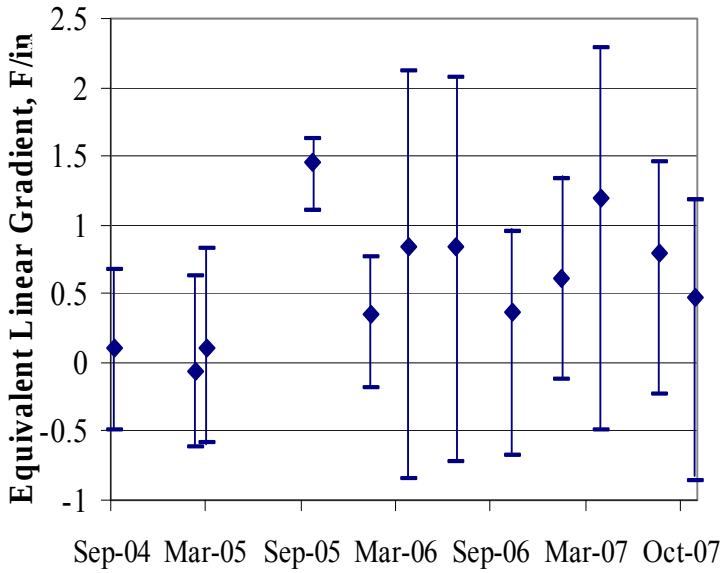

Comparing temperature gradients present at the time the data was collected with the calculated Void parameter in Figure 4.31 through Figure 4.33, a good correlation is found between the magnitude of the Void parameter and the size of the gradient. Large positive gradients produce negative Void parameters (indicating that a void is not present) while large negative gradients produce large positive Void parameters (indicating increased support conditions). This shows the effect of gradients on void detection.

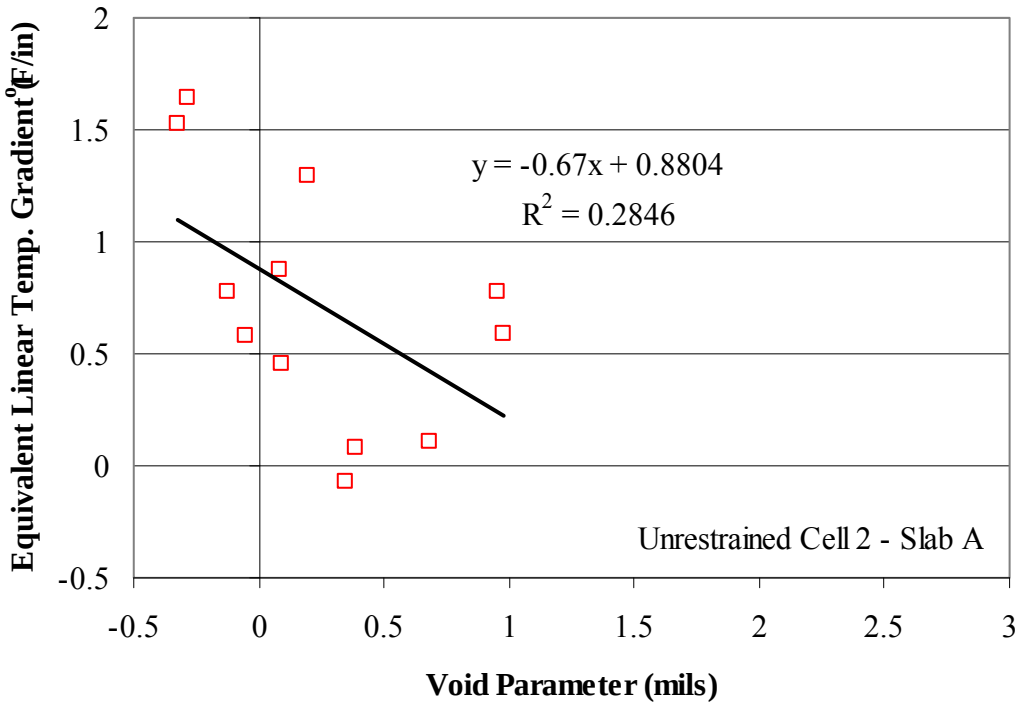

Figure 4.31. Relationship between the Void parameter and the equivalent linear temperature gradient present for unrestrained Slab A in Cell 2.

A linear regression was performed to determine if the y-intercept of the relationship between the equivalent linear temperature gradient and Void parameter is near the set gradient of the slab. The set gradient of both the restrained and unrestrained slabs was determined to be 0.31 °F/in (Asbahan 2008). As Figure 4.31 shows, there is little correlation between the equivalent linear temperature gradient and Void parameter for the unrestrained slab and the y-intercept of 0.88 °F/in is larger than the set gradient. The unrestrained slabs show less correlation and subsequently a higher set gradient because the majority of the time the slab does not experience full support. Figure 4.32 shows the relationship between the equivalent linear temperature gradient and the Void parameter for unrestrained Slab B. A number is placed next to each data

marker indicating the data collection periods that data point represents. For example, the first data collection period immediately following construction is represented by 1. This graph indicates factors other than the gradient present at the time of testing and the age of the pavement most likely have a greater impact on the estimated Void parameter. Of course, the age of the pavement might be a more significant factor is the pavement was more than three years old.

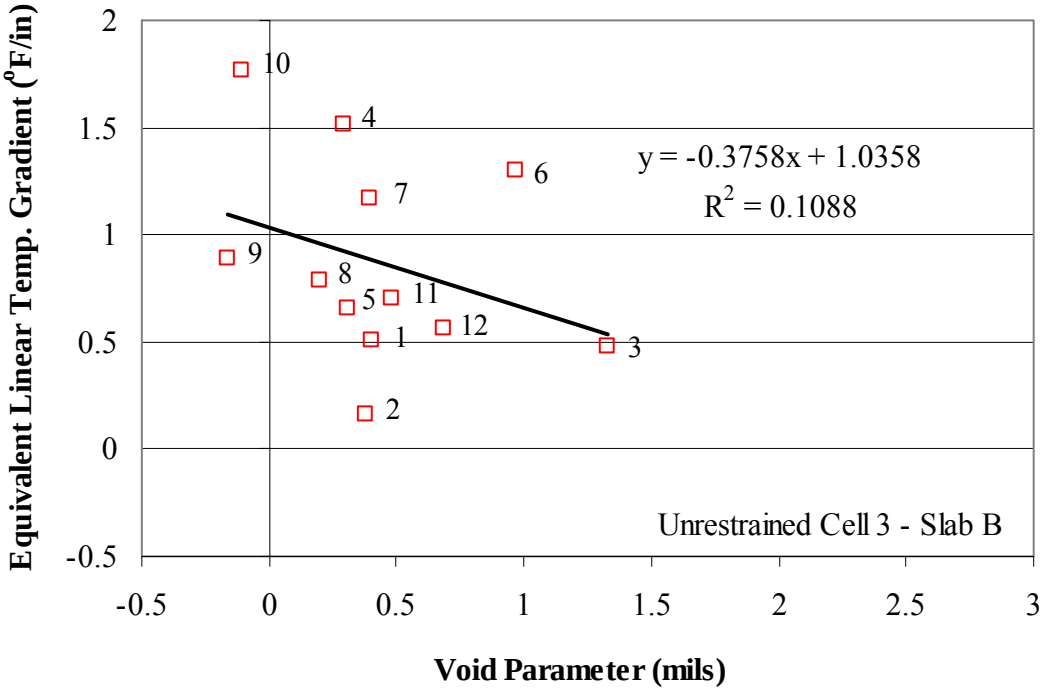

Figure 4.32. Relationship between the Void parameter and the equivalent linear temperature gradient present for unrestrained Slab B in Cell 3.

The Void calculated for the unrestrained slabs was dependent on the temperature gradient present at the time of testing for all cells, as seen in Figure 4.33. The change in the estimated void size with changes in temperature gradient was substantially smaller for the restrained slabs when compared to the unrestrained slabs. This is due to the restraint provided by the dowel and

tie-bars in the restrained slabs. A large positive temperature gradient of 1.5 °F/in produced an average Void parameter of -0.18 for the unrestrained slabs, but was only -0.11 for the restrained slabs. The restrained slabs exhibited a 37 percent reduction in Void parameter for the same temperature gradient, indicating the effectiveness of the dowel bars in limiting slab deformation due to temperature and moisture gradients. This observation indicated that restrained slabs have less potential for temperature gradients to significantly affect performance. Graphs similar to Figure 4.32 and Figure 4.33 have been developed for each cell in both the unrestrained and restrained cells to confirm the relationship between Void parameter and temperature gradient. Graphs of this type for all of the slabs of both the restrained and unrestrained cells can be found in appendix A.

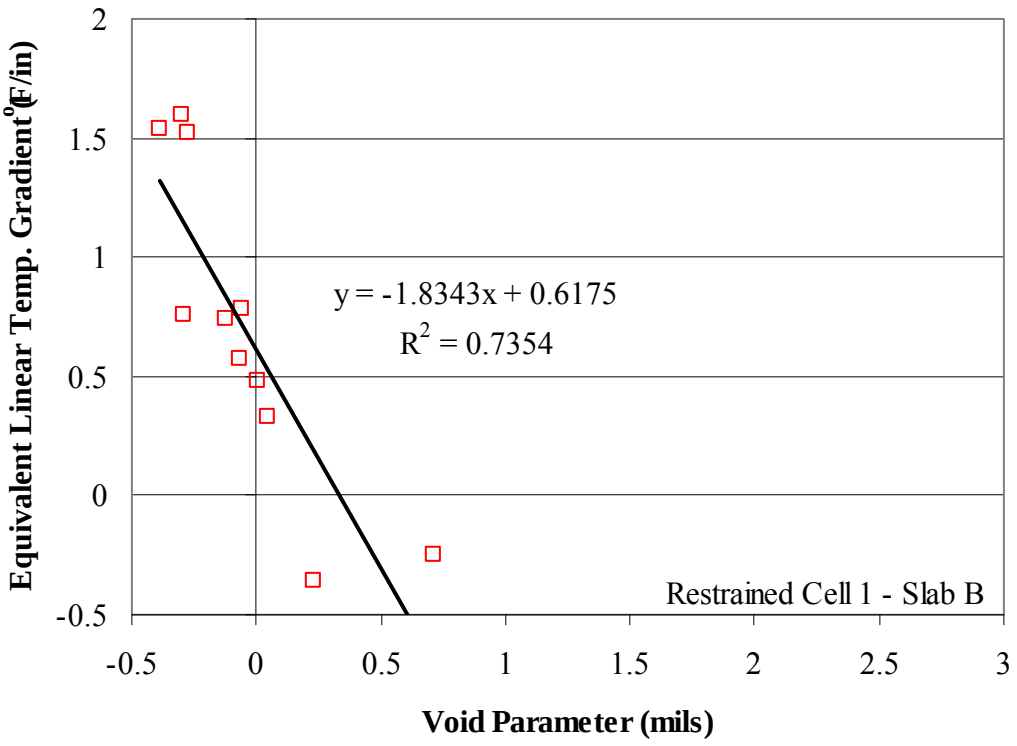

Figure 4.33. Relationship between the Void parameter and the equivalent linear temperature gradient for restrained Slab B in Cell 1.

A linear regression was performed to determine if the y-intercept of the restrained slabs was near the set gradient. As previously mentioned, the set gradient for all the restrained slabs is 0.31 °F/in. Figure 4.33 shows a better correlation between the temperature gradient and Void parameter in the restrained slabs. This is because the majority of the time full support or near full support is experienced in the restrained slabs (indicating no voids are present). Additionally, the regression provided a closer estimate of the set gradient with an intercept of approximately 0.62 °F/in.

4.5 SUPPORT CONDITIONS

The k-value representing the composite stiffness of all layers beneath the slab was backcalculated seasonally for the first three years after construction. This value is backcalculated using the AREA method presented by Hall and et. al. using deflections collected at midpanel (Hall 1990). As Figure 4.34 shows, there is considerable variation in the magnitude of the k-values measured throughout the Smart Pavement section. All backcalculated k-values represent dynamic k-values. The restrained slabs in Cell 1 had highest measured k-values throughout the three years of testing, indicating a stiffer support condition in this area. The support conditions under the slabs in Cell 1 are approximately 21 percent higher than the support conditions under the restrained slabs in Cell 4, 31 percent higher than the unrestrained slabs in Cell 2 and 29 percent higher than Cell 3. This is a fairly high level of variability but still within an acceptable range. The unrestrained cells had lower k-values (average k-value 304 pci) then both of the restrained cells (average k-value 388 pci) and also showed less variation. The average deviation for the unrestrained cells was 62 pci, while the restrained cells had an average standard deviation of 79 pci.

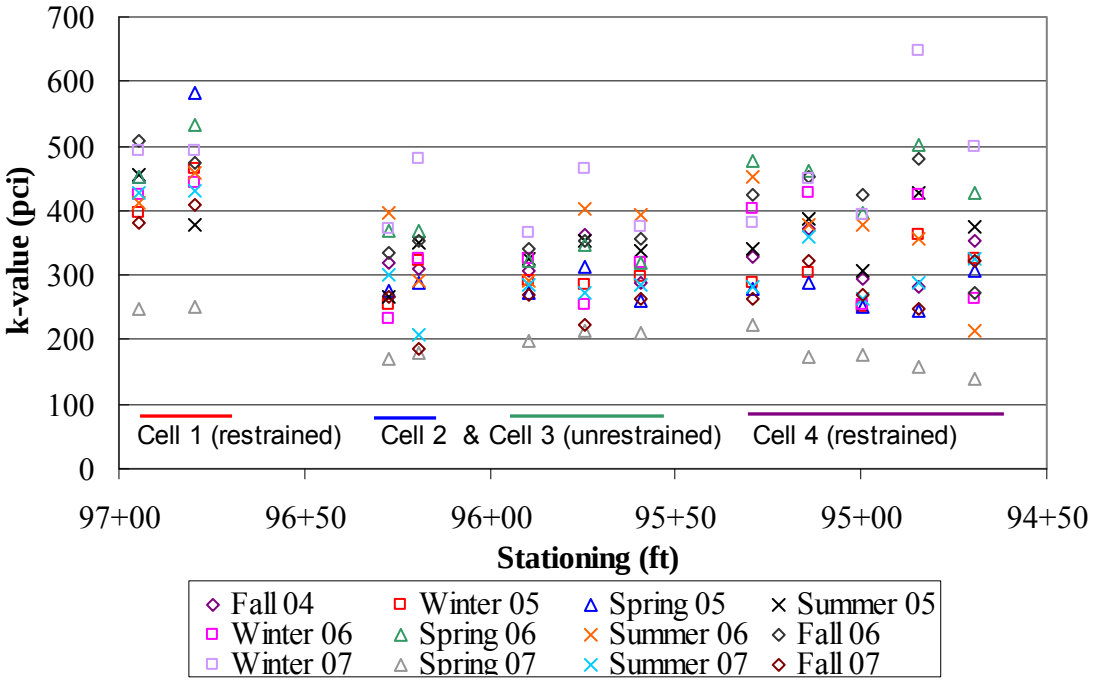

Figure 4.34. The calculated k-value across the Smart Pavement.

Figure 4.35 shows that support conditions beneath the slab do vary seasonally throughout the year. Typically, in climates like Pennsylvania, the highest k-value is found during the winter months due to the frozen subgrade. The spring and fall tend to show lower k-values due to the increase in moisture in the lower layers of the pavement structure. However, these typical support conditions were not experienced during the first and second years of testing. During the first year after construction, from the fall of 2004 to the summer of 2005, the k-value was relatively constant at approximately 320 pci. In the summer of 2005, the k-value indicated stiffer support conditions in summer then spring. There are several reasons for the unusually low winter k-value. Due to scheduling difficulties the winter FWD testing was not performed until March 10, 2005, which was less than a month before the spring testing performed on April 1, 2005. Throughout this time period there was also an increase in rainfall. Due to the significant

rainfall the moisture content throughout the pavement increases, thus decreasing support beneath the slab. Even though a stabilized base is present, the stiffness of subbase and fill materials used are highly dependent on the moisture content.

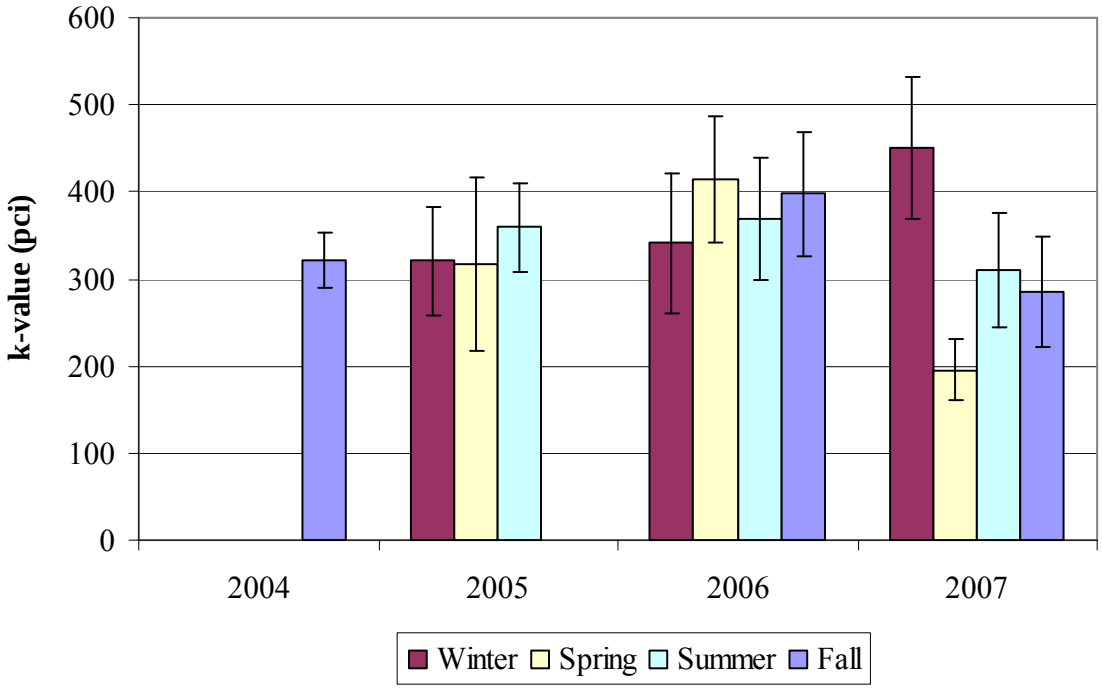

Figure 4.35. Average annual seasonal support conditions across the Smart Pavement.

Throughout the second year of testing (2006), measured k-values also did not behave typically of the Pennsylvania climate and there was not a substantial difference between the k-values backcalculated. The spring had the highest measured k-value and for the winter the lowest k-value was observed. Although this may seem unusual, there are several reasons why the calculated k-value was low in the winter. The winter testing was conducted on February 2. During testing, the temperature of all the underlying layers varied between 40 and 46 degrees Fahrenheit. This signifies that the supporting layers were not frozen when winter testing was

conducted. Also, the thawing that had recently taken place increased the moisture in the underlying layers, which decreases support beneath the slab. It can be concluded that the winter testing actually had conditions typical of early spring which deceased the support of the underlying layers. The spring testing, which was conducted April 19, had a higher average k-value than that of the summer measured three months later on July 19. As Figure 4.36 shows the cumulative precipitation for April was approximately 3 inches but in July this was doubled with 6 inches of rainfall. Therefore, increased moisture levels caused lower measured k-values during the summer.

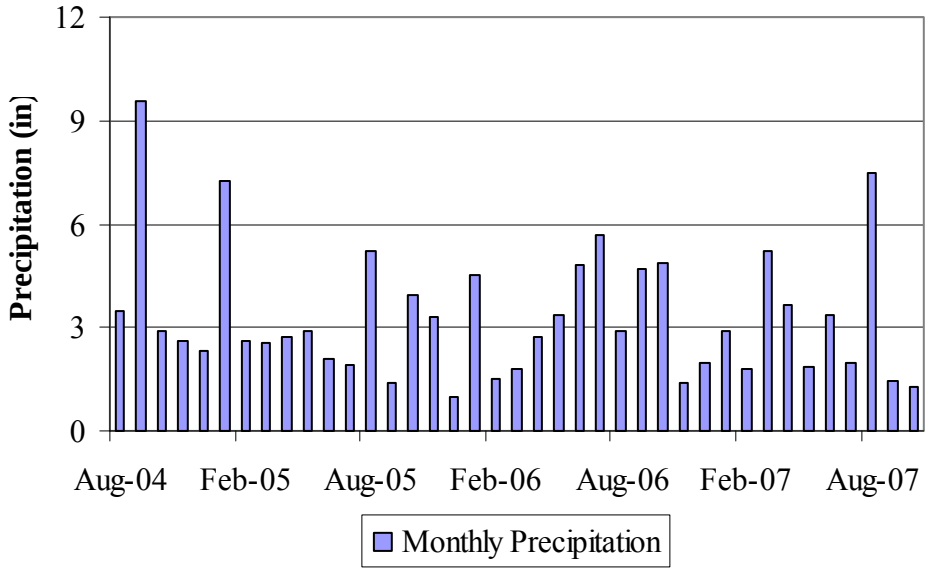

Figure 4.36. The cumulative monthly precipitation measured since construction of the Smart Pavement.

The k-values measured throughout year three (2007) show results typical of that anticipated for Pennsylvania climate. The winter had the highest average k-value of 451 pci and the spring had the lowest with an average of 195 pci. The summer season experienced the

normal condition for the year with an average k-value of 310 pci and the k-value measured in the fall was approximately 285 pci.

As previously observed, seasonal trends are exhibited in the measured k-values. Also, it has been observed that temperature and moisture conditions of the supporting layers affect the backcaluclated k-value. Therefore, a comparison was performed to investigate the average measured k-value and average mid-depth temperature of the ATPB during testing. As Figure 4.37 shows, there is no distinguishable trend between the measured k-value and the mid-depth temperature of the ATPB. The k-value varies substantially between the various slabs of the restrained and the unrestrained slabs during individual test outings even though the temperature of the base does not.

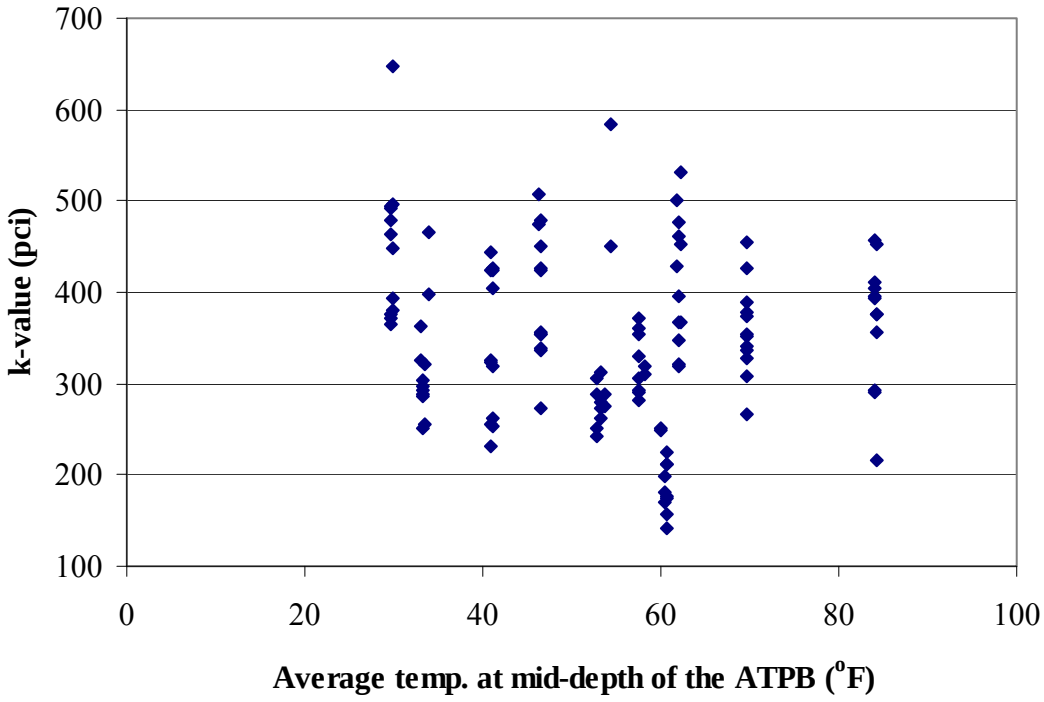

Figure 4.37. Comparison of the support conditions beneath the slab and the average temperature of the asphalt treated permeable base throughout testing.

A final analysis was performed to determine if any correlation existed between the measured k-value and equivalent linear temperature gradient of the slab during testing. As Figure 4.38 and Figure 4.39 show, there is no distinguishable trend between the measured k-value and the slab gradient in both the restrained and unrestrained slabs. The gradient varies considerably while the support conditions do not. A previous study by Khazanovich et al. determined that time of day of FWD testing can significantly affect the backcalculated k-value; this effect is most likely due to the slab gradient present during testing (Khazanovich et. al 2001). However, as Figure 4.39 shows, this trend was not experienced in the slabs of the Smart Pavement. The three squares represent backcalculated values from summer testing. The k-value varied between 412 and 455 pci as the gradient varied between 1.5 and 2.0 °F/in. FWD testing at the Smart Pavement was primarily conducted in the afternoons and typically the gradient did not vary significantly. Therefore, no trend was found between the backcalculated k-value and the slab gradient. Graphs similar to Figure 4.38 and Figure 4.39 have been developed for each slab in both the unrestrained and restrained cells to confirm that no relationship exists between the backcalculated k-value and gradient and can be found in appendix A.

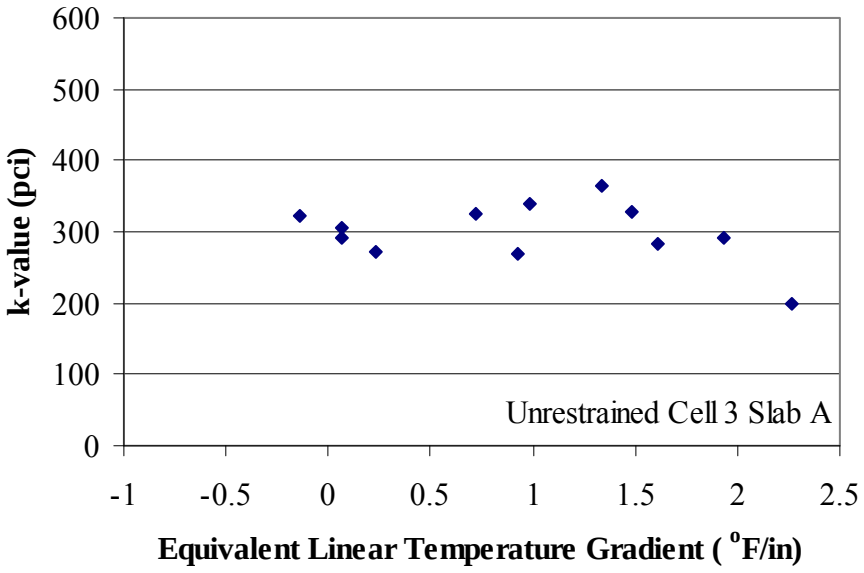

Figure 4.38. Comparison of the support conditions beneath the slab and the equivalent linear temperature gradient of the slab during testing for unrestrained Slab A in Cell 3.

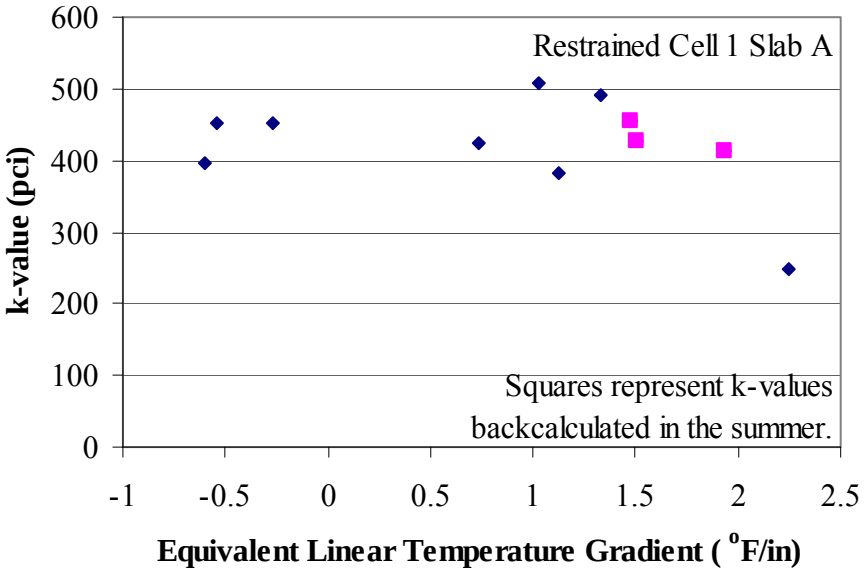

Figure 4.39. Comparison of support conditions beneath the slab and the equivalent linear temperature gradient of the slab during testing for restrained Slab A in Cell 1.

4.6 DEFLECTIONS AT EACH LOCATION

Analyzing deflection data at various locations within the slab can be very useful in determining the performance of a pavement. Differential deflections along the transverse joint in the wheelpath are used in estimating joint performance and normalized deflections along at the corner of the slab can be used in predicting possible voids along a project. Additionally, deflections measured at any location within the slab can used to access project variability.

Figure 4.40 through Figure 4.43 present the deflections measured at each test location throughout the three years of testing. Each deflection is normalized to a 9,000 lb load. Generally, as shown in the preceding figures, the unrestrained slabs exhibit larger deflections and more variation. This can be attributed not only to the unrestrained joints, but also to the weaker support layers in those locations.

The largest average deflections measured in both the restrained and unrestrained slabs were at the corner. Deflections at the corner of the unrestrained slabs were 2.5 times larger those measured at midpanel, 86 percent larger than those measured along the lane/shoulder joint, and 34 percent larger than the wheelpath, adjacent to the transverse joint. The deflections measured at the corner for the restrained slabs were 71 percent larger those measured at midpanel, 38 percent larger than those measured along the lane/shoulder joint, and 22 percent larger than the wheelpath, adjacent to the transverse joint. The corner location also showed the most variation for the unrestrained slabs with an average standard deviation of 0.97 mils. The midpanel of the restrained slabs had the largest variation with an average standard deviation of 0.29 mils.

The corner and wheelpath along the transverse joint had the largest measured deflections and variation due to its proximity to the joint. Temperature gradients greatly affect the deflections measured at these locations. Large positive gradients decrease deflection while large

negative gradients increase deflections. The performance of the joint also affects deflections at these locations. The unrestrained slabs are affected by joint opening, temperature of the PCC slab, and temperature gradients present during testing. For example deflections measured at the corner and wheelpath of the slab are decreased when temperature is high, joint opening is small, and temperature gradients are negative.

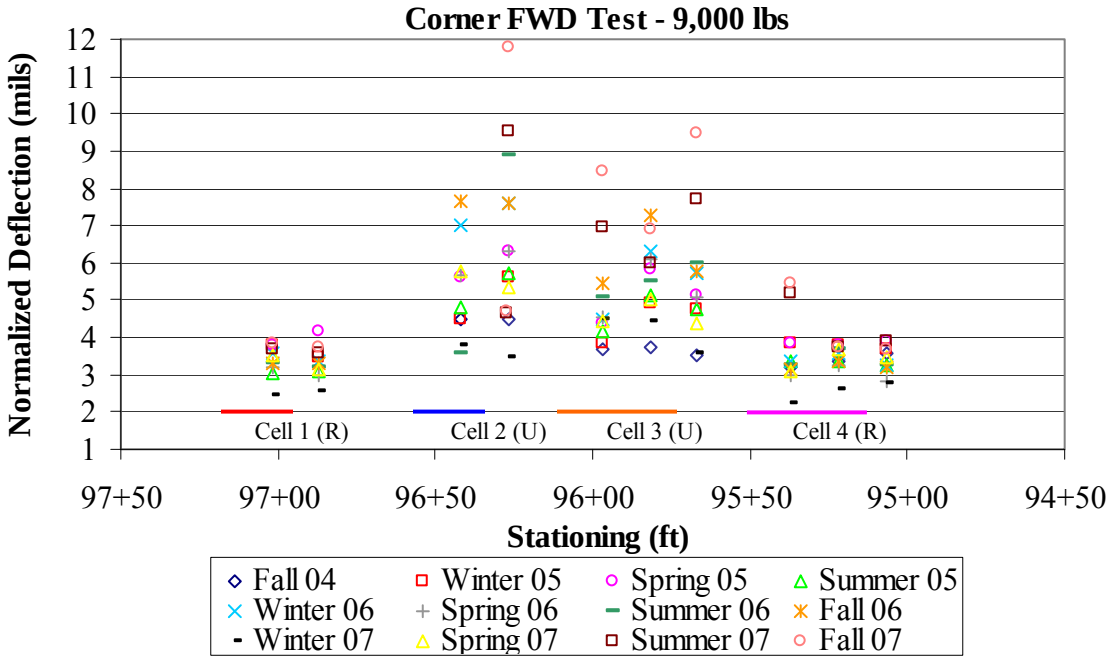

Figure 4.40. Deflections measured in the corner of each slab.

At the corner location, see Figure 4.40, the unrestrained slabs exhibit a 65 percent increase in deflection compared to the restrained slabs when averaged seasonally over the life of the pavement. This variation between the restrained and unrestrained slabs was greatest during summer testing and was lowest during spring. The summer testing was always completed during the afternoon when large positive gradients were present. This increases the deflections

measured at the corner of the unrestrained slabs. The restrained slabs, due to the presence of dowel and tie bars, are unable to deform to the same magnitude as the unrestrained slabs therefore, reducing the deflections measured in the corner. The deviation in the deflections measured in the unrestrained slabs at the corner was also greater than that of the restrained. The average deviation in the unrestrained slabs was 0.97 mils while the restrained was only 0.26 mils. The largest average deflections, measured at the corner location, were in the fall for both the restrained and unrestrained slabs.

As previously discussed, deflections measured at the corner can be used in predicting possible voids beneath the slab. In section 4.4 the variable corner deflection analysis was used in predicting voids beneath the slab and it was determined that there was one possible void at station 96+25. Figure 4.40 also shows large deflections at this station which further suggests that a void may be present.

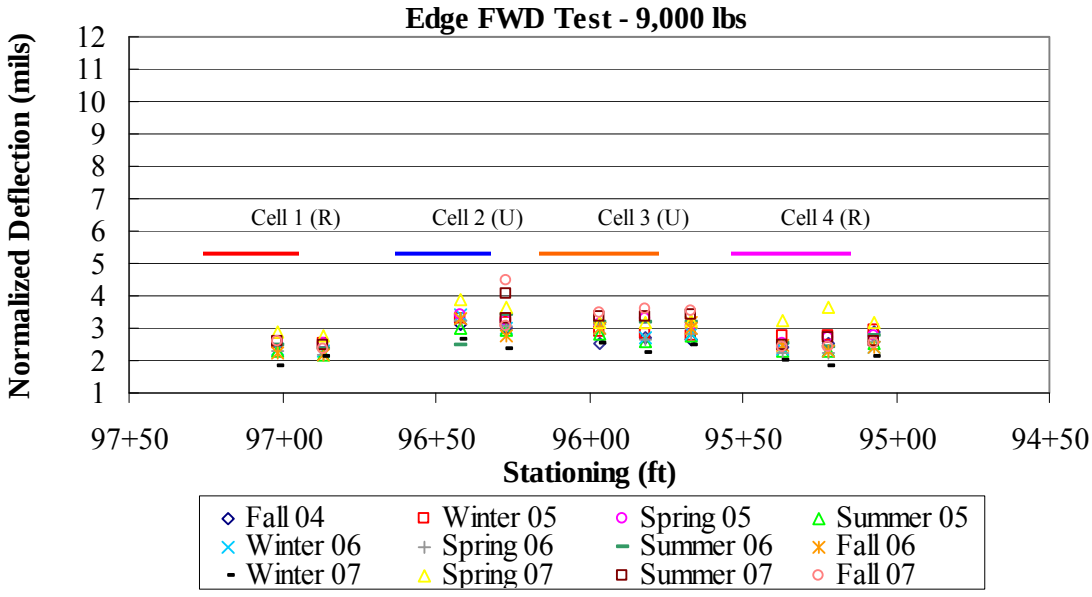

Figure 4.41. Deflections measured along the lane/shoulder joint.

Figure 4.41, shown above, displays the normalized deflections measured along the lane/shoulder joint for both restrained and unrestrained slabs. The total average deflection, along the lane/shoulder joint, for the unrestrained slab was 3 mils while the restrained slab had an average of 2.5 mils. There is not a significant difference between these two averages indicating that increased support provided by the tied curb and gutter is not substantial. The deviation of the deflections measured in the unrestrained slabs was also greater with a standard deviation of 0.23. The standard deviation of the restrained was 0.16. The largest average deflections were measured during the spring testing for both restrained and unrestrained slabs. This can be attributed to the weakened support conditions of the underlying layers.

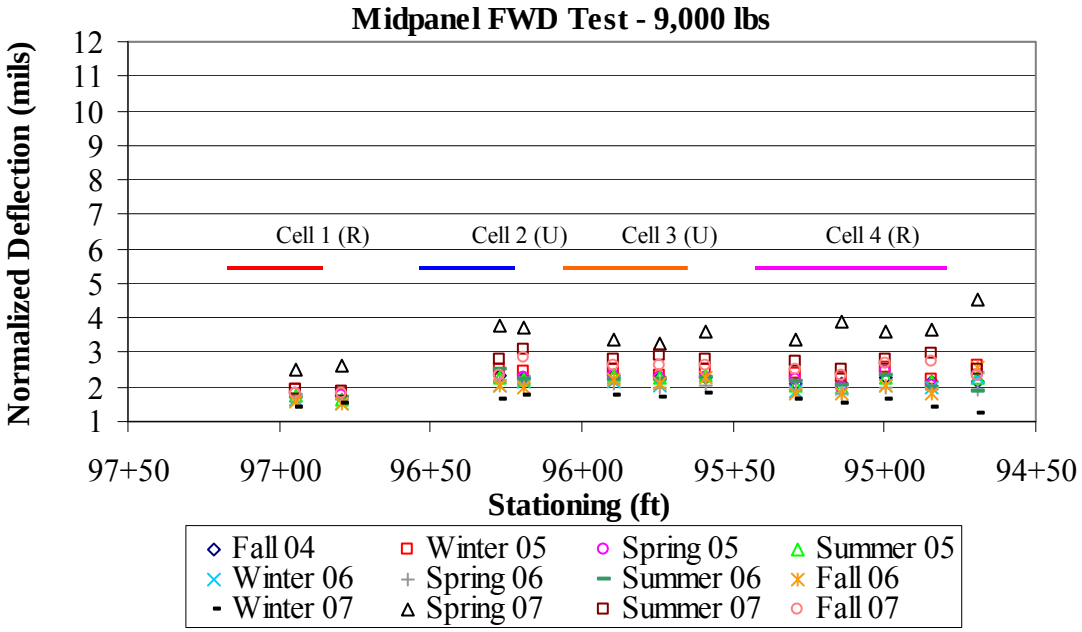

Figure 4.42. Deflections measured at midpanel.

At the midpanel location, see Figure 4.42, the unrestrained slabs exhibit 13 percent higher deflections than the restrained slabs when averaged seasonally over the life of the pavement.

This variation was greatest during summer testing and was lowest during the spring. Due to the large positive gradients present during summer testing, support is lost between the slab and base layer, thus increasing the deflections at midpanel. The largest average deflections, measured at midpanel, were in the summer for the unrestrained slabs and in the fall for the restrained slabs. This is most likely caused by the higher positive gradients experienced during the summer.

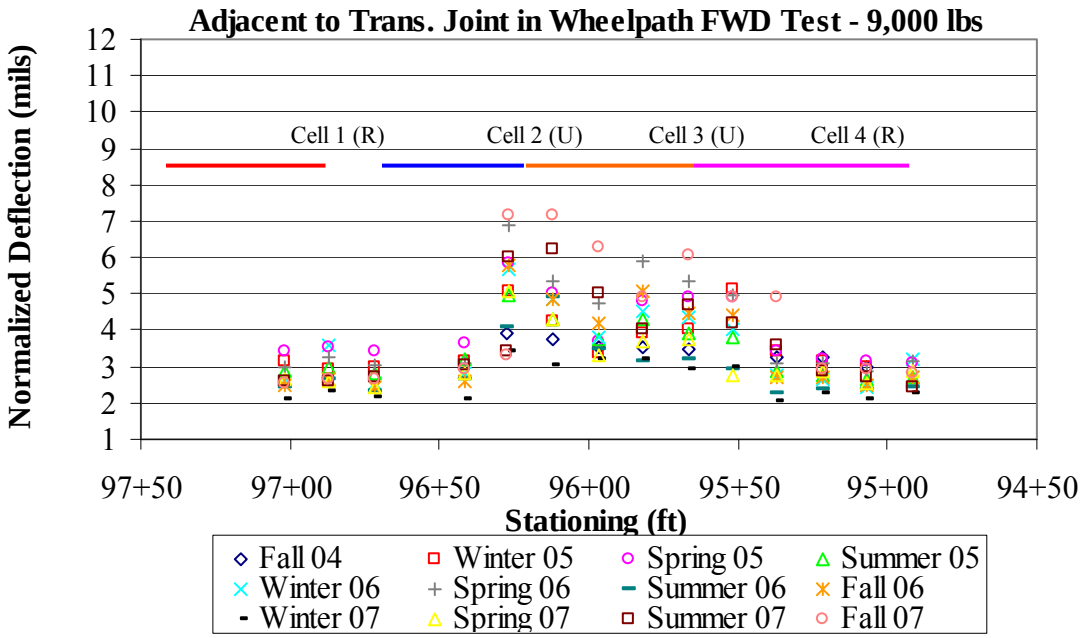

Figure 4.43. Deflections measured in the wheelpath, adjacent to the transverse joint.

Figure 4.43, shown above, displays the normalized deflections measured in the wheelpath, adjacent to the transverse joint, for both restrained and unrestrained slabs. The total average deflection, along for the unrestrained slabs was 4.2 mils while the restrained slabs had an average of 2.8 mils. At the wheelpath, the unrestrained slabs exhibited 51 percent higher deflections than the restrained slabs. The deviation of the deflections measured in the unrestrained slabs was also greater with a standard deviation of 0.65. The standard deviation of

the restrained was 0.29. The largest average deflections were measured during the spring testing for both restrained and unrestrained slabs and the smallest were measured during the winter.

5.0 PAVEMENT RESPONSE TO TRUCK LOADING

This chapter presents the characterization of the pavement response to dynamic strains measured for truck loadings. Dynamic strain was measured from trucks of known axle loads and configurations and was preformed four times a year so seasonal effects could be characterized. A summary of the results for the first three years of testing after pavement construction is provided.

This chapter begins with a brief background of the truck load testing. This description includes a summary of all truck types, configurations, and weights. Following this, is the characterization of the temperature and moisture distribution throughout the PCC slab during truck testing, which is critical in analyzing pavement response. This chapter will then discuss the variation of strain at different locations within the slab. Analyses of the affect of axle configuration and load magnitude on the response of the pavement will be presented. Additionally, an investigation of the variation of strains measured at the top and bottom of the restrained and unrestrained slabs will be presented. Finally, the effect of variations in the temperature and gradient of the slab on measured strain will be discussed.

5.1 TRUCK LOAD TESTING

Seasonal truck load testing was conducted over the slabs in Cells 1 and 2 where dynamic strain gages are installed. Three different axle configurations are used, as shown in Figure 5.1. The three trucks consisted of the following:

1. 6-axle semi (FHWA Class 10);
2. 4-axle dump truck with a triple axle in the rear (FHWA Class 7) and
3. 3-axle dump truck with a tandem axle in the rear (FHWA Class 6).

Each truck is loaded with three different loads representing an average, high and overload condition. The axle loads used for each axle configuration is shown in Table 5.1.

For each axle and load configuration, the truck makes two passes over the test section. One pass was with the outside wheel passing directly adjacent to the lane/shoulder joint. The other pass was in the wheelpath, approximately two feet from the lane/shoulder joint. Each truck pass was completed at creep speed.

To ensure that the axles are loaded to the appropriate weights prior to each run, a weigh team was provided by PennDOT to weigh each axle, as shown in Figure 5.2. The load of the truck was adjusted until the target axle loads were achieved. As the truck passed over each test cell, measurements were recorded from the dynamic strain and pressure gages. The locations of the dynamic strain gages and pressure cells were defined in chapter 3.

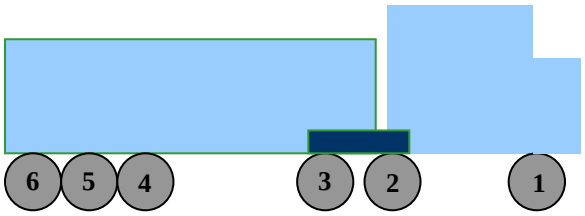

6- Axle Semi
FHWA Class 10

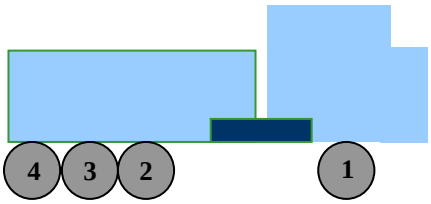

4- Axle Dump Truck
FHWA Class 7

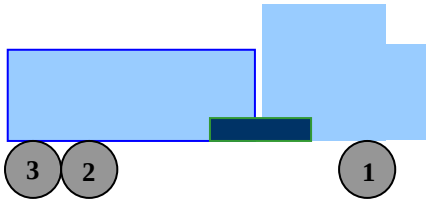

3- Axle Dump Truck
FHWA Class 6

Figure 5.1. Axle configurations for truck testing.

Table 5.1. Target axle loads for each truck.

		Weight on Axle (lbs)					
		1	2	3	4	5	6
Class 10	Standard	12,000	12,000	12,000	12,000	12,000	
	Standard	18,000	18,000	18,000	18,000	18,000	
	Standard	25,000	25,000	25,000	25,000	25,000	
Class 7	Standard	15,000	15,000	15,000			
	Standard	20,000	20,000	20,000			
	Standard	25,000	25,000	25,000			
Class 6	Standard	15,000	15,000				
	Standard	20,000	20,000				
	Standard	25,000	25,000				

Figure 5.2. Verification of axle loads.

5.2 CONCRETE TEMPERATURE AND MOISTURE DISTRIBUTIONS DURING TRUCK TESTING

The characterization of the temperature and moisture distributions throughout the PCC slab during truck testing is critical in analyzing pavement response. The weighted average

temperature and equivalent linear temperature gradient significantly affect the shape and critical stress locations in the slab. The moisture content throughout the slab also will affect the shape and critical stress locations in the slab. Therefore, determination of these factors helps in the characterization of strain.

5.2.1 Concrete Temperature Distribution

Table 5.2, shown below, presents the variation of the weighted average temperature of the slabs at midpanel during truck testing. The largest variation in temperature during truck testing was experienced during the summer of 2005, spring of 2006, and summer of 2007 with a range of 9 degrees Fahrenheit. The smallest variation in temperature was experienced during the winter of 2006 when the weighted average temperature did not fluctuate during testing. All results are typical seasonal variations of temperature.

Table 5.2. Temperature variation during truck testing.

Test Time Season	Truck Type	Testing Time	Ave. Weighted Ave. Temp, °F	Min. Weighted Ave. Temp, °F	Max. Weighted Ave. Temp, °F
Fall 2004	Class 10	11:00 am - 2:30 pm	72	69	75
Fall 2004	Class 6 & 7	9:00 am -2:30 pm	55	52	58
Winter 2005	Class 10	9:00 am - 4:00 pm	40	38	42
Winter 2005	Class 6 & 7	8:30 am - 1:30 pm	38	37	40
Spring 2005	Class 6 & 7	3:00 pm - 5:30 pm	62	62	62
Spring 2005	Class 10	2:15 pm - 5:15 pm	69	67	70
Summer 2005	Class 10	11:15 am - 4:00 pm	74	69	79
Summer 2005	Class 6 & 7	9:30 am - 4:00 pm	67	64	69
Fall 2005	Class 10	8:45 am - 11:45 am	45	42	46
Fall 2005	Class 6	11:30 am - 4:00 pm	43	42	46
Winter 2006	Class 6 & 7	9:00 am - 3:00 pm	44	40	46
Winter 2006	Class 10	9:00 am - 3:00 pm	42	42	42
Spring 2006	Class 10	12:30 pm - 5:00 pm	60	55	64
Spring 2006	Class 6 & 7	8:45 am - 12:00 pm	53	50	57
Summer 2006	Class 10	11:00 am - 1:00 pm	81	78	83
Summer 2006	Class 6 & 7	8:45 am - 11:30 pm	79	77	81
Fall 2006	Class 10	8:30 am - 10:45 am	52	51	53
Fall 2006	Class 6 & 7	8:45 am - 11:30 am	53	52	54
Winter 2007	Class 6 & 7	10:00 am - 2:30 pm	30	27	32
Winter 2007	Class 10	10:00 am - 1:45 pm	18	15	21
Spring 2007	Class 6 & 7	8:45 am - 12:45 pm	50	47	53
Spring 2007	Class 10	8:45 am - 12:00 pm	70	67	72
Summer 2007	ALL	9:00 am - 2:30 pm	80	76	85
Fall 2007	ALL	8:45 am - 1:30 pm	65	63	67

Figure 5.3 through Figure 5.26 show the variation in weighted average temperature, equivalent linear temperature gradient of the slab, and middepth temperature of the ATPB during

test periods. Summary statistics of all test seasons are discussed below. Each season for all three years was combined to determine the overall range and average values of each factor.

During the fall testing the weighted average temperature in the PCC slab ranged between 42 and 75 degrees Fahrenheit with an average of 55 degrees Fahrenheit. The equivalent linear temperature gradient of the PCC slab varied between -0.46 and 1.36 °F/in during the fall, with an average of 0.36 °F/in. The middepth temperature of the ATPB varied between 49 and 69 degrees Fahrenheit with an average of 57 degrees Fahrenheit. As shown in the proceeding figures, the weighted average temperature of the concrete varied minimally during the three test periods. The fall encountered the least variation in weighted average temperature with an average range of less than 1 °F.

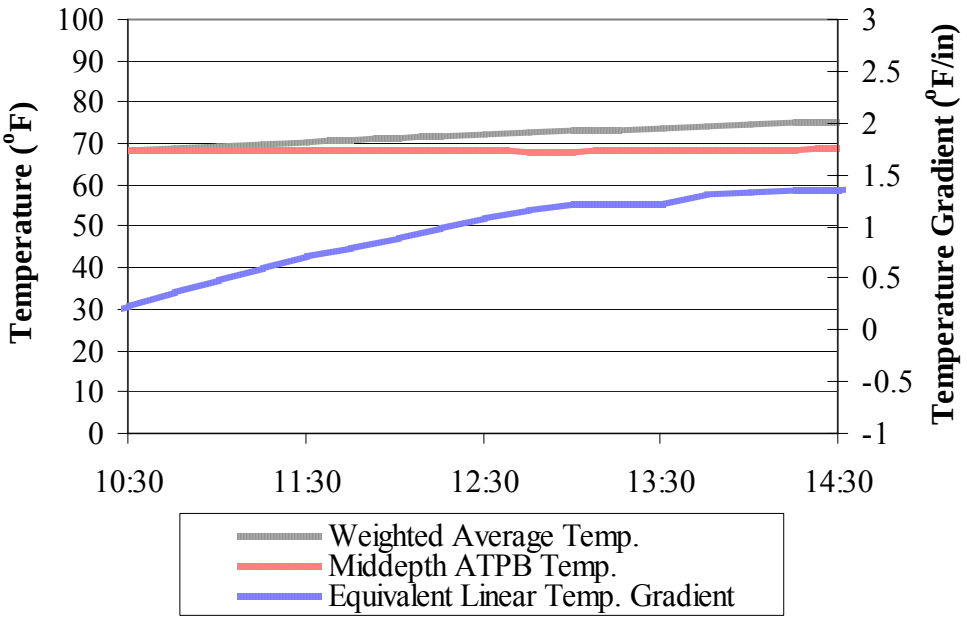

Figure 5.3. Midpanel temperature conditions during Class 10 truck testing performed in the fall of 2004.

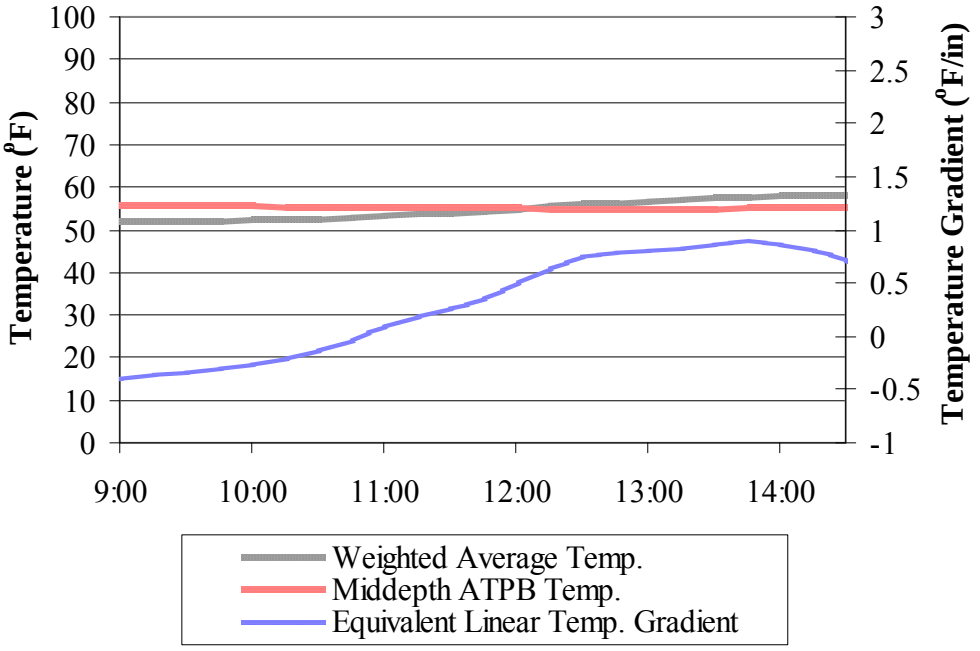

Figure 5.4. Midpanel temperature conditions during Class 6 and 7 truck testing performed in the fall of 2004.

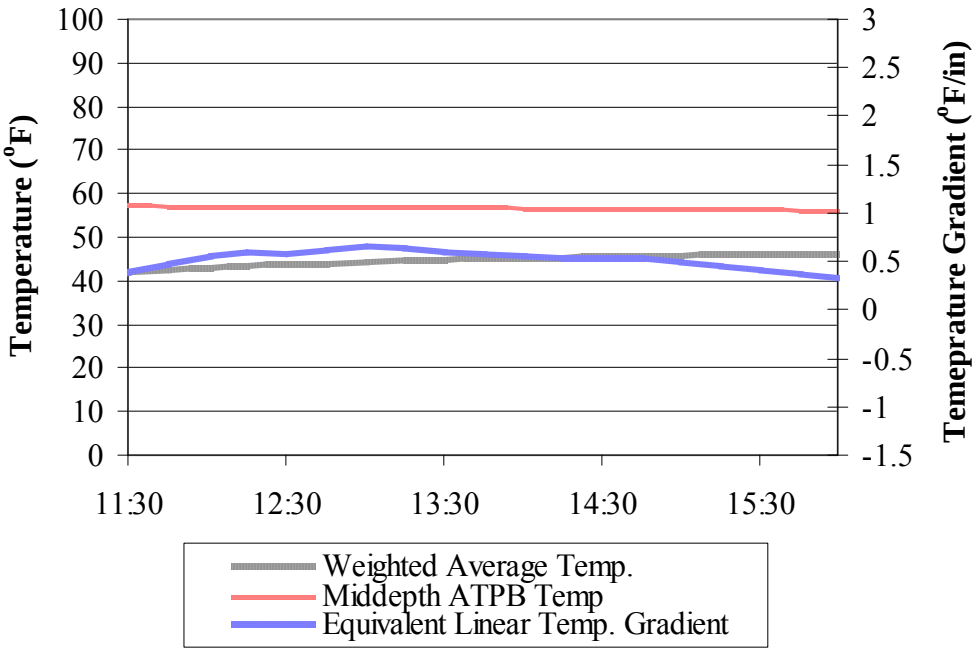

Figure 5.5. Midpanel temperature conditions during Class 10 truck testing performed in the fall of 2005.

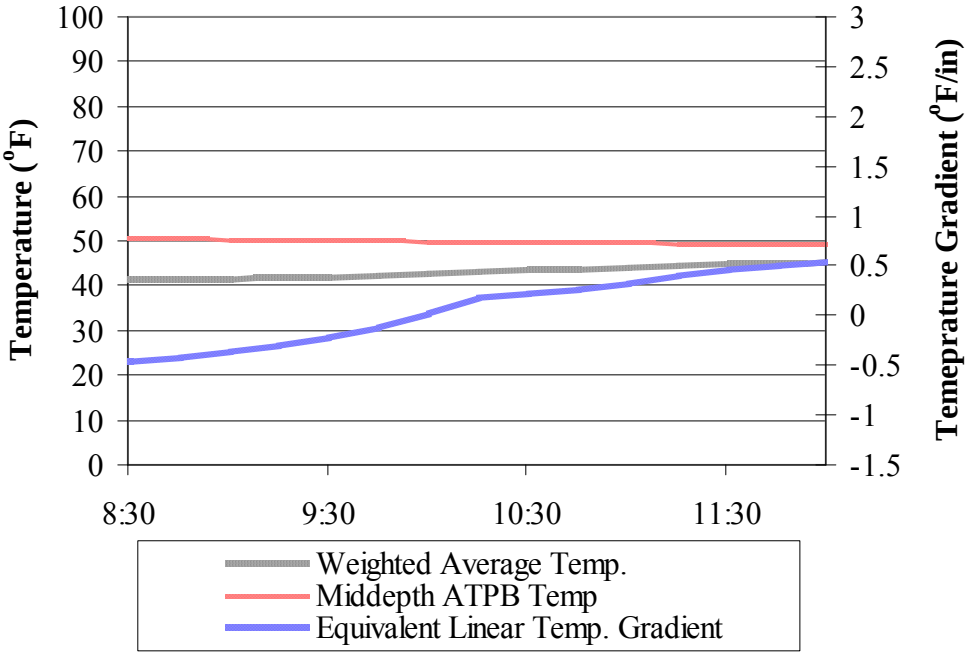

Figure 5.6. Midpanel temperature conditions during Class 6 truck testing performed in the fall of 2005.

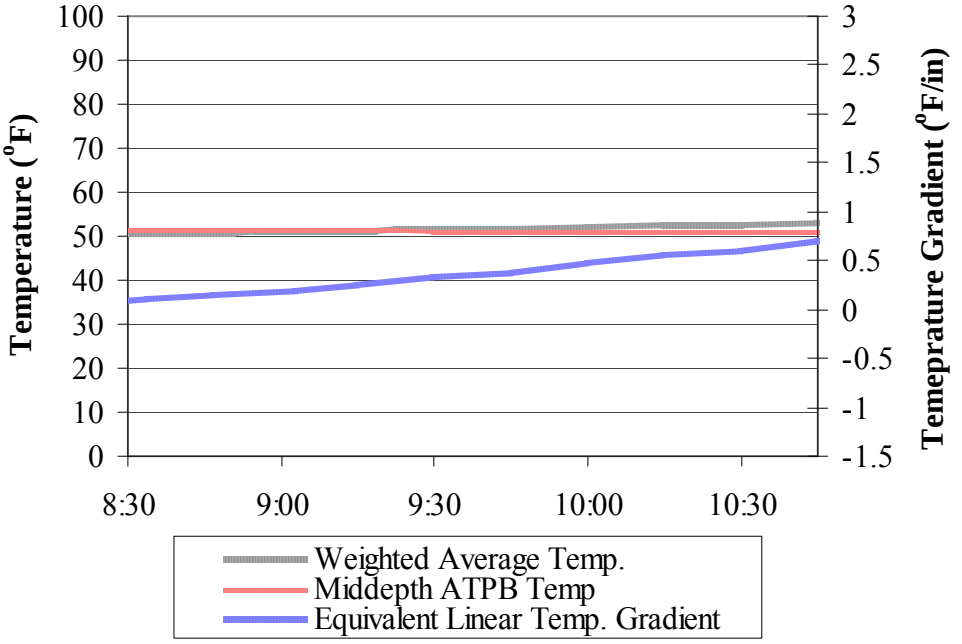

Figure 5.7. Midpanel temperature conditions during Class 10 truck testing performed in the fall of 2006.

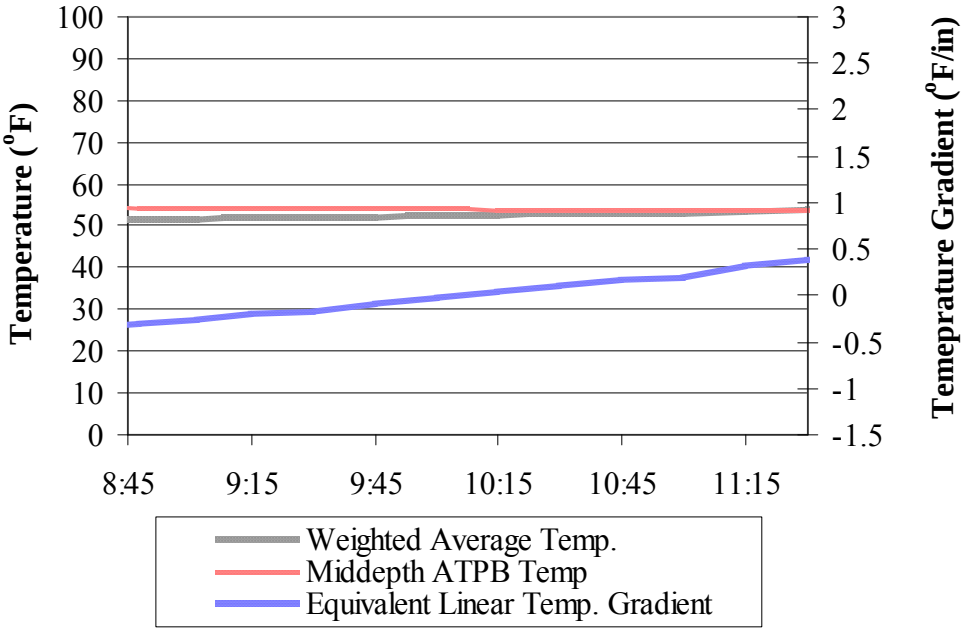

Figure 5.8. Midpanel temperature conditions during Class 6 and 7 truck testing performed in the fall of 2006.

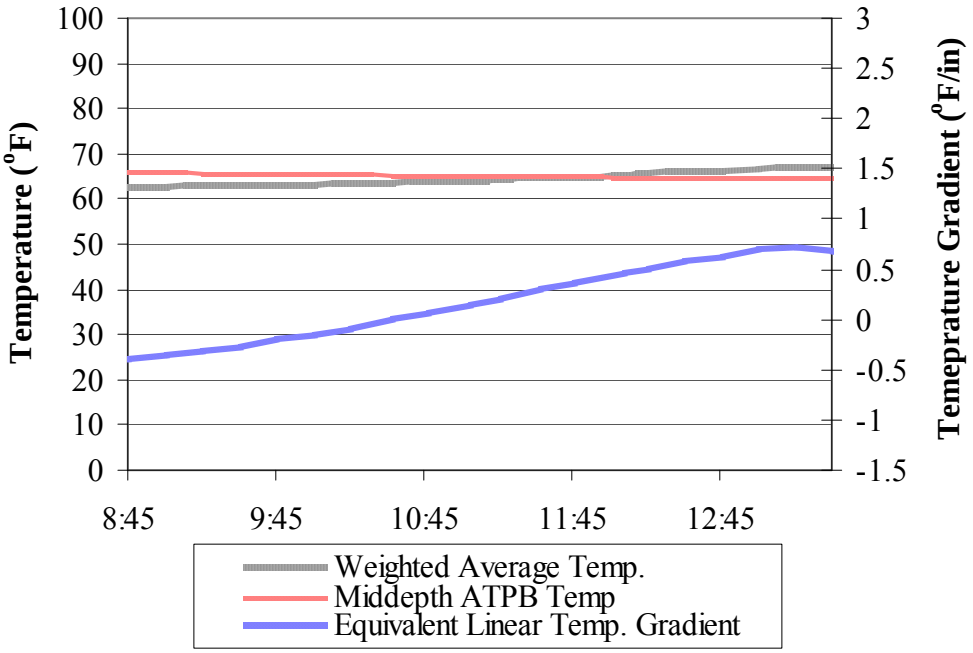

Figure 5.9. Midpanel temperature conditions during Class 6, 7, and 10 truck testing performed in the fall of 2007.

Figure 5.10 through Figure 5.15 present the temperature of the concrete and ATPB and gradient of the slab during winter testing. The weighted average temperature for winter testing ranged between 15 and 46 degrees Fahrenheit with an average of 35 degrees Fahrenheit. The equivalent linear temperature gradient varied between -0.61 and 0.86 °F/in with an average of 0.18 °F/in. The middepth temperature of the ATPB, measured during the winter periods, fluctuated between 23 and 44 degrees Fahrenheit with an average of 36 degrees Fahrenheit. Additionally, the smallest variations in temperature and gradient of the slab were experienced during the winter with an average range of 4 °F and approximately 0.7 °F/in.

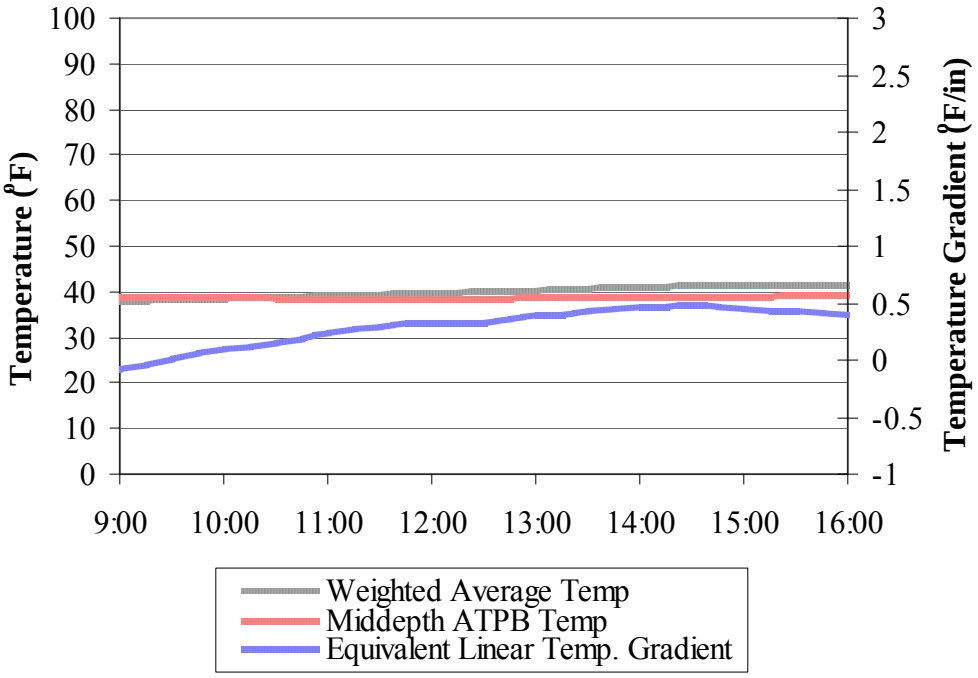

Figure 5.10. Midpanel temperature conditions during Class 10 truck testing performed in the winter of 2005.

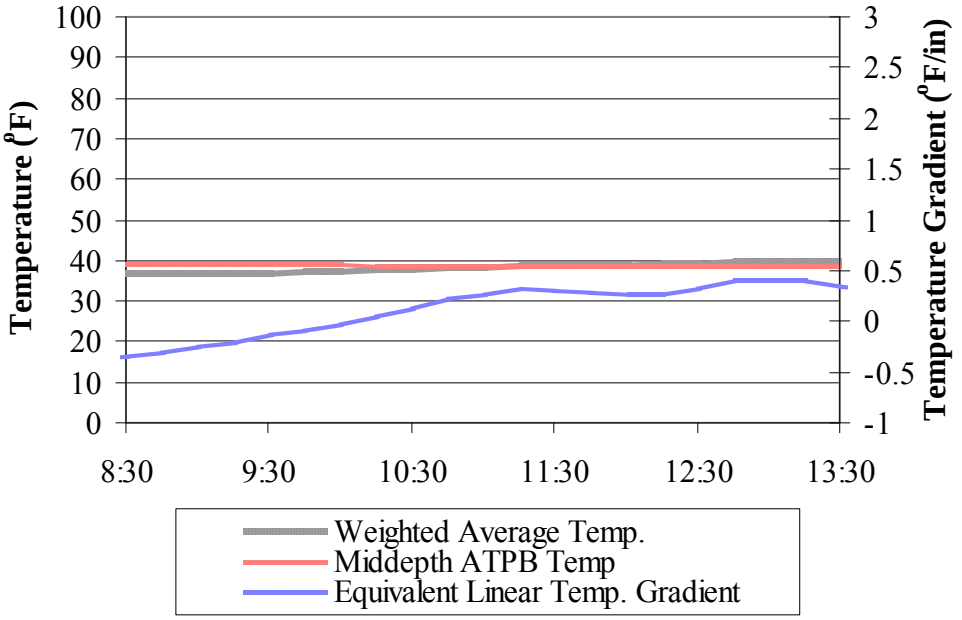

Figure 5.11. Midpanel temperature conditions during Class 6 and 7 truck testing performed in the winter of 2005.

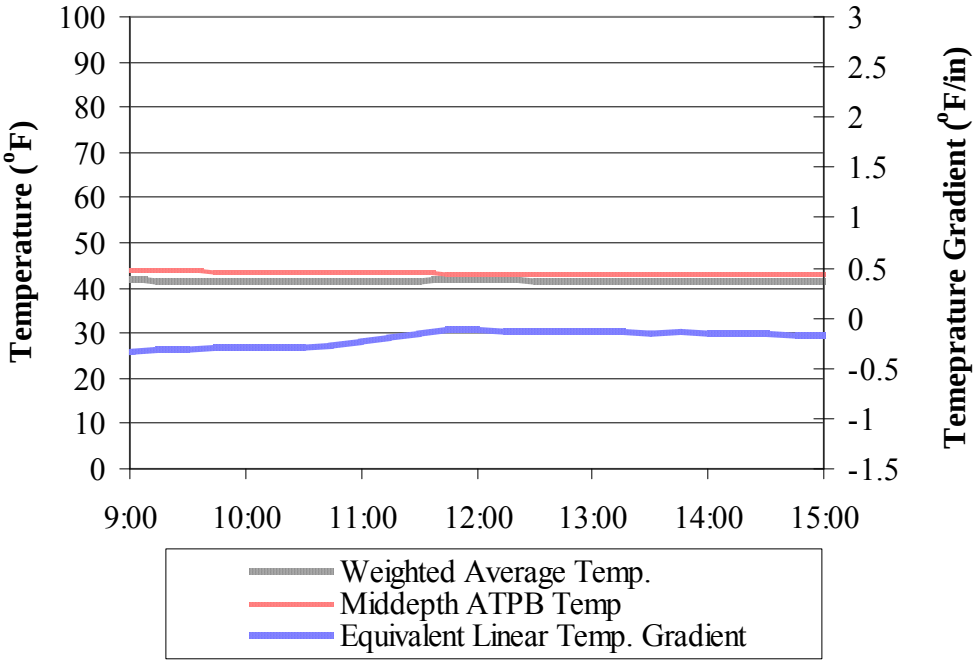

Figure 5.12. Midpanel temperature conditions during Class 10 truck testing performed in the winter of 2006.

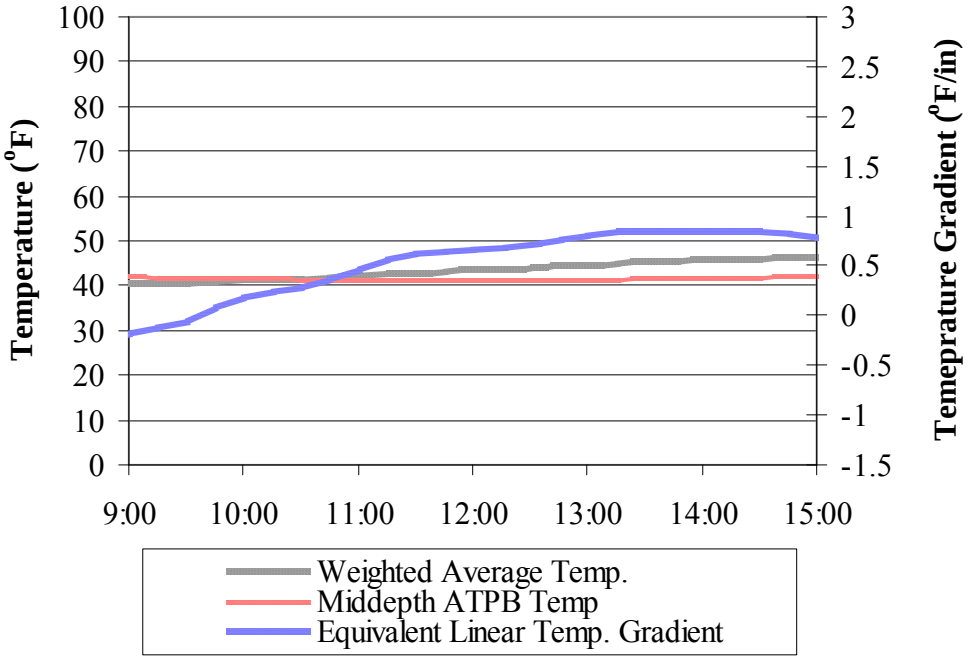

Figure 5.13. Midpanel temperature conditions during Class 6 and 7 truck testing performed in the winter of 2006.

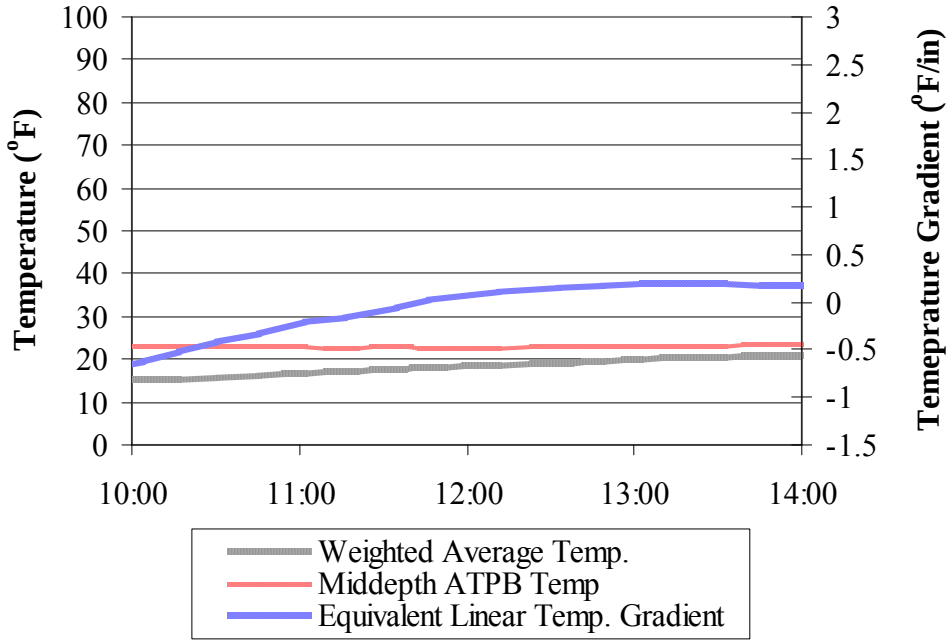

Figure 5.14. Midpanel temperature conditions during Class 10 truck testing performed in the winter of 2007.

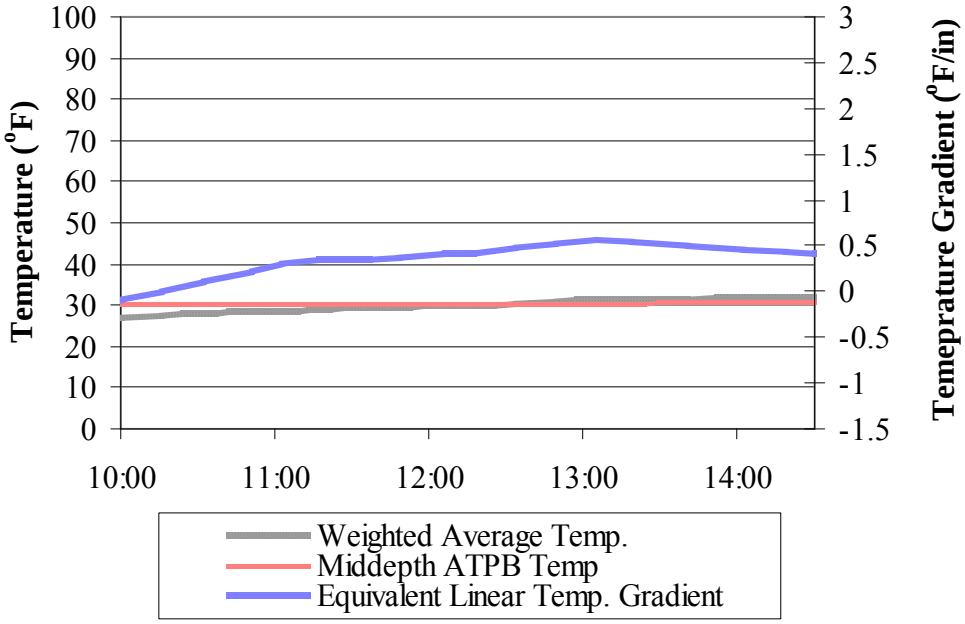

Figure 5.15. Midpanel temperature conditions during Class 6 and 7 truck testing performed in the winter of 2007.

During spring testing- the weighted average temperature in the PCC slab ranged between 47 and 72 degrees Fahrenheit with an average of 61 degrees Fahrenheit. The equivalent linear temperature gradient of the PCC slab varied between -0.52 and 2.11 °F/in during spring testing, with an average of 1.06 °F/in. The temperature at middepth of the ATPB ranged between 46 and 67 degrees Fahrenheit with an average of 55 degrees Fahrenheit. As shown in Figure 5.16 through Figure 5.21, the equivalent linear temperature gradient of the concrete varied significantly during most of the spring test period. The average difference between the peak maximum and peak minimum equivalent linear gradient for all spring test periods is 0.9 °F/in. The temperature of the ATPB also remained relatively constant.

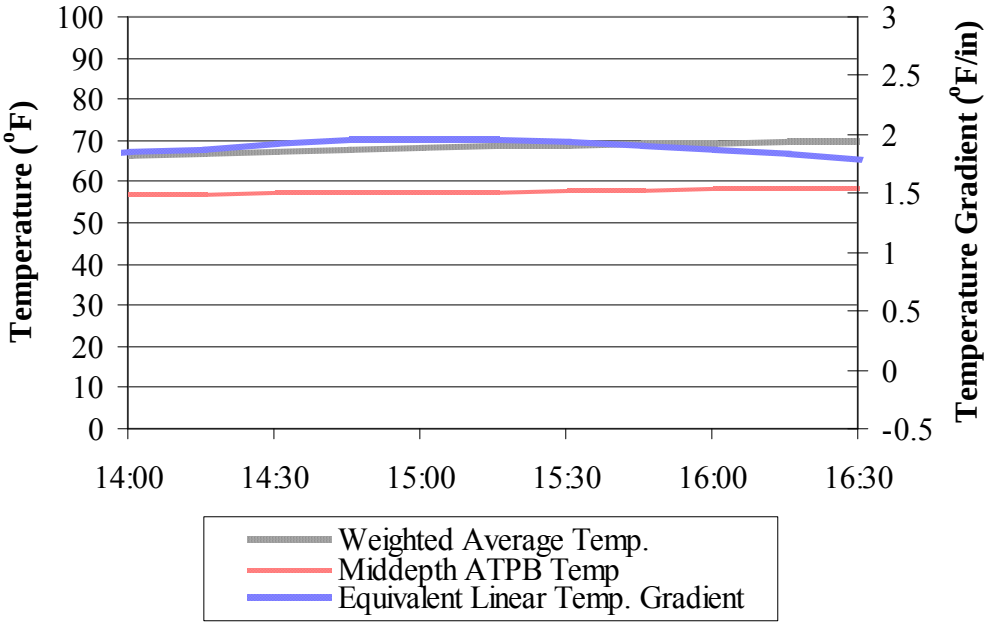

Figure 5.16. Midpanel temperature conditions during Class 10 truck testing performed in the spring of 2005.

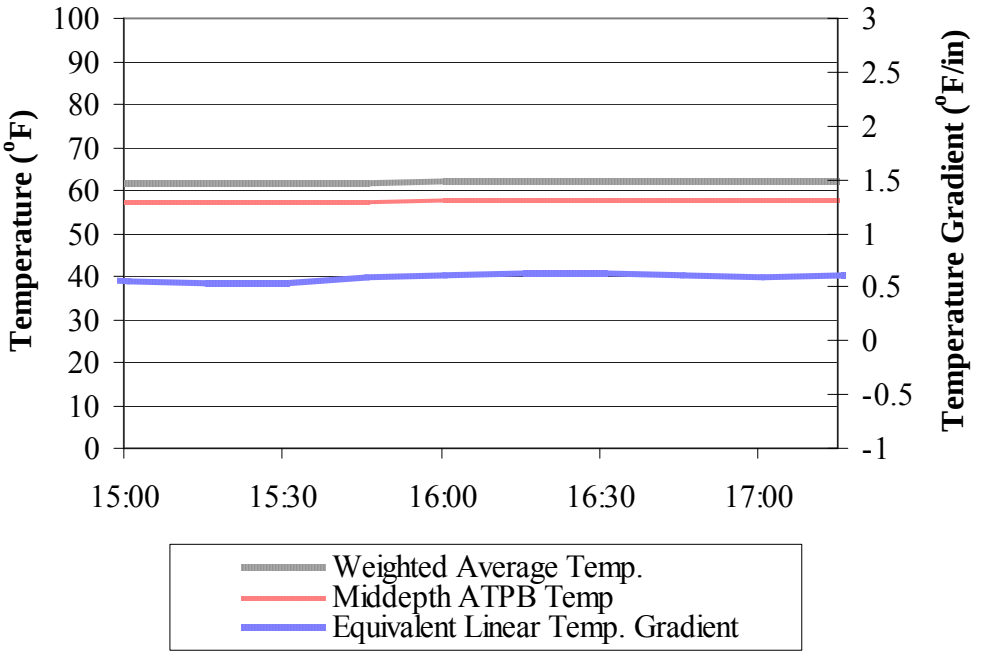

Figure 5.17. Midpanel temperature conditions during Class 6 and 7 truck testing performed in the spring of 2005.

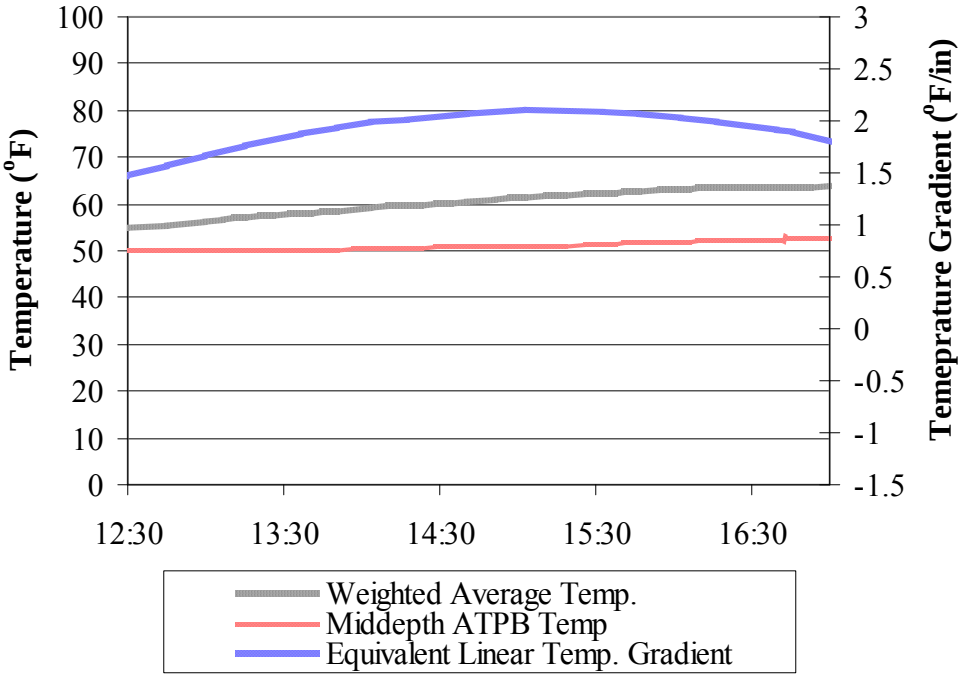

Figure 5.18. Midpanel temperature conditions during Class 10 truck testing performed in the spring of 2006.

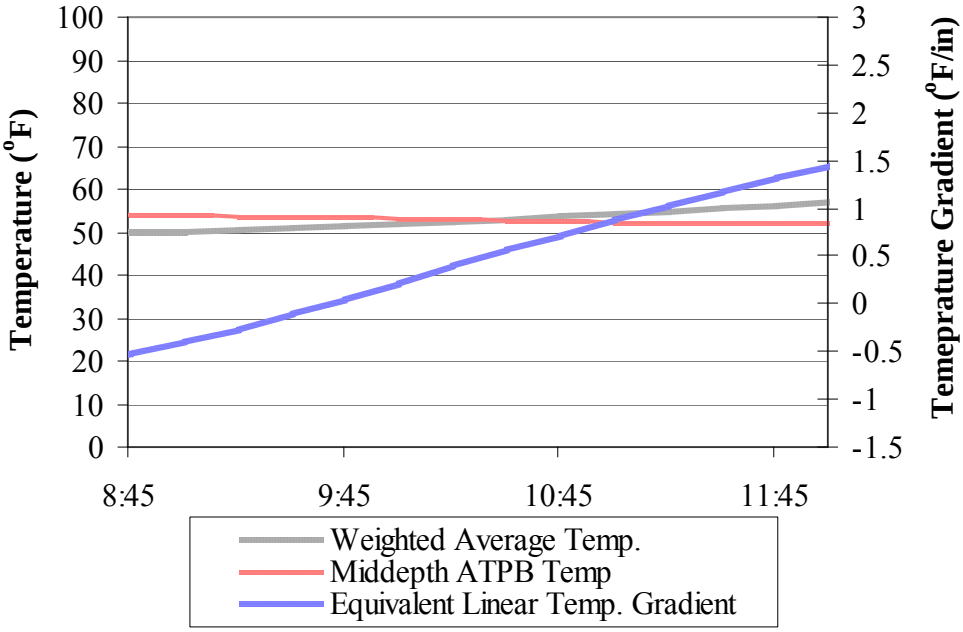

Figure 5.19. Midpanel temperature conditions during Class 6 and 7 truck testing performed in the spring of 2006.

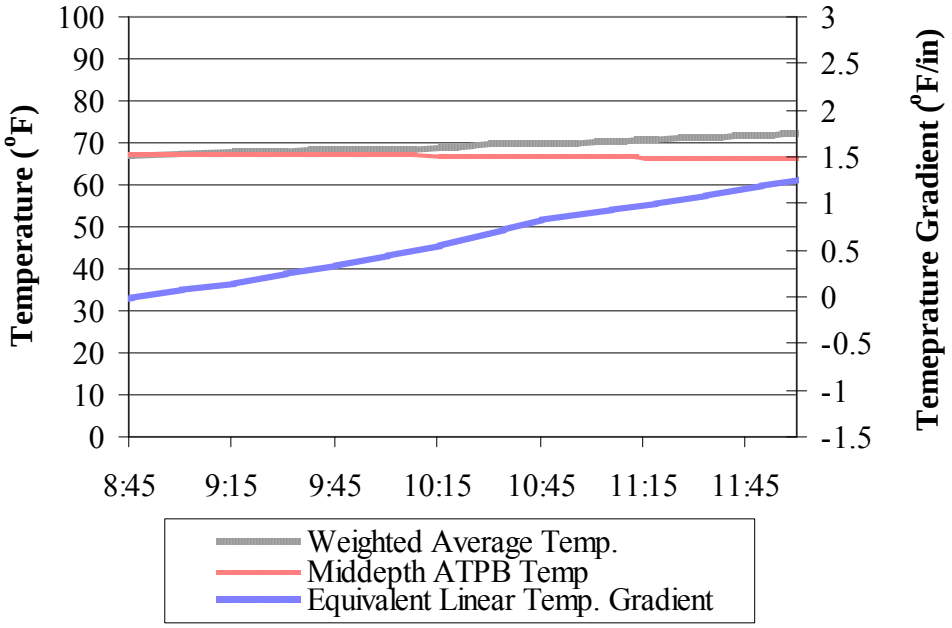

Figure 5.20. Midpanel temperature conditions during Class 10 truck testing performed in the spring of 2007.

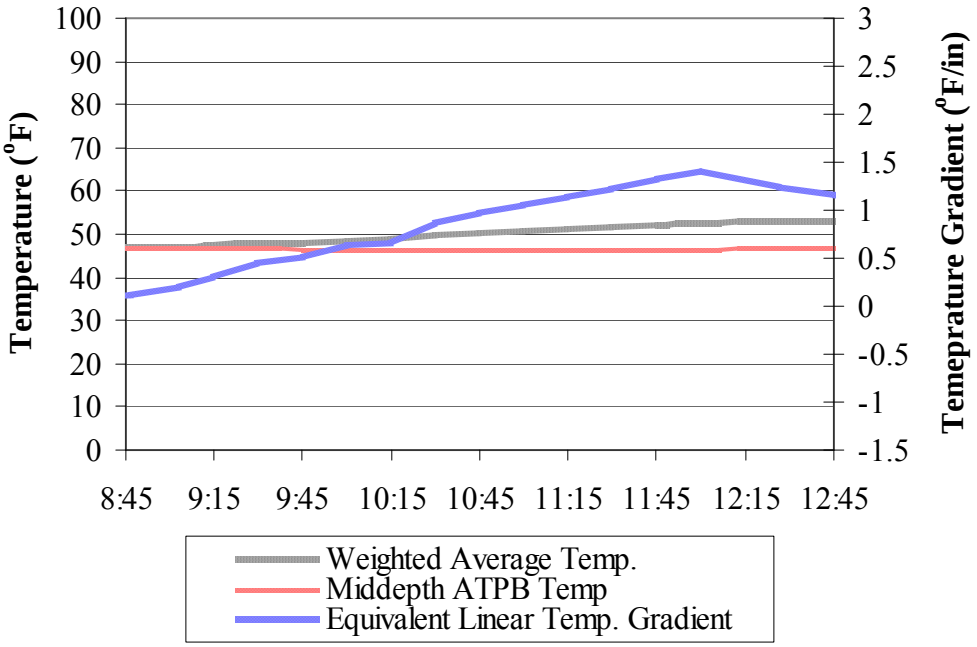

Figure 5.21. Midpanel temperature conditions during Class 6 and 7 truck testing performed in the spring of 2007.

The weighted average temperature for the summer testing periods ranged between 64 and 85 degrees Fahrenheit with an average of 76 degrees Fahrenheit. The equivalent linear temperature gradient varied between -0.62 and 1.67 °F/in with an average of 0.83 °F/in. The mid-depth temperature of the ATPB fluctuated between 65 and 81 degrees Fahrenheit with an average of 73 degrees Fahrenheit. As shown in Figure 5.22 through Figure 5.26, the weighted average temperature of the concrete varied considerably (approximately 7 °F on average) during summer testing. Both the average temperature and the temperature gradient in the slab experienced the largest fluctuation during summer. The average difference between the peak minimum and peak maximum temperature gradient for the summer test periods is 1.2°F/in.

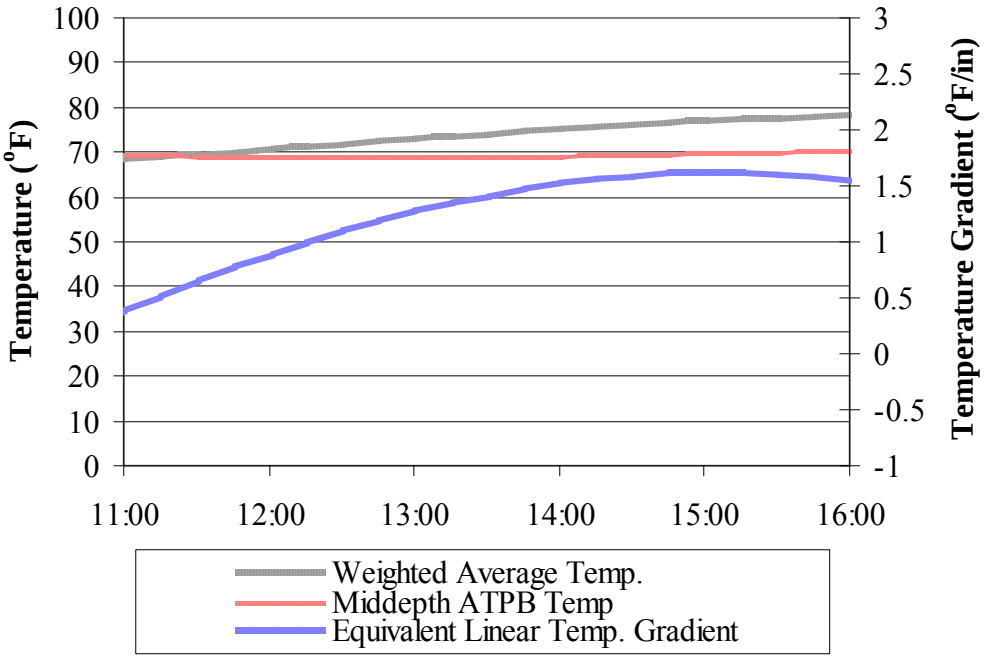

Figure 5.22. Midpanel temperature conditions during Class 10 truck testing performed in the summer of 2005.

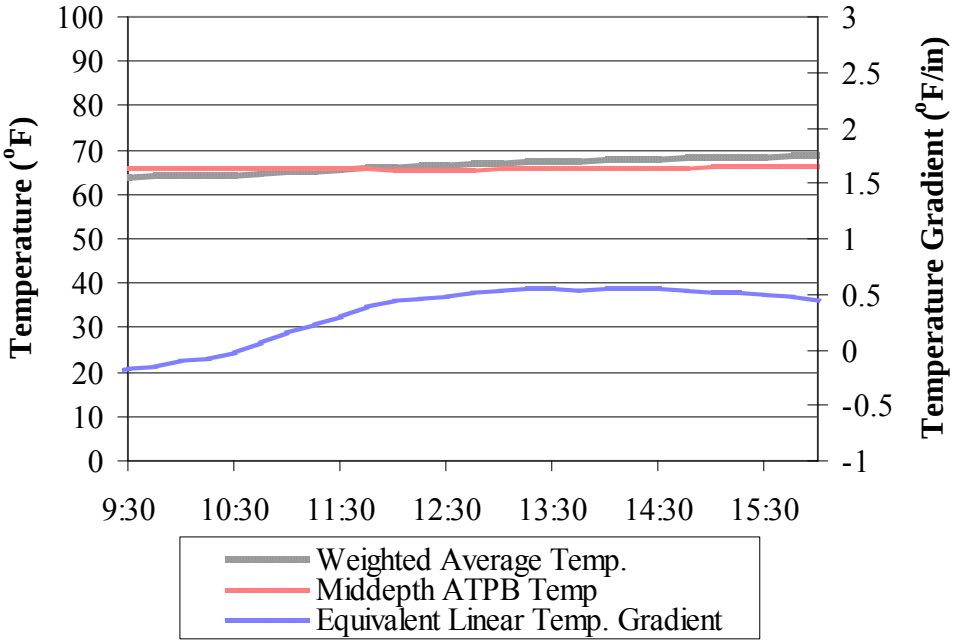

Figure 5.23. Midpanel temperature conditions during Class 6 and 7 truck testing performed in the summer of 2005.

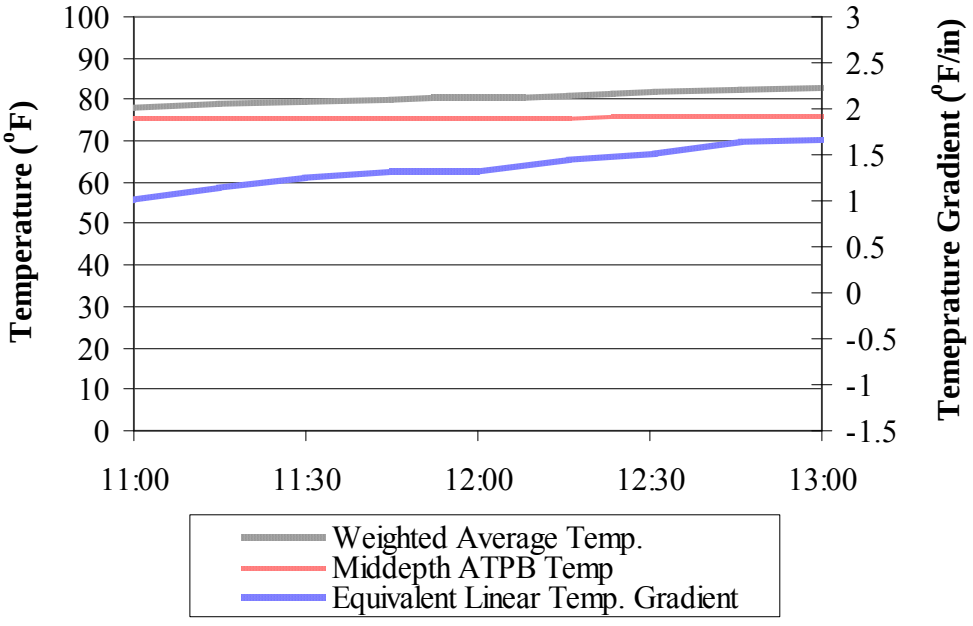

Figure 5.24. Midpanel temperature conditions during Class 10 truck testing performed in the summer of 2006.

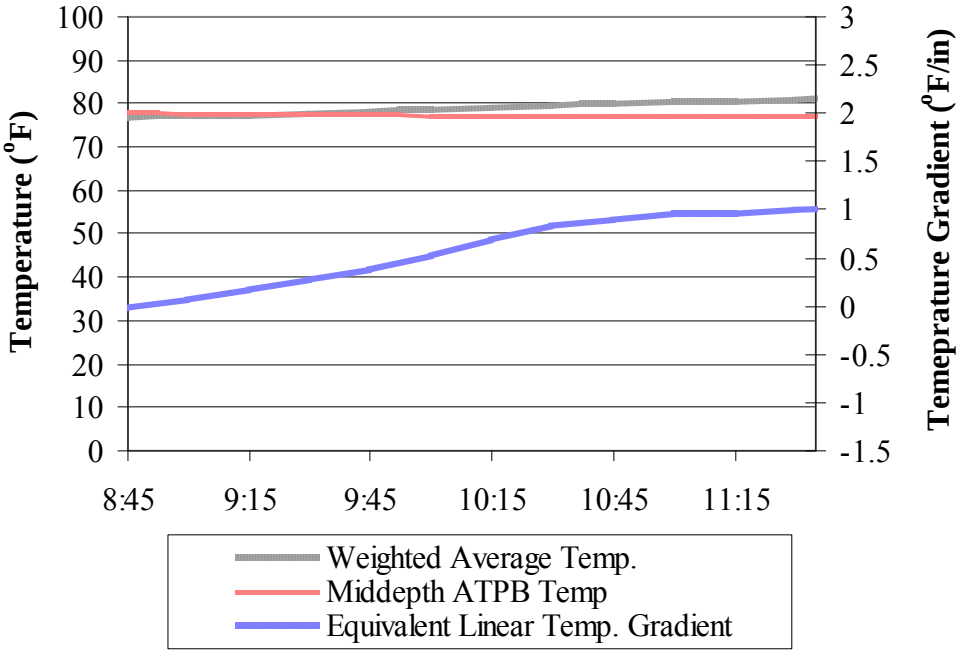

Figure 5.25. Midpanel temperature conditions during Class 6 and 7 truck testing performed in the summer of 2006.

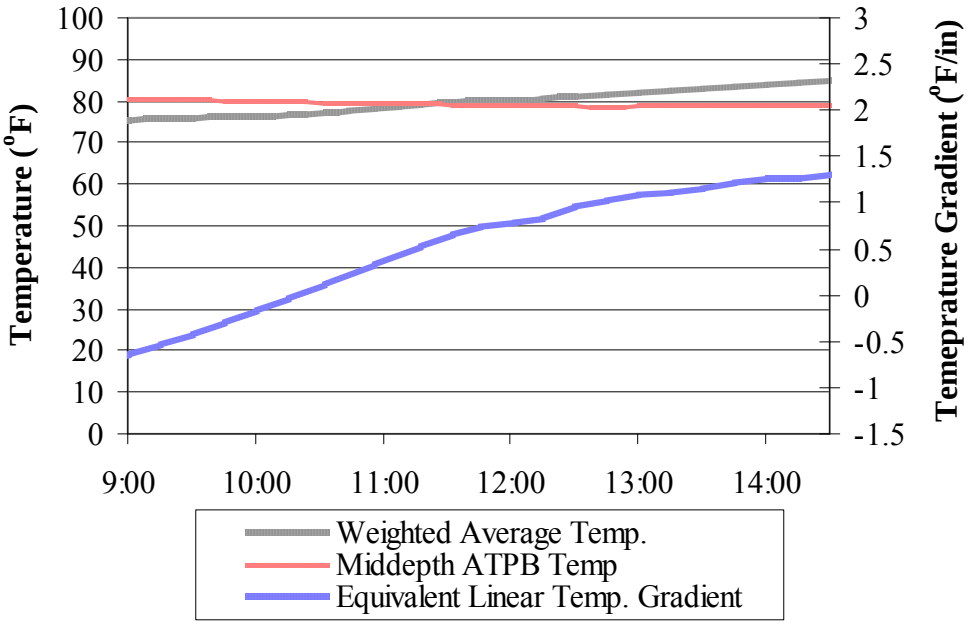

Figure 5.26. Midpanel temperature conditions during Class 6, 7, and 10 truck testing performed in the summer of 2007.

5.2.2 Concrete Moisture Distribution

Figure 5.26 and Figure 5.28, shown below, present the variation of relative humidity throughout the PCC slab at the midpanel and edge during truck testing. The largest variation in relative humidity was experienced during the winter of 2007 with a difference of 22 percent between the top and bottom of the slab. The smallest variation in relative humidity was experienced during the first test outing in the fall of 2004, with a 1 percent difference. All results are typical seasonal variations of relative humidity. Summary statistics of all test seasons are discussed below.

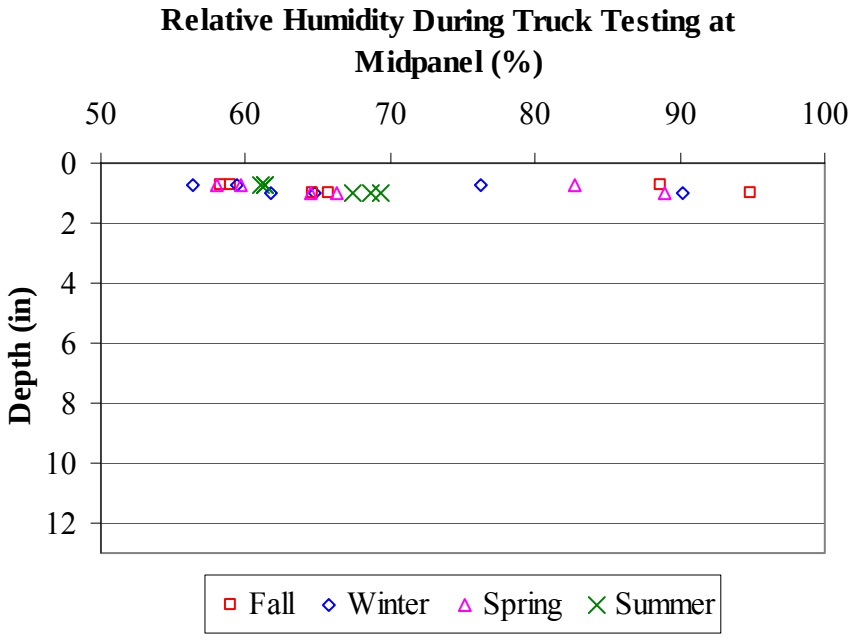

Figure 5.27. Midpanel moisture distribution throughout the PCC slab during truck testing.

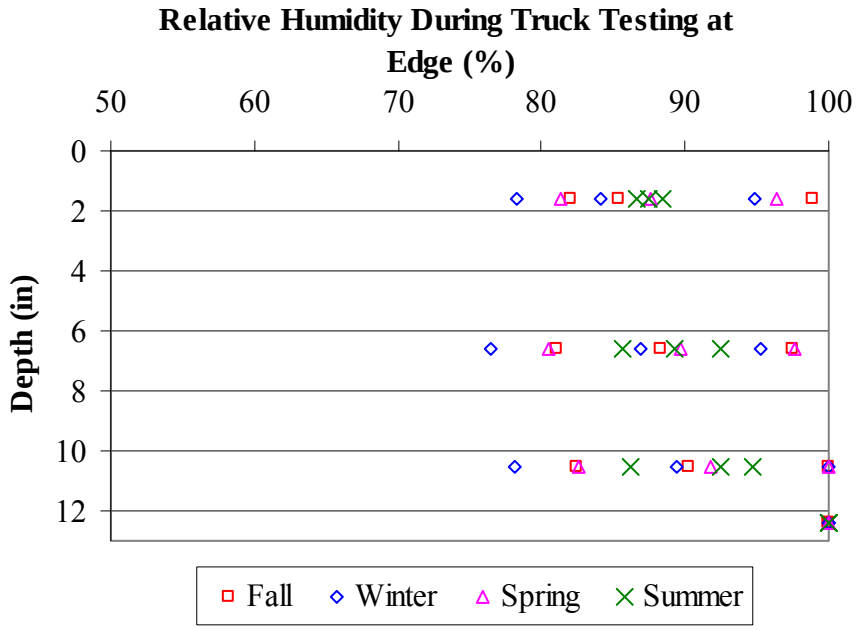

Figure 5.28. Edge moisture distribution throughout the PCC slab during Class 10 truck testing.

First the uniform change in the moisture throughout the depth of the slab will be discussed because it affects the width of the crack at the joint. The uniform moisture content throughout the depth of the slab has continually declined since the construction of the pavement. Starting out at 100 percent relative humidity immediately after construction the relative humidity throughout the slab dropped to approximately 92 percent the first year after construction, 89 percent the second year and 81 percent the third year. The crack width at the joint will continue to increase with time until the relativity humidity within the slab stabilizes.

Now, the change in moisture content throughout the depth of the slab will be discussed. The relative humidity near the slab surface fluctuates more over time compared to other depths within the slab since it is exposed to the ambient climatic conditions. The lowest measured relative humidity in the upper two inches of the slab was found during the winter at 56 percent. The largest was measured during the summer with an average of 87 percent. The fall and spring

relative humidity was between the winter and spring and typically ranged between of 81 and 88 percent. At mid-depth of the slab, the relative humidity varied between 78 and 100 percent and the bottom of the slab remained saturated. The largest variation in relative humidity throughout the depth of the slab was found during the winter with an average difference of 14 percent. The spring had the smallest variation in relative humidity with an average of 11 percent. The summer and fall relative humidity fell between these two values with an average difference in relative humidity of 12 percent for both seasons.

5.3 COMPARISON OF STRAINS MEASURED AT DIFFERENT LOCATIONS WITHIN THE SLAB

The first task was to compare strains measured at different locations within the slab. In this analysis, strains measured from the Class 10 truck for a 25,000 lb load level were used. Each strain measurement was normalized to help eliminate variations in strain due to variations between the target load level and the actual load applied for each of the test dates. Both the restrained (Cell 1) and unrestrained (Cell 2) test sections were analyzed. Strain measurements were measured seasonally throughout the first three years after construction and averaged to determine the strain at each location.

The strain locations evaluated were in the corner; in the wheelpath adjacent to the transverse joint; and at midpanel, adjacent to the lane/shoulder longitudinal joint. The sensors used for the corner location are CE01-02 and CE35-36, edge sensors are CE17-18 and CE43-44, and wheelpath sensors are CE05-06 and CE31-32. See figure 3.15. The corner and edge strains represent the strains measured for the truck pass that traverses directly along the edge of the

lane/shoulder joint. Strains measured in the wheelpath were generated when the truck ran along the wheelpath (approximately two feet from the edge of the pavement). These passes were used for the analysis because the truck travels directly over the corner and edge strain sensors when it is traveling along the edge of the lane/shoulder joint so maximum strains are being measured.

5.3.1 Strain in the Restrained Slabs

Figure 5.29 and Figure 5.30 display the variation in strain at different locations within the restrained slabs at the top and bottom of the slab. As Figure 5.29 shows, there is considerable variation in the strain measured in Slab A compared to that in Slab B at the top of the restrained cell. This variation in strain between the slabs can be attributed to variations in the depth of the top sensor from the top of the pavement. For example, the average strain measured at the wheelpath, adjacent to the transverse joint, is -14 microstrain in Slab A and -11 microstrain in Slab B while the sensor in Slab A is 1.28 inches below the surface of the pavement and is 0.68 inches for Slab B. However, strain in the corner varies approximately 1 microstrain between the two slabs, but the variation in sensor depth is significantly less with a difference of 0.08 inches.

As Figure 5.30 shows, there is significantly less variation between strains measured in the two slabs at the bottom. This is because the bottom strain sensors were grouted directly to the top of the ATPB limiting the variation in the depth of the sensors between the two slabs. Therefore, strains measured at the bottom of the slab will be used to analyze strains at various locations within the slab.

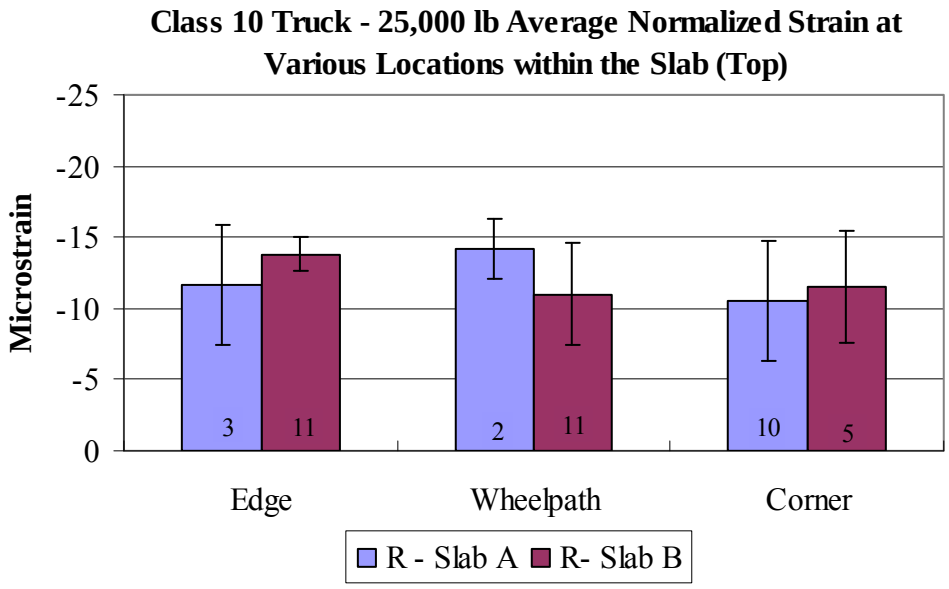

Figure 5.29. Average strains measured at various locations at the top of the restrained slabs during the first three years after construction.

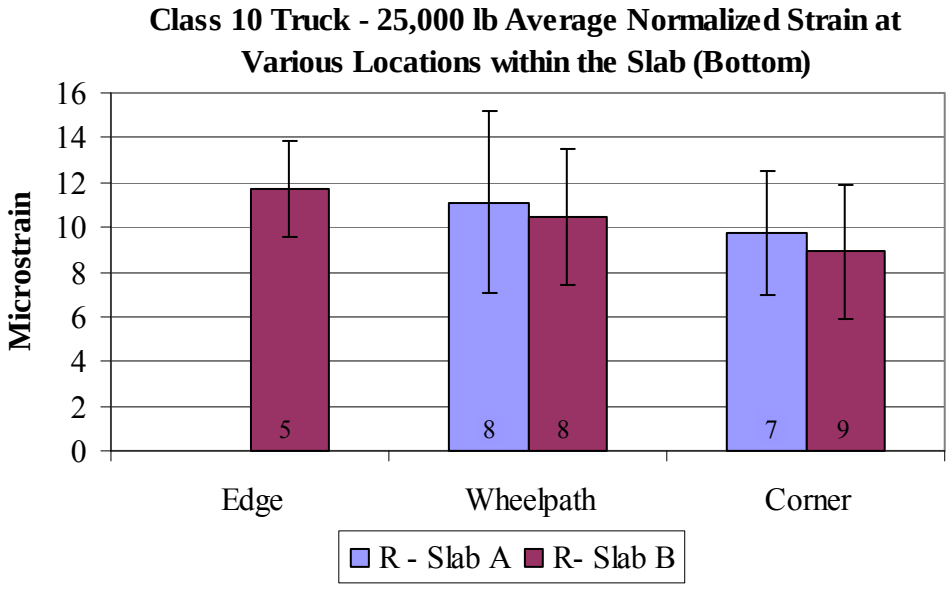

Figure 5.30. Average strains measured at various locations at the bottom of the slabs during the first three years after construction.

Table 5.3. Variation in the depth of the dynamic sensors of the restrained cell.

Restrained Slabs (Cell 1)				
Sensor	**Slab**	**Location**	**Depth of Sensor (in)**	**Slab Thickness(in)**
CE01	A	Corner	0.86	14.26
CE02	A	Corner	13.99	
CE05	A	Wheelpath	1.28	14.68
CE06	A	Wheelpath	14.17	
CE17	A	Edge	0.88	14.65
CE18	A	Edge	14.37	
CE31	B	Wheelpath	0.68	14.41
CE32	B	Wheelpath	14.08	
CE35	B	Corner	0.94	14.53
CE36	B	Corner	14.12	
CE43	B	Edge	1.09	14.47
CE44	B	Edge	14.02	

The average strain at the edge for the restrained slab B is 12 microstrain. In the corner and wheelpath locations the measured strain is 9 and 10 microstrain respectively. The average strain measured in the restrained slabs along the edge of the lane/shoulder joints is approximately 12 percent larger than strain measured in the wheelpath along the transverse joints and 31 percent larger than strain measured in the corners. There are several possible reasons why the edge strains are larger in the restrained slabs. First, the edge location was measured at the midpanel of the slab and because of the restraint provided by the dowel and tie-bars and daily curling and warping of the slabs, stress/strain at this location is higher. Also, because of the proximity of the wheelpath and corner locations to the transverse joint and presence of a positive built-in temperature gradient strains in these locations are reduced due to increased support and restraint.

The standard deviation for the measured strains was larger in areas that had the greatest variability in the edge support conditions. For example the corner gages, which had a standard deviation of 3 microstrain, are adjacent to two edges and the support provided by these edges varies seasonally as a function of the width of the transverse and longitudinal joints. The change in the transverse joint width also affects the edge support conditions for the strains measured adjacent to the transverse joint. The strains measured along the edge are affected by the width of the lane/shoulder joint. The width of the lane/shoulder joint varies less than the width of the transverse joint which resulted in a higher standard deviation in the strains measured along the wheelpath adjacent to the transverse joint compared to that measured at midslab adjacent to the lane/shoulder joint. The strains measured in the wheelpath are also in close proximity to the lane/shoulder joint so the change in support conditions at the lane/shoulder joint also influences the strains measured in the wheelpath.

In an analysis of the response of a pavement to wheel loads Guo and Pecht determined that strains, measured in the slab interior, showed the least variability due to the distance from the joints (Guo and Pecht 2006). Unfortunately, strain data in the interior of the slab is not available due to malfunctions with the strain gages. However, a similar trend is expected from the results of the variability in strain measured along the longitudinal and transverse joints of the slab.

5.3.2 Strain in the Unrestrained Slabs

Like the restrained slabs, the unrestrained slabs experienced considerable variation in the location of the top sensor beneath the slab (see Table 5.4). Therefore, strains at the bottom of the slab were used to analyze the variation in strain at various locations within the slab.

Table 5.4. Variation in the depth of the dynamic sensors in the unrestrained cell.

Unrestrained Slabs (Cell 2)				
Sensor	**Slab**	**Location**	**Depth of Sensor (in)**	**Slab Thickness(in)**
CE01	A	Corner	1.06	
CE02	A	Corner	11.43	11.76
CE05	A	Wheelpath	0.87	
CE06	A	Wheelpath	11.52	11.93
CE17	A	Edge	0.80	
CE18	A	Edge	11.25	11.69
CE31	B	Wheelpath	1.17	
CE32	B	Wheelpath	11.94	12.14
CE35	B	Corner	1.37	
CE36	B	Corner	11.49	12.14
CE43	B	Edge	0.84	
CE44	B	Edge	11.56	11.96

As Figure 5.31 shows, the unrestrained slabs also have the largest average strain at the edge location. The average strain measured at the edge location of Slab B is approximately 18 microstrain, in the corner and wheelpath locations the strain is 15 microstrain. The strain at the edge location is approximately 20 percent larger than strains in the corner and along the wheelpath.

Although strains observed in the corner location were the smallest, the deviation of these strains was the largest in the unrestrained slabs with an average of 4 standard deviations. This variation can be attributed to the affect changing support conditions and daily temperature and moisture fluctuations have on strains measured in the corner of the slab.

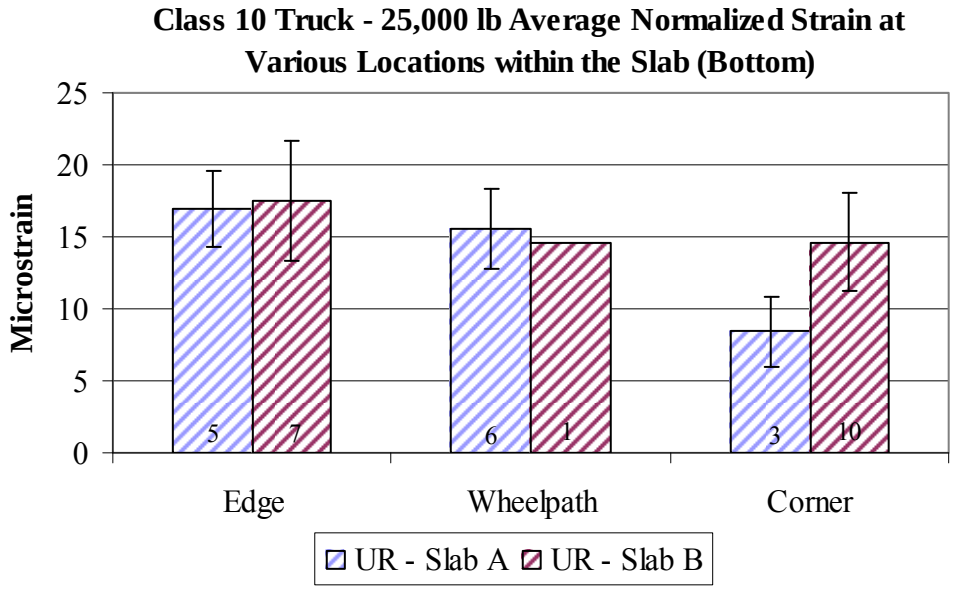

Figure 5.31. Average strains measured at various locations at the bottom of the slabs during the first three years after construction.

5.4 EFFECT OF AXLE CONFIGURATION ON MEASURED STRAIN

A closer examination of the strains measured at the edge location was performed to analyze the response of the pavement to various axle configurations. The average strain measured for the 25,000-lb load for each truck type (Class 6, 7, and 10) is reported in Figure 5.32 through Figure 5.34. All loads were normalized to a 25,000-lb load. Additionally, the first axle (standard axle) of each truck was not included in the analysis because the actual load applied was typically much less (approximately 10,000 lbs) than the target load. This load difference is too large for applying a linear interpolation between load and strain.

As Figure 5.32 shows, the critical axle for the Class 6 truck is axle three (second axle of the tandem) in both the restrained and unrestrained cells. The average strain for the third axle of the Class 6 truck was 11 microstrain for the restrained cell and 16 microstrain for the

unrestrained cell. Strain measured for the third axle was approximately 15 percent larger than the second axle in the restrained slabs and 13 percent larger in the unrestrained when averaged over the three year period. The variation in the strain measured for each of the two axles of the tandem axle was approximately equal with 2 microstrain in the restrained slabs and 3 microstrain in the unrestrained slabs. It was expected that strains in the unrestrained slabs would be larger and have more variation then the restrained slabs because they are free to move.

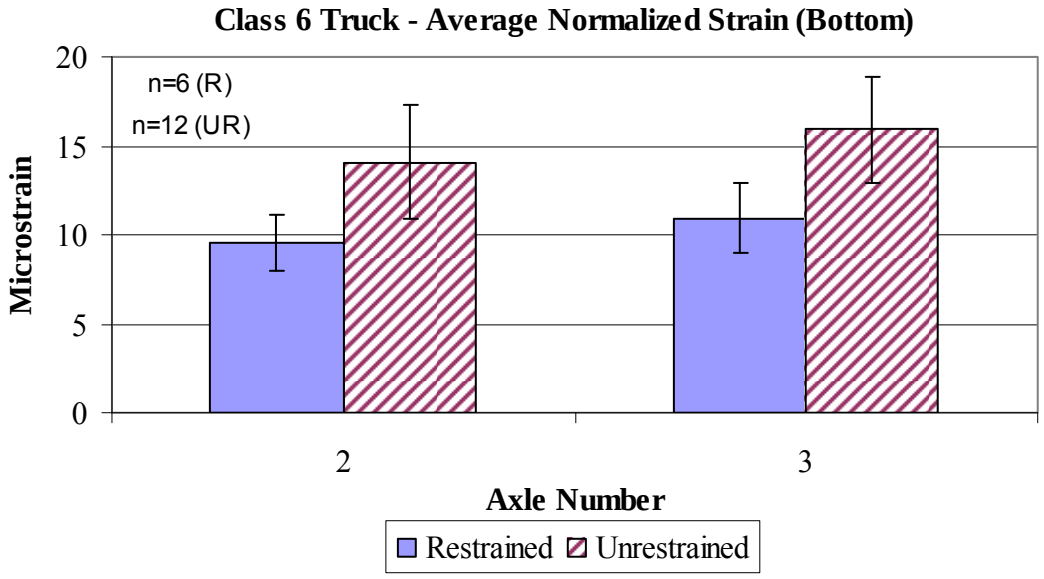

Figure 5.32. Average normalized strains measured along the edge of the restrained and unrestrained slabs for the Class 6 truck with 25,000 lb axle loads.

The fourth axle (third axle of tridem) was found to be the critical axle for the Class 7 truck, as shown in Figure 5.33. The average strain for the fourth axle of the Class 7 truck was 10 microstrain for the restrained cell and 16 microstrain for the unrestrained cell. In the unrestrained slabs, the fourth axle is approximately 26 percent larger than the second and 14 percent larger than the third. The same trend was also found in the restrained slabs with the

fourth axle having on average a 14 percent larger strain than the remaining axles. A similar trend to the Class 6 truck was experienced with strains in unrestrained slabs being larger and having more variation then the restrained slabs.

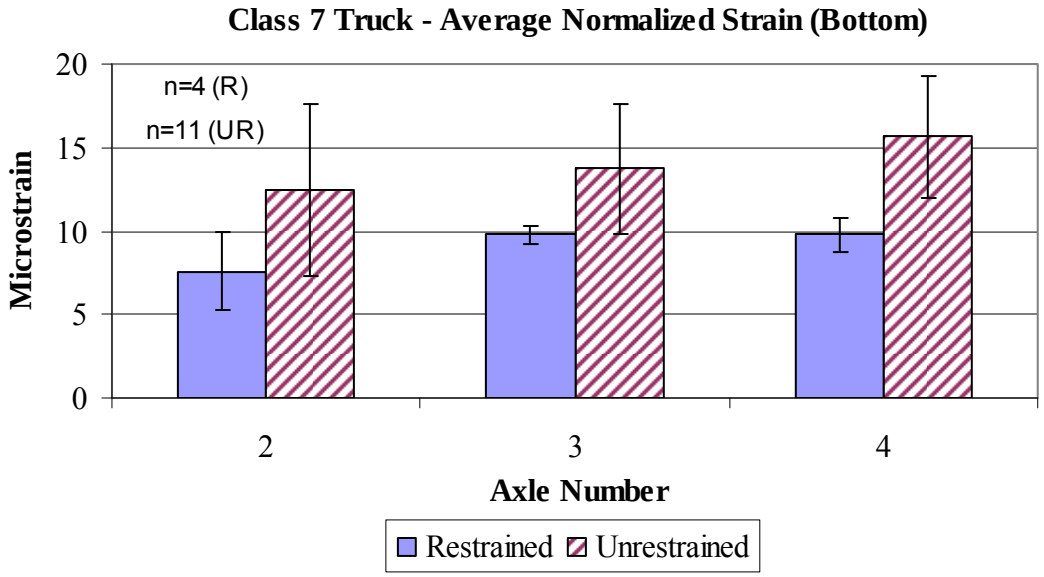

Figure 5.33. Average normalized strains measured along the edge of the restrained and unrestrained slabs for the Class 7 truck with 25,000 lb axle loads.

As Figure 5.34 shows, the third axle (second axle of tandem) exhibited the largest strain in the restrained and unrestrained slabs for the Class 10 truck. The average strain for the third axle of the Class 10 truck was 12 microstrain for the restrained cell and 18 microstrain for the unrestrained cell. In the restrained slabs, the third axle is approximately 34 percent larger than the second and 27 percent larger than the fourth, 7 percent larger than the fifth, and 22 percent than the sixth axle. The same trend was also found in the unrestrained slabs with the fourth axle having an average 18 percent larger strain than the remaining axles. Strains measured when the

Class 10 truck traversed the edge of the slab were larger and had more variation in the unrestrained slabs, as would be expected.

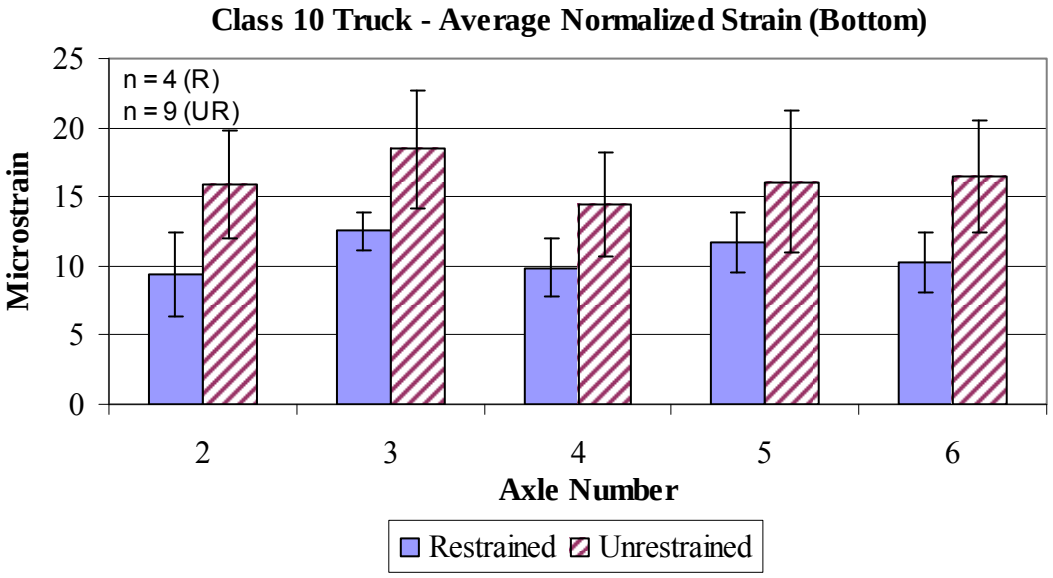

Figure 5.34. Average normalized strains measured along the edge of the restrained and unrestrained slabs for the Class 10 truck with 25,000 lb axle loads.

The Class 6 and Class 10 trucks both have a tandem axle therefore an analysis was performed to investigate the measured strain for the tandem axle of the different truck classifications. As Figure 5.35 shows, the strain measured in the first axle for the tandem was approximately the same in the restrained slabs but in the unrestrained slabs the difference between the Class 6 and 10 trucks was approximately 1.6 microstrain. The larger difference in the unrestrained slabs may be attributed to wheel wander as the different trucks traversed the sensor or differences in the temperature and gradient present at the time of testing between the trucks. The affect of slab temperature and gradient affects the unrestrained slabs more because there is no restraint provided by dowel and tie-bars.

Strain measured for the second axle of the tandem was larger for the Class 10 truck in both the restrained and unrestrained slabs. The difference in axle spacing between the trucks contributes to the difference between strains measured in the Class 6 and 10 trucks. The Class 6 truck axle spacing is 54 inches while the Class 10 truck spacing is less at 50 inches. Therefore, strains measured for the Class 10 truck are larger in the second axle since a higher percentage of the load contributed by the adjacent axle is distributed to the location of the gage.

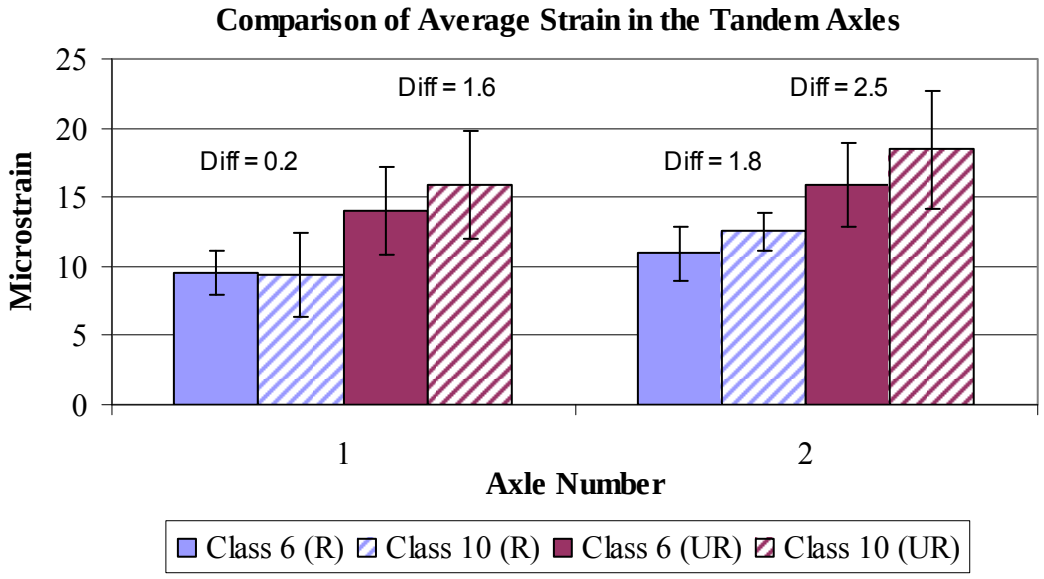

Figure 5.35. Average normalized strains measured along the edge of the restrained and unrestrained slabs for the tandem axle of the Class 6 and 10 trucks.

As Figure 5.36 displays, similar trends were experienced between the tridem axle of the Class 7 and 10 trucks. The unrestrained slabs experience a larger difference in measured strains between the different truck classifications. Additionally, differences between the measured strains of each axle can be attributed to differences in the spacing of the axles between the Class 7 and 10 trucks.

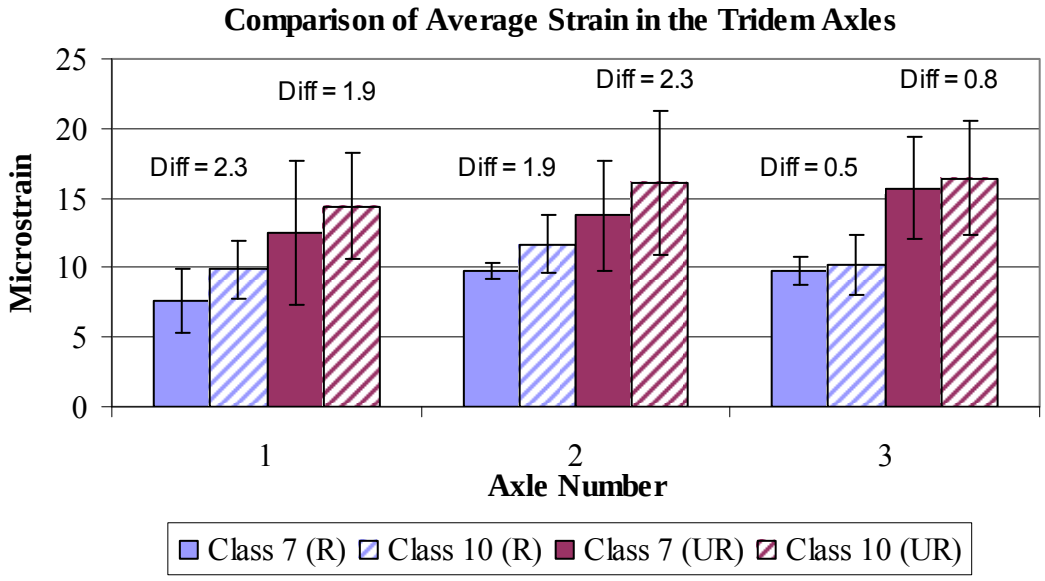

Figure 5.36. Average normalized strains measured along the edge of the restrained and unrestrained slabs for the tridem axle of the Class 7 and 10 trucks.

5.5 EFFECT OF AXLE LOAD MAGNITUDE ON MEASURED STRAIN

This section examines the effects of the magnitude of the load on the measured strains. Figure 5.37 through Figure 5.39 display the average strain normalized to the target load level for each truck class (Class 6, 7 and 10). The critical axle determined in the previous section (reference section 5.4) was used for each truck type.

As observed in Figure 5.37, there is a significant difference in strain generated at the three different load levels (15,000, 20,000 and 25,000 lb) for the Class 6 truck in both the restrained and unrestrained cells. The 15,000-lb load level generated an average strain of 7 microstrain; the 20,000-lb load produced an average of 9 microstrain and the 25,000-lb load measured 12 microstrain in the restrained cell. As expected, the unrestrained cell experiences higher strains at each load level. The 15,000 lb-load has an average strain of 10 microstrain, the

20,000-lb load has an average of 13 microstrain and average strain for the 25,000-lb load is 16 microstrain.

There is an average difference of 4 microstrain between the minimum and maximum load level and a 2.5 microstrain difference between the 20,000 and 25,000-lb load levels. The strain observed from the 25,000-lb load level is 64 percent greater than strain observed by the 15,000-lb load level and 23 percent greater than strain observed by the 20,000-lb load. Therefore, it can be concluded that strain induced by different loads increases with increasing load in a nonlinear manner.

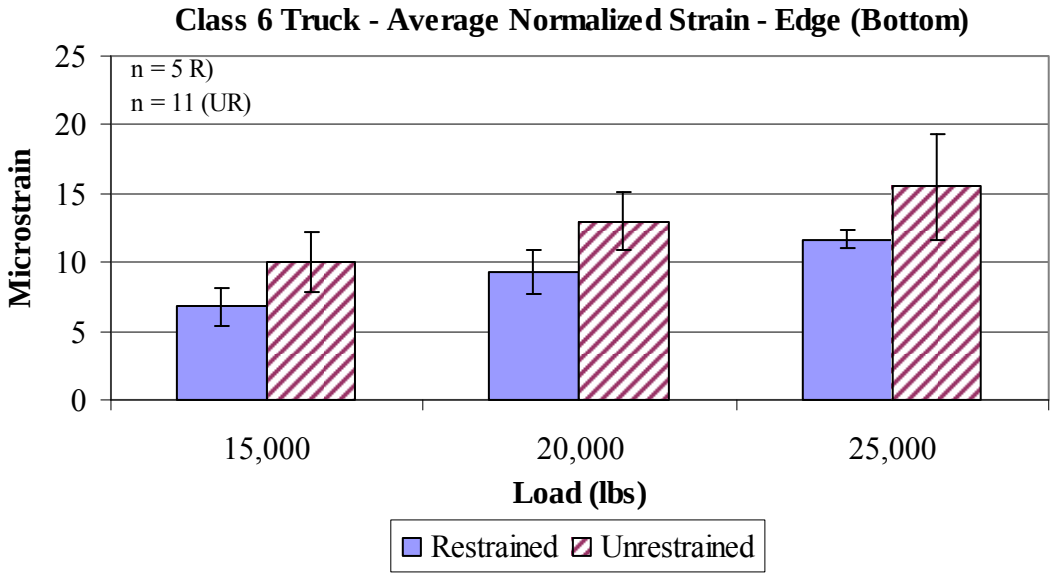

Figure 5.37. Strains measured along the edge for the critical axle of the Class 6 truck for various load levels.

Like the Class 6 truck, a similar trend of increasing strain with increasing load magnitude was observed in the Class 7 and 10 trucks (Figure 5.38 and Figure 5.39). As Figure 5.38 shows, the strain increases an average of 2 microstrain between the 15,000-lb and 20,000-lb load levels and increases 2.5 microstrain between the 20,000-lb and 25,000-lb load levels. The results are

very similar in the Class 10 truck, but it appears as though the increase is larger, this is due to the larger load increase between the load levels.

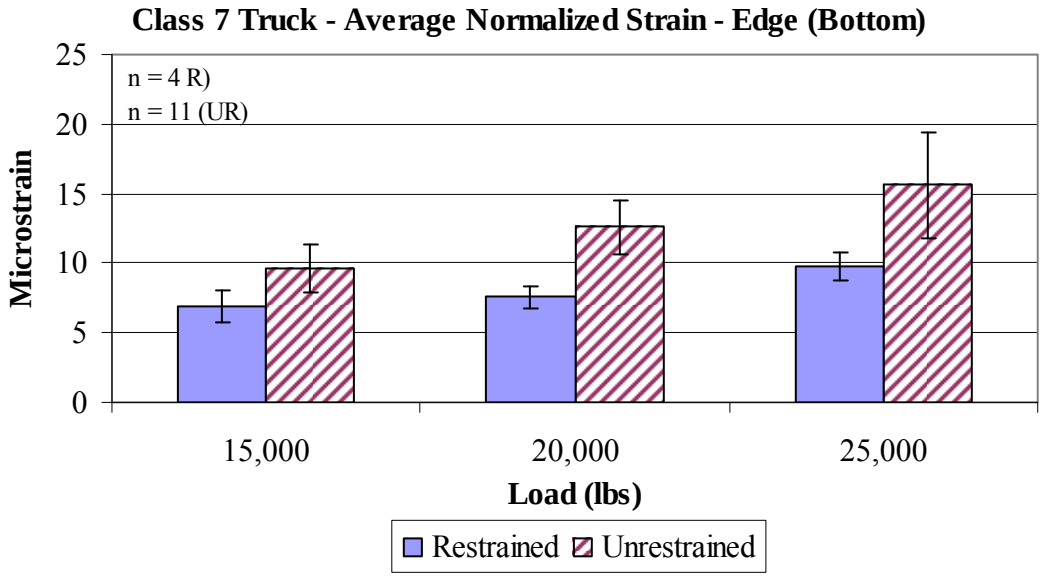

Figure 5.38. Strains measured along the edge for the critical axle of the Class 7 for various load levels.

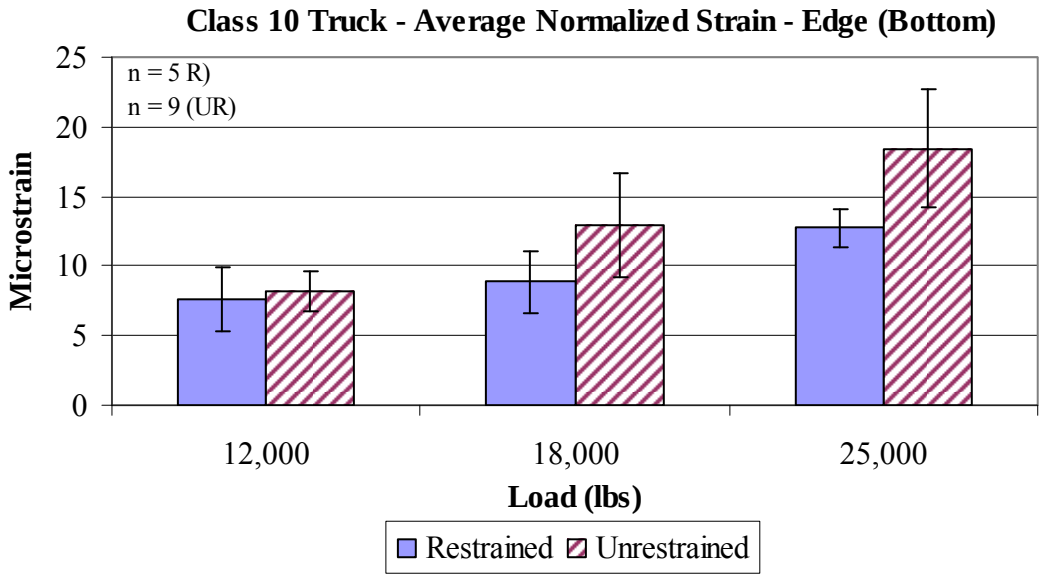

Figure 5.39. Strains measured along the edge in the unrestrained slabs for the critical axle of the Class 10 for various load levels.

A regression analysis was performed to see if a correlation existed between load magnitudes and measured strain. As Figure 5.40 shows, this relationship does exist in both the restrained and unrestrained cells. The restrained slab shows good correlation to an exponential fit with a coefficient of 0.72. The unrestrained slabs show a strong correlation with the power function with a correlation coefficient of 0.95.

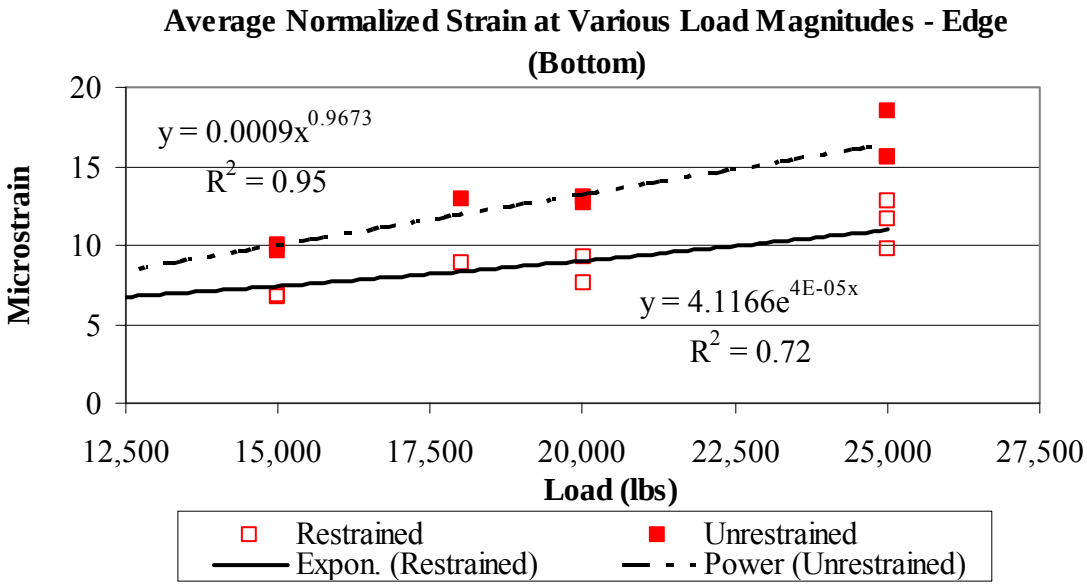

Figure 5.40. Strains measured along the edge of the slabs for the critical axle of all the truck classes and load levels.

5.6 DYANMIC STRAINS MEASURED AT THE TOP AND BOTTOM OF THE SLAB

A closer examination of the critical axle strains measured for each truck classification at the edge location was performed to compare strains measured at the top of the slab versus those measured at the bottom. The strains were normalized for a 25,000 lb load level. The strains were also extrapolated to the exact top and bottom of the slab using linear interpolation since the distance

of the upper sensor to the slab surface was approximately 1 inch. The survey data was used to define the exact distance of each sensor from the pavement surface. The following subsections provide the analysis for the restrained and unrestrained slabs respectively.

5.6.1 Strain at the Top and Bottom of the Restrained Slabs

Figure 5.41 displays the average strain at the top and bottom of the restrained slabs for the various truck classifications. There is a general trend of higher strains at the surface of the slab compared to the bottom of the slab. An analysis of the average of all of the strains, measured at the top of the slab, for all three truck classifications shows that these strains are approximately 27 percent larger than those at the bottom of the slab. A paired t-test was performed to determine if the measured strain at the top is statistically different from strain at the bottom of the slab. It was determined with 95 percent confidence that strain at the top of the slab is indeed larger than the strain at the bottom of the slab. This difference, in the magnitude of the measured strains, indicates that the slab must be bonded to the asphalt treated permeable base.

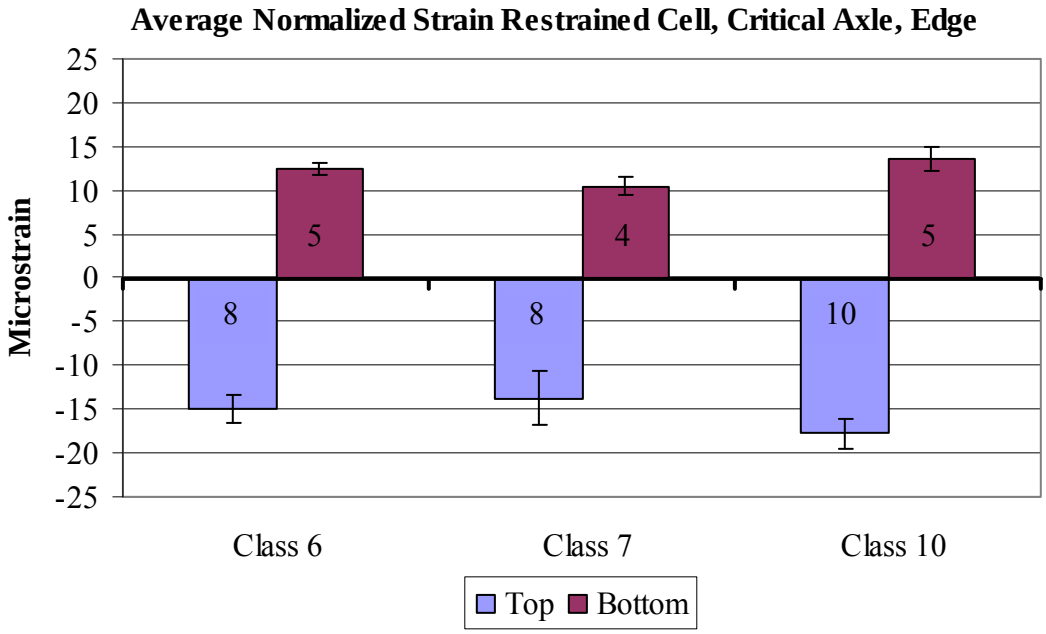

Figure 5.41. Strain measured at the top and bottom along the edge of the restrained slabs for the 1st axle of a Class 6 truck.

As previously discussed, temperature gradients develop daily in the concrete slab. For example, during the evening when the temperature on top of the slab is colder than that at the bottom, the slab curves upward. Although the slab is deflecting upward, the base and slab remain in contact as long as the curvature does not exceed the precompression produced by the weight of the slab (Huang 2004). Therefore, the two layers act as one monolithic section and the neutral axis is shifted downward resulting in a higher strain/stress at the top of the slab that at the bottom of the slab. This is beneficial to the service life of the slab since the tensile stresses at the bottom of the slab are reduced. This result that strain at the top of the slab is larger than the bottom, due to bonding between the slab and base, supports the findings of Rufino and Roesler and Guo and Pecht (Rufino and Roesler 2006, Guo and Pecht 2006).

There is also a larger amount of variation among the extrapolated strains at the top of the slab compared to those measured at the bottom in the restrained slabs. An analysis of the variation, between the top and bottom strains, showed that strains at the top of the slab vary twice as much as those on the bottom. One explanation for this might be related to defining the exact position of the gage. The gages at the bottom of the slab were bonded to the surface of the base while the gages in the upper portion of the slab were hung from wooden dowel rods. The elevation and location of each gage was surveyed prior to the passing of the paver but the weight of the concrete head in front of the paver or errors in the survey could result in changes in the actual location of the sensor with respected to the surveyed location.

5.6.2 Strain at the Top and Bottom of the Unrestrained Slabs

As previously discussed, when the slab is bonded to the base, the two layers act as one monolithic section, the neutral axis is shifted downward and strain at the top of the slab will be higher than that at the bottom of the slab. However, when the slab is not bonded to the base, the strain at the top of the slab will be equal in magnitude and opposite in sign to the strain at the bottom of the slab. This trend is observed in the unrestrained slabs of Cell 2 and is shown in Figure 5.42. Although Figure 5.42 shows that strain is larger at the bottom in the Class 6 and 7 trucks and at the top in the Class 10, significant variation was experienced between the measured strains. Therefore, a paired t-test was performed to determine if there is a statistical difference between strain at the top and bottom of the slab. It was determined with 95 percent confidence that there is no difference between strain measured at the top and bottom of the unrestrained slabs. Unlike the restrained slabs, the unrestrained slabs appear to be unbonded to the asphalt treated permeable base. This can contribute to the higher strains that were measured for the

unrestrained slabs. The performance of a pavement as predicted by the MEPDG is significantly affected by the age at which friction (bond) between the slab and underlying layer is lost. Unfortunately, very limited information is available on the degradation of friction over time. These findings do shed some light on this phenomenon. It appears that the friction can degrade more readily for an unrestrained slab when compared to a retrained slab as a result of the increased thermal and moisture related expansion and contraction of the slabs.

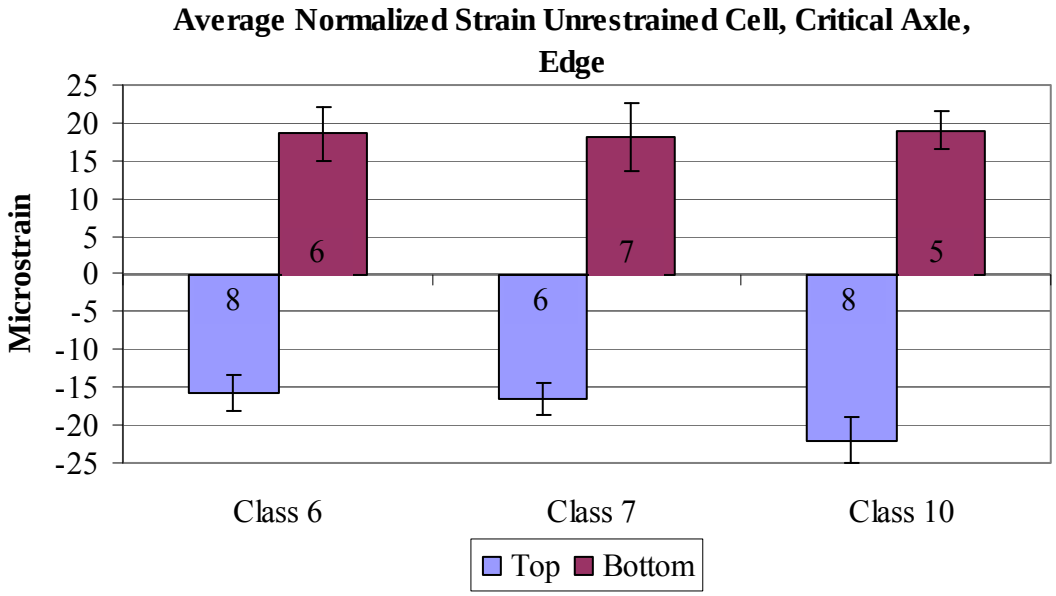

Figure 5.42. Strain measured at the top and bottom of the slab along the edge of the restrained cell.

5.7 EFFECT OF SLAB TEMPERATURE AND GRADIENTS ON DYNAMIC STRAIN

The dynamic strain measurements collected in the corner and wheelpath during the first three years after construction were evaluated for both the restrained (Cell 1) and unrestrained (Cell 2)

cells to characterize the effects of slab temperature and temperature gradients. These strains were plotted against the average slab temperature and equivalent linear gradient present at the time of testing to see if any correlation existed. The fourth axle for the Class 7 truck and the sixth axle for the Class 10 truck were evaluated at the 25,000-lb load level. Refer to Figure 5.43 through Figure 5.45.

The scatter depicted in Figure 5.43 and Figure 5.44 indicates there is little variation or no relationship between the measured strain and change in temperature for either the corner or wheelpath locations for the restrained slabs. Figure 5.45 indicates that there is also not a relationship between the slab temperature and measured strain for the unrestrained slabs. Additional graphs supporting this conclusion can be found in appendix B.

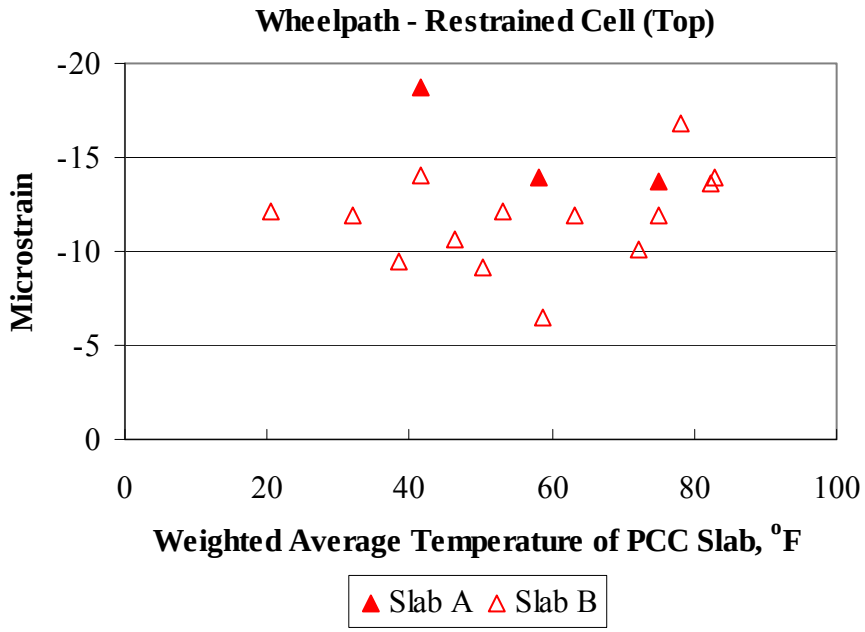

Figure 5.43. Relationship between strains measured in the wheelpath at the bottom of the restrained slabs and slab temperature.

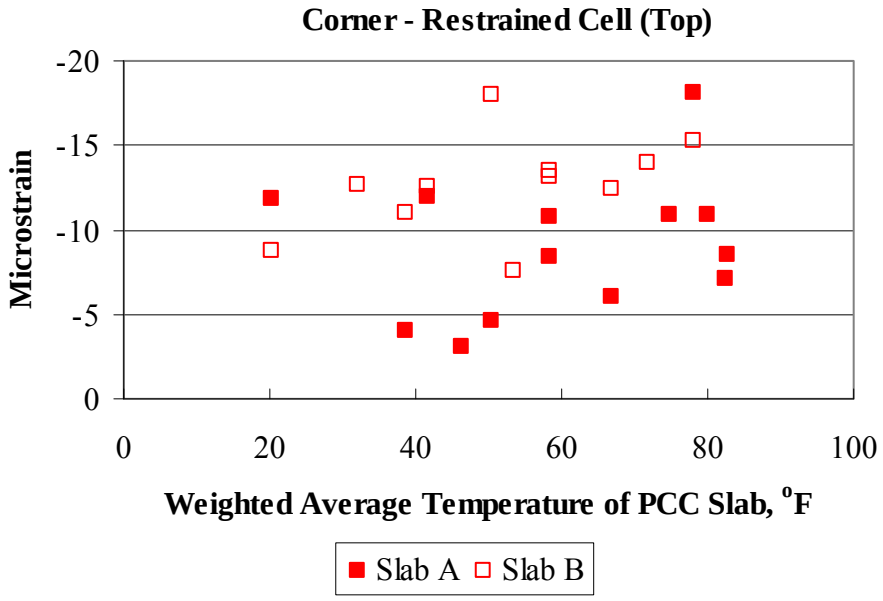

Figure 5.44. Relationship between strains measured in the corner at the bottom of the restrained slabs and slab temperature.

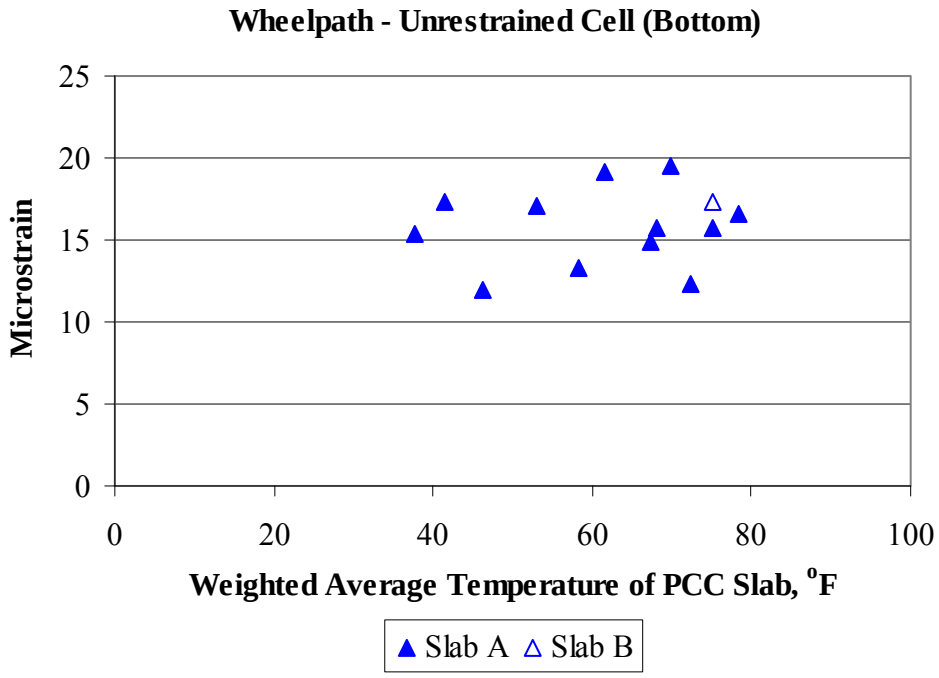

Figure 5.45. Relationship between strains measured in the wheelpath at the bottom of the unrestrained slabs and slab temperature.

The relationship between the strain measured in the wheelpath and the equivalent linear gradient present at the time of testing for both the restrained and unrestrained cells are provided in Figure 5.46 and Figure 5.47. These figures show that there is a trend of increased strain with increasing positive temperature gradients at the top of the slab in both the restrained and unrestrained slabs. As Figure 5.46 shows, when the gradient in Slab B was -0.15 °F/in the measured strain was -6 microstrain and when the gradient increased to 1.91 °F/in the strain increased to -14 microstrain. Similar results were experienced in the unrestrained Slab A (Figure 5.47), when the gradient was 0.05 °F/in strain was -5 microstrain, but when the gradient increased to 1.91 °F/in strain increased to -14 microstrain.

Other researchers have investigated the affect of the equivalent linear temperature gradient on dynamic strain with varying results. In 1998, Yu et al. determined that load induced strains are not significantly affected by temperature gradients, but a trend of increasing strain with increasing negative temperature gradients was experienced (Yu et al. 1998). However, in 2002 Burnham showed that dynamic strain depends on slab shape and saw trends of increased strain with increasing positive temperature gradients (Burnham 2003). The results of this analysis support Burnham's finding that dynamic strain increases with increasing positive temperature gradients.

This trend of increasing strain with increasing positive temperature gradients was experienced in both the restrained and unrestrained slabs at both the top and bottom of the slab for both locations (corner and wheelpath). The figures of this relationship for the remaining locations can be found in appendix B.

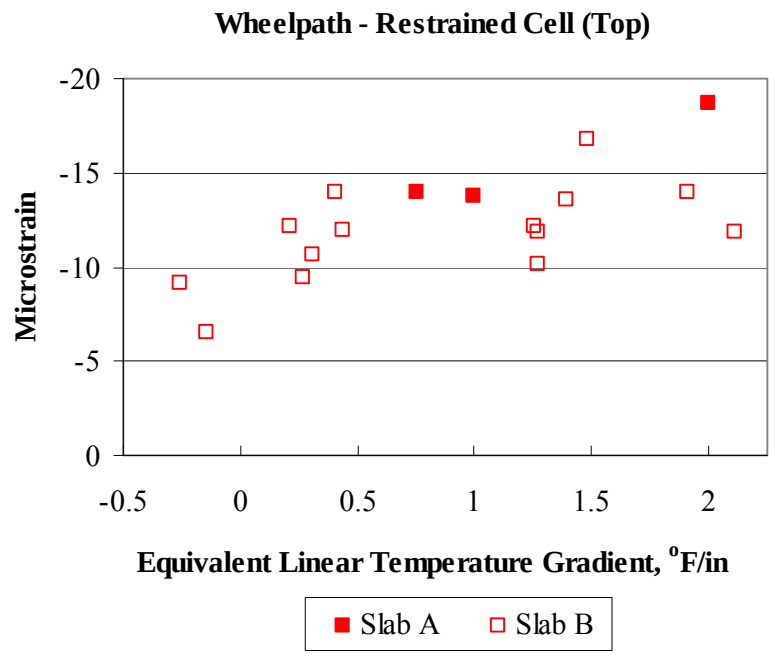

Figure 5.46. Relationship between strains measured in the wheelpath at the top of the restrained slabs and the temperature gradient in the slab.

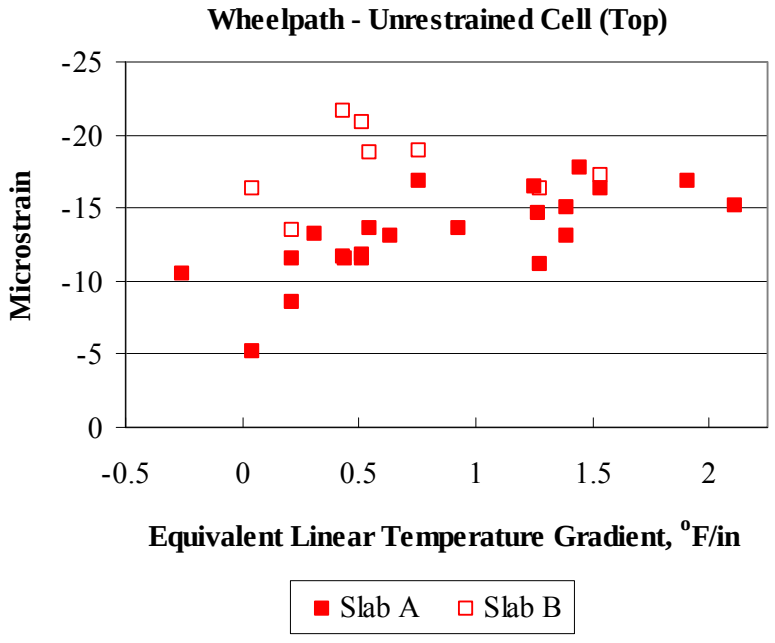

Figure 5.47. Relationship between strains measured in the wheelpath at the top of the unrestrained slabs and the temperature gradient in the slab.

6.0 DEVELOPMENT AND VALIDATION OF FINITE ELEMENT MODELS

The performance of rigid pavements is predicted as a function of stress. Since it is not possible to measure stress directly, the measured strains are used in the development of finite element models that can be employed to determine the stress in the pavement. This chapter presents the development and validation of rigid pavement models for predicting stress. The results of the seasonal FWD data are used to define the model inputs including: elastic modulus, k-value, and load transfer efficiency. Upon determination of all inputs, the finite element program Illislab will be used to model the pavement structure. This program was chosen because it is frequently used in the pavement community, it is user-friendly and the modeling assumptions inherent to this program are representative of those used in the majority of the other finite element pavement analysis programs frequently used. The slab is modeled as a medium-thick plate and the pavement structure is modeled as an equivalent three-layer system. The Illislab model will be calibrated using strain measurements recorded during the dynamic testing of trucks with known axle weight and configurations.

6.1 MODEL INPUTS

The development of a pavement model in finite element involves the determination of several inputs. These inputs can be grouped into three categories: mesh generation and material property

inputs, joint inputs, and loading inputs. The mesh generation and material property inputs include: the determination of the optimal mesh fineness, the elastic modulus, Poisson's ratio, the unit weight of the concrete and ATPB, thickness of the slab and base, gradient at the time of loading, k-value and coefficient of thermal expansion. The joint stiffness was calibrated using the LTE's measured in the field. The third classification of model inputs are those related to the applied and temperature loads. The pertinent load information includes the type of vehicle loading (three axle truck, four axle trucks or six axle truck), axle spacing, axle configuration, tire pressure, and contact area. The following sections provide the classification of the inputs for development of the finite element model of the Smart Pavement.

6.1.1 Mesh-Slab Model Inputs

The pavement was modeled as a six-slab system with three slabs in the longitudinal direction and two in the transverse direction. Each slab is 15 ft long and 12 ft wide. The number of elements used during the model calibration was varied based on the location of the strain sensors in the slab. When predicting strain along the transverse joint, the sensors are spaced 10 in apart in the longitudinal direction and are located 6 in from the transverse joint. A mesh with 30 elements in the longitudinal direction and 72 in the transverse direction was used. All elements are the same size. Computational time for each model is minimal so it was not necessary to restrict the increased fineness in the mesh to the regions where sensors are located. Table 6.1 provides the slab meshing used for model calibration of the three sensor groups (adjacent to transverse joint, adjacent to lane/shoulder joint and midpanel) of the Smart Pavement.

Table 6.1. Number of element used for generating the finite element models.

Sensor Group	Elements in Transverse Direction	Elements in Longitudinal Direction
Adjacent to Transverse Joint	72	30
Adjacent to Shoulder Joint	36	60
Midpanel	72	30

The models consist of a concrete pavement and ATPB resting on a dense liquid foundation. The material properties for the concrete were measured for cores cast at the time of paving. The thickness of the pavement was determined using an average of the depths established based on the survey data for the restrained (Cell 1) and unrestrained (Cell 2) slabs. The concrete material inputs for both slab types are provided in Table 6.2.

Table 6.2. PCC model inputs for each slab type based on measured values.

PCC Model Input	Restrained (Cell 1)	Unrestrained (Cell 2)
Thickness	14.5 in	12 in
Elastic Modulus (365-days)	5,050,000 psi	5,050,000 psi
Poisson's Ratio	0.17	0.17
Unit Weight	143 lbs/ft^3	143 lbs/ft^3
Coefficient of Thermal Expansion	5.90 με/°F	5.90 με/°F

The measured material properties for the ATPB were determined from laboratory testing following proper ASTM specifications. The material inputs for the ATPB are provided in Table 6.3.

Table 6.3. ATPB model inputs based on measured values.

ATPB Model Input	Cell 1 and 2
Thickness	4 inches
Elastic Modulus	(varies)
Poisson's Ratio	0.35
Coefficient of Thermal Expansion	1.10 με/°F
Unit Weight	148 lbs/ft^3
Interface with PCC layer	Bonded

As previously mentioned, the pavement was modeled as a three layer system with the slab and ATPB layers resting on a dense liquid foundation. The elastic modulus of the ATPB and modulus of subgrade reaction (k-value), representing the composite stiffness of all layers beneath the slab at the time the testing was performed, must be determined. FWD testing was performed during each season in conjunction with the truck testing so that an elastic modulus and k-value representive of the conditions during truck testing could be determined. A summary of these backcalculated values is provided in Chapter 4. The average seasonal elastic moduli for both the restrained and unrestrained cells are provided in Table 6.4 and the average seasonal k-values are provided in Table 6.5. The static k-value was taken as half of the dynamic k-value. Previous studies like the AASHO Road Test showed that reducing backcalculated dynamic k-values by approximately two produced reasonable static k-values measured in the field (AASHTO 1993)

Table 6.4. Average seasonal elastic moduli of the ATPB for the restrained and unrestrained slabs.

		E_{ATPB} (ksi)		Standard Deviation	
Year	**Season**	**Cell 1**	**Cell 2**	**Cell 1**	**Cell 2**
2004	Fall	327	360	72	7
2005	Winter	293	429	4	103
2005	Spring	198	390	19	11
2005	Summer	304	335	100	24
2006	Winter	325	578	43	268
2006	Spring	322	421	65	7
2006	Summer	329	403	15	166
2006	Fall	296	437	76	19
2007	Winter	396	639	5	277
2007	Spring	243	295	2	29
2007	Summer	245	317	24	11
2007	Fall	230	359	6	32

Table 6.5. Average seasonal backcalculated static k-values for the restrained and unrestrained slabs.

		k-value (psi/in)		Standard Deviation	
Year	**Season**	**Cell 1**	**Cell 2**	**Cell 1**	**Cell 2**
2004	Fall	163	157	38	7
2005	Winter	216	144	49	48
2005	Spring	259	141	94	8
2005	Summer	208	155	54	60
2006	Winter	217	139	14	65
2006	Spring	246	184	57	1
2006	Summer	217	172	32	73
2006	Fall	245	172	24	12
2007	Winter	246	213	1	77
2007	Spring	125	88	1	7
2007	Summer	214	127	4	65
2007	Fall	198	113	20	56

6.1.2 Inputs for Modeling Slab Joints

Insuring that the finite element model accurately represents the joint stiffness observed in the field is extremely important since the stiffness of the joint greatly affects stress development. The pavement consists of both restrained and unrestrained slabs. The restrained slabs contain No. 5 (5/8-in) epoxy-coated tie bars placed 2.5 ft apart along the lane/shoulder and centerline joints. The transverse joints have epoxy coated 1.5-in dowel bars spaced every 12 inches. Load transfer efficiency along the transverse joint was measured seasonally in the restrained and unrestrained slabs and will be used to specify the stiffness of these joints. The longitudinal LTE along the centerline joint will be estimated using a relationship between the geometry of the transverse and longitudinal joints for the unrestrained slabs. The LTE along the centerline joint for the restrained slab will be a function of the properties of the tie bars. As previously discussed in Chapter 4, the load transfer efficiency was determined for each of the joints during each season. Table 6.6 provides the LTE for the transverse joints of the restrained and unrestrained slabs and Table 6.7 provides the longitudinal LTE for the unrestrained slabs incorporated into the finite element models.

Table 6.6. The measured load transfer efficiency along the transverse joint of the restrained and unrestrained slabs.

Season	Restrained Cell		Unrestrained Cell	
	LTE (%)	St. Dev	LTE (%)	St. Dev
Fall 2004	88	1.8	87	1.2
Winter 2005	89	3.0	66	15.0
Spring 2005	83	4.0	60	15.5
Summer 2005	76	4.3	59	7.2
Fall 2005	-	-	-	-
Winter 2006	81	2.0	41	6.3

Table 6.6 (continued).

Spring 2006	80	3.8	39	4.6
Summer 2006	86	4.2	84	12.5
Fall 2006	81	2.3	37	5.6
Winter 2007	80	1.5	72	8.0
Spring 2007	87	2.5	67	4.9
Summer 2007	84	2.5	61	19.5
Fall 2007	84	3	51	30

Table 6.7. The measured load transfer efficiency along the longitudinal joint for the unrestrained slabs.

Season	Unrestrained
	LTE (%)
Fall 2004	100
Winter 2005	82
Spring 2005	74
Summer 2005	74
Fall 2005	-
Winter 2006	52
Spring 2006	49
Summer 2006	100
Fall 2006	46
Winter 2007	90
Spring 2007	84
Summer 2007	77
Fall 2007	64

6.1.3 Modeling of the Loads Applied to the Pavement Structure

To properly model the loads applied to the Smart Pavement several parameters needed to be determined for the three trucks used during dynamic testing. These parameters included: dimensions of the axle configuration, and tire spacing, and the tire size and pressure. The tire pressure for all truck types was determined from standard manufacturer's performance charts and

a value of 100 psi was used. Figure 6.1 through Figure 6.3 provide the axle configuration, tire spacing, and tire size of the Class 6, 7, and 10 trucks used during truck testing on SR 22.

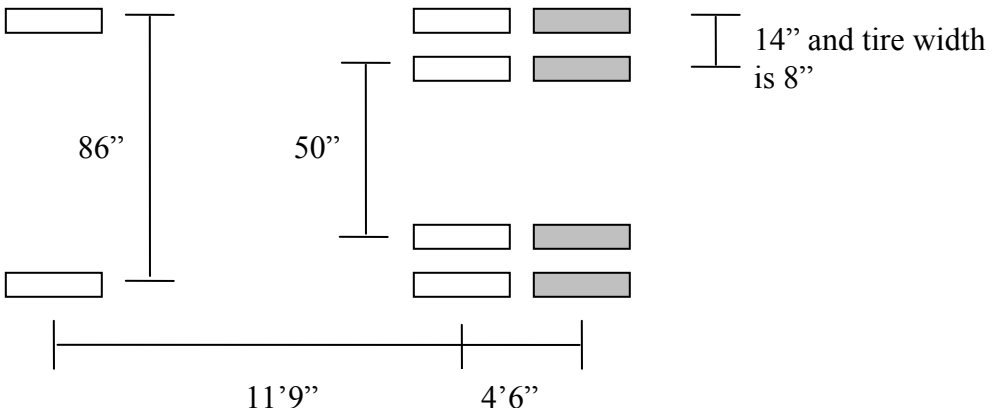

Figure 6.1. Axle configuration and tire spacing of the Class 6 truck.

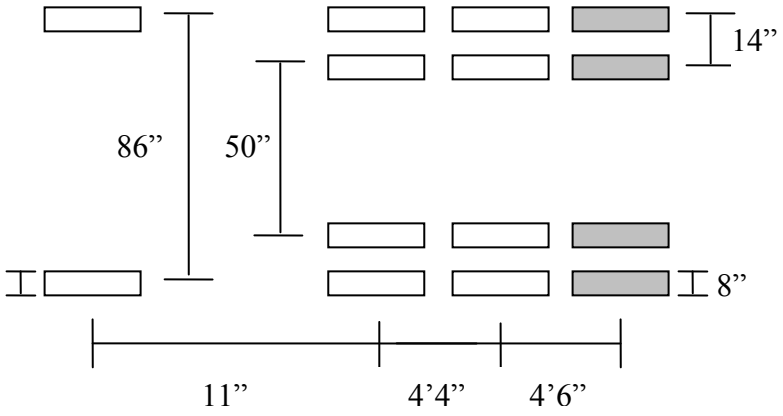

Figure 6.2. Axle configuration and tire spacing of the Class 7 truck.

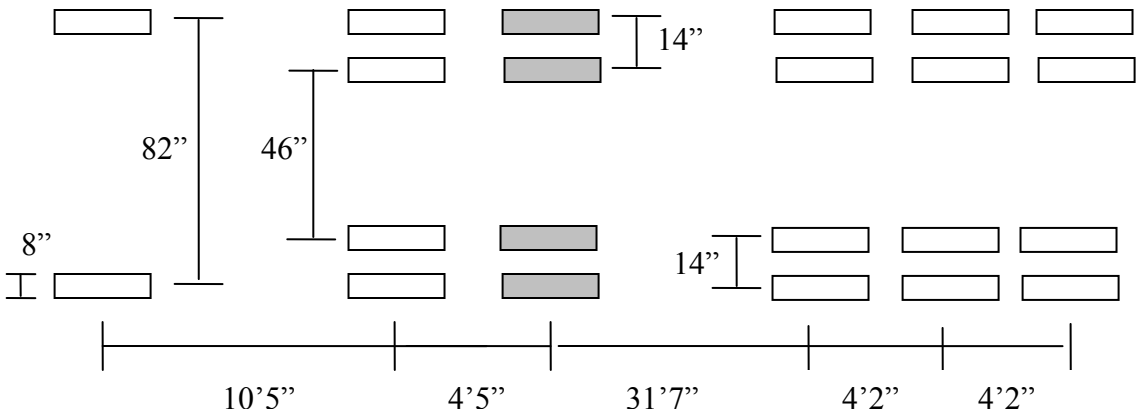

Figure 6.3. Axle configuration and tire spacing of the Class 10 truck.

6.2 FINITE ELEMENT MODEL CALIBRATION

The following presents the results of the calibration of the finite element models for the restrained and unrestrained slabs of the Smart Pavement. As previously discussed, the dynamic sensors of the Smart Pavement are arranged in three groups that correspond to different locations in the slab. As Figure 6.4 shows, the three sensor groups are located adjacent to the transverse joint (Group 1), along the edge/shoulder joint (Group 2), and at midpanel (Group 3). All three sensor groups for each of the three truck classes were used to validate/calibrate the models. The gages used were restricted to the gages at the bottom of the slab since there was less variability compared to the top sensors, as previously discussed in Chapter 5.

The following subsections provide the results of the calibration for the three sensors groups for each truck class (Class 6, 7, and 10). Strains measured from the critical axle identified in Chapter 5 for each truck type were used to calibrate the models. The critical axles for each truck type are highlighted in Figure 6.1 through Figure 6.3. Additionally, strains

measured when the effective gradient in the slab was approximately zero were used for model calibration. The strain gage measures changes in electrical resistance when an external force is applied to the concrete. This measure of resistance does not account for the additional expansion and contraction of the slab due to environmental changes, therefore the additional stress caused by the slab movement due to temperature differences between the top and bottom of the slab is not accounted for. The built-in gradient was established as 0.31 ^{o}F/in so the strains measured when a gradient is 0.31 ^{o}F/in is desired so that the slab is flat. This allows the models to be validated/calibrated using loads that are applied on a flat slab so that strain that can not be accounted for in the strain gages is eliminated.

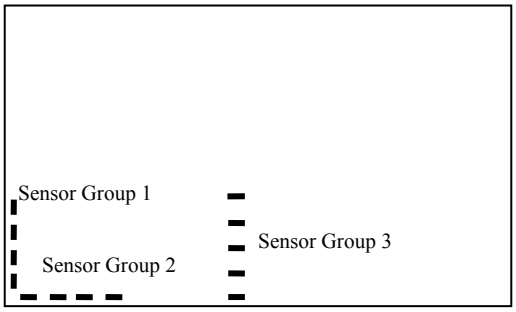

Figure 6.4. Dynamic strain sensor layout.

6.2.1 Calibration Using Group 1 Sensors (Adjacent to the Transverse Joint)

The following presents the results of the validation/calibration of the Group 1 sensors located adjacent to the transverse joint in both the restrained and unrestrained slabs. This sensor group is located approximately 4 in from the transverse joint in the longitudinal direction. The four sensors are located at distances of 6, 16, 26, and 36 in from the lane/shoulder joint in the transverse direction. The gages measure strains in the wheelpath directly adjacent to the

transverse joints. Only the strain measurements captured when the critical axle of each truck traversed the pavement in the wheelpath (approximately 24 inches from the lane/shoulder joint) were used. The following provides the calibration results for the Class 6, 7, and 10 trucks for the Group 1 sensor in both the restrained and unrestrained slabs.

6.2.1.1 Calibration of the Restrained Slabs Using the Group 1 Sensors

Figure 6.5 present the results of the measured and predicted Class 6 critical strain for the Group 1 sensors in the restrained slabs. Strains recorded in the summer of 2005 when the Class 6 truck traversed the slab in the wheelpath were used to investigate the correlation between predicted and measured strain since this is when the slab was close to flat. The truck was loaded with 15,000 lbs per axle and the gradient during testing was 0.16 °F/in. The values used to define the stiffness of the joints, the modulus of the ATPB, and the k-value were based on the average of the values determined using the FWD collected for the summer of 2005. As can be seen below, the predicted strain is following the same trend as the measured. Additionally, the predicted measurements are within 2 microstrain of the measured values.

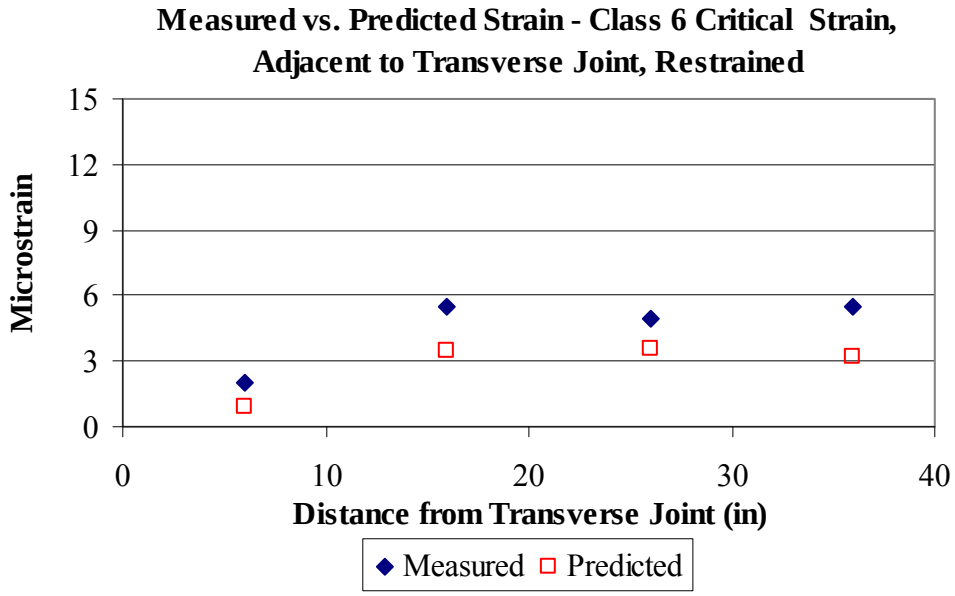

Figure 6.5. Calibration results for the sensors located adjacent to the transverse joint in the restrained slabs for the Class 6 truck.

Figure 6.6 and Figure 6.7 present the measured and predicted strains along the transverse joint for the critical axle for the Class 7 and 10 trucks. Similar to the analysis for the Class 6 truck, the predicted strain along the transverse joint follows the same shape as the measured values and all strain measurements are within 2 microstrain indicating a good correlation between predicted and measured values. Although, the predicted and the measured strains do tend to diverge slightly when approaching the transverse joint, with the predicted strain underestimating the measured strain. The stiffness of the joint stiffness might be slightly higher in the model than that observed in the field.

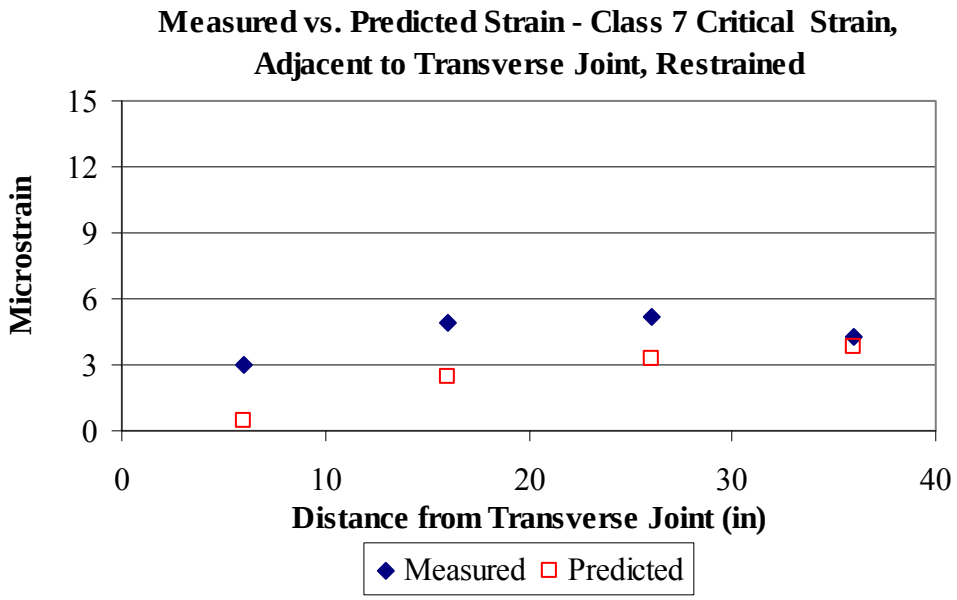

Figure 6.6. Calibration results for the sensors located adjacent to the transverse joint in the restrained slabs for the Class 7 truck.

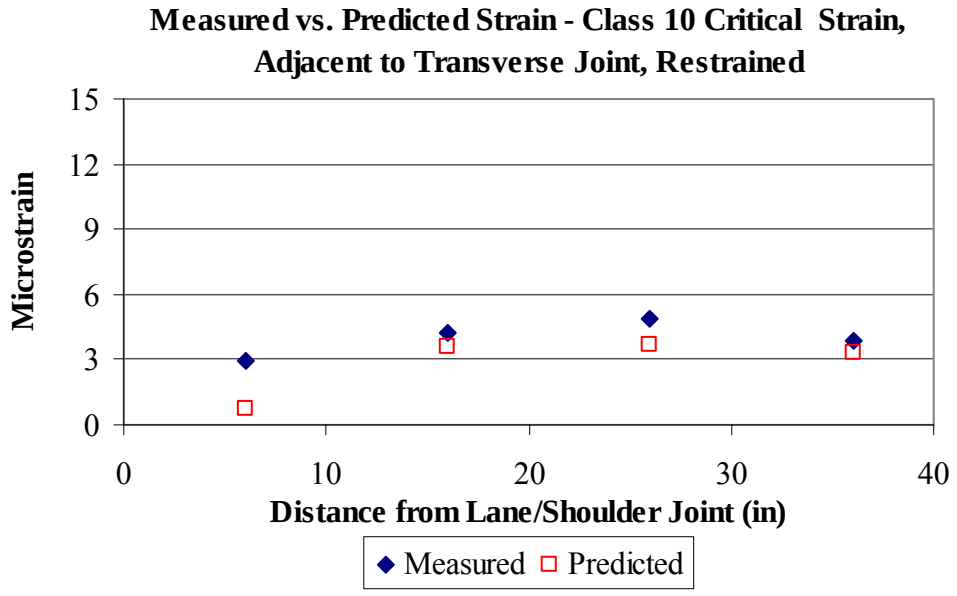

Figure 6.7. Calibration results for the sensors located adjacent to the transverse joint in the restrained slabs for the Class 10 truck.

6.2.1.2 Calibration of the Unrestrained Slabs Using the Group 1 Sensors

Figure 6.8 through Figure 6.10 present the results for the sensors adjacent to the transverse joint in the unrestrained slabs for the Class 6, 7, and 10 trucks with 18,000-lb axle loads. All of the predicted strain measurements are within two microstrain except the strain predicted for the Class 6 truck at a distance of 26 in from the transverse joint. The predicted strain in this location was approximately 3 microstrain smaller than the measured value. This is an acceptable difference because the gradient of the slab during measurement was 0.18 °F/in, while the gradient present during the Class 7 and 10 trucks was closer to zero at 0.10 °F/in. The strain gages measure changes in electrical resistance when an external force is applied to the concrete. This measure of resistance does not account for the additional expansion and contraction of the slab due to environmental changes, therefore the additional stress caused by the slab movement due to temperature differences between the top and bottom of the slab is not accounted for. Therefore, a difference of 3 microstrain in this calibration is acceptable.

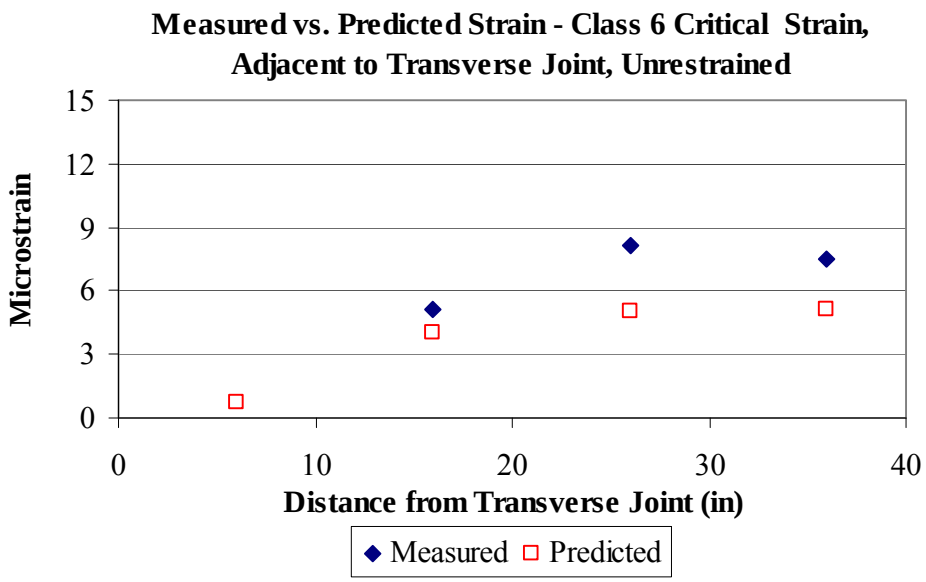

Figure 6.8. Calibration results for the sensors located adjacent to the transverse joint in the unrestrained slabs for the Class 6 truck.

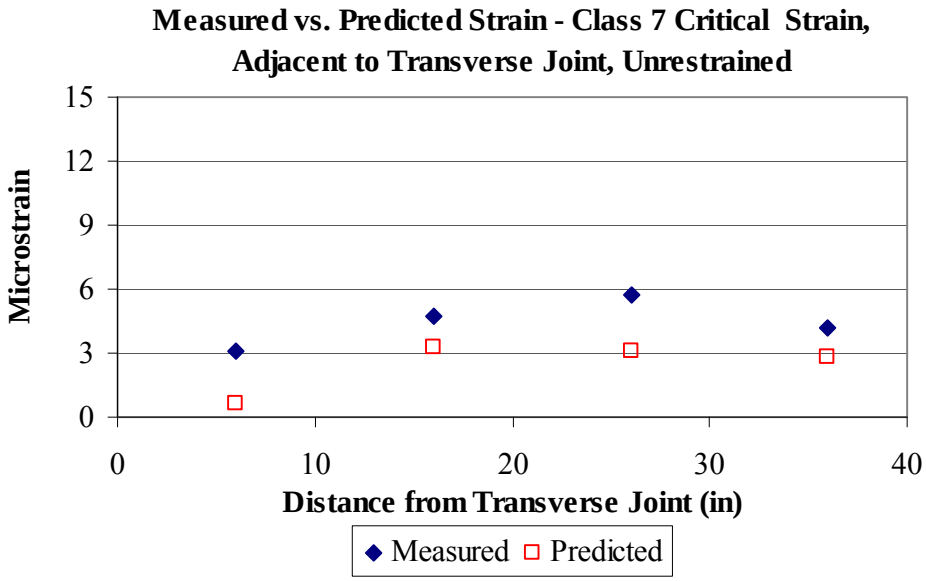

Figure 6.9. Calibration results for the sensors located adjacent to the transverse joint in the unrestrained slabs for the Class 7 truck.

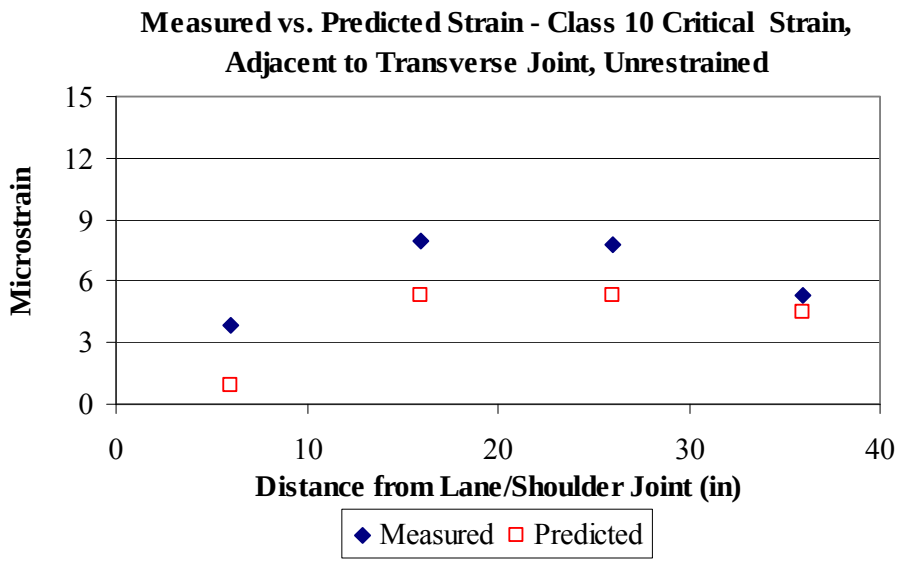

Figure 6.10. Calibration results for the sensors located adjacent to the transverse joint in the unrestrained slabs for the Class 10 truck

6.2.2 Calibration Using Group 2 Sensors (Along the Lane/Shoulder Joint)

The following presents the results of the calibration of the sensors in Group 2 (adjacent to the lane/shoulder joint) in the restrained and unrestrained slabs. This sensor group is located 4 in from the lane/shoulder joint in the transverse direction and the sensors are located at distances of 20, 30, 39, and 49 in from the transverse joint in the longitudinal direction. These sensors are longitudinally oriented and measure strain in the longitudinal direction. Strain measurements captured when the critical axle of each truck traversed along the edge of the pavement were used in this analysis. The critical axle for each truck was placed directly on top of each sensor along the lane/shoulder joint. Strains measured for the load testing performed in fall of 2004 were used for calibration/validation of the Class 7 and 10 trucks and strains measured in winter of 2005 were used for the Class 6 truck. The gradient present at the time of testing was 0.17 °F/in for the Class 7 and 10 trucks and was -0.04 °F/in for the Class 6 truck.

6.2.2.1 Calibration of the Restrained Slabs Using Group 2 Sensors

Figure 6.11 through Figure 6.13 present the results from the analysis of measured versus predicted strain for the sensors located adjacent to the lane/shoulder joint in the restrained slabs. As can be seen below, the predicted strain is following the same trend as the measured. The predicted strain for the Class 6 and 10 trucks is within 1 microstrain of the measured values for all of the sensors along the lane/shoulder joint. The predicted strains for the Class 7 truck is within 2 microstrain of the measured values. This larger variation between predicted and measured values can be attributed to the larger temperature gradient (0.17 °F/in) during testing.

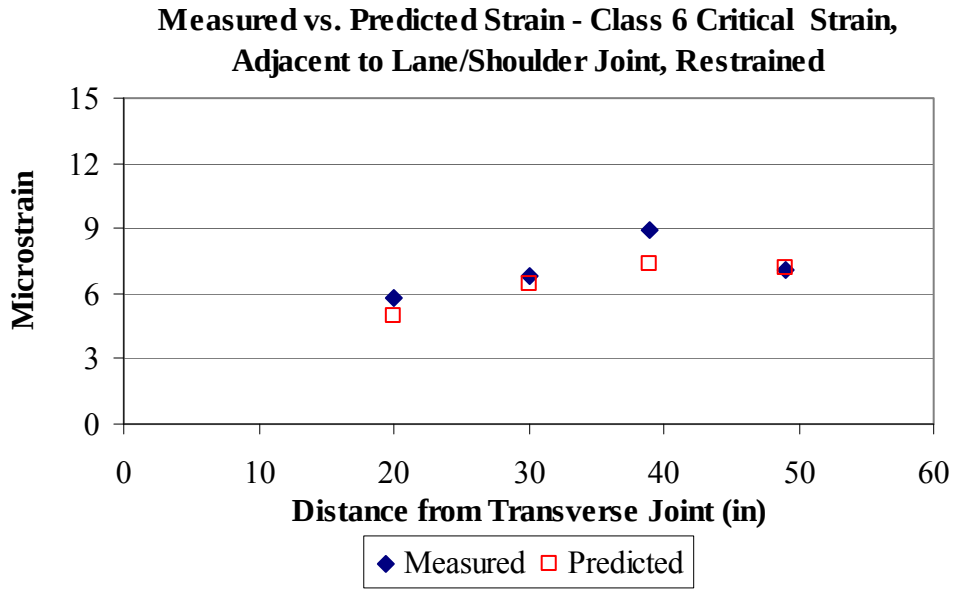

Figure 6.11. Calibration results for the sensors located adjacent to lane/shoulder joint in the restrained slabs for the Class 6 truck.

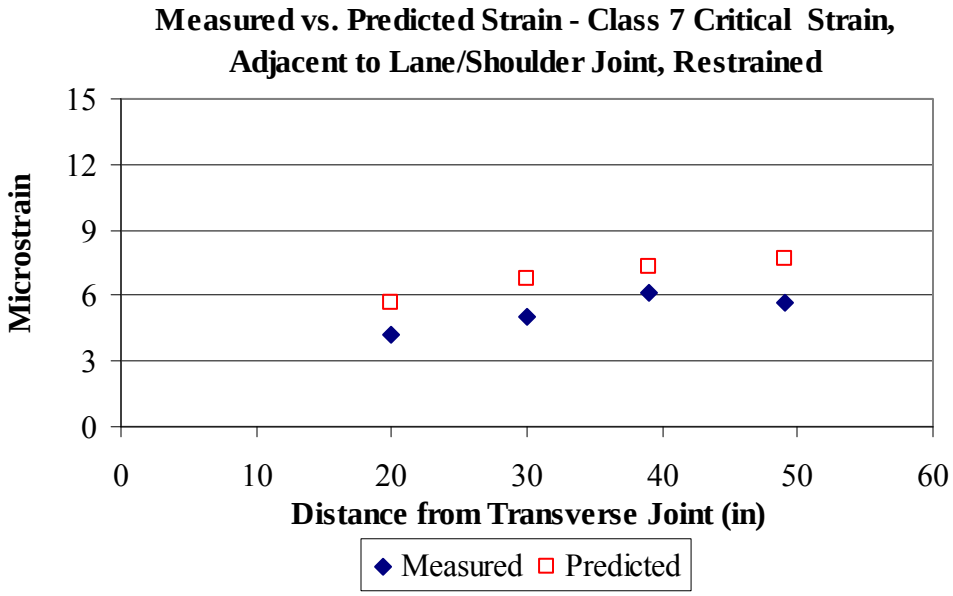

Figure 6.12. Calibration results for the sensors located adjacent to lane/shoulder joint in the restrained slabs for the Class 7 truck.

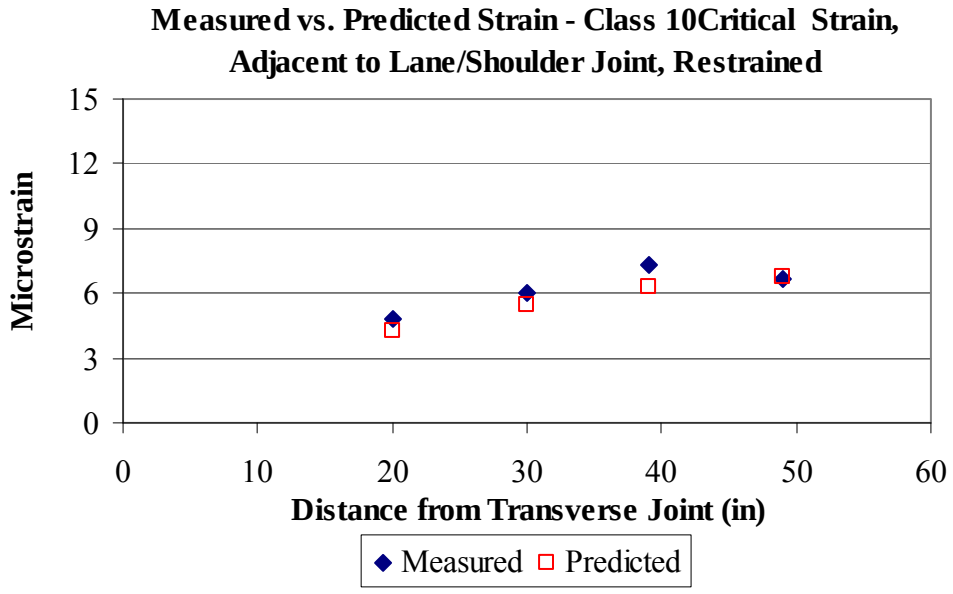

Figure 6.13. Calibration results for the sensors located adjacent to lane/shoulder joint in the restrained slabs for the Class 10 truck.

6.2.2.2 Calibration of the Unrestrained Slabs Using the Group 2 Sensors

Figure 6.14 through Figure 6.16 present the calibration results of the sensors adjacent to the lane/shoulder joint in the unrestrained slabs for the Class 6, 7, and 10 critical strains. All of the predicted strain measurements are within 2 microstrain except the strain predicted for the Class 7 truck at a distance of 49 inches from the transverse joint. The predicted strain in this location was 3 microstrain larger than the measured value. As previously discussed, the dynamic strain gages can not account for stress/strain generated from slab restraint and movement. Therefore, this difference between predicted and measured strain is acceptable because the gradient of the slab during measurement was 0.17 °F/in.

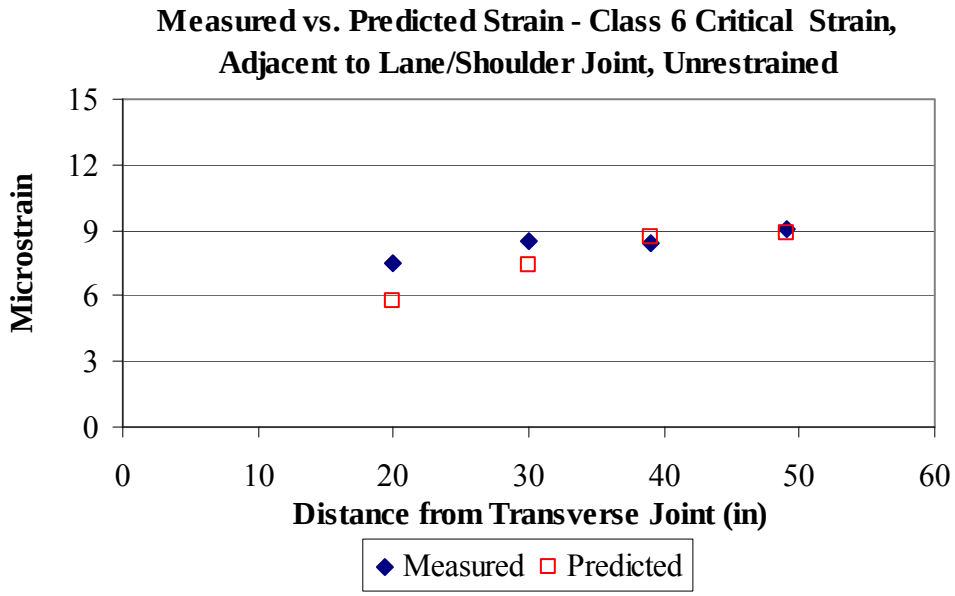

Figure 6.14. Calibration results for the sensors located adjacent to lane/shoulder joint in the unrestrained slabs for the Class 6 truck.

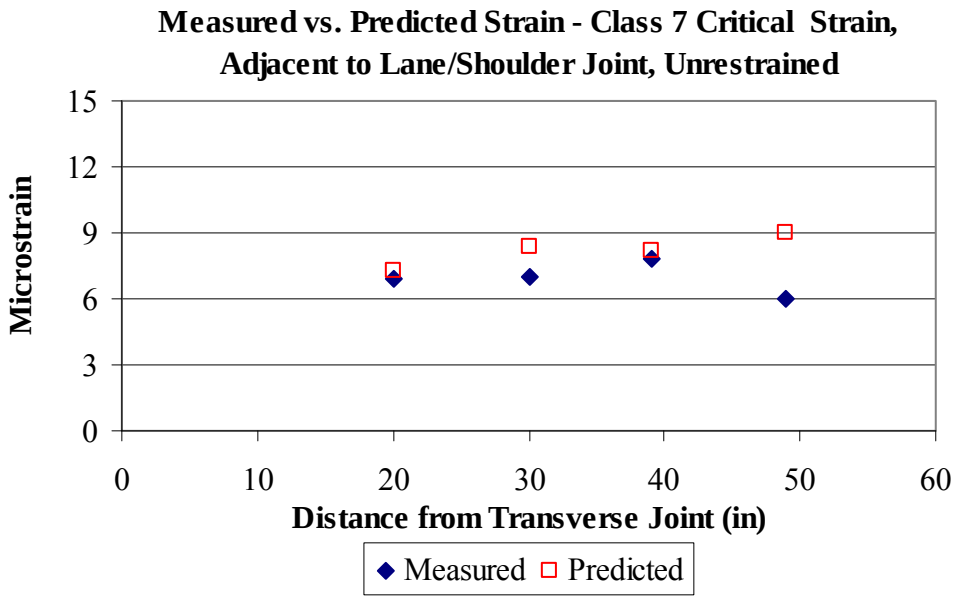

Figure 6.15. Calibration results for the sensors located adjacent to lane/shoulder joint in the unrestrained slabs for the Class 7 truck.

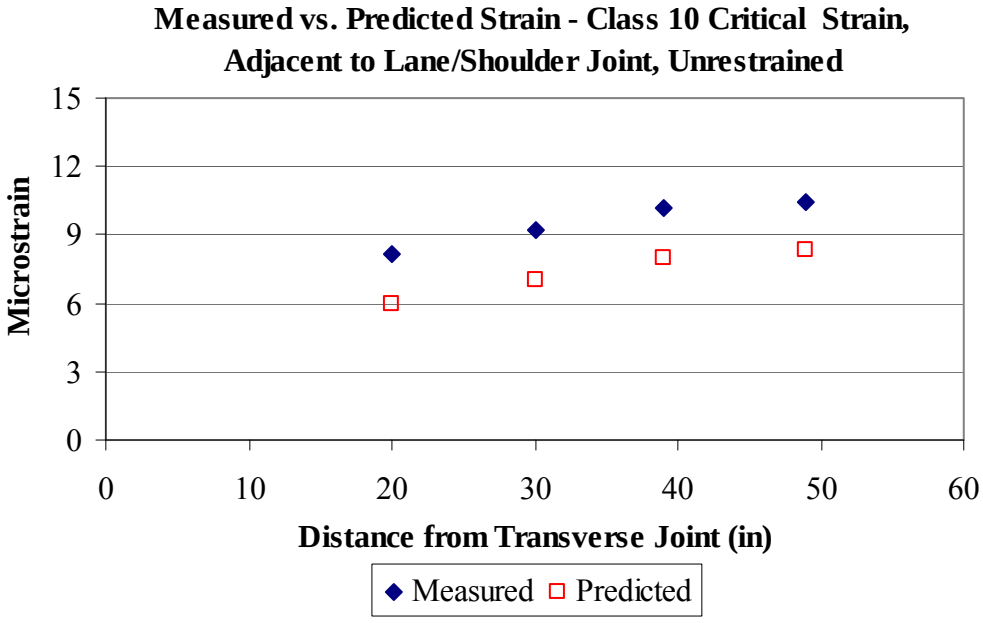

Figure 6.16. Calibration results for the sensors located adjacent to lane/shoulder joint in the unrestrained slabs for the Class 10 truck.

6.2.3 Calibration Using Group 3 Sensors (Midpanel)

The following presents the results of the validation of the model using sensor Group 3 located at midpanel in both the restrained and unrestrained slabs. This sensor group is located approximately 90 inches (midpanel) from the transverse joint in the longitudinal direction and the five sensors are located at distances of 10, 16, 22, 28, and 34 inches from the lane/shoulder joint in the transverse direction. These sensors measure strain in the longitudinal direction. The analysis used strain measurements captured when the critical axle of each truck traversed the pavement in the wheelpath (approximately 24 inches from the lane/shoulder joint). Strains measured during the winter of 2005 when the Class 7 and 10 trucks were loaded with 18,000 lbs per axle and strains measured during the summer of 2005 when the Class 6 truck was loaded with 15,000 lbs per axle were used to calibrate/validate the model.

6.2.3.1 Calibration of the Restrained Slabs Using the Group 3 Sensors

Figure 6.17 through Figure 6.19 present the results from the analysis of measured versus predicted strain for the Group 3 sensors in the restrained slabs. As can be seen below, the predicted strain is following the same trend as the measured. All of the predicted strain measurements are within 2 microstrain of the measured values except the strain predicted for the Class 10 truck at a distance of 10 inches from the lane/shoulder joint. The predicted strain in this location was approximately 3 microstrain smaller than the measured value.

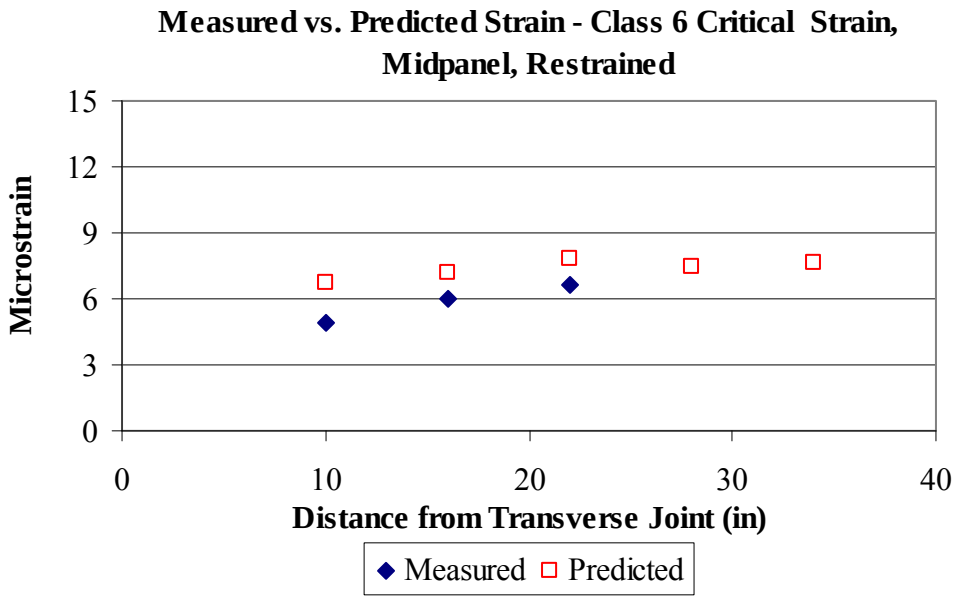

Figure 6.17. Calibration results for the sensors at midpanel in the restrained slabs for the Class 6 truck.

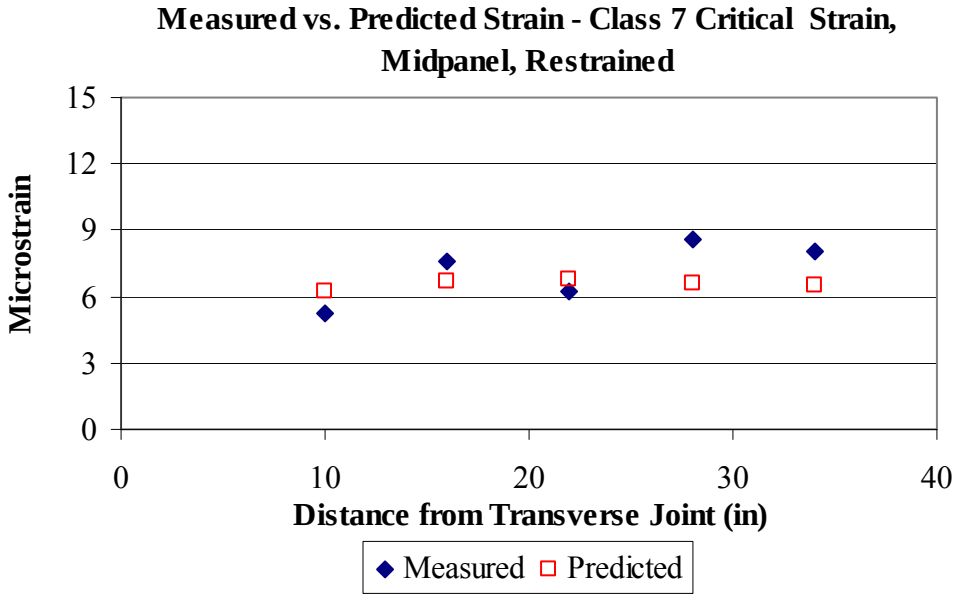

Figure 6.18. Calibration results for the sensors at midpanel in the restrained slabs for the Class 7 truck.

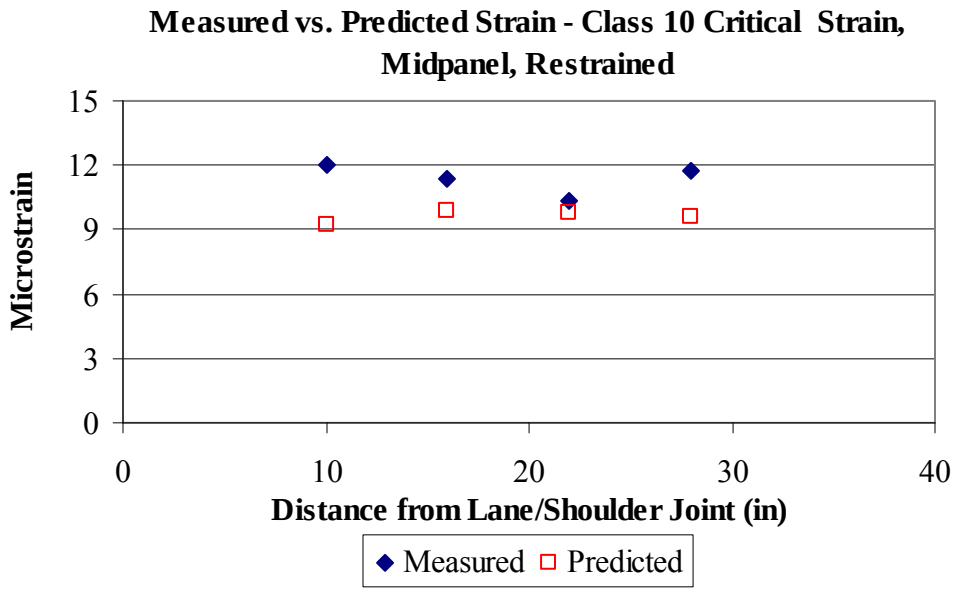

Figure 6.19. Calibration results for the sensors at midpanel in the restrained slabs for the Class 10 truck.

6.2.3.2 Calibration of the Unrestrained Slabs Using the Group 3 Sensors

Figure 6.20 through Figure 6.22 present the results for the sensors located at midpanel in the unrestrained slabs for the Class 6, 7, and 10 trucks. All of the predicted strain measurements are within 2 microstrain of the measured field values.

The finite element models generated using the inputs established with the FWD deflection data provide a relatively accurate estimate of the measured strain. The models were adjusted based on the inputs established for the season in which the truck load testing was performed. These seasonal inputs were established based on the FWD data representing that particular season. For all load cases considered, there was a good match between the measured and predicted strains for both the restrained and unrestrained slabs. Therefore, the strains measured in the field validated the finite element models and calibration is not necessary. These models can now be used to predict stress in the slab for any combination of vehicle and environmental loads.

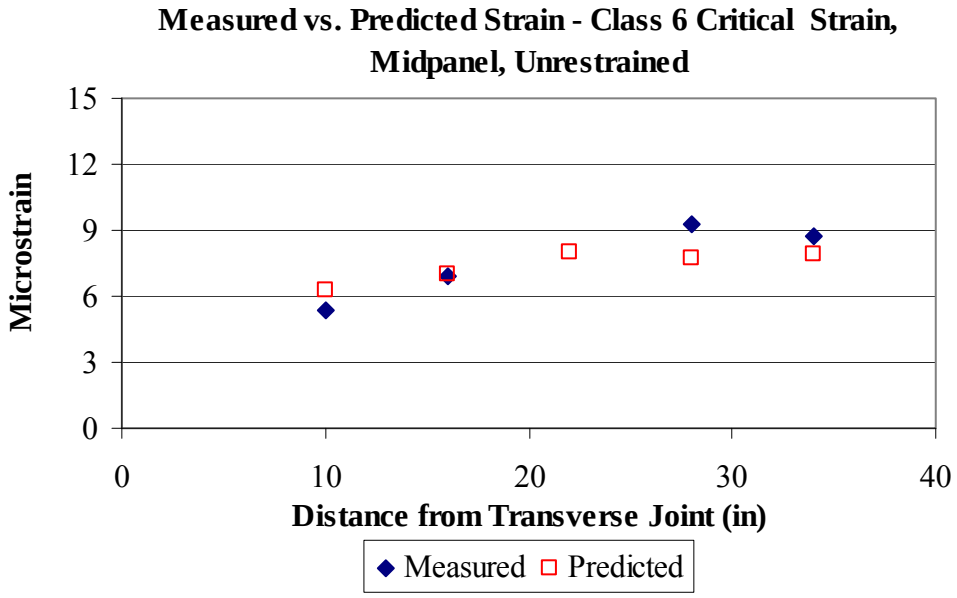

Figure 6.20. Calibration results for the sensors at midpanel in the unrestrained slabs for the Class 6 truck.

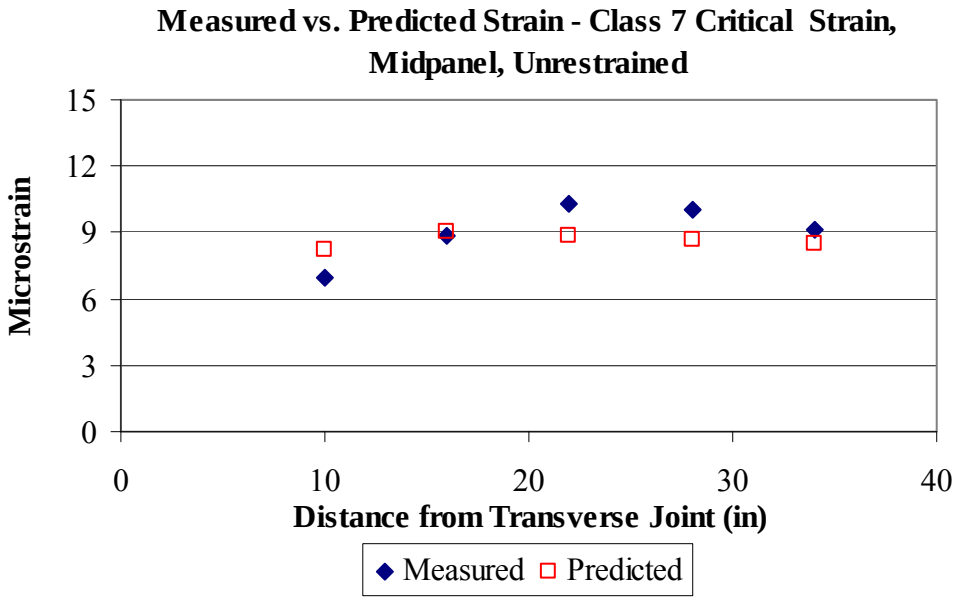

Figure 6.21. Calibration results for the sensors at midpanel in the unrestrained slabs for the Class 7 truck.

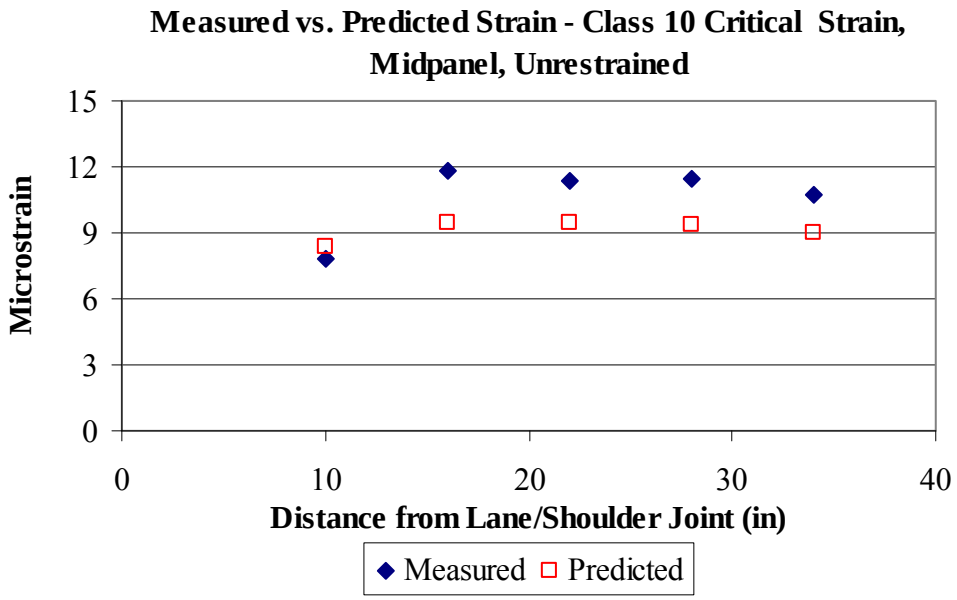

Figure 6.22. Calibration results for the sensors at midpanel in the unrestrained slabs for the Class 10 truck.

7.0 CONCLUSIONS AND RECOMMENDATIONS

This research has provided a better understanding of the response of a jointed plain concrete pavement to applied loads. The FWD and truck load testing provided valuable insight that enabled the development and validation of finite element models used to characterize stress that develops in the pavement as a result of these applied loads. The following section provides a summary of the conclusions drawn from this study. Following this, recommendations for further research will be presented.

7.1 CONCLUSIONS

The following conclusions were made based on the results of this study:

- Undoweled pavements in Pennsylvania will have low load transfer efficiencies the majority of the time even for a short 15-ft joint spacing (Section 4.3).
- The load transfer measured for the unrestrained slabs is dependent on the temperature gradient present at the time of testing. The load transfer measured for the restrained slabs was found to not be affected by temperature gradients or slab temperature (Section 4.3.1).

- The load transfer efficiency was found to not significantly affect the magnitude of the measured strain along the transverse joint in both the restrained and unrestrained slabs for the range of load transfer efficiencies included in this study (Section 4.3.2).
- Temperature gradients have a larger affect on the measured deflections than moisture gradients (Section 4.4).
- A good correlation was found between the magnitude of the Void parameter and the size of the gradient for both the restrained and unrestrained slabs (Section 4.4).
- No correlation was found between the support conditions beneath the slab and the gradient of the slab during testing or the temperature of the ATPB (Section 4.5).
- The unrestrained slabs exhibit more variation in the measured deflections than the restrained slabs (Section 4.6).
- Strain measured along the edge of the slab was the largest in both the restrained and unrestrained slabs. Additionally, measured strains showed the most variation in areas that had the greatest variability in edge support conditions, which is a function of the width of the transverse and longitudinal joints, and temperature and moisture conditions throughout the slab (Section 5.3).
- The measured strains indicate the interface between the base and the slab is unbonded for the unrestrained slabs and bonded for the restrained slabs, indicating that the life of the bond might be a function of the restraint conditions (Section 5.6).
- The average slab temperature did not affect the magnitude of the strain measured for either the restrained or unrestrained slabs (Section 5.7).

- A relationship was found between the measured strain and the temperature gradient present in the slab at the time of testing for both the restrained and unrestrained slabs (Section 5.7).

7.2 RECOMMENDATIONS

The following recommendations were developed based on the findings from this study:

- The finite element models developed in this research should be used in future research to evaluate stress in the pavement for a wider range of temperature and moisture gradients, support conditions, and a wider range of vehicle loads and configurations.
- The finite element models developed in this research should also be used to evaluate the accuracy of the calculated stress and deflection in the MEPDG.
- Further research is needed in determining the effect of the gradient in the slab and the slab temperature on backcalculated k-values, Void parameters, and load transfer efficiency. Establishing relationships between these parameters would provide the tools needed by practitioners for interpreting FWD data collected throughout the day. This would increase the hours available each day in which FWD testing could be performed.

APPENDIX A

PAVEMENT RESPONSE TO FWD LOADS

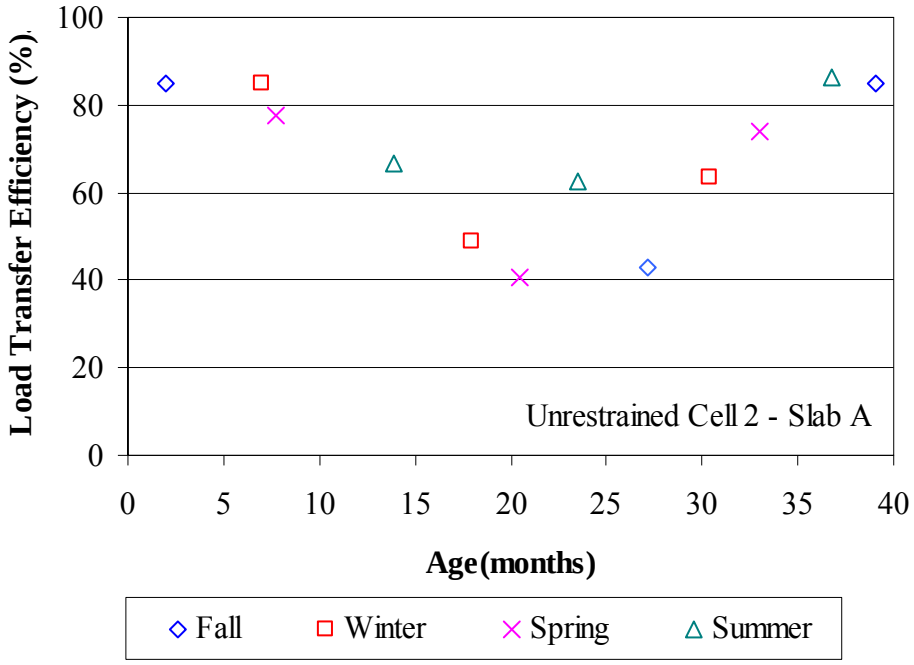

Figure A1. Relationship between load transfer efficiency and age of the pavement for the unrestrained Cell 2.

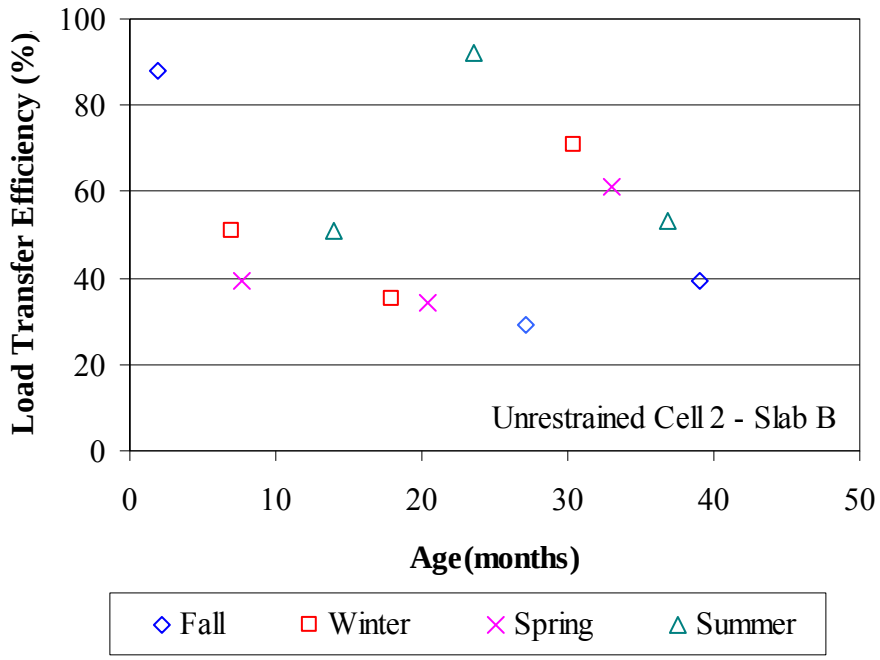

Figure A2. Relationship between load transfer efficiency and age of the pavement for the unrestrained Cell 2.

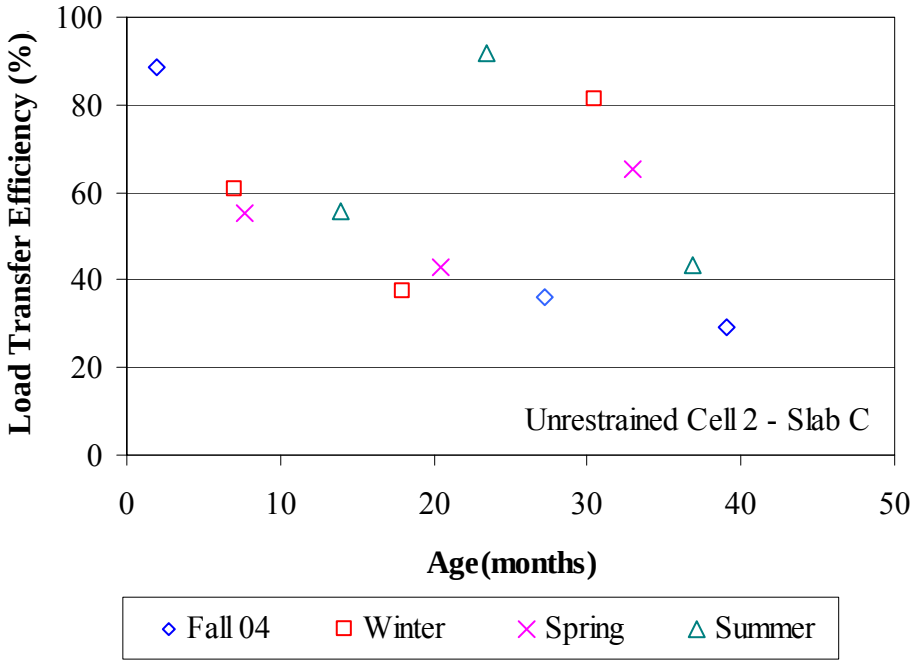

Figure A3. Relationship between load transfer efficiency and age of the pavement for the unrestrained Cell 2.

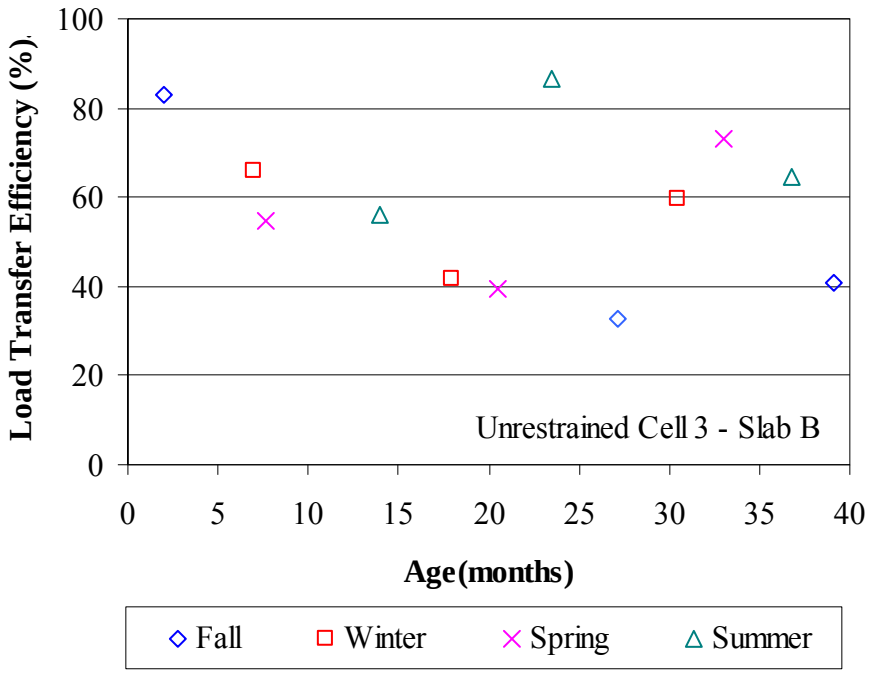

Figure A4. Relationship between load transfer efficiency and age of the pavement for the unrestrained Cell 3.

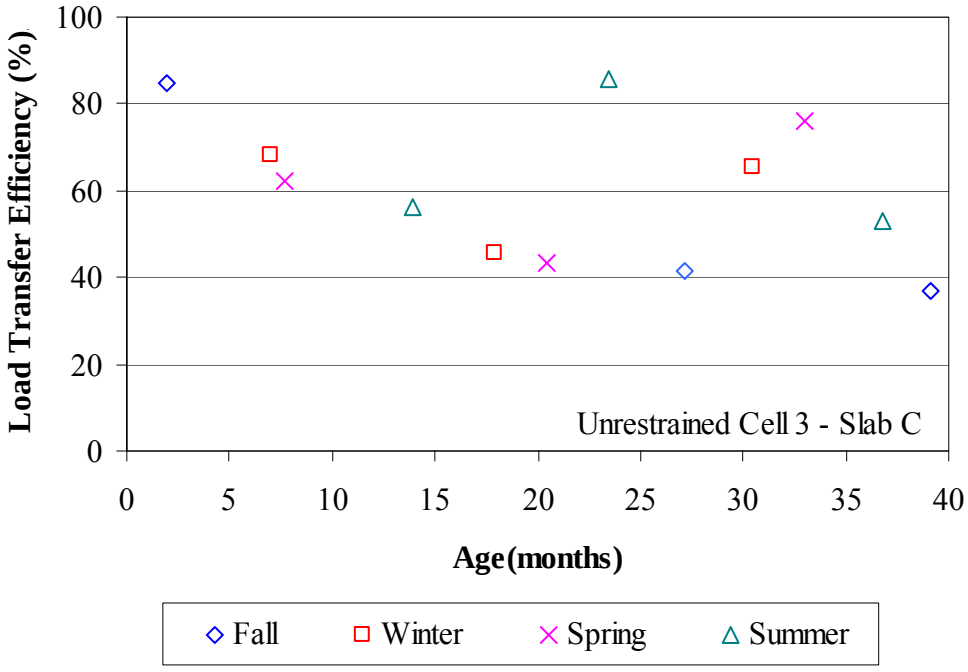

Figure A5. Relationship between load transfer efficiency and age of the pavement for the unrestrained Cell 3.

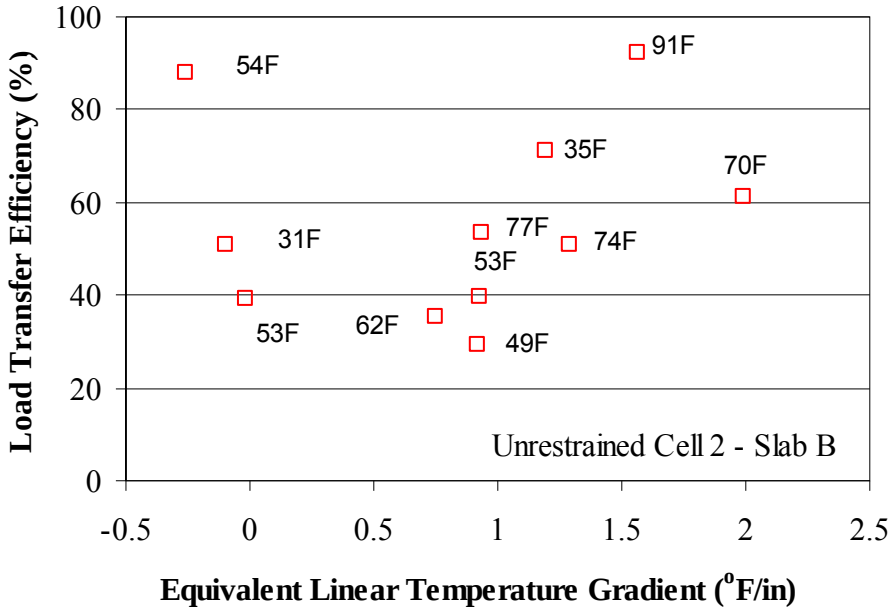

Figure A6. Relationship between load transfer efficiency and equivalent linear temperature gradient for the unrestrained Cell 2.

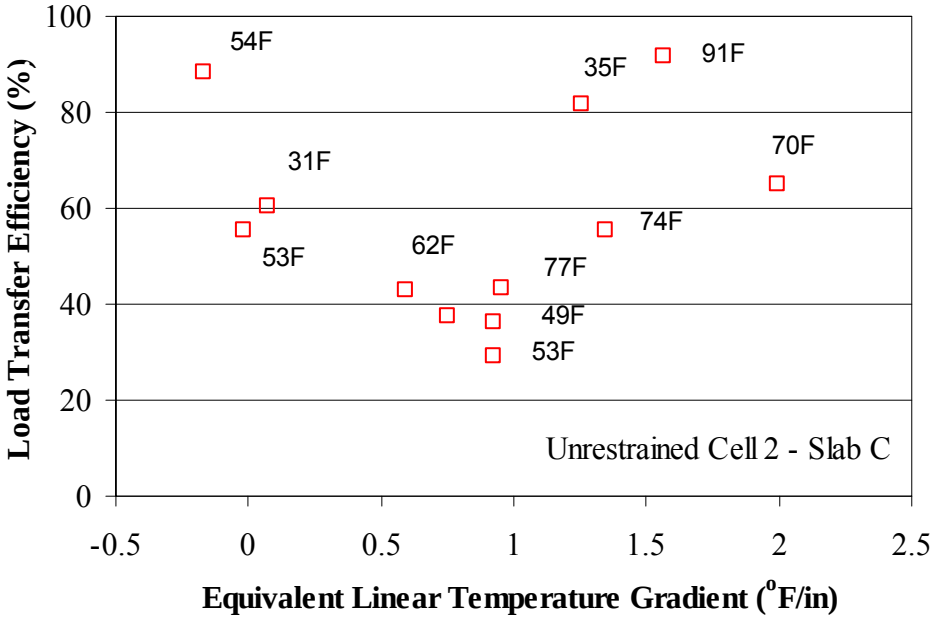

Figure A7. Relationship between load transfer efficiency and equivalent linear temperature gradient for the unrestrained Cell 2.

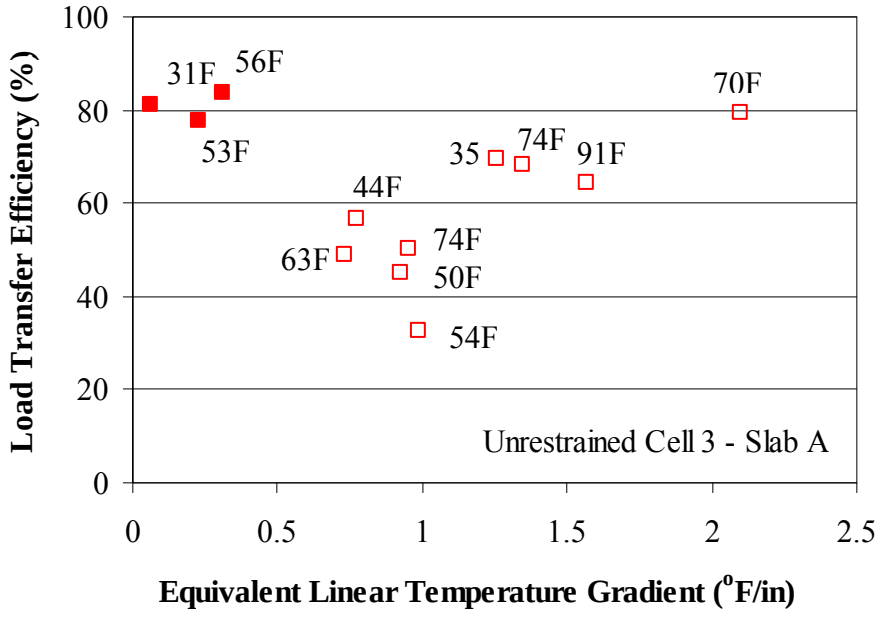

Figure A8. Relationship between load transfer efficiency and equivalent linear temperature gradient for the unrestrained Cell 3.

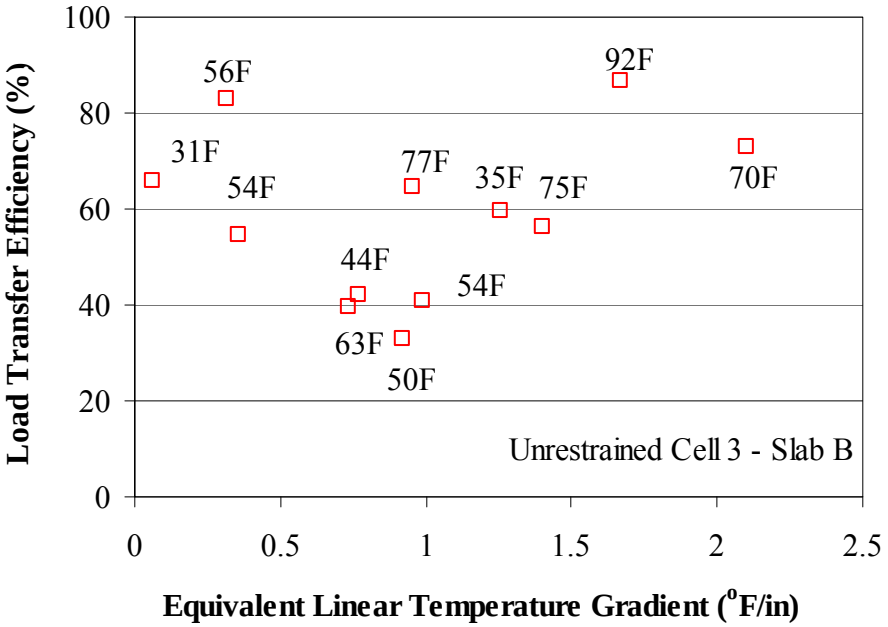

Figure A9. Relationship between load transfer efficiency and equivalent linear temperature gradient for the unrestrained Cell 3.

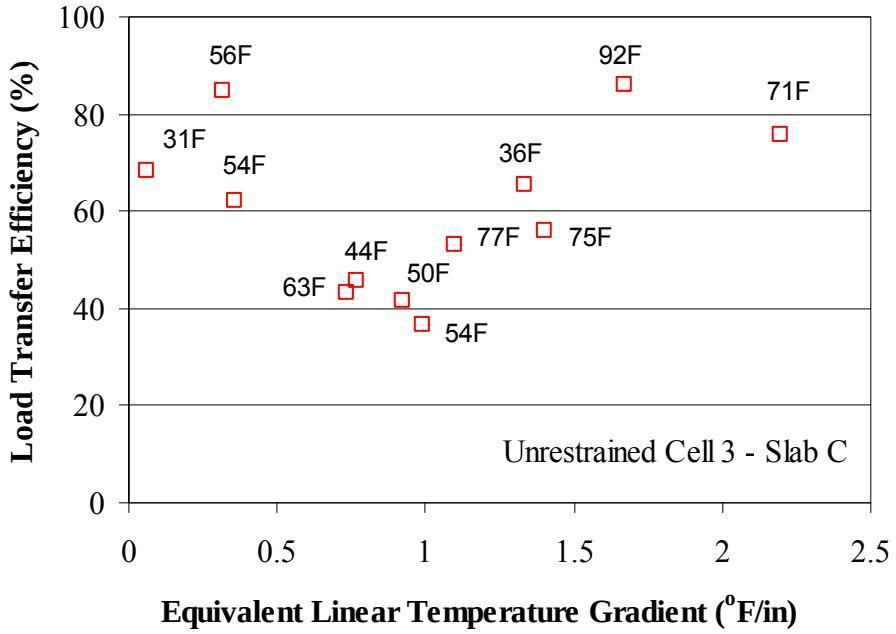

Figure A10. Relationship between load transfer efficiency and equivalent linear temperature gradient for the unrestrained Cell 3.

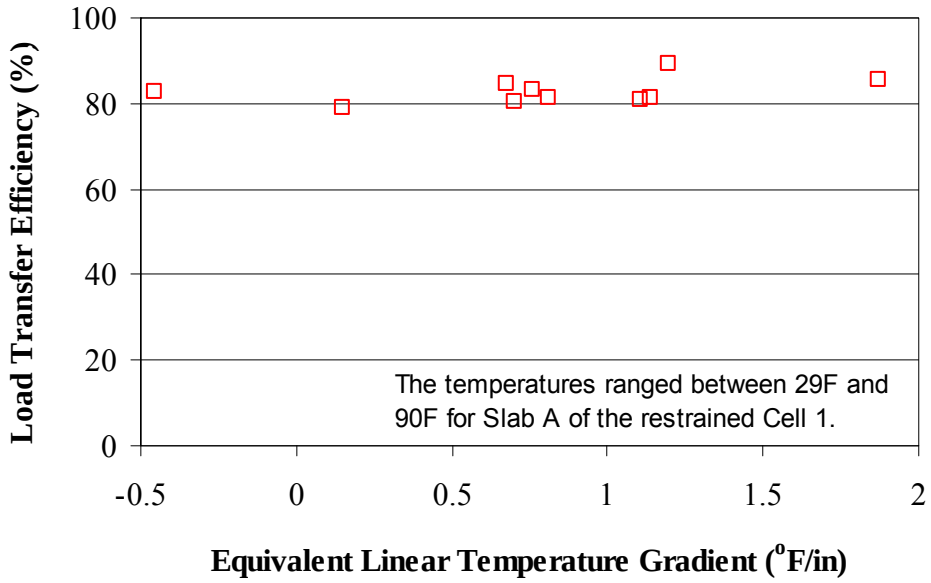

Figure A11. Relationship between load transfer efficiency and equivalent linear temperature gradient for the restrained Cell 1.

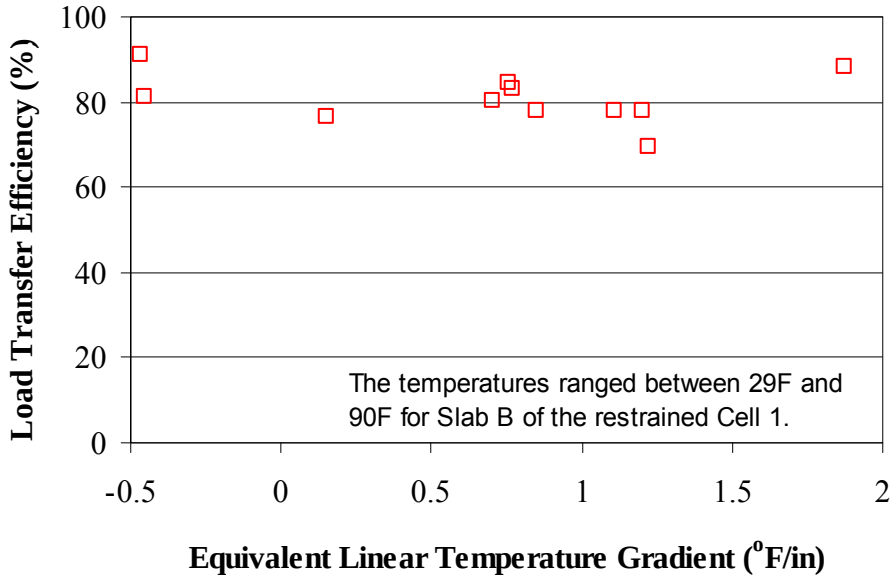

Figure A12. Relationship between load transfer efficiency and equivalent linear temperature gradient for the restrained Cell 1.

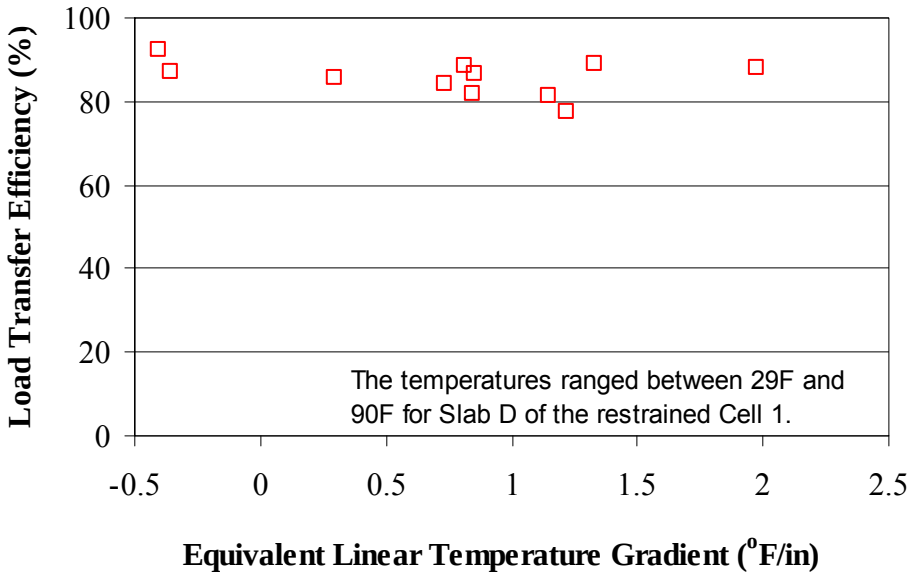

Figure A13. Relationship between load transfer efficiency and equivalent linear temperature gradient for the restrained Cell 1.

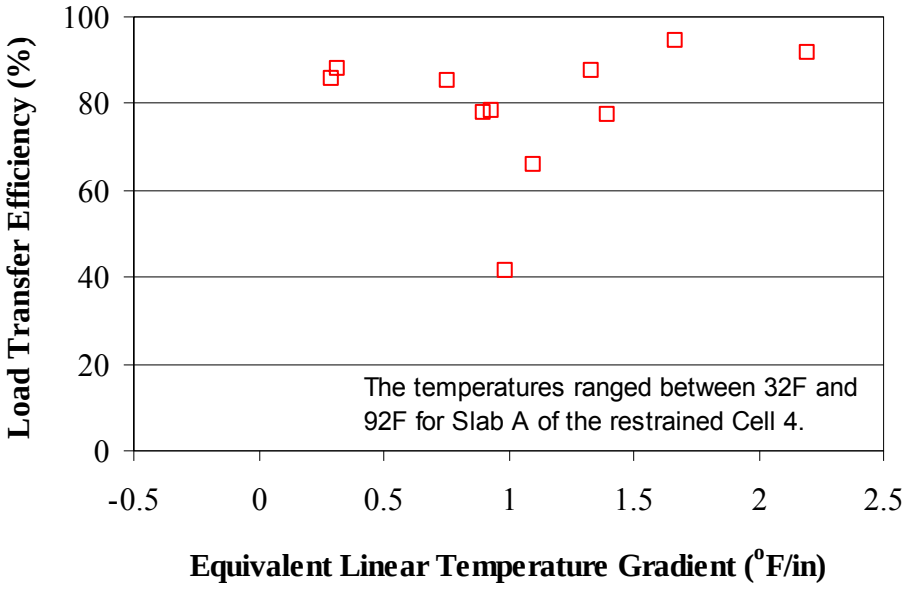

Figure A14. Relationship between load transfer efficiency and equivalent linear temperature gradient for the restrained Cell 4.

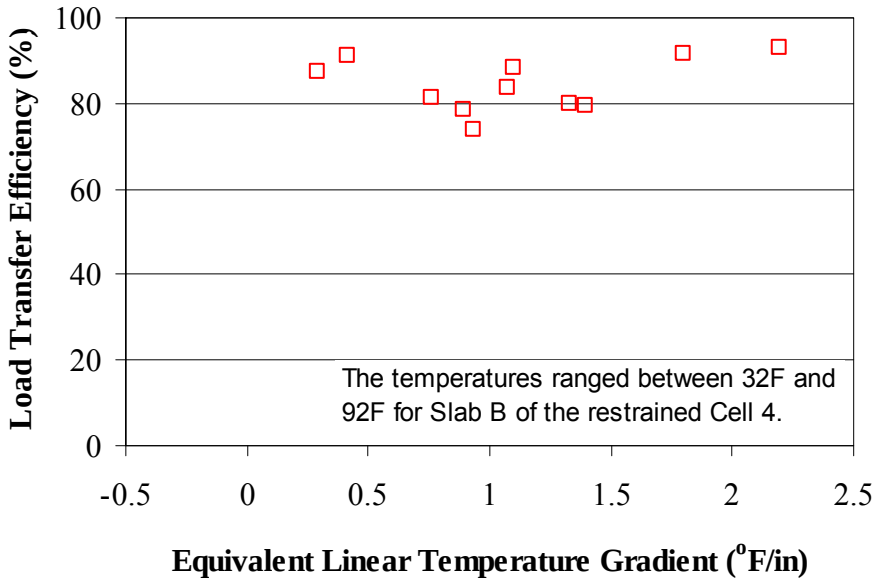

Figure A15. Relationship between load transfer efficiency and equivalent linear temperature gradient for the restrained Cell 4.

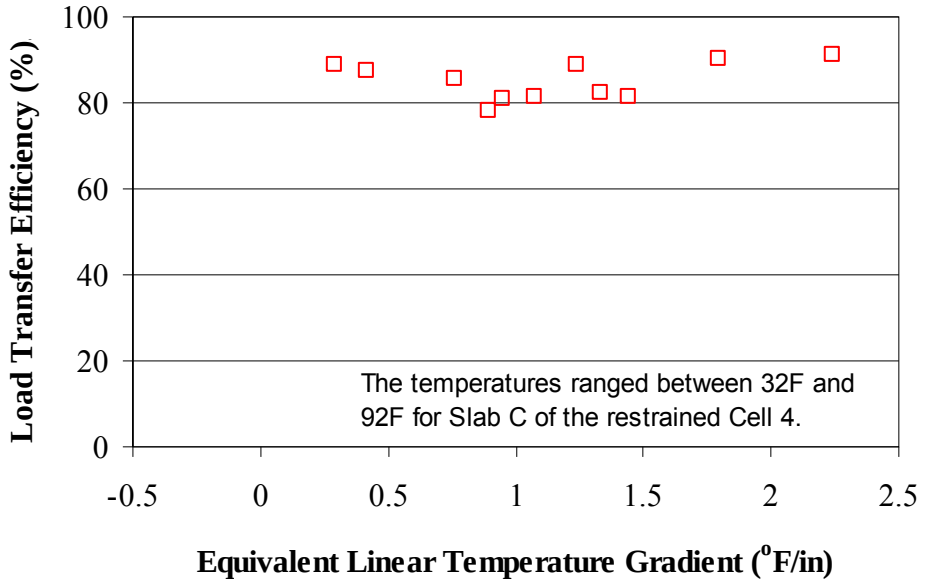

Figure A16. Relationship between load transfer efficiency and equivalent linear temperature gradient for the restrained Cell 4.

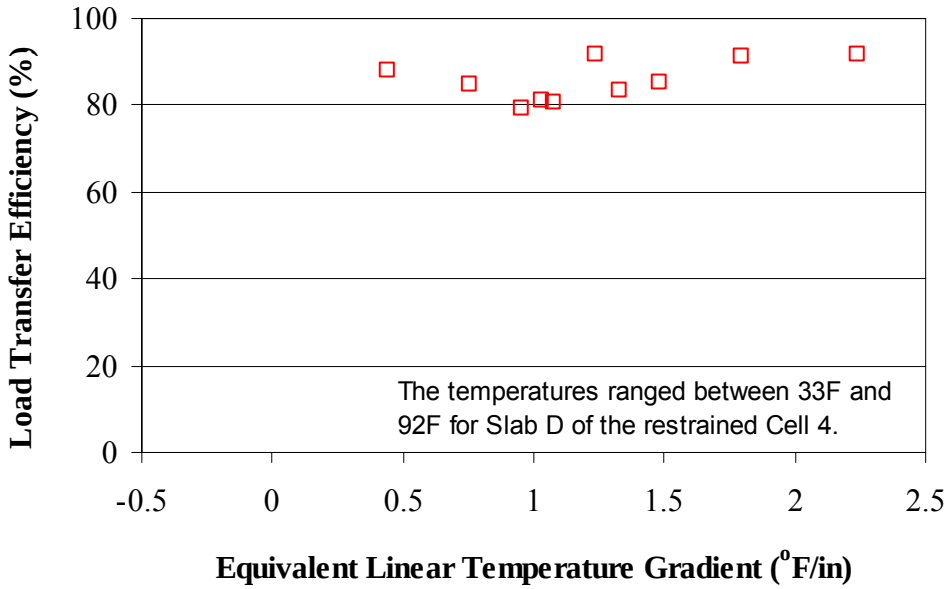

Figure A17. Relationship between load transfer efficiency and equivalent linear temperature gradient for the restrained Cell 4.

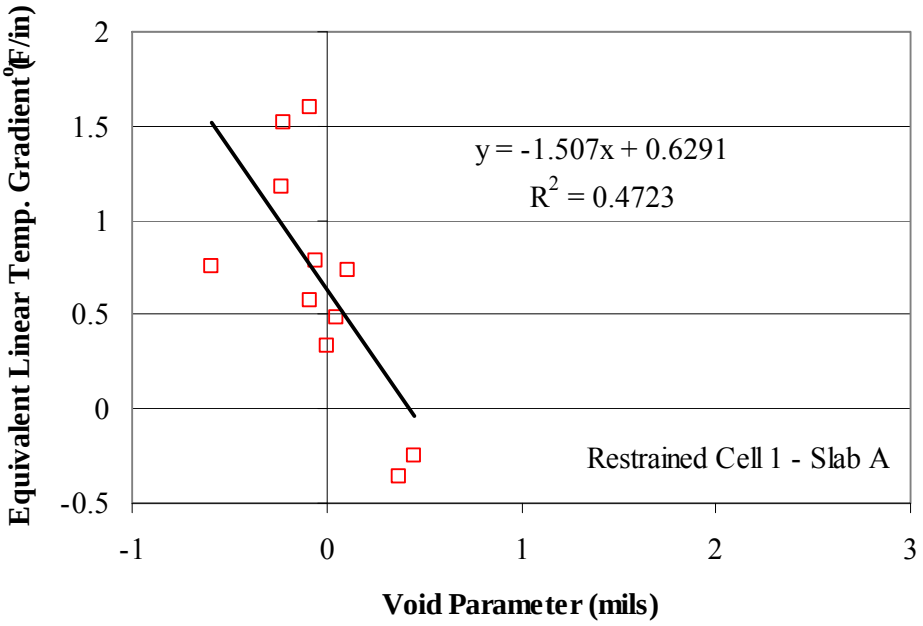

Figure A18. Relationship between the Void parameter and the equivalent linear temperature gradient present during testing for the restrained Slab A in Cell 1.

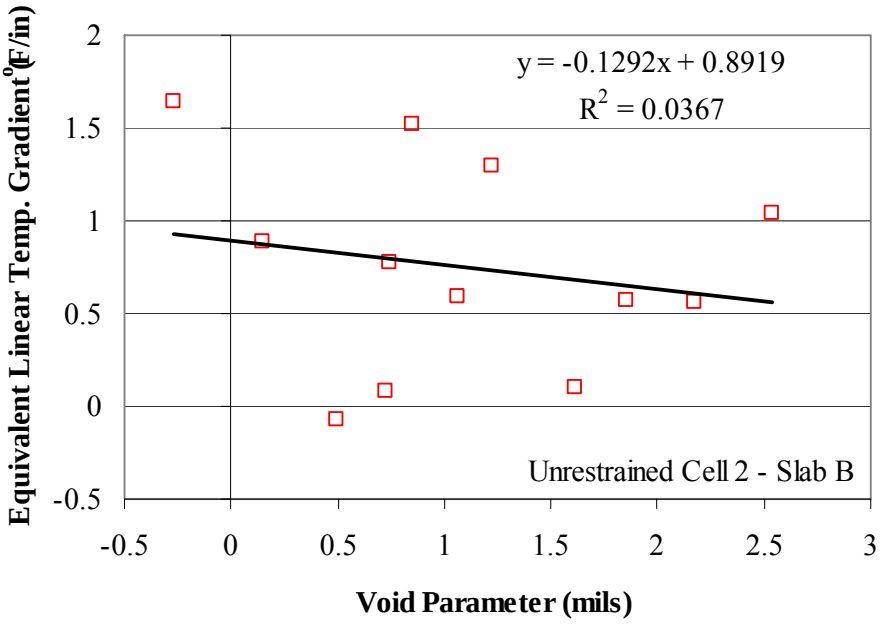

Figure A19. Relationship between the Void parameter and the equivalent linear temperature gradient present during testing for the unrestrained Slab B in Cell 2.

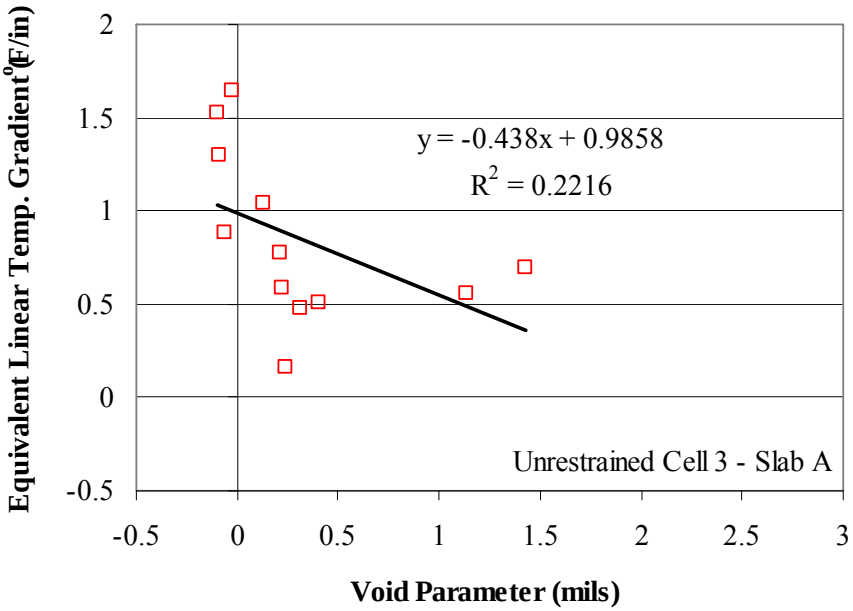

Figure A20. Relationship between the Void parameter and the equivalent linear temperature gradient present during testing for the unrestrained Slab A in Cell 3.

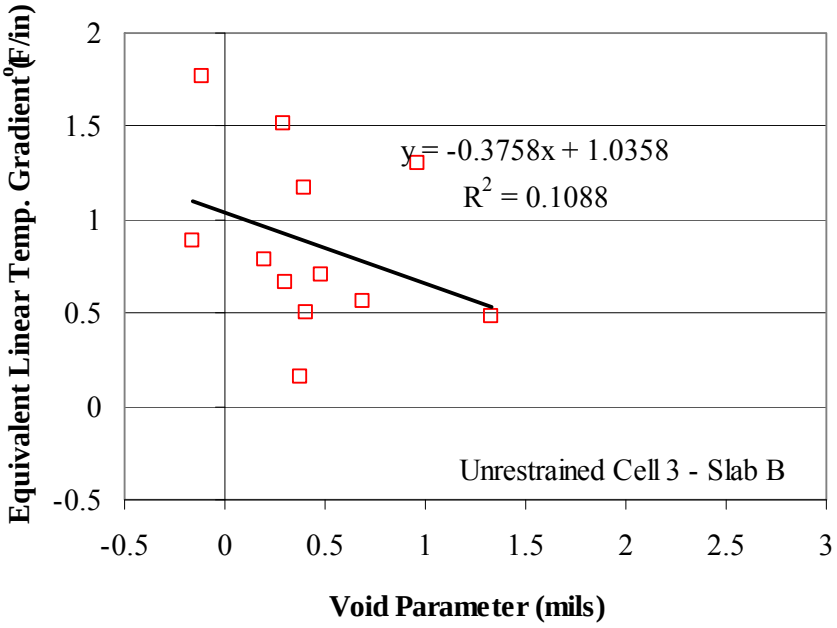

Figure A21. Relationship between the Void parameter and the equivalent linear temperature gradient present during testing for the unrestrained Slab B in Cell 3.

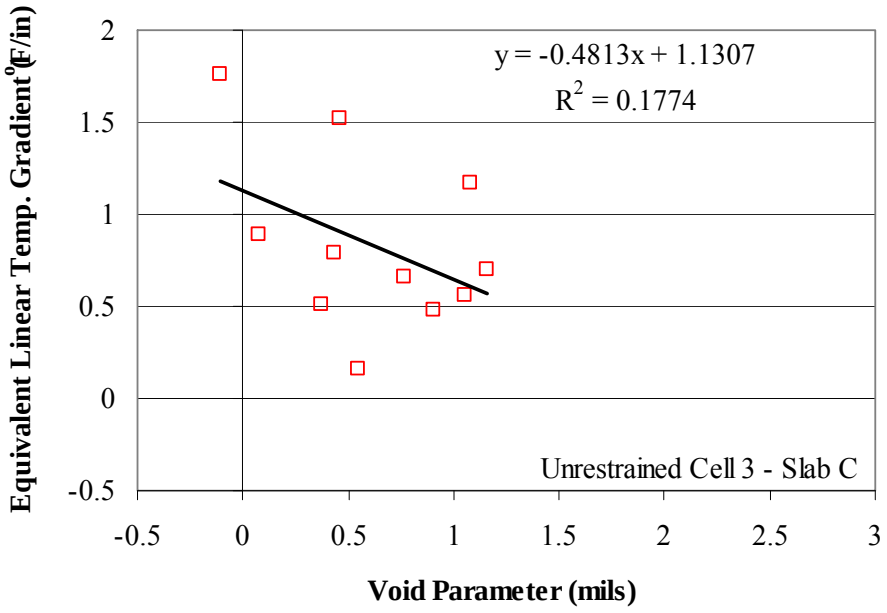

Figure A22. Relationship between the Void parameter and the equivalent linear temperature gradient present during testing for the unrestrained Slab C in Cell 3.

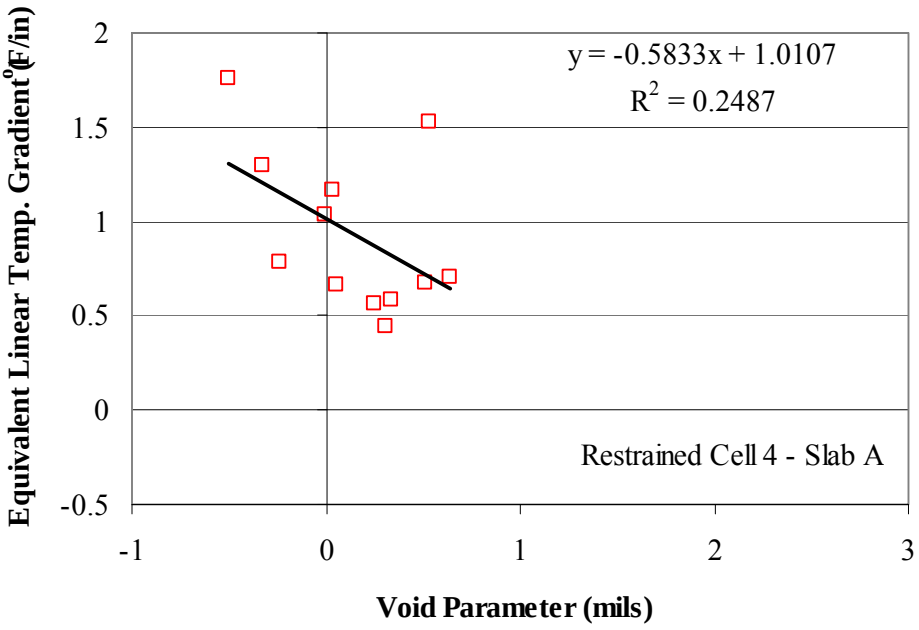

Figure A23. Relationship between the Void parameter and the equivalent linear temperature gradient present during testing for the restrained Slab A in Cell 4.

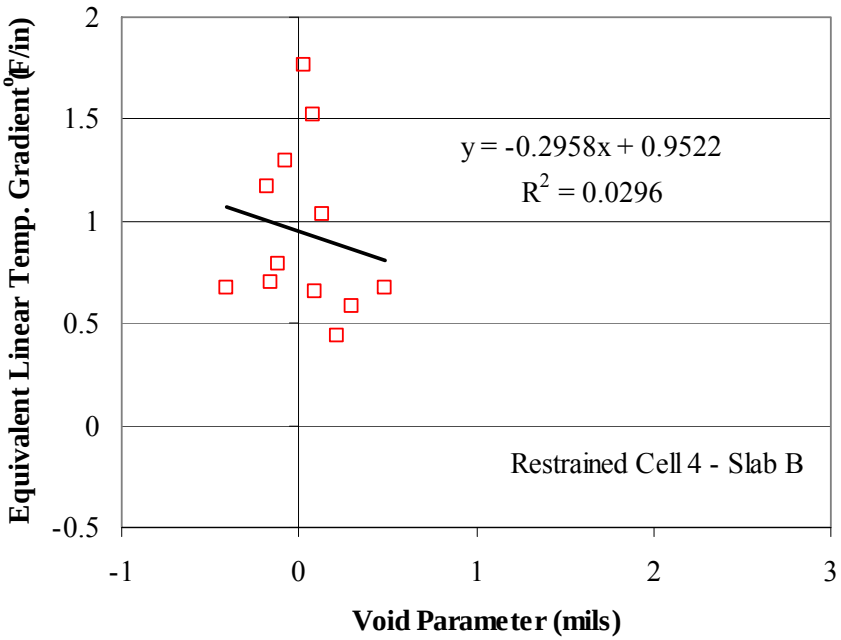

Figure A24. Relationship between the Void parameter and the equivalent linear temperature gradient present during testing for the restrained Slab B in Cell 4.

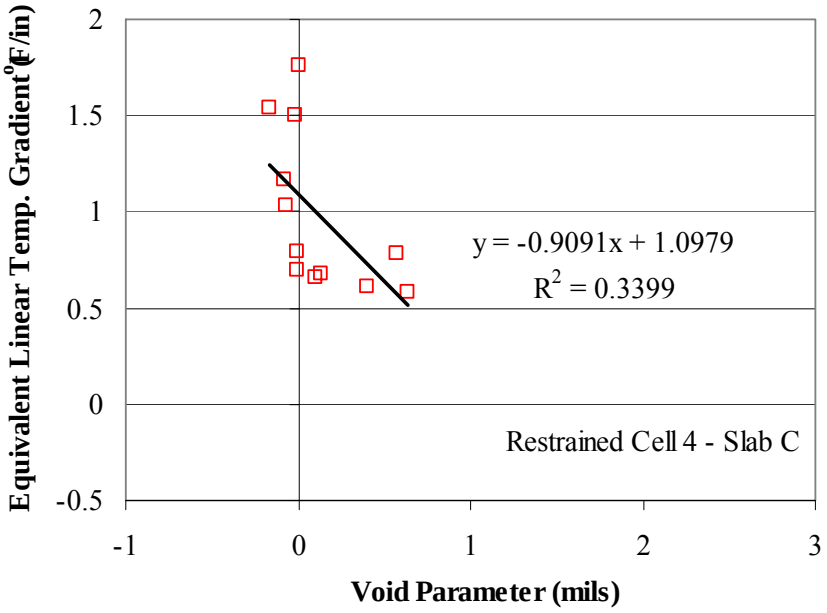

Figure A25. Relationship between the Void parameter and the equivalent linear temperature gradient present during testing for the restrained Slab C in Cell 4.

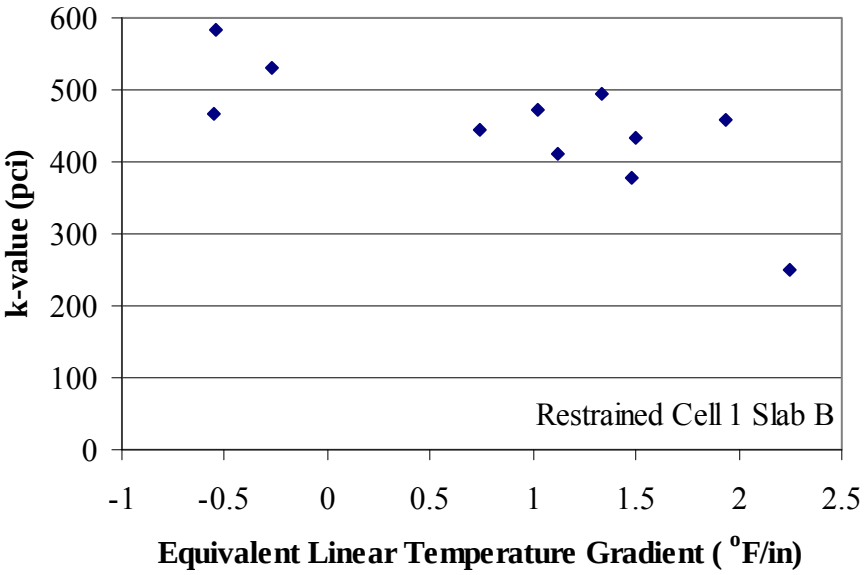

Figure A26. Comparison of the support conditions beneath the slab and the equivalent linear temperature gradient of the slab during testing for restrained Slab B in Cell 1.

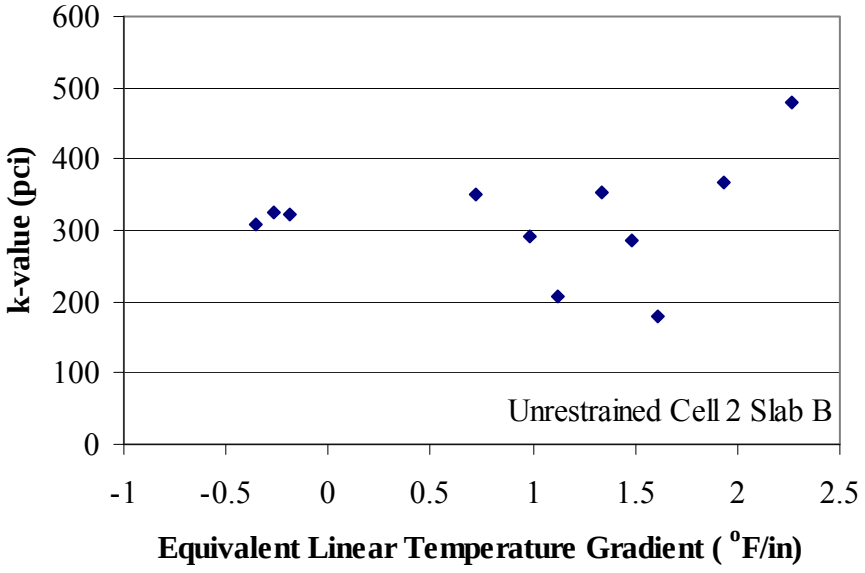

Figure A27. Comparison of the support conditions beneath the slab and the equivalent linear temperature gradient of the slab during testing for unrestrained Slab B in Cell 2.

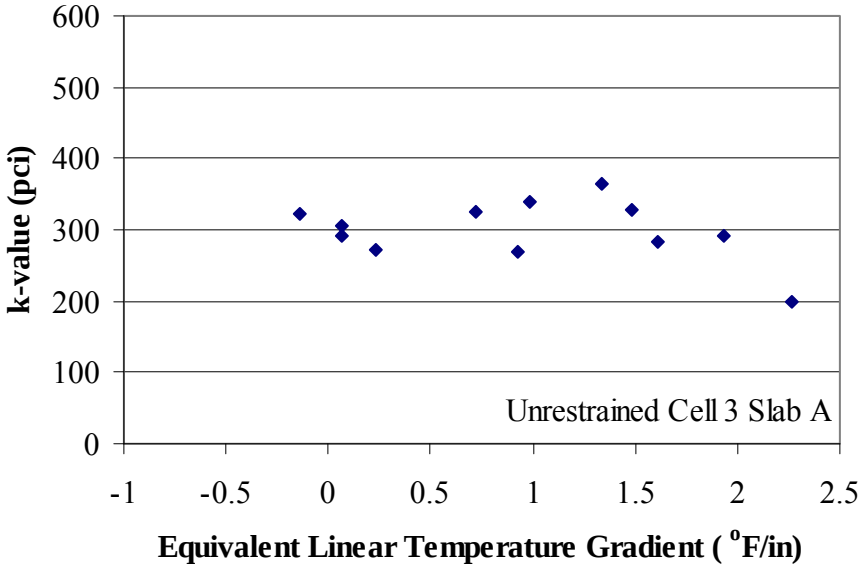

Figure A28. Comparison of the support conditions beneath the slab and the equivalent linear temperature gradient of the slab during testing for unrestrained Slab A in Cell 3.

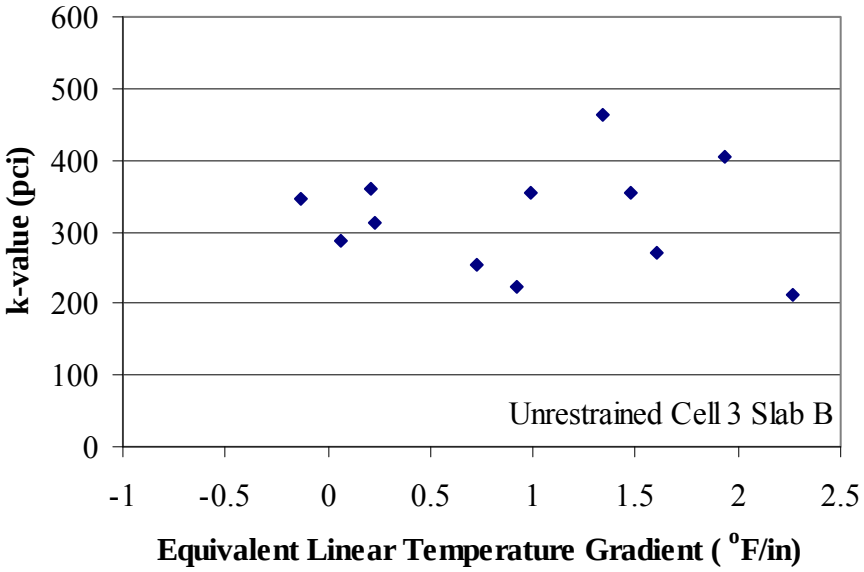

Figure A29. Comparison of the support conditions beneath the slab and the equivalent linear temperature gradient of the slab during testing for unrestrained Slab B in Cell 3.

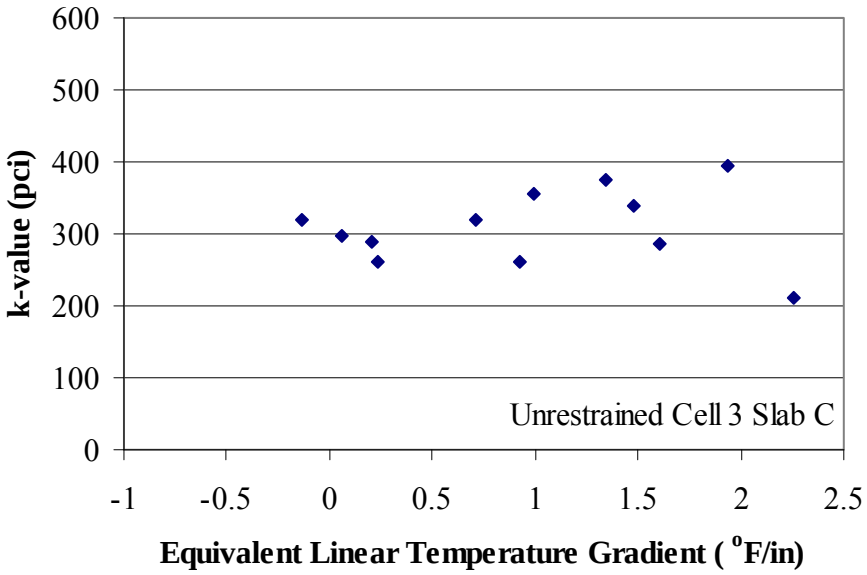

Figure A30. Comparison of the support conditions beneath the slab and the equivalent linear temperature gradient of the slab during testing for unrestrained Slab C in Cell 3.

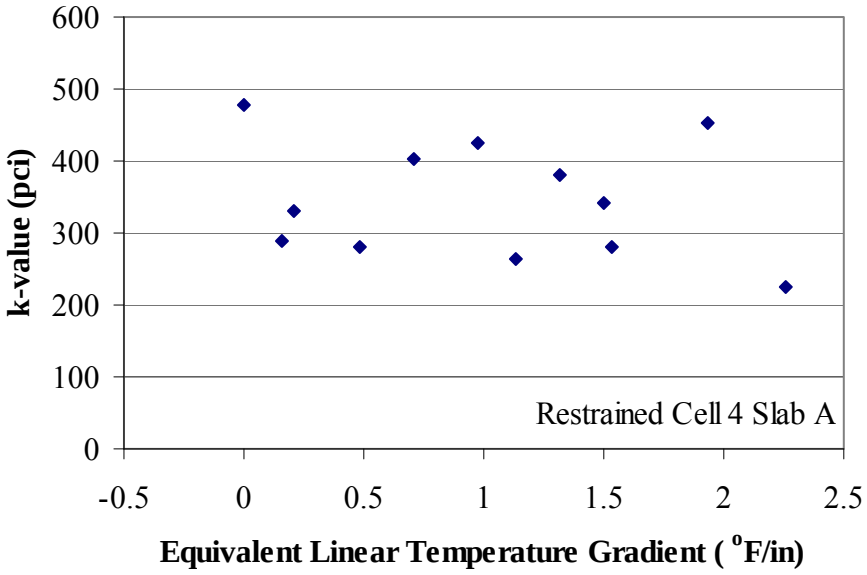

Figure A31. Comparison of the support conditions beneath the slab and the equivalent linear temperature gradient of the slab during testing for restrained Slab A in Cell 4.

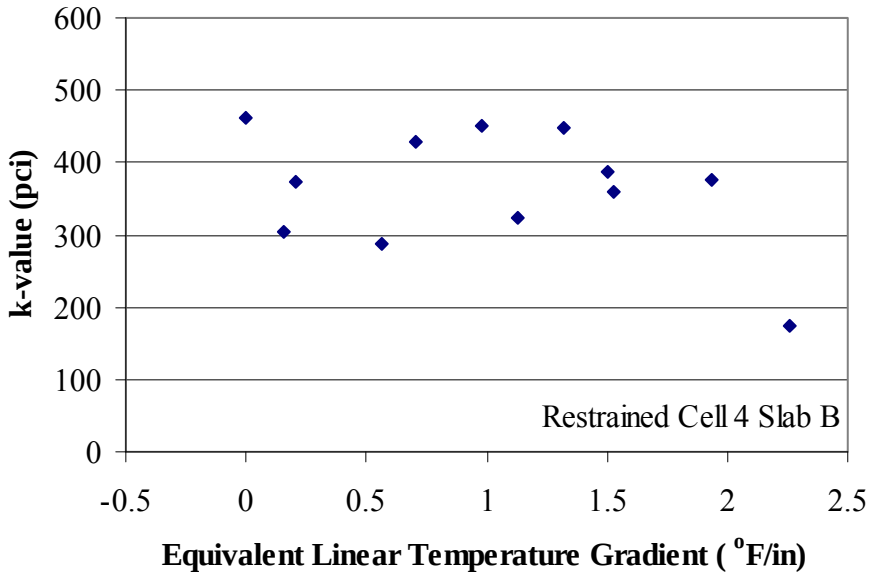

Figure A32. Comparison of the support conditions beneath the slab and the equivalent linear temperature gradient of the slab during testing for restrained Slab B in Cell 4.

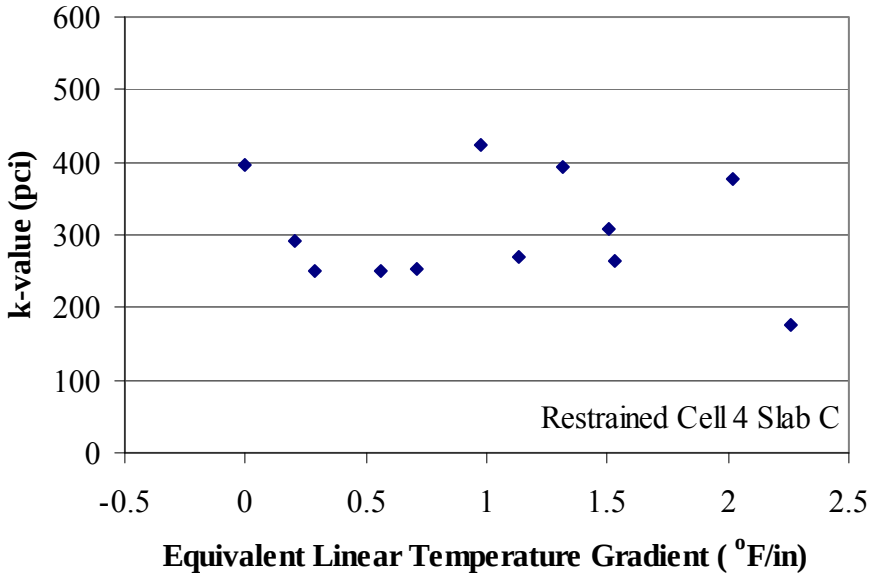

Figure A33. Comparison of the support conditions beneath the slab and the equivalent linear temperature gradient of the slab during testing for restrained Slab C in Cell 4.

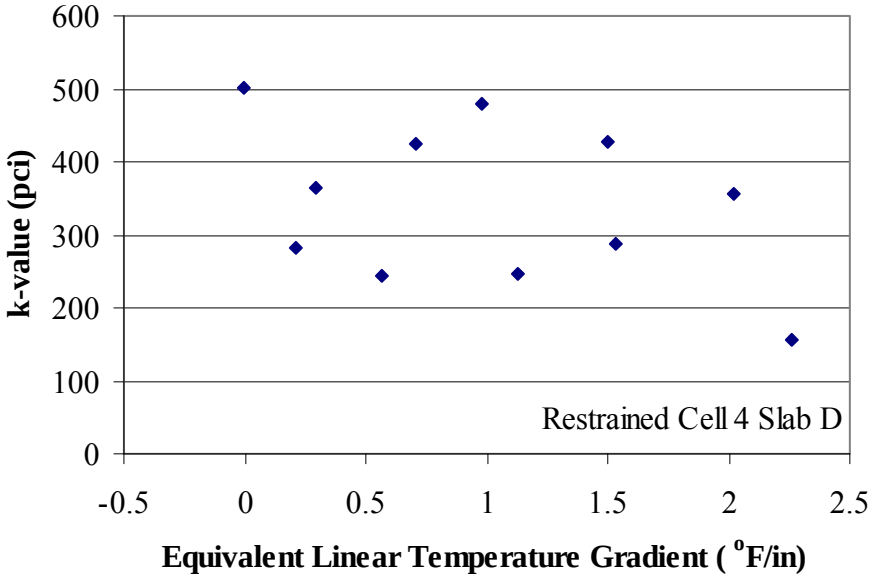

Figure A34. Comparison of the support conditions beneath the slab and the equivalent linear temperature gradient of the slab during testing for restrained Slab D in Cell 4.

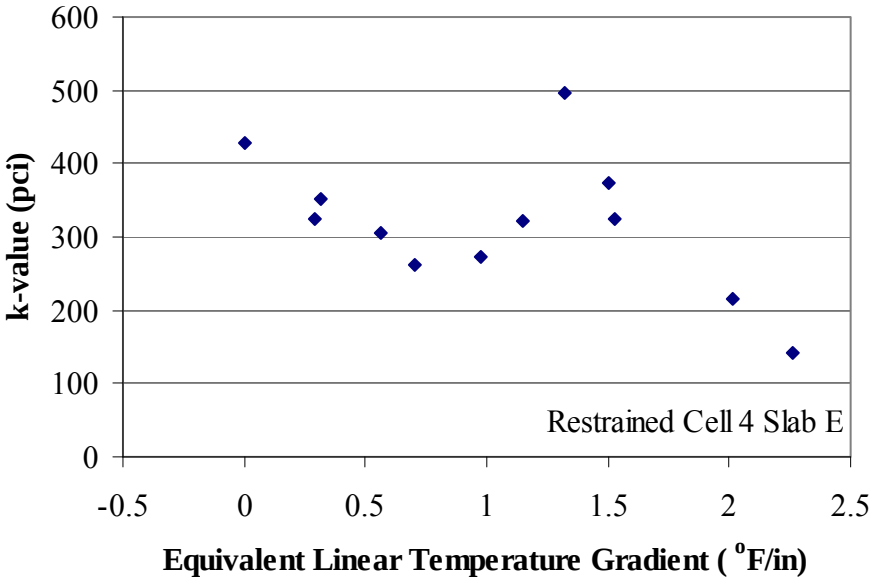

Figure A35. Comparison of the support conditions beneath the slab and the equivalent linear temperature gradient of the slab during testing for restrained Slab E in Cell 4.

APPENDIX B

PAVEMENT RESPONSE TO TRUCK LOADS

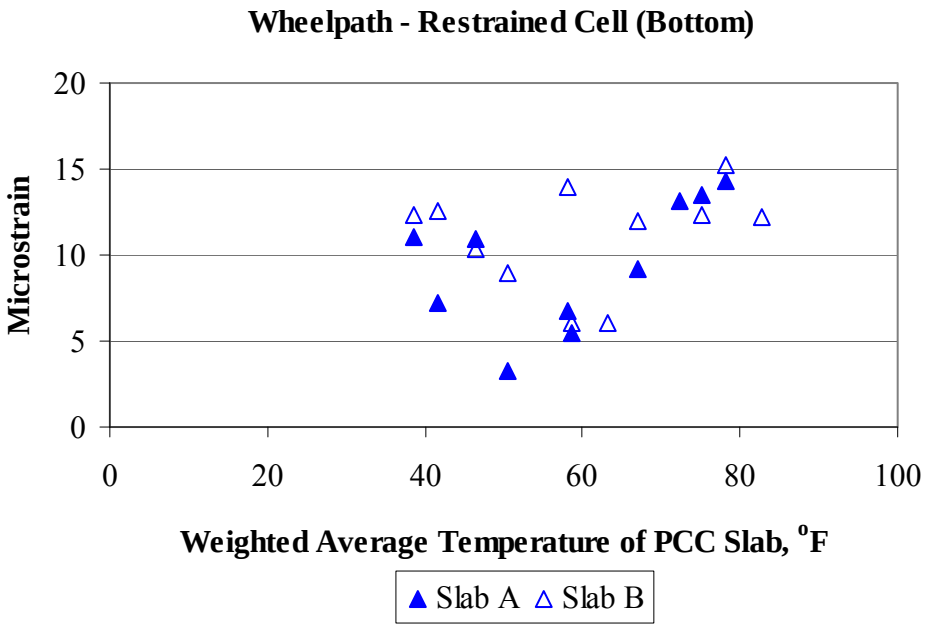

Figure B 1. Relationship between strain measured in the wheelpath at the bottom of the restrained slabs and slab temperature.

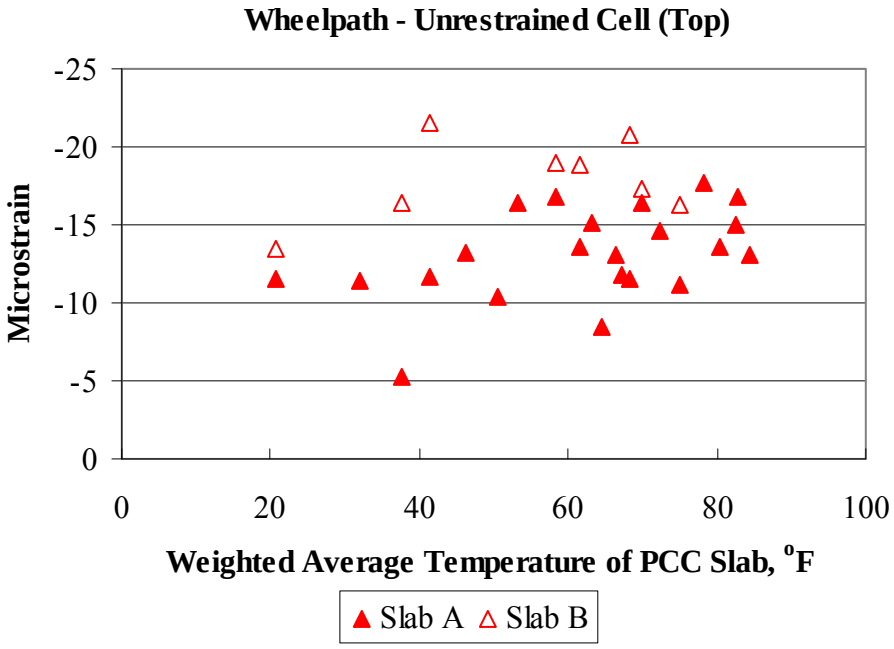

Figure B 2. Relationship between strain measured in the wheelpath at the top of the unrestrained slabs and slab temperature.

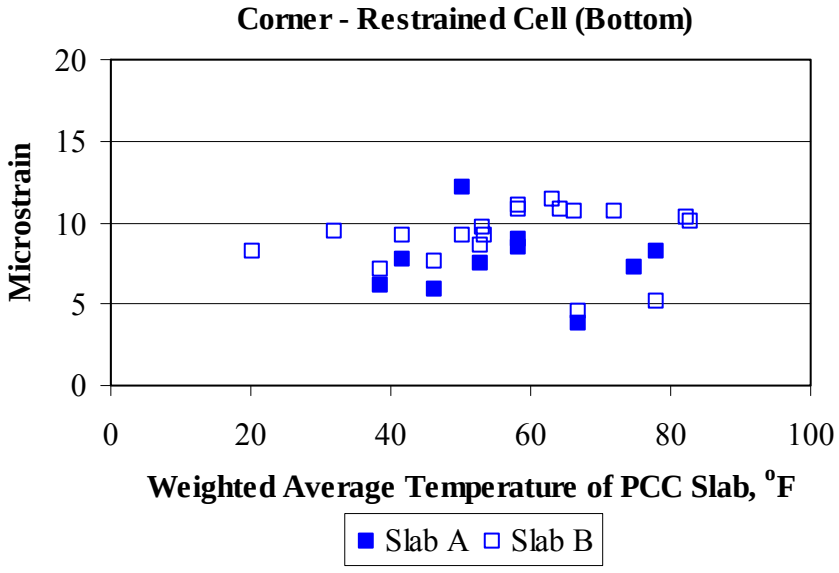

Figure B 3. Relationship between strain measured in the corner at the bottom of the restrained slabs and slab temperature.

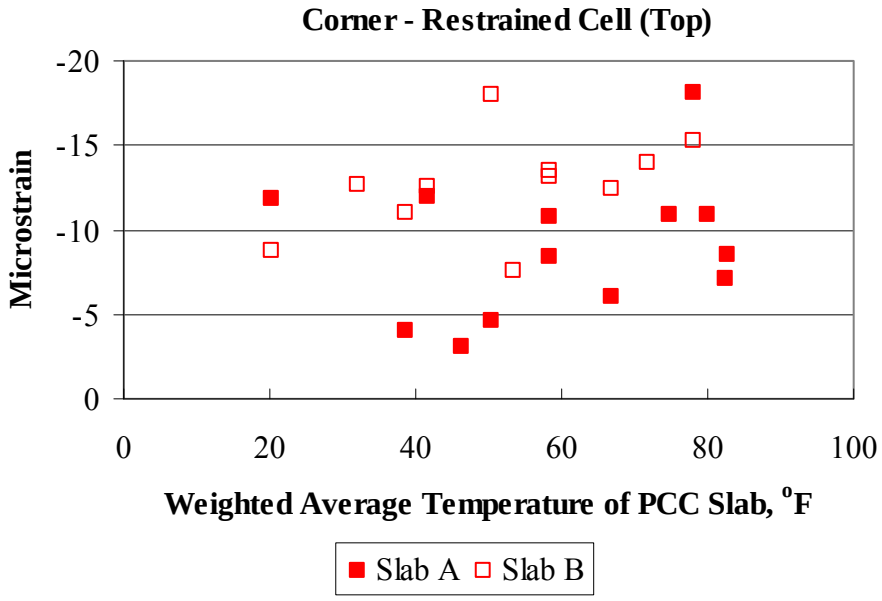

Figure B 4. Relationship between strain measured in the corner at the top of the unrestrained slabs and slab temperature.

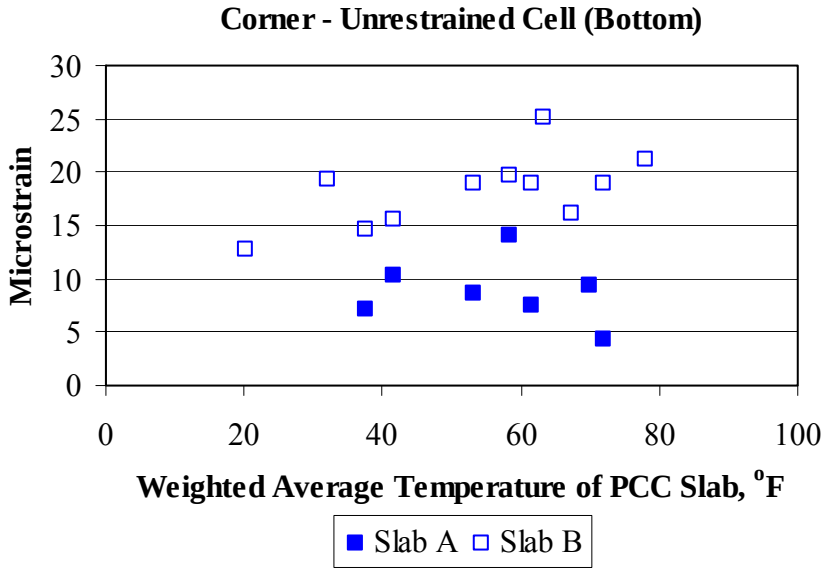

Figure B5. Relationship between strain measured in the corner at the bottom of the unrestrained slabs and slab temperature.

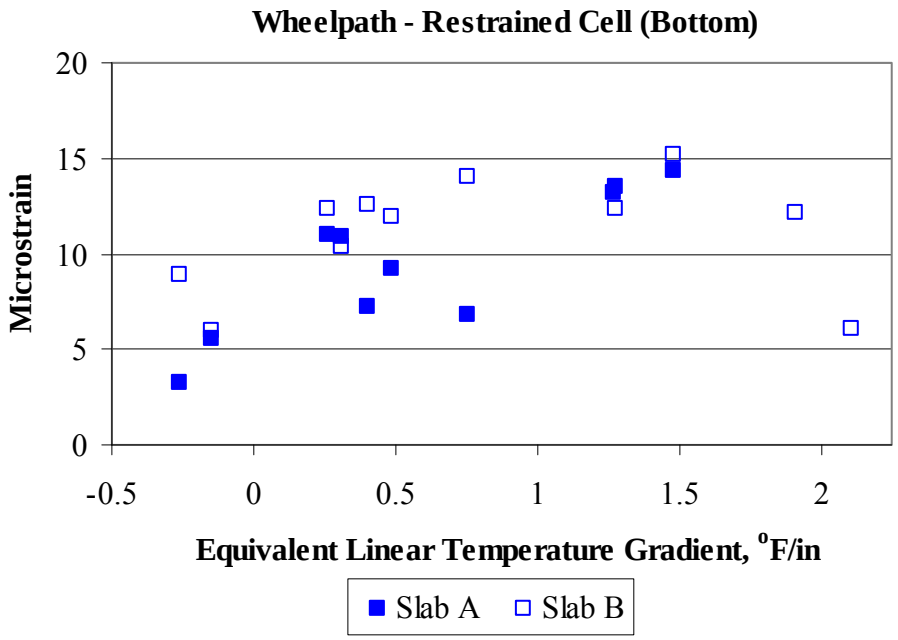

Figure B6. Relationship between strain measured in the wheelpath at the bottom of the restrained slabs and the temperature gradient in the slab.

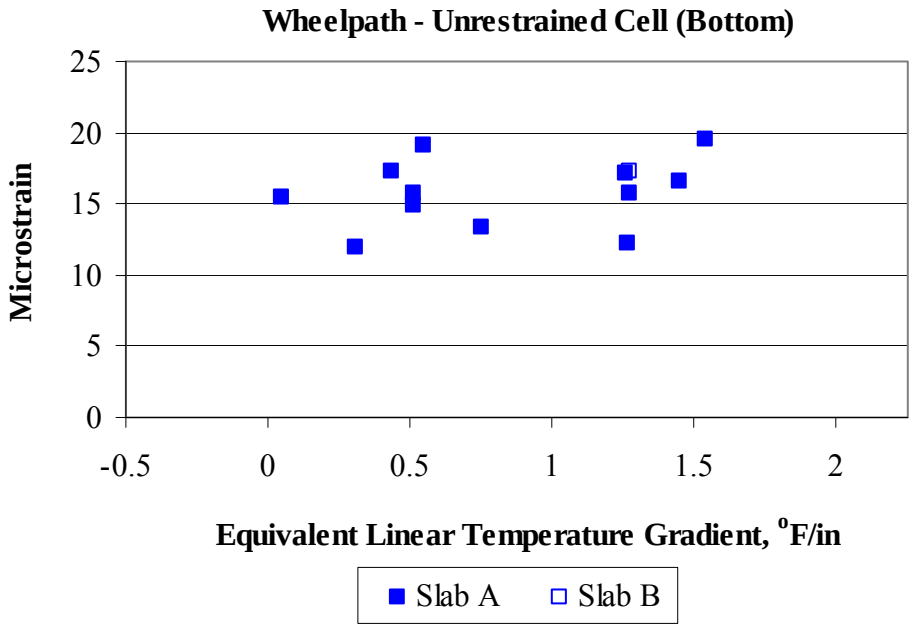

Figure B7. Relationship between strain measured in the wheelpath at the bottom of the unrestrained slabs and the temperature gradient in the slab.

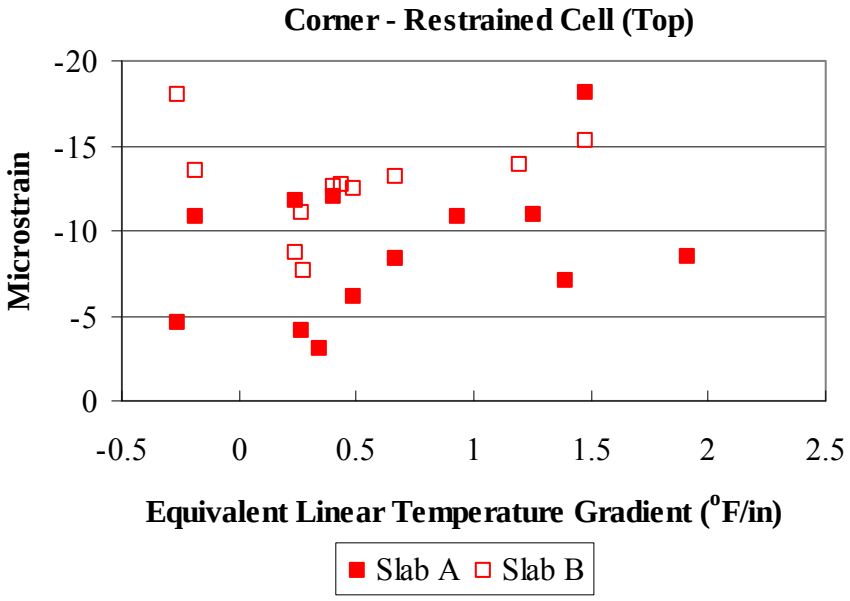

Figure B8. Relationship between strain measured in the corner at the top of the restrained slabs and the temperature gradient in the slab.

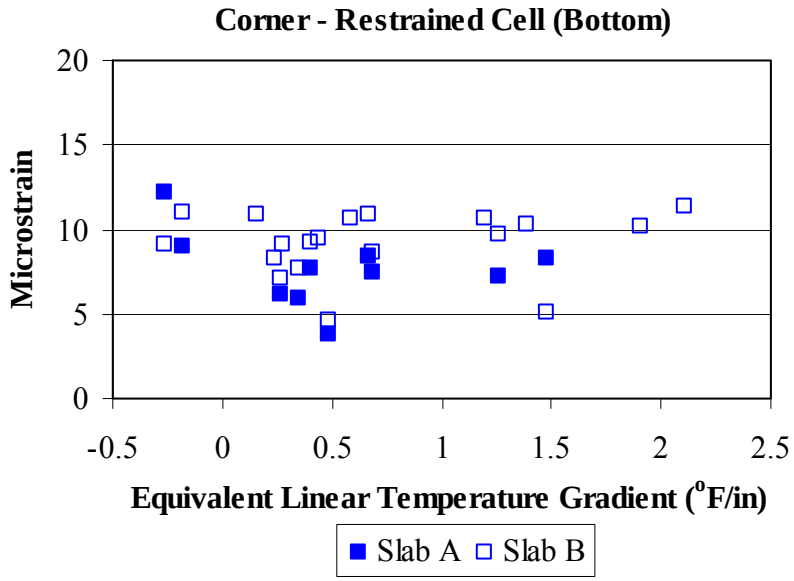

Figure B9. Relationship between strain measured in the corner at the bottom of the restrained slabs and the temperature gradient in the slab.

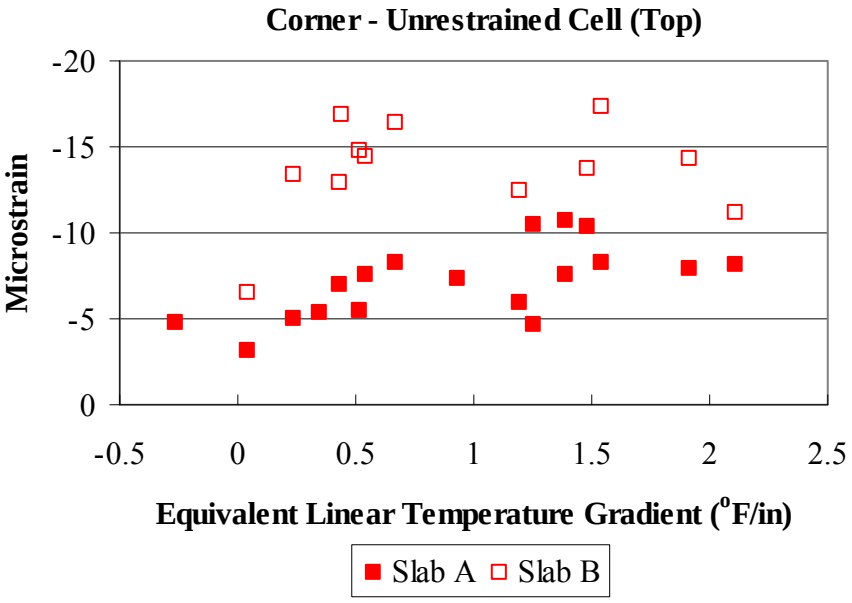

Figure B10. Relationship between strain measured in the corner at the top of the unrestrained slabs and the temperature gradient in the slab.

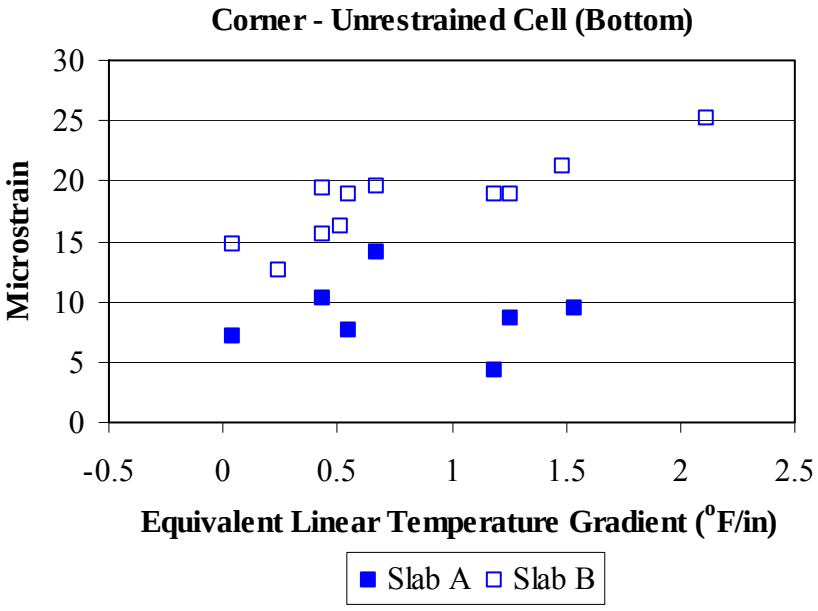

Figure B11. Relationship between strain measured in the corner at the bottom of the unrestrained slabs and the temperature gradient in the slab.

BIBLIOGRAPHY

American Association of State Highway and Transportation Officials, "AASHTO Guide for Design of Pavement Structures," *AASHTO*, Washington, D.C, 1993.

Asbahan, R.E., J.K. McCracken, and J.M. Vandenbossche, "S.R.-22 Smart Pavement Phase II: One-Year Material Properties and Pavement Response Characteristics for Jointed Plain Concrete Pavements," *Pennsylvania Department of Transportation and the Federal Highway Administration*, University of Pittsburgh, Department of Civil and Environmental Engineering, Pittsburgh, Pennsylvania, November 2006.

Asbahan, R. E., "Defining the Built-In Construction Gradient and Evaluating the Effects of Environmental Conditions on a Jointed Plain Concrete Pavement," Department of Civil and Environmental Engineering, Pittsburgh, Pittsburgh, Doctor of Philosophy Dissertation, Work-In-Progress, 2008.

Brill, R.D., "Field Verification of a 3D Finite Element Rigid Airport Pavement Model," Federal Aviation Administration DOT/FAA/AR-00/33, Washington D.C, July 2000.

Burnham, T., "Seasonal Load Response Behavior of a Thin Portland Cement Concrete Pavement," *Transportation Research Journal: Transportation Research Record 1819*, National Research Council, Washington, DC, 2003.

Crovetti, J.A. and M.I. Darter, "Void Detection for Jointed Concrete Pavements," Transportation Research Record 1041, Transportation Research Board, 1985.

Dong, M., G. Hayhoe, and Y.W. Fang, "Runway Instrumentation at Denver International Airport: Dynamic Sensor Data Processing," Aircraft/Pavement Technology – In the Midst of Change, Proceeding of the 1997 Airfield Pavement Conference, Seattle, Washington, F.V. Hermann, editor, ASCE, 1997.

Federal Highway Administration, "Concrete Pavement Rehabilitation Guide for Load Transfer Restoration," FHWA-SA-97103, Washington, DC, 1997.

Guo, E. and M. Dong, "Evaluation Criteria of a Computer Program for Pavement Response Analysis," Galaxy Scientific Corporation, Egg Harbor Twp, New Jersey, June 2003.

Guo, E. and F. Pecht, "Critical Gear Configurations and Positions for Rigid Airport Pavements – Observations and Analysis," ASCE Geotechnical Special Publication No. 154. Pavement Mechanics and Performance, Proceedings of Sessions of Conference GeoShanghai, June 6-8, Shanghai, China, 2006.

Hall, K. T., M. I. Darter, T. E. Hoerner and L. Khazanovich, *LTPP Data Analysis-Phase I, Validation of Guidelines for k-Value Selection and Concrete Pavement Performance Prediction*, Technical Report FHWA-RD-96-198, Washington, DC, 1997.

Huang, Y. H., *Pavement Analysis and Design, Second Edition*, Pearson Prentice Hall, Upper Saddle River, NJ, 2004.

Janssen, D., "Moisture in Portland Cement Concrete," Transportation *Research Journal: Transportation Research Record 1121*, National Research Council, Washington DC, 1987.

Janssen, D. J. and M. B. Snyder, "Temperature-Moment Concept for Evaluating Pavement Temperature Data Technical Note No. 19948," *Journal of Infrastructure Systems*, Vol. 6, No. 2, American Society of Civil Engineers. Reston, VA, pp. 81-83, June 2000.

Joeng, J.H. and D. Zollinger, "Environmental Effects on the Behavior of Jointed Plain Concrete Pavements," Journal *of Transportation Engineering,* ASCE, pg 140-148, February 2005.

Khazanovich, L. S.D. Tayabji, and M.I. Darter, "Backcalculation of Layer Parameters for LTPP Test Sections, Volume I: Slab on Elastic Solid and Slab on Dense-Liquid Foundation Analysis of Rigid Pavements," Technical Report FHWA-RD-00-086, Federal Highway Administration, McLean, VA, 2001.

Khazanovich, L. and A. Gotlif, (October 2003), "Evaluation of Joint and Crack Load Transfer Final Report," Technical Report FHWA-RD-02-088, Federal Highway Administration, McLean, VA.

Lee, X., M. Hovan, R. King, M. Dong, and G. Hayhoe, "Runway Instrumentation at Denver International Airport: Development of Database," Aircraft/Pavement technology – In the Midst of Change, Proceeding of the 1997 Airfield Pavement Conference, Seattle, Washington, F.V. Hermann, editor, ASCE, 1997.

Rufino, D. and J. Roesler, "Effect of Slab-Base Interaction on Measured Concrete Pavement Response," *Journal of Transportation Engineering*, 132(5), 425-433, May 2006.

Tayabji, S.D., C.G. Hall, and P.A. Okamoto, "Effect of Frozen Support and Tridem Axles on Concrete Pavement Performance," *Transportation Research Journal: Transportation Research Record 954*, National Research Council, Washington DC, 1984.

Vandenbossche, J. M., "Effects of Slab Temperature Profiles on the Use of Falling Weight Deflectometer Data to Monitor Joint Performance and Detect Voids," *Transportation*

Research Journal: Transportation Research Record 2005, National Research Council, Washington, DC, 2007.

Wells, S. A., B.M. Phillips, and J.M. Vandenbossche, (June 2005), "S.R.-22 Smart Pavement Phase I: Early-Age Material Properties and Pavement Response Characteristics for Jointed Plain Concrete Pavements; 28-Day Report Final Revision," *Pennsylvania Department of Transportation and the Federal Highway Administration*, University of Pittsburgh, Department of Civil and Environmental Engineering, Pittsburgh, Pennsylvania.

Yoder, E.J. and M.W. Witzak, *Principles of Pavement Design*. Second Edition. New York: John Wiley & Sons, Inc, 1975.

Yu, H. T., L. Khazanovich, M.I. Darter, and A. Ardani, "Analysis of Concrete Pavement Responses to Temperature and Wheel Loads Measured from Instrumented Slabs," *Transportation Research Journal: Transportation Research Record 1639*, National Research Council, Washington, DC, 1998.